Investigation of Turbulent Flow in Transitions by Large Eddy Simulation

Rui Zeng

A Thesis
in the Department
of
Building, Civil, and Environmental Engineering

Presented in Partial Fulfilment of the Requirements
For the Degree of
Doctor of Philosophy (Civil Engineering)
at Concordia University
Montreal, Quebec, Canada

July 2023

CONCORDIA UNIVERSITY
SCHOOL OF GRADUATE STUDIES

This is to certify that the thesis prepared

By: Rui Zeng

Entitled: Investigation of Turbulent Flow in Transitions by Large Eddy Simulation

and submitted in partial fulfillment of the requirements for the degree of

Doctor Of Philosophy

complies with the regulations of the University and meets the accepted standards with respect to originality and quality.

Signed by the final examining committee:

Chair
Dr. Mustafa K. Mehmet Ali

External Examiner
Dr. Ioan Nistor

Examiner
Dr. Ebenezer Ekow Essel

Examiner
Dr. Catherine Mulligan

Examiner
Dr. Liangzhu (Leon) Wang

Thesis Supervisor (s)
Dr. S. Samuel Li

Approved by
Dr. Chunjiang An Chair of Department or Graduate Program Director

08/24/2023
Date of Defence

Dr. Mourad Debbabi Dean,

ABSTRACT

Investigation of Turbulent Flow in Transitions by Large Eddy Simulation

Rui Zeng, Ph.D.
Concordia University, 2023

In hydraulic engineering, a transition facilitates a change in the direction, slope or cross-section of an open channel or pipeline. This thesis focuses on expanding flows in open-channel expansions and hydraulic jumps. This thesis uses wall-resolved Large Eddy Simulation (LES) to study the two-phase turbulent flows in several three-dimensional (3-D) geometries, including non-prismatic open channels and sloping pipes. The LES predictions compare well with corresponding experimental results and benchmark solutions.

First, for a turbulent bistable flow approaching a straight-wall channel expansion, either of two stable flow states can occur, depending on the flow history. The thesis aims to reveal the ensemble-average flow characteristics and explore effective ways to control bistability. Turbulent eddies initiated by shear instability dominate those associated with sidewall-friction force, which is responsible for the occurrence of bistability. Fitting a simple hump at a flat-bottom expansion is an effective way to suppress bistability.

Next, hydraulic jumps in sloping pipes are investigated to achieve an improved understanding of jump behaviours driven by different discharges and slopes. Flow behaviours such as free-surface fluctuations and jump-toe oscillations resemble the classical hydraulic jump on horizontal floors. Depending on the discharge and slope, the resulting jump can be a complete or an incomplete jump. The latter causes flow choking downstream, which has severe consequences on drainage conditions in sewer pipes. The Okubo-Weiss parameter is a new way to subtly delineate the region of hydraulic jump.

Last, to study turbulent flows in a non-prismatic warped expansion using LES, the thesis discusses rigorous strategies for model setup, parameter selection and parametric value assignment. Mapping mean-velocity distributions from experimental data, combined with the spectral synthesiser approach for velocity fluctuations, gives a satisfactory inlet condition; alternatively, a 1/7th power-law for the mean-velocity, combined with the vortex method for the fluctuations, is acceptable.

Compared to a prismatic channel, a non-prismatic channel exhibits more complicated eddy motions and turbulence interactions. This thesis contributes to a systematic assessment of computational strategies, result visualisation, and analysis, all relevant to practical applications.

ACKNOWLEDGEMENT

Thank my supervisor Dr. S. Li for his tireless guidance and endless confidence in me,
Otherwise, this thesis would not exist, and
I would have already given up, a million times, this journey.

Thank all three group of researchers for collecting the invaluable experimental data before me,
Otherwise, this thesis would not exist, and
I would have got nothing to compare with and believe.

Thank the committees and paper reviewers for all comments provided to me,
Otherwise, this thesis would not exist, and
I would have had to leave it as it was, imperfect and incomplete.

Thank Pengfei Zhao and other friends for the patient listening and occasional chatting with me,
Otherwise, this thesis would not exist, and
I would have gotten drown in the darkness, long ago, and gone crazy.

Thank M. Oscar A. Quijano X. for the positive influence and steadfast company around me,
Otherwise, this thesis would not exist, and
I would have lost faith in the kindness, the falling leaves and other little drops of beauty.

Thank my parents for giving me life and introducing this world to me,
Otherwise, I would not exist, and this thesis would not exist, and
I would not have been laughing or struggling, or enjoying, or pondering what will be my destiny.

Contribution of Authors

In this manuscript-based thesis, three manuscripts were involved and submitted to different scientific journals.

All the projects were conceptualized and supervised by my supervisor Dr. S. S. Li. Computations were performed and the results were analyzed by R. Zeng. The results were validated by Dr. S. S. Li. The first draft and final draft of manuscripts were jointly written by Dr. S. S. Li and R. Zeng. The thesis was written by R. Zeng.

Rui Zeng	Dr. S. S. Li
Ph.D. Student	Academic Advisor

TABLE OF CONTENTS

List of Figures

List of Tables

List of Symbols

The following symbols have been used in this thesis:

A_0	Water flow area at the inlet of the pipe
A_1, A_2	Cross-sectional water area before and after the open-channel expansion (m^2)
b_1, b_2	Channel widths before and after the expansion, respectively (m)
C	Courant number
C_e, C_e'	Expansion coefficient
C_s	Smagorinsky coefficient
D	For Froude number, hydraulic depth (m); for length scale estimation, hydraulic diameter (Chapter 5) (m)
d_0	Pipe diameter (m)
d_1, d_2	Initial and sequent depths before and after the hydraulic jump (m)
E	Specific energy at a certain cross-section in the channel (m)
$E_{u_i u_i}$	Velocity spectral densities $[(\mathrm{m/s})^2/\mathrm{Hz}]$
Fr_1	Froude number of the approach flow
F_2	Factor of two
f	Output sampling frequency (1/s)
g_i	Gravitational acceleration (m/s^2), $g_1 = g_2 = 0, g_3 = -9.81\ m/s^2$
H	Total height of the geometry (m)
h, h'	Head loss in gradual expansions, calculated using C_e or C_e' (m)
h''	Head loss in sudden expansions (m)
h_e	Water depth at the outlet (m)
h_o	Water depth at the inlet (m)
h_r	Hit-rate
k	Turbulence kinetic energy (m^2/s^2); for autocorrelation calculation, time lag (s)
$\bar{k}$	Ensemble-averaged turbulence kinetic energy (m^2/s^2)
L	Expansion length (m)
L_a	Aeration length (m)
L_r	Roller length (m)
L_s	Mixing length (m)
L_u	Upstream section length (m)
l	Integral scale of turbulence (m); turbulent length scale *l* (m)
l_0	Random length scale (m)
N, n	Number of snapshots used for ensemble averaging
p	Static pressure (Pa); For LES, resolvable-scale pressure (Pa)
$\bar{p}$	Ensemble-averaged pressure (Pa)
$\bar{p}_o$	Reference pressure (Pa)
$\nabla_h \bar{p}$	Horizontal component of pressure gradient (N/m^3)
Q	Discharge of open-channel flow (m^3/s)
q	Discharge of pipe flow (m^3/s)
Re	Reynolds number
R_{ij}	Reynolds stress tensor (m^2/s^2)
r	Correlation coefficient

r_{k}	Autocorrelation
S_{ij}	Resolved strain-rate tensor (s^{-1})
T, t_a	Advection time (s)
T'	Turbulence intensity
T_s	Spin-up time or turn-over time in wind engineering (s)
T_o	Output time (s)
t	Time (s)
t_f	Time scale associated with the fluctuation frequencies of energy-bearing eddies (s)
t_N or t_n	Duration of ensemble averaging (s)
U	Outflow velocity (boundary layer theory) (m/s)
U_2	Cross-sectionally averaged velocity in u_2-direction (Chapter 4) (m/s)
U_o	Cross-sectional average water velocity at the inlet of an open channel (m/s)
u, v, w	Instantaneous velocity components in x, y, z directions (m/s)
$\boldsymbol{u}$	Plane velocity $\boldsymbol{u} = \bar{u}_1\hat{\boldsymbol{x}}_1 + \bar{u}_2\hat{\boldsymbol{x}}_2$ (Chapter 3), $\boldsymbol{u} = \bar{u}_3\hat{\boldsymbol{x}}_3 + \bar{u}_2\hat{\boldsymbol{x}}_2$ (Chapter 4), where $\hat{\boldsymbol{x}}_i$ is a unit vector in the x_i direction (m/s)
u_i	Resolvable-scale filtered velocity component in x_i-direction (m/s)
$\bar{u}_i$	Ensemble-averaged velocity (m/s)
$\langle u_j \rangle$	Accumulatively averaged velocity (m/s)
$\langle \bar{u}_2 \rangle$	Vertically averaged velocity over one line normal to the pipe invert (m/s)
u_m	Cross-sectional mean velocity in the streamwise direction; subscript 1 and 2 denote the cross-sections before and after the expansion, respectively (m/s)
u_p	Velocity parallel to the pipe invert (m/s)
u_0	Cross-sectional average water velocity at the inlet of a pipe (m/s)
u_*	Friction velocity (m/s)
V	Velocity magnitude (m/s), $V = (\bar{u}_1^2 + \bar{u}_2^2 + \bar{u}_3^2)^{1/2}$ (Chapter 3); Cross-sectional average water velocity at the jump toe (Chapter 4) (m/s)
v_0	Peak velocity over a profile normal to the pipe invert (Chapter 4); mean-inflow velocity (Chapter 5) (m/s)
w	Okubo-Weiss parameter (m^2/s^2)
x, y, z	Rectangular Cartesian coordinates (m). For boundary layer theory derivation, x is parallel to the wall and y is normal to the wall. For the derivation of energy coefficient α, x is the streamwise direction.
x_i, x_j	Position vectors in tensor notation (m), i and j = 1, 2, 3 for the transverse, longitudinal and vertical directions, respectively
Y	Pressure head (m)
y	For y^+ estimation, distance to the wall (m)
y_0	Prescribed depth of water inflow at the inlet of the pipe (m)
y^+	Dimensionless wall distance
α	Energy coefficient; slope angle of the upstream pipe (Chapter 4) (°)
α_i	Volume fraction of the fluid, the subscripts 1 and 2, respectively, refer to air and water
$\bar{\alpha}_i$	Ensemble-averaged volume fraction
β	Momentum coefficient
Δ	Local grid scale (m)
Δh_v	Difference in velocity head across the expansion (m)

ΔT	Difference of top widths of the upstream and downstream channels (m)
Δt	Timestep size (s)
Δu_i	Root-mean-square-deviation between the instantaneous and ensemble-averaged velocity (m/s), see Section 5.5.1 for more information
Δx_i	Local mesh size in the x_i-direction (m)
$\Delta x_{\mathrm{i}}^{+}$	Dimensionless mesh size
δ	height of the hump (m)
$\delta \bar{u}_2$	Root-mean-square-error of streamwise-velocity compared to experimental data (m/s) , see Section 5.5.1 for more information
ε	Turbulent dissipation rate (m^2/s^3)
η	Free surface elevation (m)
$\bar{\eta}$	Ensemble averaged free surface elevation (m)
θ	Expansion angle (°), $\theta = \arctan \Delta T/2L$
θ_0	Characteristic angle to calculate the cross-sectional area in a partially full pipe (°)
κ	Wave number, corresponding to a random length scale by $\kappa = 2\pi/l_0$
λ	Eddy length scale (m)
μ, μ_i	Dynamic viscosity of the fluid (Pa·s); the subscripts 1 and 2, respectively, refer to air and water
μ_t	subgrid-scale turbulent viscosity (Pa·s)
ν	Kinematic viscosity of the fluid, $\nu = \mu/\rho$ (m^2/s); the subscripts 1 and 2, respectively, refer to air and water
ν_τ	eddy viscosity (m^2/s)
ρ	Mass density of the fluid (kg/m^3); the subscripts 1 and 2, respectively, refer to air and water
σ_w	Standard deviation of Okubo-Weiss parameter (m^2/s^2)
τ	Wall shear stress (Pa)
τ_b	Bottom shear stress (Pa)
τ_{ij}	Subgrid-scale stress tensor (Pa)
ω_i	Vorticity with the axis along the x_i-direction (1/s)

List of Abbreviations

ABL	Atmospheric boundary layer
AVF	Air volume fraction
CCW	Counterclockwise
CW	Clockwise
CFD	Comuputational fluid mechanis
CHJ	Classical hydraulic jump
CS	Cross-section
DES	Detached eddy simulation
DNS	Direct numerical simulation
DKE	Dynamic kinetic energy
DSM	Dynamic Smagorinsky-Lilly
IC	Initial condition
ITL	Inlet turbulent fluctuation
LES	Large eddy simulation
NBT	Numerical beach technique
RANS	Reynolds-averaged Navier–Stokes
RMSD	Root-mean-square-deviation
RMSE	Root-mean-square-error
RSM	Reynolds Stress Model
SGS	Subgrid-scale
SS	Spectral synthesizer
TBF	Turbulent bistable flow
TKE	Turbulence kinetic energy
VM	vortex method
WALE	Wall-adapting local eddy-viscosity
WVF	Water volume fraction
2-D	Two-dimensional
3-D	Three-dimensional

1 Introduction

1.1 Background

In hydraulic engineering, a transition can be defined as a change in the direction, slope or cross-section of a channel or pipeline that results in a change in the flow state (Henderson, 1966, p. 235). This thesis focuses on flows of which the cross-sectional area expands in the streamwise direction, usually seen in open-channel expansions or hydraulic jumps where the flow expands vertically.

1.1.1 Expanding flow in open-channel expansions

Open-channel expansions can be found in both natural open channels and constructed hydraulics facilities, such as flows past subdivided channels, bridge piers, culverts, and siphons. They are also used in stormwater drainage systems and water treatment plants to manage and control the flow. In irrigation canals and hydropower channels, where the flow is generally subcritical and turbulent in nature, the amount of energy loss in the expansion is of great importance as it reduces the efficiency of the irrigation systems and their command (Asnaashari et al., 2016) and leads to less hydropower generation (Najafi-Nejad-Nasser & Li, 2015). This research focuses on the energy-saving perspective of these hydraulic structures.

Why is there strong energy loss in open channel expansions? As the cross-sectional area increases in the streamwise direction, the entrance velocity is higher than the exit velocity. Therefore, based on the energy principle, there is an increase in flow depth. This adverse pressure gradient leads to flow separation, resulting in a continuous reduction of kinetic energy and its partial conversion to pressure energy in open channel expansions. This partial conversion, known as energy loss, is caused by both form loss due to flow separation and friction loss.

Flow separation in a channel expansion can also increase the risk of channel erosion. The flow separates near one side of the cross section, which is unable to convey water downstream, pushes the main flow to the other side. This results in irregular velocity distributions and stronger velocity extremes, causing high wall shear stresses on the channel boundaries (sidewalls and bottom). These high wall shear stresses can scour the channel materials, including sediments and linings. In the case of a sudden expansion, the resulting channel erosion can create a scour hole at the transition outlet as deep as upstream flow depth (Smith & Yu, 1966).

The design criteria of channel expansions are as follows: avoiding excessive energy losses, eliminating turbulent flow disturbances, and providing safety for the structure and waterway (Chow, 1959, p. 310). Short expansions are economical to construct and easy to maintain, but they are more likely to cause flow separation. A balance must be sought between construction costs and acceptable levels of energy losses while considering channel boundary erosion (Austin et al., 1970). An efficient transition should confine flow non-uniformity to a short distance downstream of its exit, and therefore, requires less boundary protection. Generally speaking, a transition structure that results in a smooth water surface profile is considered satisfactory. The suppression of flow separation is a direct solution to improving the channel expansion performance.

To reduce the flow separation or achieve a more uniform flow at the expansion exit, researchers have attempted to design more efficient transition profiles, including both sidewall and bed profiles (Asnaashari et al., 2016; Hartley et al., 1940; Hinds, 1928; Swamee & Basak, 1993; Thapa et al., 2018; Vittal & Chiranjeevi, 1983), use vanes (Hinds, 1928; Ippen, 1949; Ramamurthy et al., 2017;

Scobey, 1933) or baffles (Austin et al., 1970; Hyatt, 1965; Smith & Yu, 1966) to direct the flow, and install a hump at the bottom of the expansion (Haque, 2009; Najafi-Nejad-Nasser & Li, 2015; Ramamurthy et al., 1970). Recent numerical work using comuputational fluid mechanis (CFD) regarding this matter includes the research of Najmeddin and Li (2016) and Li et al. (2019), but these are limited to the use of Reynolds-averaged Navier–Stokes (RANS) models. This thesis aims to continue the previous experimental work and utilize the inherently more accurate large eddy simulation (LES) technique to explore feasible methods for suppressing flow separation and reducing the associated energy loss.

Turbulent bistable flow (TBF) is a fundamental phenomenon in fluid dynamics whereby the flow exhibits two stable equilibrium states, which are asymmetrical about the centerline in perfectly symmetrical open-channel expansions (Smith & Yu, 1966; Thapa et al., 2018). Asymmetrical flow patterns have been observed in sediment settling/deposition tanks (Camnasio et al., 2013; Dewals et al., 2012; Ferrara et al., 2018), as well as behind symmetrical automotive bodies, square ship bodies and fuselages in wind tunnels. However, previous studies have not addressed the question of turbulent flow bistability and asymmetry in open-channel expansions. The studies on settling tanks highlight the need to investigate how initial conditions influence TBF through the use of advanced three-dimensional (3-D) modelling, such as LES.

This study will perform two-phase LES of 3-D turbulent flow with a free surface, which offers an advantage over LES that uses the rigid-lid approximation (Rodi et al., 2013) and/or a two-dimension (2-D) simplification with the cross-sectional dimension missing (e.g., Yue et al., 2005). The depth increase of subcritical flow and flow separation are important characteristics of expanding flow but are ignored in the rigid-lid approximation and 2-D simplification. Moreover, the proper selection of setups and parameters for numerical simulations of 3-D flows in open-channel expansions (non-prismatic channels) remain unclear. These include not only traditional questions such as the selection of mesh size, timestep size, and ensemble average time, but also determining the appropriate inlet velocity profiles, specifying the inlet turbulence, and establishing the inlet channel length for flow development, all of which are critical to achieving accurate simulations.

1.1.2 Expanding flow through hydraulic jump phenomenon

Flooding in cities is a growing problem, and one of its causes is related to sewer pipes under the roads. They constantly transport dirty water and rainwater from the city to nearby rivers. However, sometimes the water in these pipes can suddenly jump from a low elevation to a high elevation and expand vertically. This phenomenon is known as a hydraulic jump and occurs when water changes from supercritical flow to subcritical flow. The hydraulic jump occurs in pipes because the pipeline connecting our homes to nearby rivers is not a straight line; it has to turn to adapt to the up and down of the city roads. A small turn in the pipeline can cause the water to jump higher and even create a blockage in the flow. The blockage can cause dirty water to burst out like a fountain or a volcano, resulting in urban flooding.

Previous researchers have conducted experimental studies on this phenomenon, but with very few choices of pipe slopes or a focus solely on air flow (Qian et al., 2017). However, the internal relationship between flow conditions, pipe slopes and this phenomenon has not been investigated. CFD has the advantage of obtaining detailed flow information to complement the experimental

work and enable the calculation of speed, pressure, water percentage at every single nodal point in these pipes.

Given the current state of knowledge, it is important to address the following questions in this thesis: Is it possible to capture TBF through numerical simulation using advanced LES techniques? What are the effective ways to suppress the TBF and flow asymmetry in open-channel expansions? Can the "dirty water volcano" caused by a hydraulic jump in sewer pipes be predicted using LES? Where exactly does the water jump in the pipe transitions, and how can it be controlled? Is the hydraulic jump more sensitive to discharge or pipe slopes? How can the inlet boundary condition be set up to best replicate the flow conditions of an experiment? What is the proper ensemble average time to obtain accurate results in the numerical simulations?

1.2 Objectives

This research performs numerical simulations using LES to investigate 3-D turbulent flows in open-channel expansions, including a straight-wall expansion connecting two rectangular channels, a warped expansion connecting a rectangular channel to a trapezoidal channel, and pipe transitions with hydraulic jump phenomenon. After validating the results using the benchmark solution and experimental data, the objectives are as follows:

(1) To reveal the ensemble-average 3-D complex flow characteristics in open-channel expansions, such as the velocity field, pressure field, fluid volume fraction, eddy motions and kinetic energy distribution, as well as in pipe transitions involving the hydraulic jump phenomenon, including air and water velocities, 3-D eddies, free-surface profiles, roller length and aeration length
(2) To investigate the principle and cause of flow bistability and explore effective ways to control or suppress bistability and flow separation
(3) To observe the complex jump behaviour in pipes with changes in pipe slope and discharge
(4) To investigate proper setups and parameters for obtaining accurate simulation results, especially the setup of inlet velocity profiles, inlet turbulent fluctuations, and inlet channel length.

The objectives are achieved with access to a sufficient amount of data for LES model validation.

1.3 Scope of this Research Work

This research is primarily focused on assessing the viability of employing two-phase 3-D LES for the analysis of turbulent expanding flows within various non-prismatic hydraulic structures. The investigation is limited to numerical simulations and validation through comparison with relevant experimental studies of laboratory scale and benchmark solutions. In reality, there are always suspended particles in the flow. This aspect is not considered in the present study. The research holds significance in enhancing the comprehension of turbulent flow behaviours within open-channel expansions and hydraulic jumps occurring in drainage pipes. These insights are of paramount importance in the optimal design of critical hydraulic systems, such as irrigation canals, hydropower channels and drainage pipes. By confining its scope to the aforementioned aspects, this study contributes to a deeper understanding of complex fluid dynamics and their application in real-world hydraulic engineering scenarios.

To achieve the objectives, the remaining part of the thesis is organised as follows:

Chapter Two provides a summary of literature review on expanding flows in open-channel expansions and hydraulic jump in pipe transitions. It also includes the theory and characteristics of flow separation, previous attempts to suppress the flow separation in expansions and the effective methods for inlet turbulence specification.

Chapter Three presents the numerical study of 3-D TBF in an open channel expansion and a method to suppress bistability. This chapter contains information published in Physics of Fluids: https://doi.org/10.1063/5.0089093

Chapter Four presents LES results of hydraulic jumps in sloping pipes, which improves the understanding of hydraulic jump behaviour under the influence of changing pipe slopes and discharges. This chapter contains information published in Journal of Hydrodynamics: https://doi.org/10.1007/s42241-023-0090-3

Chapter Five presents the behavior of turbulent flow in a non-prismatic open channel using LES. This channel under study is characterized by a warped transition. The chapter discusses comprehensive strategies for model setup, parameter selection and parametric value assignment. These strategies are developed through comparisons of velocity profiles with experimental data. To assess the accuracy of a given strategy and assist in the selection process, validation metrics such as root-mean-square-error, hit-rate and factor-of-two are employed.

Chapter Six summarizes the LES results presented in this thesis and provides suggestions for further research related to turbulent expanding flows.

1.4 Contributions

Several contributions from this research are outlined below:

(1) This thesis presented numerical results for turbulent open-channel flows using 3-D two-phase LES. The procedures and strategies developed in this study contribute to the establishment of best practices for LES simulations of turbulent open-channel flows, which are obtained through a comparative analysis of open-boundary treatments, flow initializations, and turbulence closures for non-prismatic channels.

(2) The study of flows in three different geometries has revealed the presence of 3-D complex structures caused by eddy motions that are translated from upstream and locally generated by asymmetrical flow separation in the expansion or through the hydraulic jump phenomenon in pipe transitions. In circular pipes, the hydraulic jump exhibits flow features such as free-surface fluctuation and jump-toe oscillation that resemble the classical hydraulic jump on horizontal floors. These findings contribute to a better understanding of the 3-D complex behavior of turbulent expanding flows in open channels or circular pipes.

(3) This thesis uses the Okubo-Weiss parameter to identify and characterize 3-D instantaneous coherent turbulence structures, which are useful to address channel erosion risks. This parameter is also more efficient and less ambiguous than traditional visual inspections in delineating the region of hydraulic jump. Furthermore, this parameter helps explain the occurrence of flow bistability.

(4) This thesis highlights the effectiveness of a simple hump installed at the channel bottom in suppressing bistability, improving flow uniformity and increasing hydraulic efficiency of an open channel.

(5) The investigation of choked flow related to incomplete hydraulic jump in circular pipes provides insight into reducing the risk of urban flooding in sloping terrain.
(6) The LES methods in this research are reliable, efficient, and cost-effective. This LES study offers an attractive complement to physical models, laboratory experiments, and field measurements.
(7) The extensive computational simulations, each spanning a duration of 20 to 30 days, underscore the depth and rigor of this research effort. The resultant findings and conclusions stand to offer subsequent researchers a substantial reduction in the effort required. By providing these valuable insights, this study not only advances the field but also alleviates the significant time and resources that would otherwise be invested in similar explorations.

2 Literature Review

2.1 Flow separation

The Energy loss in open-channel expansion is directly related to the flow separation phenomenon. This section begins with an introduction to the concept of flow separation based on the boundary layer theory and explores the main factors that determine the strength of flow separation. The section then discusses the characteristics of flow separation in channel expansions. Lastly, it summarizes different types of open-channel expansions.

2.1.1 Flow separation phenomenon

When a fluid is forced to flow over a curved surface (Figure 2.1), such as the sidewall of a channel expansion, the back of a cylinder, or an airfoil, the boundary layer may no longer remain attached and separates from the surface, taking the forms of eddies and vortices. This process is called flow separation.

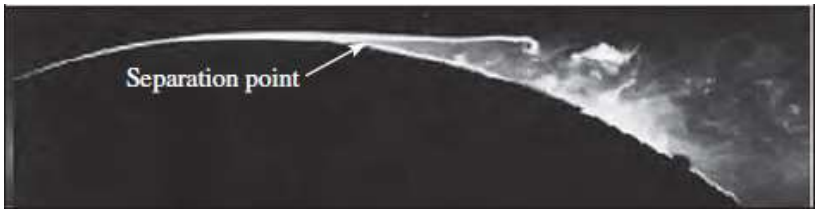

Figure 2.1 Flow separation during flow over a curved surface (Çengel & Cimbala, 2018, p. 9)

In aerodynamics, flow separation often results in increased drag, particularly pressure drag, which is caused by the pressure difference between the front and rear surfaces of the object as it travels through the air. For an automobile, most of the energy generated in a combustion engine is used to overcome the energy loss resulting from the flow resistance. Therefore, it is critical to optimize the automobile body to prevent the airflow from breaking from the body (Durst, 2008, p. 3). For an airplane, the airfoils are designed to give good performance during both take-off and landing. While taking off, the plane avoids flow separation to better overcome air resistance. When the plane lands, the angle of attack of airfoil changes, inducing flow separation to help in deceleration. When flying at high altitude, the plane requires minimal losses while maintaining a high lift. Numerous methods have been developed to reduce flow separation on an airfoil. One such method involves introducing a fast-moving jet to mix with the flow in the boundary layer and accelerate the slow-moving air layer near the body. The Handley Page leading edge slot is a notable application of this principle, as it allows high-velocity air from below the wing to pass into the upper wing surface boundary layer before separation (Figure 2.2(a)). Another method involves suction at the end of an airfoil to revitalize the slow-moving flow in the boundary layer. Furthermore, as turbulent flow boundary layer can better resist flow separation, gliders use a turbulator (Figure 2.2(b)) to induce an early transition to turbulent flow regime, which is another way to reduce the flow separation. Similarly, fuzzes and dimples are added to tennis balls and golf balls to achieve the same purpose.

In hydraulics, flow separation occurs when the flow in a typical pipe system passes through various fittings, such as valves, bends, elbows, inlets, exits, expansions, and contractions. These components interrupt the smooth flow of the fluid and cause additional losses due to flow separation and mixing. All pumps experience irreversible losses due to friction, internal leakage, flow separation on blade surfaces and turbulent dissipations (Çengel & Cimbala, 2018, p. 797).

Flow separation is a common phenomenon in decelerated turbulent subcritical flows in open channels. It can occur before a facing step, after a backward-facing step, after a weir, and past sudden expansions and gradual expansions.

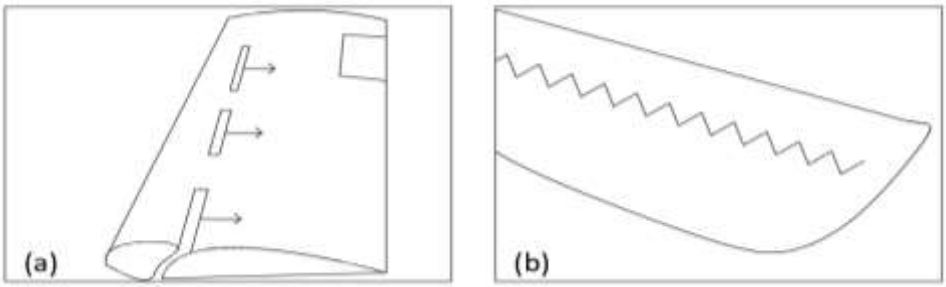

Figure 2.2 (a) Leading edge slot on an airfoil; (b) turbulator on a glider

2.1.2 Boundary layer theory

To better understand the flow separation concept, it is important to introduce the boundary layer theory. Ludwig Prandtl formulated the boundary layer theory and found that at high Reynolds numbers, flow separation is caused by the separation of boundary layer from the solid boundary. When an object moves through a fluid or is exposed to moving fluid, a layer of fluid (known as the boundary layer) forms around it, which experiences viscous forces. The boundary layer theory can be used to identify the separation point and compute the flow characteristics up to that point; however, it cannot predict the behavior of the separated-flow region and its interaction with the outer flow. This is because the separated-flow region contains reverse flow near the wall, which causes the parabolic nature of the boundary layer equations to disappear. In such cases, the Navier–Stokes equations are required to replace the boundary layer approximation. Researchers often employ CFD simulations to gain more insight into separated flow and the associated wakes.

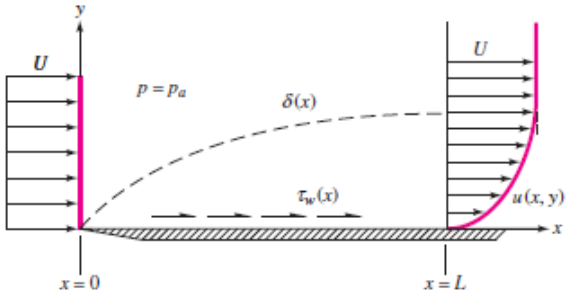

Figure 2.3 Growth of a boundary layer on a flat plate (White, 2009, p. 461)

When the boundary layer theory is applied to the flow over a flat plate, Figure 2.3 shows the steady 2-D incompressible viscous flow with x-direction along the wall and y-direction normal to the wall, u and v are the velocities, respectively, p is the pressure, δ is the thickness of the boundary layer, and U is the outflow velocity. By starting from the continuity equation and momentum equations, and the Bernoulli equation, and making some assumptions, the following relationship can be established at the wall:

$$\left.\frac{\partial \tau}{\partial y}\right|_{y=0} = \mu \left.\frac{\partial^2 u}{\partial y^2}\right|_{y=0} = -\rho U \left(\frac{\partial U}{\partial x}\right) = \frac{dp}{dx} \tag{2.1}$$

where τ is the wall shear stress, μ is the dynamic viscosity and ρ is the density. Prandtl showed that flow separation arises from excessive momentum loss near the wall when a boundary layer moves downstream against increasing pressure ($dp/dx > 0$), which is known as an adverse pressure gradient. The opposite scenario of decreasing pressure ($dp/dx < 0$) is termed a favorable pressure gradient, where flow separation can never occur.

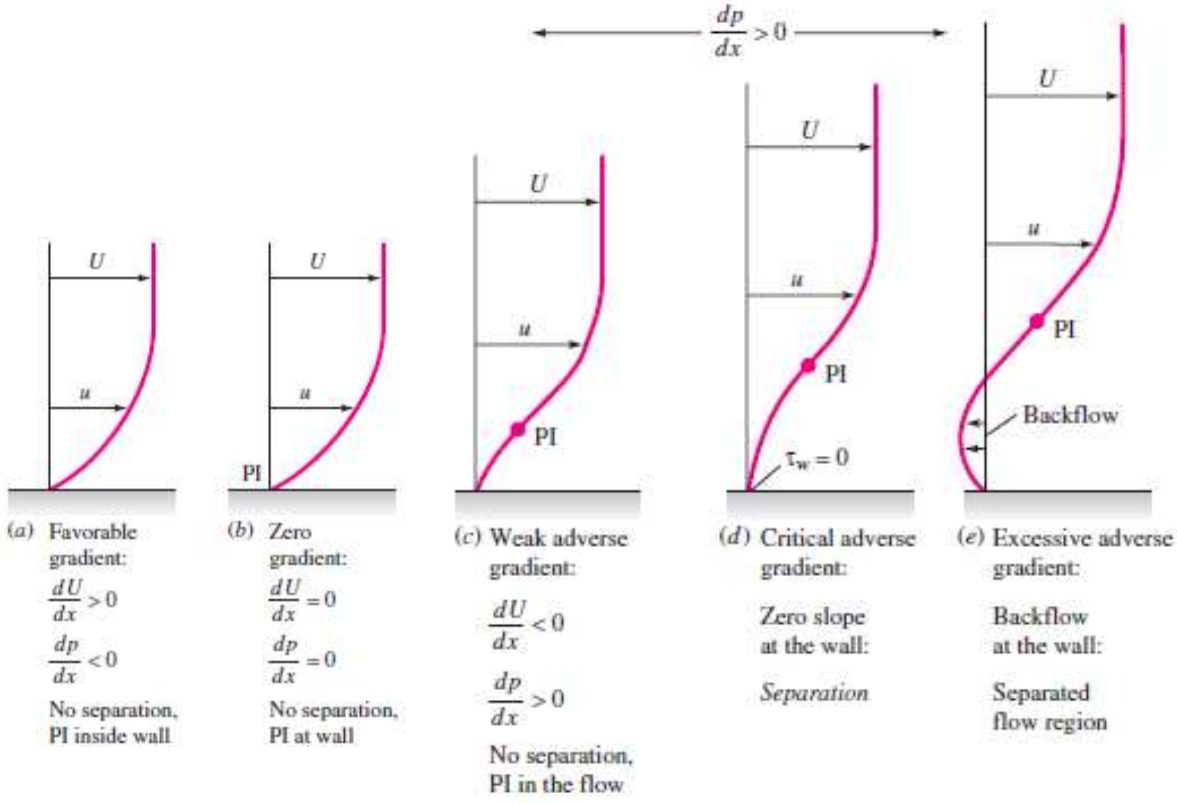

Figure 2.4 Effects of pressure gradient on boundary layer profiles; PI: point of inflection (White, 2009, p. 477)

Under a favorable pressure gradient ($dp/dx < 0$) and an accelerating outflow ($dU/dx > 0$), the second derivative of u at the wall is negative ($\partial^2 u/\partial y^2|_{y=0} < 0$) and it must remain negative as u approaches $U(x)$ at the edge of the boundary layer. The boundary layer profile has a rounded shape without any inflection point under this condition (Figure 2.4(a)). Similarly, a zero pressure gradient ($dp/dx = 0$) indicates a linear growth of u with respect to y near the wall ($\partial^2 u/\partial y^2|_{y=0} = 0$) (Figure 2.4(b)). Under an adverse pressure gradient ($dp/dx > 0$) and a decelerating outflow ($dU/dx < 0$), the second derivative of velocity u at the wall ($\partial^2 u/\partial y^2|_{y=0} > 0$) is positive. However, this value must change to negative as u approaches $U(x)$ at the edge of the boundary layer to merge smoothly with the mainstream flow. This indicates an inflection point ($\partial^2 u/\partial y^2|_{y=0} = 0$) (PI) somewhere in the boundary layer. Any boundary layer profile in an adverse gradient must exhibit a characteristic S shape (Figure 2.4(c)–(e)). If the adverse pressure is large enough, wall shear stress ($\tau = \partial u/\partial y|_{y=0}$) becomes zero at a certain point, indicating the separation point (Figure 2.4(d)). Beyond the separation point, there will be reverse flow and a region of recirculation called a separation bubble (Figure 2.4(e)), and the wall shear stress changes

to negative. The location of separation point depends on several factors such as Reynolds number (Re), surface roughness, and the level of fluctuations in the freestream. It is usually difficult to predict exactly where separation occurs unless there are sharp corners or abrupt changes on the solid surface.

2.1.3 Flow separation in open-channel expansion

External flow refers to the flow of a fluid over a surface object, such as when fluid flows past a cylinder or airfoil, while internal flow occurs when fluid flows through a confined space, such as closed ducts or pipes. Flow in open-channel expansion is an example of internal flow. Flow separation can occur either on one side of the expansion with the formation of a large return eddy or on both sides with a large central jet (Austin et al., 1970). Flow separation causes head loss in the expansion and downstream of the expansion because maintaining constant moving vortices consume lots of energy. The head loss in a gradual channel expansion is often expressed in terms of the change in the velocity head as

$$h = C_e \Delta h_v \tag{2.2}$$

or

$$h' = C_e' \frac{(u_{m2} - u_{m1})^2}{2\mathrm{g}} \tag{2.3}$$

where h is the expansion head loss, Δh_v is the difference in velocity head across the expansion, and C_e is the expansion coefficient (Henderson, 1966, p. 237). Another expression for expansion head loss is h' with a respective expansion coefficient of C_e' (Akan, 2006, p. 244); u_{m1} and u_{m2} are the cross-sectional mean velocity before and after the expansion, respectively. The energy loss expressed in Eqs. 2.2 and 2.3 consists of both friction loss and form loss. Friction loss can be estimated using Manning's equation, but it generally has very little effect on the flow profile and may be ignored in preliminary design of the expansion (Chow, 1959, p. 310). However, Ramamurthy et al. (2017) have commented that friction loss is important in channel expansions and should not be neglected.

The expansion angle is defined as $\theta = \arctan \Delta T/2L$, where ΔT is the difference of top widths of the upstream and downstream channels and L is the expansion length. A small θ leads to weak flow separation (Ramamurthy et al., 2017). Researchers define the efficiency of expansion as the ratio of the gain in potential energy to the loss in kinetic energy. As the upstream Froude number and inlet discharge increase, the efficiency of the transition decreases (Alauddin & Basak, 2006; Asnaashari et al., 2016).

The number of recirculation zones in the streamwise direction is highest in the middle and decreases towards the exit of the expansion. Meanwhile, the mean bed shear at one cross-section decreases from the entrance towards the middle and then increases at the exit of the expansion. The maximum bed shear stress at the expansion entrance increases with the Froude number at inlet (Asnaashari et al., 2016). Moreover, flow separation is stronger near the water surface and occupies about one-fifth of the expansion area when the expansion angle and Froude number are large (Najmeddin & Li, 2016). The strength of flow separation depends on the upstream Froude number, inlet discharge and expansion angle. Specifically, the larger the upstream Froude number, inlet discharge and expansion angle, the stronger the flow separation.

Asymmetric flow patterns in gradual channel expansion occur when the expansion angle is large (Mehta, 1979; Smith & Yu, 1966) or when the flow discharge is greater than 10 L/s (Asnaashari et al., 2016; Thapa et al., 2018). The asymmetrical separated flow region results in a deviation between the maximum velocity line and the centerline. Initially, the maximum velocity line coincides with the centerline of the channel, but it shifts towards the side to which the main flow is tilted after a short distance from the expansion entrance.

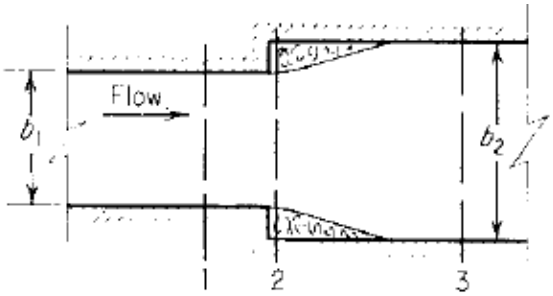

Figure 2.5 Plan view of rectangular channel sudden expansion (Henderson, 1966, p. 236)

2.1.4 Type of expansions

Open-channel expansion can vary from sudden expansions, such as straight-line headwalls, to very elaborate gradual expansions. In a sudden channel expansion, two channels of different sizes are directly connected with a wall normal to the flow direction (Figure 2.5). Flow separation begins at the point where the cross-section changes. This type of connection is considered satisfactory for small structures or situations where saving head loss is not a priority. Henderson (1966, p. 236) developed an expression for energy loss h'' in sudden expansions. By applying the momentum equation, energy equation and some assumptions, the energy loss is given by:

$$h'' = \frac{\bar{u}_{m1}^2(1 - A_1/A_2)^2}{2\mathrm{g}} + \frac{2Fr_1^2 b_1^3(b_2 - b_1)}{b_2^4} \tag{2.4}$$

where b_1 and b_2 are the width before and after the expansion, and A_1 and A_2 are the cross-sectional area before and after the expansion, respectively.

Note that this equation has an open-channel flow term at the end that does not contribute much to the total head loss. Durst (2008, p. 207) studied sudden expansions under various Reynolds numbers. The streamlines of the unsteady flow separation fields are identical for all Newtonian fluids and all dimensions if they have the same corresponding Reynolds number.

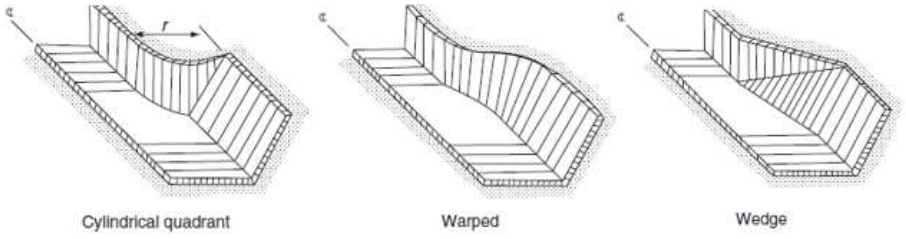

(a) (b) (c)

Figure 2.6 Common types of expansions (Akan, 2006, p. 245), (a) cylindrical transition (b) warped transition, (c) wedge transition

A gradual open-channel expansion has a gradual change in the elevation or width of the transition bed or in the slope of sidewalls. In most cases, the geometry of channel expansion changes laterally, resulting in a gradual change in flow conditions. The straight-wall expansion connects channels of the same shape but with different dimensions. Using a smaller expansion angle would cause a longer and more expensive structure but with a weaker flow separation (Smith & Yu, 1966). Figure 2.6 shows the most common expansions connecting rectangular and trapezoidal channels. The warped transition has the lowest head loss, but it is also the most expensive to construct due to its large dimension (Hinds, 1928). The expansion angle θ should be less than 12.5° (Akan, 2006, p. 249; Morris & Wiggert, 1972, p. 187). The cylindrical expansion (Figure 2.6(a)) comprises two circular wings or vertical walls that are tangent to the flume sides and curve through a quarter turn to meet the sides of the trapezoidal channel. It was introduced as a cost-effective alternative to the expensive warped transition in the last century (Figure 2.6(b)). It is suitable for small structures from the construction perspective, but it is the least effective among the three (Thapa et al., 2018). The radius is proposed to be half of the difference between the top widths of the connected channels (Akan, 2006, p. 262). The wedge-type expansion (Figure 2.6(c)) is a further simplification of the cylindrical expansion. The suggested value for θ is 22.5° (Akan, 2006, p. 249). The wedge expansion is easy to build but less effective.

Energy loss can be calculated as the difference between specific energy upstream and downstream of the expansion. The specific energy *E* is defined as pressure head *Y* plus the velocity head,

$$E = Y + \alpha \frac{u_m^2}{2g} \tag{2.5}$$

where u_m is the cross-sectional average velocity and α is the uniformity velocity coefficient

$$\alpha = \frac{\iint u^3 dA}{u_m^3 A} \tag{2.6}$$

The warped expansion and the cylindrical expansion have the energy loss coefficient C_e (Eq. 2.2) as low as 0.2 and 0.25 (Chow, 1959, p. 311), respectively. In contrast, both the wedge expansion and a straight-wall expansion that connect rectangular channels have a C_e value of 0.5. The sudden expansion has C_e of 0.75. Morris and Wiggert (1972) measured C_e values ranging from 0.3 for a warped transition to 0.75 for a sudden expansion. For the straight-wall expansion connecting two rectangular channels, Henderson (Henderson, 1966, p. 236) suggested a length to width ratio of sidewall to be 1:4 (expansion angle θ = 14°), resulting in C_e = 0.1 (Eq. 2.2) and C_e' = 0.3 (Eq. 2.3). The exact form of the sidewalls is not a matter of great importance if there is no flow separation (Henderson, 1966, p. 237).

The proper design of the open channel expansion is important because the complex subcritical flow at the expansion can cause water blockage, bank erosion and energy loss. The internal shear between the flow in the middle and that close to the sidewalls generates coherent structures consisting of intermittent large-scale eddies. These eddy motions form recirculation zones, and therefore cause a flow blockage with less effective flow area. As these large eddies maintain roughly the same size and rotate almost at the same place (Holmes et al., 2012, p. 38), there exists constant erosion against channel banks (Alauddin & Basak, 2006; Smith & Yu, 1966) and significant energy loss (form loss).

2.2 Suppressing flow separation in expansion

2.2.1 Efficient profiles

In the design of a channel expansion connecting a rectangular and a trapezoidal cross-section, researchers have investigated expansion profiles to minimize flow separation and energy loss for a specific transition length and expansion angle. Hinds (1928) developed sidewall, water-surface and bed width profiles assuming that the form loss (Eq. 2.2) depends solely on the upstream and downstream velocity, which was later invalidated by Alauddin and Basak (2006). Hartley et al. (1940) developed bed width profiles based on a constant depth assumption. Swamee and Basak (1993) used the continuity equation and the form head loss equation (Eq. 2.2) and applied the optimal control theory to design the gradual expansion. However, Asnaashari et al. (2016) found the efficiency of the expansion is lower than 50% and energy loss coefficient C_e is about $0.4-0.6$ for Froude number larger than 0.47. Strong flow separation phenomenon still exists near the exit of the expansion and the model used a constant flow depth assumption. Moreover, it is necessary to account for the friction losses when boundary profile changes gradually (Thapa et al., 2018).

Other researchers have utilized flow separation streamlines in sudden expansions to design gradual expansions. Vittal and Chiranjeevi (1983) developed equations to determine the expansion length, flow depth, and sidewall and bottom width profiles by using only the bottom and top separation lines and connecting them in each cross section with a straight line. The optimal bed width profile for a gradual channel expansion coincided with the separation streamline near the bed in a sudden expansion. Alauddin and Basak (2006) continued the development of a streamlined channel transition model using streamlines in rectangular expansions, which results in significant head loss (Asnaashari et al., 2016). While the idea reduces the flow separation to a certain extent, it cannot eliminate or entirely suppress the flow separation due to the development of a boundary layer along the streamlined boundary of the gradual expansion.

2.2.2 Baffles

To date, no perfect transition profile has been identified. After conducting numerous experiments with various expansion angles and combinations of vanes, block and columns, a three-triangular baffle arrangement (Figure 2.7(a)) was found effective in smoothly spreading the flow in trapezoidal open channel transitions (Hyatt, 1965). This arrangement eliminated the flow separation and ensured uniform velocity distribution at the exit of the trapezoidal channel expansion. However, the head loss in the trapezoidal expansion remained nearly the same with or without the columns, which could be attributed to the friction loss caused by the triangular baffles and the resistance force acting normal to the flow by the baffle fronts. Alternatively, Smith and Yu (1966) developed a three-square baffle arrangement (Figure 2.7(b)) to guide the flow in a straight-wall channel expansion, connecting the approach rectangular flume to the downstream trapezoidal erodible channel, with an expansion angle of 14°. To ensure uniform flow in the transition, the baffles need to extend through the entire depth of the flow. Additionally, there needed to be considerably more space in the cross section than the cross-sectional area of baffles. Otherwise, the baffles would constitute a barrier or obstruction. Austin et al. (1970) experimentally studied the geometrical placement of baffles in open channel expansions by trial and error. The best arrangement of baffles for uniform velocity distribution is only applicable to certain fixed discharges and tail water conditions.

At that time, velocity reduction was the primary objective and head loss saving was of secondary importance. As a result, the maximum velocity at the end of the outlet was effectively reduced, and channel scour was completely absent. However, the head loss in the baffled expansion was greater than the plain expansion. More energy was dissipated in the wake created by the baffles than in the eddies that form in the plain expansion. Therefore, this arrangement is not applicable to power canals and irrigation canals.

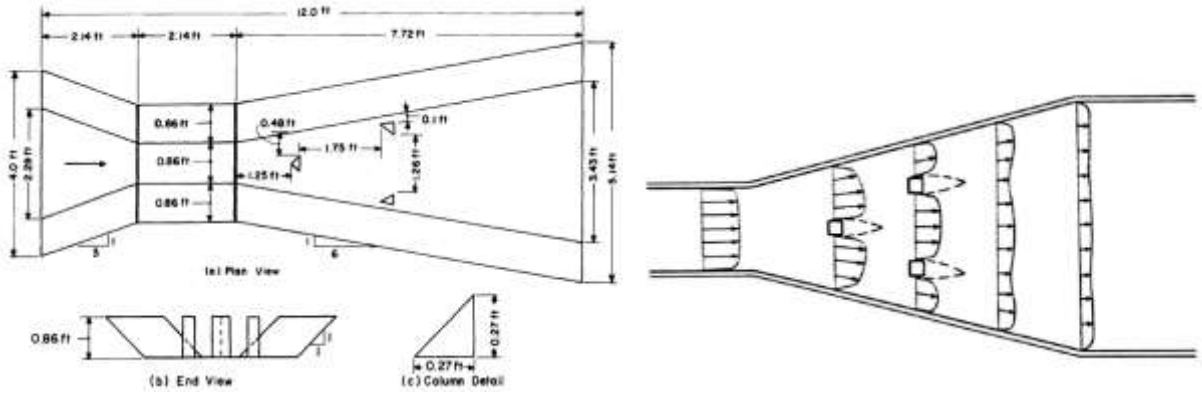

(a) (b)

Figure 2.7 Plan view of arrangements of baffles in a transition (a) connecting trapezoidal channels (Hyatt, 1965) or (b) connecting rectangular channels (Smith & Yu, 1966)

2.2.3 Fitting a hump

Expansions typically have a flat bottom. Researchers have focused mostly on optimizing the shape of expansion sidewalls to suppress the flow separation, as discussed in section 2.2.1. For existing expansions, incorporating a hump at the bottom is less expensive than modifying the sidewalls. The hump accelerates the flow, neutralizes the decelerating effects of channel width expansion, and creates favorable pressure gradients, which prevent flow separation and efficiently reduce energy loss. As the flow passes over the hump, a portion of the flow energy is converted to elevation head and preserved.

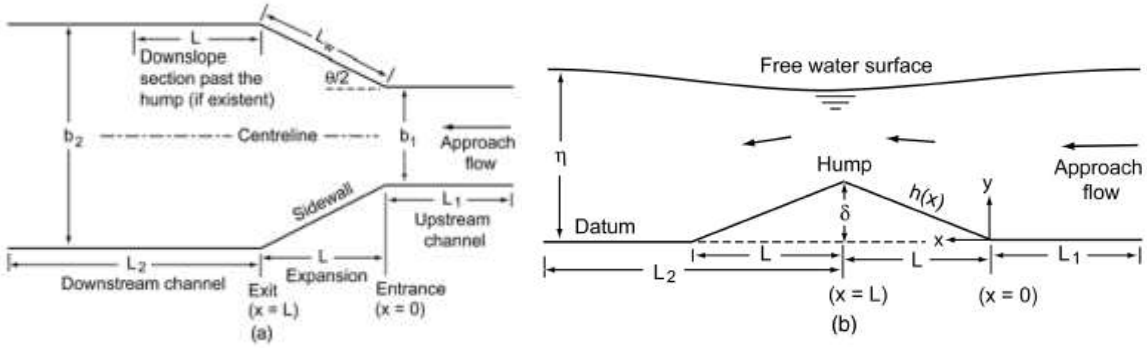

(a) (b)

Figure 2.8 (a) Plan view and (b) elevation view of a simple hump fitted at the bottom (Najafi-Nejad-Nasser & Li, 2015)

To obtain velocity pattern, laboratory measurements were conducted with a focus on velocity uniformity at the exit of the expansion, with or without a hump at the expansion bottom (Haque, 2009). Najafi-Nejad-Nasser and Li (2015) developed an analytical model to predict the

downstream water depth of a rectangular expansion fitted with a triangular hump at the bottom (Figure 2.8). The experimental results demonstrated a hydrostatic pressure distribution, and the use of a hump can effectively reduce energy loss by 0.45 velocity head based on the entrance velocity. The hump crest height, the only design parameter, is suggested to be 5–9% of the approach flow depth. Najmeddin and Li (Najmeddin & Li, 2016) obtained the velocity field, eddy structures, and flow separation streamlines in channel expansions using RANS modelling, where they investigated the influence of the expansion angle, hump crest height, and Froude number on the flow characteristics. There were relatively strong eddy motions downstream of the expansions, possibly created and maintained by local flow resistance at the sidewalls.

2.2.4 Split vanes

Split vanes were used to reduce the expansion angle and alleviate the adverse effects of flow separation in channel expansions (Hinds, 1928; Ippen, 1949; Scobey, 1933). The concept originated from aerodynamics, where a single vane positioned behind a cylinder could significantly reduce the pressure drag experienced by the cylinder (Roshko, 1953). The mechanism behind this method is that the vanes partition the expansion sections, setting a limit on the maximum possible eddy size and reducing form loss. For field installations, thin, stainless-steel vanes can be embedded at the bottom of the channel in a narrow concrete floor strip. Steel bar bracing can be installed at intervals on top to ensure stability.

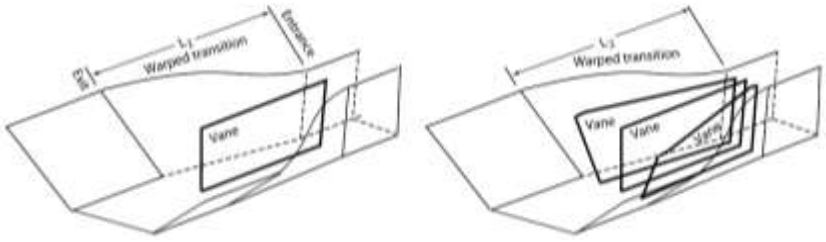

(a) (b)

Figure 2.9 (a) A single vane or (b) three vanes installed along the warped transition centerline (Li et al., 2019)

Ramamurthy et al. (2017) conducted a study using one vane (Figure 2.9(a)) or three vanes (Figure 2.9(b)) to reduce flow separation in a warped channel expansion. Laser Doppler Anemometry was used to determine 3-D flow parameters, including the longitudinal flow profile, energy loss, and maximum velocity in the exit flow. The experimental results showed that the three-vane system was the most efficient in reducing flow separiton and energy loss, generating favourable characteristics, such as flow uniformity, reduced secondary flow intensity, and decreased maximum velocity in the downstream channel. Li et al. (2019) continued the study using Reynolds Stress Model (RSM). While the predictions of separation zones and velocity structures were validated by the experimental results, the model overpredicted the maximum length and underpredicted the maximum width of the separation zone to some extent. It was shown vanes do not have significant impact on the approach flow, though the flow is subcritical.

According to Ramamurthy et al. (2017), additional vane surfaces cause an increase in friction loss, which offsets the gain in energy head. The net gain from three vanes is only marginallly better compared to using one vane. This suggests that using four vanes to achieve an extremly uniform

velocity distribution at the exit of the expansion, as done by Ippen (1949), leads to significant friction loss due to increased contact surfaces. Morris and Wiggert (1972, p. 185) noted that boundary friction losses can be as significant as form losses, or even the controlling factor when the transition change is gradual. Optimizing the length, heigh, and orientation of vanes could further improve the performance of the vane system.

2.2.5 Modified wedge channel expansion

Among common types of transitions, a wedge transition is simple to construct. Thapa et al. (2018) explored modifications to a wedge transition to reduce the flow separation and head loss. The characteristics of 3-D flows in both the wedge (Figure 2.10(a)) and modified wedge (Figure 2.10(b)) systems were investigated. The modified wedge transition with diagonal narrow strips attached to the sidewalls can effectively guide the flow and prevent abrupt changes in the direction of the flow. This results in a much lower levels of turbulence, and a less strong secondary flow. More importantly, it achieves a small gain in the energy at the flow recovery location and reduces the head loss coefficient as a result of the reduced separation zone. The performance of modified wedge transition is slightly better than a normal warped transition (Ramamurthy et al., 2017).

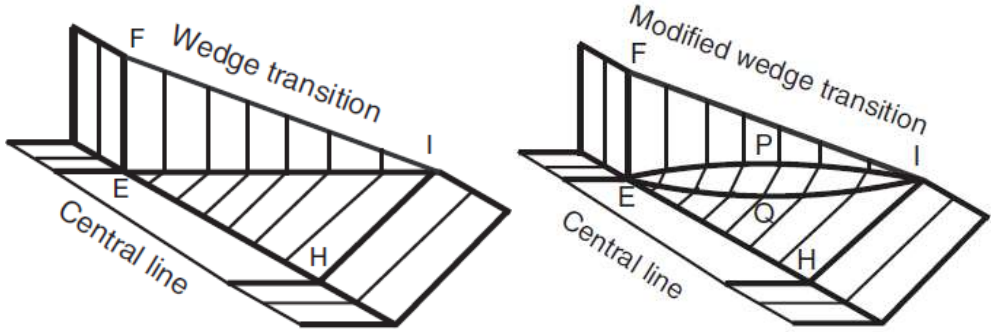

(a) (b)

Figure 2.10 (a) Details of the wedge transition and (b) the modified wedge transition (Thapa et al., 2018)

2.3 Turbulent flow and coherent structures

2.3.1 Turbulent flow and eddies

Most flows in natural channels, such as brooks, streams, and rivers, as well as flows in hydraulic engineering applications, such as navigation channels, hydroelectric power channels, and irrigation canals, are turbulent. Turbulent flows possess some common characteristics, including temporal fluctuations, random eddy motions, high rates of momentum, heat and mass transfer, dissipation and 3-D rotation (Tennekes & Lumley, 1972, p. 2). Turbulence is a property of flows, and its dynamics are consistent across all types of fluids.

The velocity field of turbulent flow exhibits 3-D structures and rotational eddies of varying scales, ranging from large eddies comparable in size to the width of the flow to the smallest eddies that decrease in size as the Reynolds number increases (Pope, 2001, p. 4). The integral scale of turbulence l represents the large scale at which most energy resides, while the Kolmogorov scale η, represents the smallest scale in the flow where dissipation takes place. Large-scale motions, which arise from inherent instabilities in various base flows, are strongly influenced by the channel geometry and boundary conditions. In contrast, small-scale motions are statistically independent

of the large-scale turbulence and the mean flow but depend solely on the rate at which the energy is supplied by the large-scale motion and on the kinematic viscosity of the fluid (Kolmogorov, 1941). The energy supplied is equal to the rate of dissipation ε. The small-scale motion is quite viscous (Pope, 2001, p. 186).

Kolmogorov's hypothesis of local isotropy introduces the length scale $l_{EI} = 1/6l$ to distinguish between isotropic small eddies and anisotropic large eddies. The size range smaller than l_{EI} constitutes the universal equilibrium range, while the larger size range constitutes the energy-containing range. Kolmogorov's second similarity hypothesis further subdivides the universal equilibrium range into the inertial subrange and the dissipation range, using a length scale $l_{DI} = 60\eta$ (Figure 2.11). Inertial effects solely affect the motions in the inertial subrange, while both the energy dissipation rate ε and viscous effects affect the motions in the dissipation range (Pope, 2001, p. 188).

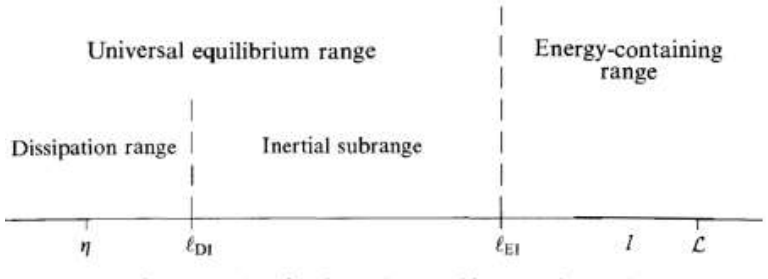

Figure 2.11 Eddy sizes at very high Reynolds number showing various length scales and ranges. EI is the demarcation line between energy-containing range and inertial subrange; DI is the demarcation line between the dissipation and inertial subranges (Pope, 2001, p. 188)

Turbulence is characterized by an energy cascading process. Kinetic energy enters the turbulence at the largest scales of motion. The unstable large eddies tend to break up and transfer their energy to smaller eddies. These smaller eddies undergo a similar break-up process, perpetuating the energy cascade into even smaller eddies. This process continues until the Reynolds number is sufficiently low to allow molecular viscosity to dissipate small-scale energy into heat (Tennekes & Lumley, 1972, p. 19). The rate of dissipation ε is independent of molecular viscosity ν. A random length scale l_0 corresponds to a wave number $\kappa = 2\pi/l_0$, which implies that the large eddies have low wave numbers while the small eddies have high ones. The energy in the wave number range (κ_a, κ_b) is $k_{(\kappa_a,\kappa_b)} = \int_{\kappa_a}^{\kappa_b} E(\kappa)d\kappa$, where the energy spectrum of turbulence $E(k)$ represents the contribution to turbulence kinetic energy by wave numbers from κ to $\kappa + d\kappa$. If the wave number includes all the eddies, $k\,(0,\infty)$ will represent the turbulence kinetic energy. The energy cascade is equivalent to the energy transfer from the low wavenumbers to the high wavenumbers. For the inertial subrange, Kolmogorov obtained the universal form of the spectrum of turbulence $E(k) = C\varepsilon^{2/3}k^{-5/3}$, characterized by a negative $-5/3$ slope (Pope, 2001, p. 189). The transfer of eddy energy is related to vortex stretching. Due to the conservation of angular momentum, the lengthening of vortices results in an increase in the component of vorticity in the stretching direction, while the fluid elements become thinner in the directions perpendicular to the stretching direction.

2.3.2 Turbulence closure

A parameterized model based on empirical coefficients may not provide accurate simulations for unprecedented discharges and water stages (Uijttewaal, 2014). Instead, it is crucial to have a thorough understanding of turbulence in open-channel flow to ensure the safety of hydraulic structures, maintain channel stability, and promote healthy aquatic habitats. The governing equations of CFD modelling, the Navier-stokes equations, are time-dependent and 3-D partial differential equations that lack a general solution due to their nonlinearity and randomness. The importance of large eddies requires eddy-resolving models. However, the resolution requirements differ for specific problems, and the accuracy may be sacrificed for lower computational costs.

RANS models separate quantities in the governing equations into a mean part and a fluctuating part with zero mean. The turbulent velocity fluctuations can generate large turbulent momentum fluxes, so-called Reynolds stresses, between different parts of the flow. The turbulent momentum exchange resembles molecular transport of momentum in laminar flows, and can therefore be represented by postulating a relation similar to the Newton's viscosity law $R_{ij} = -\overline{u_i' u_j'} = 2\nu_t S_{ij}$ (Boussinesq approximation), where R_{ij} is the Reynolds stress, S_{ij} is strain rate and ν_t is the eddy viscosity. Various eddy viscosity models are classified based on number of transport equations solved in addition to the RANS equations, such as zero-equation models, one-equation models (e.g. Spalart-Allmaras model) and two equation models (Tennekes & Lumley, 1972, p. 42). DNS resolves governing equations for the entire range of spatial and temporal scales of turbulence. However, DNS is not feasible for practical engineering problems since the costs required for DNS are proportional to the cube of the Reynolds number (Pope, 2001, p. 348). It is not possible from the perspective of handling input and output data (Uijttewaal, 2014). Instead, DNS is a research tool for studying small-scale processes at low Reynolds numbers and provides opportunities for testing hypotheses and turbulence closures (Singh et al., 2007).

LES uses filter techniques to filter out motions of scales smaller than the mesh size (small-scale) from those of resolvable scales (large-scale eddies). The filtered Navier-Stokes equations also generate a term similar to the Reynolds stress, which needs to be modeled and is called subgrid-scale stress tensor τ_{ij}. It represents the effect of the unresolved fluctuations on the resolved motions, and various subgrid scale (SGS) models have been established for this purpose. As the large-scale eddies are problem-dependent and small-scale eddies are more universal in nature, LES provides a compromise between computationally expensive DNS and insufficiently accurate RANS, allowing for instantaneous flow information down to the smallest resolvable scale. This leads to significant insights about the flow features in many applications. LES is often used in parallel with laboratory-scale applications to further explore the parameter space (Thomas & Williams, 1995). With ample computer capacity, LES of small rivers is now feasible (Kang & Sotiropoulos, 2011).

In Detached Eddy Simulation (DES), a RANS model resolves the near-wall regions, while LES is used for the greater part of the flow domain. However, simulating the entire river reaches with a 3-D RANS model is not feasible. Therefore, depth-averaged models or 1D models will remain important for engineering applications that do not require much detail, particularly for long-term predictions and probabilistic design (Uijttewaal, 2014).

2.3.3 Coherent structures

Around spur dikes, bridge abutments, piers and other hydraulic structures, shear instabilities of flows create coherent turbulence structures. They are large scale intermittent eddies in open-channel flow that rotate almost at the same place and maintain roughly the same size but are unsteady and never repeat in detail (Holmes et al., 2012, p. 38). Each vorticity field of these turbulent structures contains an organized component. Therefore, it is possible to separate the turbulent structures by identifying and defining the boundary of the coherent vorticity from the main flow.

2-D coherent turbulence structures are primarily caused by topographical forcing, internal transverse shear instabilities, and secondary instabilities of base flow (Jirka, 2001). Topographical forcing is the primary cause, as obstacles such as islands, headlands, and spur dikes (Figure 2.12(a)) create flow separation and a transverse shear layer (Uijttewaal, 2014). The second mechanism involves internal transverse shear instabilities that create shallow jets or shallow mixing layers (Figure 2.12(b)) due to gradual topography change (e.g., in a compound channel) or nonuniform roughness distribution. The weakest generating mechanism is secondary instabilities of the base flow, where the uniform channel flow is vertically sheared into 3-D structures (Jirka, 2001), such as 3-D burst events (Figure 2.12(c)). When the flow experiences slight imbalances, momentum exchange near the bottom boundary can be redistributed, resulting in 2-D coherent turbulence structures (Uijttewaal, 2014).

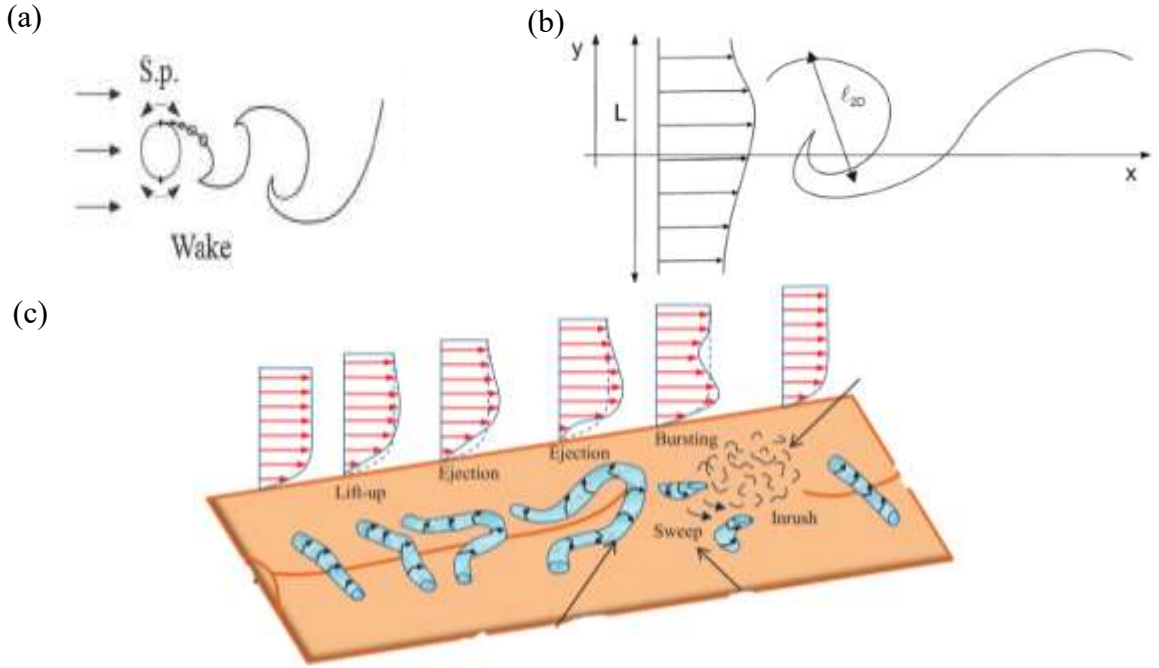

Figure 2.12 Coherent structures generated by (a) topographical forcing (Jirka, 2001), (b) transverse shear (Uijttewaal, 2014), and (c) turbulent bursting (Salim et al., 2017)

Unlike the wake flow behind a cylinder, where vorticity is shed with alternating sign, the vorticity structures in a mixing layer have the same sense of rotation. Equal-signed vortices tend to combine and form larger structures whereas opposite-signed vortices form pairs but remain separated. Therefore, as the eddies are convected downstream in a mixing layer, they grow in size and spacing

while decreasing in number. In a shallow flow flume study (Uijttewaal, 2014), eddies grow to more than 10 times the flow depth over a distance of 1000 times the water depth. In a field observation, the momentum transfer in the shear layer was visible up to 40 times the water depth downstream with decreasing intensity (Sukhodolov et al., 2010). Further downstream, the flow becomes transversely uniform through the balance between friction and gravity.

Secondary flows can be defined as flow cells with axes of rotation parallel to the main flow direction. Two types of secondary currents can be distinguished: those of Prandtl's first kind or skew-induced streamwise vorticity, which are driven by the centrifugal force and the pressure gradient (Blanckaert & Graf, 2004), and those of Prandtl's second kind or stress-induced secondary flow, which are generated by turbulent Reynolds stress gradient (Stanković et al., 2017). The former type is observed in both laminar and turbulent flows in curved geometries, while the latter is observed in turbulent straight and non-circular channel flows. It is caused by abrupt spatial variations in boundary conditions, such as corners between bed and sidewalls, corners near the free surface (Nakagawa, 1993, p. 101), and interfaces between floodplains and the main channel. For wide open channels, the number of secondary current cells depends on the aspect ratio (Albayrak & Lemmin, 2011). Between the cells, regions of alternating upwelling and downwelling motions are observed. Undulating bed shear stress distributions indicate small values near the upwelling regions and large values near the downwelling regions (Sukhodolov & Uijttewaal, 2010).

Horseshoe vortices exist at the base of hydraulic structures, such as piers, spur dikes, and abutments. These structures bring upstream flow to an immediate halt, causing the stagnation pressure in front of these obstructions to exceed the hydrostatic pressure by an amount equal to the dynamic pressure, which is proportional to the square of the local velocity. Consequently, a downward pressure gradient develops in front of the structure, driving the flow towards the bed. In the streamwise direction, the flow tends to separate from the obstruction due to the flow expansion behind it. The horseshoe vortex, wrapped around the base of the obstruction, is produced by both boundary layer separation and down-flow (Figure 2.13). This system of vortices removes bed materials from the base of the structure, creating a local scour hole. The strength of the horseshoe vortex decreases with increasing depth of the scour (Akan, 2006, p. 303).

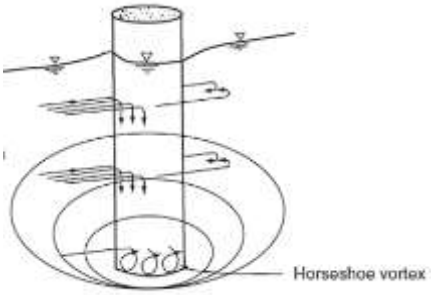

Figure 2.13 generation of horseshoe vortices near the base of a bridge pier (Akan, 2006, p. 304)

In open-channel expansions, the shear between the fast flow in the middle region and relatively slow flows in both flanks can generate intermittent turbulent eddies. These eddies evolve in strength and size, forming coherent structures. One may determine the sizes of large eddies and the extent of flow blockage by eddy motions (Holmes et al., 2012).

2.4 Characteristic turbulent flows

2.4.1 Bistable flow

The bistable flow has two possible stable equilibrium states in the same geometry and under the same flow conditions, except for slight differences in flow history (Ferrara et al., 2018). In laboratory experiments, flow bistability can be triggered by introducing small disturbances, to which the flow shows high sensitivity. These small disturbances include sediment deposits that accumulate over time on the flume bed (Camnasio et al., 2013), the introduction of thread probes for visualization (Meile et al., 2016), and the presence of an overshot of the free-stream velocity during wind tunnel start-up (Zigunov et al., 2020). Numerical simulations have shown that bistable flow can be triggered by using different initial conditions of the velocity field in shallow reservoirs (Dewals et al., 2012; Ferrara et al., 2018) and by incorporating time-varying topography that represents the effect of sediment deposition (Camnasio et al., 2013). In realistic conditions, even a gust of wind can cause bistable flow behavior behind hatchback cars (Meile et al., 2016).

This bistable flow phenomenon only occurs when the flow configuration satisfies certain requirements. Dewals et al. (2012) formulated a shape parameter for symmetric shallow reservoirs based on the length-to-width ratio of the tank and the ratio of the tank width to the inlet channel width. Similarly, various gap widths between two flat plates perpendicular to the flow direction in a water tunnel can trigger bistable, unstable flip-flopping or symmetric wake flow behind the plates (Shin & Kondo, 2019).

The bistable flow phenomenon contributes to asymmetric flow patterns in perfectly symmetric expanding channels (Durst et al., 1973; Mullin et al., 2003; Najmeddin & Li, 2016) and other symmetric geometries, such as flow measured behind an Ahmed body in a wind tunnel (Meile et al., 2016), flow simulated behind a square ship body on a helideck (Zhang et al., 2018), and low Reynolds number flow ($Re \alpha 10^3$) simulated in a channel with a suddenly expanded and contracted part (Mizushima et al., 1999) and so on.

2.4.2 Classical hydraulic jump (CHJ)

The hydraulic jump is a fundamental problem in hydraulic engineering that occurs when water flow transitions abruptly from a supercritical to a subcritical condition. The depth of flow section increases from a low elevation just before the jump to a high elevation just after the jump, leading to an abrupt decrease in flow velocity. These depths before and after the jump are respectively referred to as the initial depth and the sequent depth of a hydraulic jump (Henderson, 1966). The region where the hydraulic jump occurs features violent turbulence, eddy motions, significant energy dissipation, strong mixing, and entrainment of air into the flow.

The classical hydraulic jump occurs in smooth, horizontal, rectangular channels and is classified into different types based on the approach Froude number (Chow, 1959). It is considered stable for Froude number values ranging from 4.5 to 9.0 (Hager, 2013). The characteristics of the CHJ, including sequent depth ratio, roller length, hydraulic jump length, mean free surface profile, and mean velocity profile, have been extensively studied over the years. The formula for the depth ratio is generally the well-known Bélanger equation for rectangular channels. The roller length is the horizontal distance from the toe of the jump to the location downstream, where a surface stagnation point is reached (Hager, 2013). The hydraulic jump length is defined as the distance from the toe of the jump to the location where the water surface becomes nearly level with a

maximum mean surface elevation (Rajaratnam, 1967) or to the location where the hydraulic jump is fully deaerated. This latter definition is used as the aeration length in this research, following Stahl and Hager (1999).

Hydraulic jump is analogous to wall jet flow in which velocity decays due to the conversion of kinetic energy to pressure and potential energy (Rajaratnam, 1967). The pressure is no longer hydrostatic in the expanding region (Jesudhas et al., 2018). The free surface fluctuation intensifies with increasing Froude number (Montano & Felder, 2020). The local maxima of the void fraction indicate the shear layer of the mixture of air and water, and these maxima decrease quasi-exponentially as the shear layer expands with increasing distance from the roller toe (Gualtieri & Chanson, 2021). The turbulence production is confined to the shear layer in the upper part of the undeveloped inflow jumps (submerged jump) (Mignot & Cienfuegos, 2010).

The hydraulic jump in sloping open channels can be induced by changes in channel slopes or by the presence of a sill. Previous studies have developed characteristics and empirical formulas for various types of jumps, including B-jumps, where jumps occur partly on a sloping upstream portion and partly on a horizontal downstream portion (Roy et al., 2021); D-jumps, where jumps occur entirely on the slope (Ohtsu & Yasuda, 1991); jumps in stilling basins with step chutes and smooth chutes (Stojnic et al., 2021); and jumps over adverse-sloped beds (Pagliara & Palermo, 2015). Samadi et al. (2020) utilized artificial intelligence to examine the pressure fluctuation of a hydraulic jump in sloping channels. Smith and Chen (1989) formulated non-dimensional design curves for very steep square conduits up to 30%. Steep rectangular closed conduits entail greater energy loss than horizontal conduits (Maryami et al., 2021). Other researchers have also investigated the planar hydraulic jump in narrow rectangular conduits caused by viscous effect (Dhar et al., 2021), the circular hydraulic jump induced by impinging jet (Bhagat et al., 2018), hydraulic jumps over rough surfaces (Pagliara et al., 2008), and hydraulic jumps in a U-Shaped channel (Houichi et al., 2013).

2.4.3 Hydraulic jump in circular pipes

Despite its occurrence in tunnel spillways, drainage and sewer engineering, the hydraulic jump in closed conduits has received little attention (Stahl & Hager, 1999). For horizontal circular conduits, hydraulic jump is classified into four different types, from undular hydraulic jump to hydraulic dump with a nearly full pipe flow, based on both the filling ratio and approach Froude number (Stahl & Hager, 1999). The sequent depth ratio in circular open channels is smaller than that obtained in rectangular open channels (Ead & Ghamry, 2002). Recently, some researchers have obtained explicit equations for the sequent depth ratio using artificial intelligence model-based predictive methods, such as model tree (Vatankhah, 2021), gene expression programming and evolutionary polynomial regression (Najafzadeh, 2019).

Few studies have focused on hydraulic jumps in circular pipes with changing slopes. Qian et al. (2017) focused on the air movement in such pipes. Under these conditions, a sequent depth that is large enough can possibly lead to “choked flow” or “full conduit flow” (Stahl & Hager, 1999). This is known as an incomplete or pressure jump, which is characterized by pressurized flow downstream, as opposed to a complete or free-surface jump (Hotchkiss et al., 2003). The lack of well-established numerical modelling guidelines has led to continuous disputes over previous numerical results (Valero et al., 2018).

2.4.4 Turbulence modelling of hydraulic jump in circular pipes

Measuring hydraulic jumps in the laboratory is often time-consuming and requires expensive equipment. The turbulent nature and the presence of bubbles at the free surface make it even more challenging. Even visual estimations of roller length and aeration length are difficult due to the continuous movement of the downstream stagnation point and the inability to determine the deaeration point objectively. Phase detection probe is intrusive, insensitive to the direction of flow and sensitive to sampling parameters (Felder & Chanson, 2015). Non-intrusive equipment has limitations when it comes to measuring instantaneous 3-D velocity fields and high-resolution field gradients (Mortazavi et al., 2016). Despite the large number of experimental investigations, there are limitations in terms of accessing the complete flow field, turbulent fluctuations, and hydrodynamic parameters, where numerical modelling can provide a valuable tool for studying hydraulic jumps.

The hydraulic jump is characterized by a 3-D anisotropic turbulent field, which is based on experimental analysis of turbulent scales (Wang & Murzyn, 2017) and turbulent velocity fluctuations (Long et al., 1990). To understand the dynamics of the coherent structures responsible for free surface fluctuations and aeration in hydraulic jumps, the use of 3-D models is necessary (Bayon et al., 2016). With the advancement of cost-effective computer power, it is now feasible to gradually transition from RANS or DES towards LES to better resolve the near-wall regions. Wall-resolved LES has been applied to hydraulic jumps near cylinder structure (Zhao et al., 2021) but as far as the author knows, no wall-resolved LES study has been conducted on hydraulic jumps in 3-D circular pipes. Two-phase LES performs better in simulating momentum transfer in hydraulic jump than adding a source term (Qian et al., 2017).

2.4.5 Turbulence modelling of flow in a warped transition

By following existing guidelines (e.g., Ippen, 1949), researchers may produce warped transitions with varying shapes. Li (2022) introduced an analytical harmonic function for the 3-D warped expansion, which significantly simplifies the construction of geometry in CFD. Researchers have used LES to study the vortex dynamics in a sudden expansion (Han et al., 2022), reattachment length in an axisymmetric expansion (Choi et al., 2022), and flow separation in open channel sharp bend flow (Ramamurthy et al., 2013).

To obtain a realistic simulation of flow, it is critical to specify physically accurate boundary conditions at all boundaries of a computational domain, including the inlet, outlet, free-surface, and walls (Rodi et al., 2013). In hydraulics, convection-dominated flows are significantly influenced by the values specified at the inlet, which can impact values within the calculation domain (Xie et al., 2018). While RANS models use time-averaged inflow conditions, it is difficult to generate fluctuating inflow conditions for LES. The commonly used periodic boundary condition with spatial-averaging method (double-averaging method) (e.g., Xie et al., 2013) is unsuitable for spatially developing turbulent flows, such as an open channel expansion with non-prismatic geometry, intense flow separation, and variation of depth.

High-resolution velocity data, both spatially and temporally, are seldom directly obtainable from experiments. Consequently, the generation of inflow conditions requires the use of modeling and assumptions. Based on extensive reviews (Keating et al., 2004; Tabor & Baba-Ahmadi, 2010; X. Wu, 2017), the researchers have classified inflow generation methods into three major types: precursor method, recycling and rescaling methods, and synthetic methods. The precursor method

entails performing a separate calculation for turbulent flow in a precursor domain with periodic boundary conditions using the same hydraulic conditions, saving the spatio-temporal turbulent velocities at one cross-section, and utilizing that data as the inflow boundary condition in the primary simulation domain (Chen et al., 2022). Recycling and rescaling methods involve recycling the upstream turbulent flow until it meets specified turbulence characteristics and utilizing the velocity data of the mapping plane as the inflow condition for downstream development (Foti et al., 2017; Lund et al., 1998). While effective, these methods can be expensive.

The synthetic methods provide a standalone unsteady boundary condition in the main simulation without relying on a turbulence library, which is more efficient but less expensive than the previous two methods (Vasaturo et al., 2018). This category includes various methods, some of which are still under development and evolving in wind engineering (Bervida et al., 2020; B. Xie et al., 2018; Yu et al., 2018; Zhang et al., 2022). Two classical and versatile methods are the spectral synthesizer (SS) and vortex method (VM), both of which are widely used due to their implementation in commercial software. In SS, the fluctuating velocity components are obtained by synthesizing a divergence-free velocity-vector field using the summation of Fourier harmonics. The Fourier series was first used by Kraichnan (1970) to study the diffusion of a particle in an isotropic turbulent velocity field. Later, turbulence length and time scales and Reynolds stress tensor were incorporated into the model; scaling and orthogonal transformation were used to generate an inhomogeneous, anisotropic turbulent velocity field (Smirnov et al., 2001). It has been used to study various phenomena, such as the aerodynamics of a train (García et al., 2015), vortex ropes in a draft tube (Minakov et al., 2017), hydrodynamics of a round jet in a vegetated crossflow (Xiao et al., 2019), the boundary layer transitions under the effects of periodic passing wakes (Ruan et al., 2020), wind-structure interactions in urban topology (Zhang et al., 2021) and flow characteristics in a vegetated open channel (Liu et al., 2021). The VM generates turbulent fluctuations by superimposing coherent structures at the inlet, with a given shape, length and time scale. The method assumes a certain vorticity distribution for each vortex based on a shape function and circulation (Sergent, 2002). The transverse component of velocity is obtained by applying the Biot–Savart law once the superimposed vorticity is available at any given grid position. The streamwise component is calculated based on the influence of the 2-D vortex on the inflow plane using a linear kinematic model (Mathey et al., 2006). Each vortex has a characteristic time of existence and undergoes a random walk within the plane to add unsteadiness, mimicking the coherent eddies of turbulent flow (Wu, 2017). The VM method generates both temporally and spatially correlated turbulence (Huang et al., 2010). The VM method has been used to study urban ventilation in a real and complex urban area (Antoniou et al., 2017), wall jets in plane cabin (Thysen et al., 2021), the impact of building balcony geometry on wind flow (Zheng et al., 2021), and airflow patterns over low-rise building (Liu et al., 2020).

In synthetic methods, imperfections in the formulation or inputs provided for a specific problem require a certain adaptation distance before realistic turbulence can be established in a flow field through Navier-Stokes equations (Tabor & Baba-Ahmadi, 2010). Reducing this adaptation distance can decrease the associated computational cost, but the inherent complexity of the inflow generation requires ad-hoc adjustments and fine tuning to achieve successful results for a particular application. Moreover, methods developed or tuned for a specific problem are usually not expected to succeed in a wide variety of flows (Dhamankar et al., 2018).

In wind engineering, the suggested adaptation length in the atmospheric boundary layer (ABL) around an isolated building or building arrays is four times the building height (Ai & Mak, 2015) or three times the building height (Liu et al., 2019), respectively. Apart from the adaptation length, previous researchers have conducted sensitivity analyses of factors that can influence the LES of ABL over different geometries (Ai & Mak, 2015; Gousseau et al., 2013; J. Liu et al., 2019; Okaze et al., 2021), such as the setup and selection of inflow turbulence methods (e.g., vortex number for VM method), ensemble average time, and SGS models. However, all simulations of these wind flows are one-phase, and no sensitivity analysis of LES for two-phase 3-D open-channel flows has been conducted. Therefore, in addition to the parameters and setups studied for ABL, the interest also lies in the initial conditions and boundary conditions, such as the necessity of a numerical beach near the outlet and different inflow velocity profiles. Sensitivity analysis of parameters, such as hit-rate and factor-of-two (Ai & Mak, 2015), can enhance the quality of LES modeling of an open-channel flow in a warped expansion.

Regarding the free surface near the top boundary, accurate data of the water surface deformation using volume of fluid or level-set method is necessary, even for deep flows with very small Froude numbers. Accurate simulations of the water surface in hydraulic structures can capture flow patterns such as standing waves, obtain realistic streamwise and spanwise velocities, and observe less-coherent elongated vortices that are stretched by strong acceleration due to the water surface dip.

2.5 Urban drainage design

Based on the urban drainage design manual (Brown et al., 2013) and sewer design guide (Bailey, 2013), the information regarding the hydraulic jump in sewer and storm drain design is added to the thesis. The longitudinal slope is defined as the rate of elevation change with respect to distance in the direction of flow. Subcritical flow is characterized by low velocities, large depths, mild slopes, and a Froude number less than 1.0, whereas supercritical flow is characterized by high velocities, shallow depths, steep slopes, and a Froude number greater than 1.0.

2.5.1 Sewer pipe

Hydraulic jumps must be avoided, minimized, or positioned in a pipe upstream of the manhole or in the manhole. For pipe diameters of 24-inch and less, the height of any hydraulic jump shall not exceed 20 % of the pipe diameter ($d_{n_2} - d_{n_1} \leq 0.2\text{D}$). In cases where change in grade of the inlet and outlet pipes is greater than 10 %, or the potential for a hydraulic jump inside a manhole exists, the grade change should be made in a smooth vertical curve, upstream of the manhole, with the manhole located 25 feet downstream of the lower end of the vertical curve. The minimum horizontal length of vertical curves is calculated as $L = (S_1 - S_2)/R$, where L is the horizontal length, S_1 and S_2 are slopes of beginning and ending tangent to the vertical curves, and R is the minimum rate of slope change.

Manning's formula for open-channel flows is used to calculate flows in gravity sewer mains. Manning's coefficient of roughness is assumed to be 0.013 for all types of sewer pipe. Sewer grades are designed for velocities of 1–1.3 m/s. The minimum allowable velocity is 0.66 m/s at calculated peak dry weather flow, excluding infiltration. Sewer mains that do not sustain 0.66 m/s at peak flows are designed to have a minimum slope of 1%. The maximum allowable velocity is 3.33 m/s and should be avoided by adjusting slopes, by increasing the pipe diameter.

2.5.2 Storm drainage

A storm drain's hydraulic capacity is determined by its size, shape, slope, and friction resistance. The prevalent formula used for designing storm drains is also the Manning's Equation. A minimum flow velocity of 0.6 m/s is used at a flow depth equal to 25% of the pipe diameter. Minimum slopes required for a velocity of 0.9 m/s can be computed using the Manning's formula $S = k_u[nV/D^{0.67}]^2$. For the manning's roughness in the range of 0.012–0.024, the minimum slope has a range of 0.0003–0.0256.

When designing the preliminary storm drain conduit, the manual emphasizes the crucial nature of considering the hydraulic jump and partially full pipe flow to avoid erroneous results. In situations where the full flow does not exist, the friction slope should be set to the pipe slope. Under standard conditions, it is recommended that storm drains be sized based on a gravity flow criterion at full flow or near full flow. When pressure flow is allowed, special emphasis should be placed on the proper design of the joints so that they are able to endure the pressure flow.

The existing sewer design guideline strongly advocates for minimizing the occurrence of hydraulic jumps. Nevertheless, the present literature lacks comprehensive information concerning the implications of incomplete jumps. Crucial aspects such as the jump's precise location in relation to the pipe turning point, its length, and the depth ratios remain unknown.

2.6 Summary

This chapter begins with the flow separation phenomenon. It is shown that the generation of flow separation is caused by an adverse pressure gradient, as explained through the application of boundary layer theory to a flat plate. Flow separation is commonly observed along one or both sides of an open-channel expansion. The chapter delves into a discussion of energy loss, the number of recirculation zones, and the strength of flow separation in an open-channel expansion. Different types of expansions have their own advantages and disadvantages, and this thesis will investigate a straight-wall expansion and a warped expansion.

Various techniques are utilized to mitigate the flow separation in open-channel expansions. Streamlined and optimized sidewall profiles can only suppress the flow separation to a certain extent, due to underlying assumptions and boundary layer development. Previous researchers have tried different baffle shapes and arrangements to create uniform velocity distribution downstream. A hump at the bottom of the expansion helps neutralize the deceleration caused by the channel width expansion. Installing one-vane and three vanes reduces the flow separation effectively, but extra vanes cannot be added due to friction loss. The modified wedge expansion is simple to construct but is less efficient than the warped expansion.

Next, this chapter introduces the property of turbulent flows and coherent structures. The turbulent flow is characterized as random, fluctuating, 3-D rotational, and dissipative with high transfer of momentum, mass, and heat. The size of large eddies depends on the channel geometry while the size of small eddies depends on the Reynolds number. Kolmogorov divided eddies into energy-containing range, inertial subrange, and dissipation range. Based on the energy cascade, the large eddies continually break into smaller eddies and ultimately are dissipated by the viscosity. Large eddy simulation can solve instantaneous flow information down to the smallest resolved scale, which is currently applicable to small flume scales. Coherent eddies rotate almost in the same place

and maintain roughly the same size but are unsteady and never repeat in detail. The generation mechanisms of 2-D large coherent structures, secondary flow, recirculation zones in open-channel expansion are discussed.

Some works of characteristic turbulent flows, such as the bistable flow and hydraulic jump, are summarized. Previous researchers have observed flow bistability in laboratory experiments, numerical simulations, and fieldwork. They investigated the sequent depth ratio, roller length, aeration length, free-surface profile, and velocity profiles of the classical hydraulic jump (in rectangular open channels). They have also studied other hydraulic jumps in sloping rectangular channels, such as B-jump and D-jump. However, little is known about the incomplete hydraulic jump and choked flow in circular pipes with changing slopes. The measurement of hydraulic jump is challenging due to the presence of bubbles and equipment limitations.

3-D wall-resolved two-phase LES will be applied to study the turbulent flow in a circular pipe with changing slopes, a straight-wall expansion, and a warped expansion. When dealing with convection-dominated expanding flows, it is important to reconsider how to generate a realistic inlet condition because the commonly used periodic boundary condition is not applicable. In addition to the adaptation length, ensemble average time, and subgrid scale models, the investigation will also examine the outlet boundary treatment and inlet velocity profile specification for open-channel flows. This thesis will employ sensitivity analysis parameters, such as the factor-of-two and hit-rate, which have been used by aerodynamics researchers.

3 Bistability of turbulent flow in open-channel expansion[1]

3.1 Background

Turbulent bistable flow (TBF) is a fundamental phenomenon in fluid dynamics whereby the flow has two stable states. Bistability can occur in fluid flows through an open-channel expansion (Smith & Yu, 1966; Thapa et al., 2018), in a wastewater treatment tank (Camnasio et al., 2013; Dewals et al., 2012; Ferrara et al., 2018) and a nuclear reactor (Moreno, 2011; Olinto et al., 2006), and downstream of a bluff body in a wind tunnel (Burton et al., 2021; He et al., 2022). In Figure 3.1, the open channel has a symmetrical geometry about the centerline, but because of bistability, the transverse profiles of the longitudinal velocity component of either state are not. Asymmetrical transverse profiles were observed to exist in a sudden expansion (Smith & Yu, 1966) (Figure 3.1(a), when the divergence angle $\theta = 90°$) and a wedge expansion (Thapa et al., 2018). These expansions are examples of various types of common expansions around hydraulic structures for hydropower development, water supply, flood mitigation and so on. Bistability reduces flow uniformity in expansions and hence reduces their hydraulic efficiency of water conveyance. Also, bistability intensifies flow velocities in the left or the right flank (Figure 3.1(a)), strengthens shear stresses, and thus increases the risk of erosion on the channel-bed and banks of an erodible channel.

The motivation for this research arose from the fact that there has been little progress made to discover subtle behaviour of TBF in an expansion. In a mathematical model, the time-dependent momentum and mass conservation equations govern open-channel flow, and the two stable states are solutions satisfying the same conditions imposed on the channel boundaries, i.e., the inlet, outlet, sidewalls and channel-bottom (Figures 3.1(a), 3.1(d)). The position of the free surface (or the interface between air and water) is not known a priori. Thus, TBF should be treated using a two-phase flow model. The purpose of this study is to reveal TBF characteristics quantitatively and explore simple ways to suppress bistability. The suppression is beneficial for hydraulic efficiency.

The understanding of TBF in expansions from previous research endeavors remains qualitative. At a high Reynolds number, the shear between the fast flow in the middle region and relatively slow flows in both flanks (Figure 3.1(a)) can generate intermittent turbulent eddies, which evolve in strength and size, and form coherent structures. One may estimate the sizes of large eddies (Holmes et al., 2012), and may further determine the extent of flow blockage by eddy motions. Previous studies of expansions have mostly focused on improving their design. Some researchers tried to optimize sidewall profiles (Swamee & Basak, 1991), conform with separating streamlines (Alauddin & Basak, 2006), reduce wall surface curvatures (Thapa et al., 2018), and fit a hump at a flat channel-bottom (Najafi-Nejad-Nasser & Li, 2015). Other researchers introduced such elements as baffles (Austin et al., 1970; Smith & Yu, 1966) and split vanes (Li et al., 2019) in the flow. However, these studies have not addressed the question of flow bistability and asymmetry in an expansion.

In particular, the issue that a distinct flow history influences bistable behavior has been overlooked. In this research, the flow history provides different initial conditions in the mathematical model when solving the time-dependent governing equations for stable states satisfying the same boundary conditions. For TBF through an expansion, the approach flow velocity gives the

[1] This chapter contains information that was published in Physics of Fluids: https://doi.org/10.1063/5.0089093

characteristic velocity, the length of the expansion provides the characteristic length, and the characteristic length and velocity define the characteristic advection time (Figure 3.1). In the process of fluid advection through an expanding channel, the flowrate per unit width decreases. For subcritical flow, the water surface will rise in the primary flow direction or the x_2-direction (Figure 3.1(d)) and thus cause an adverse pressure gradient, with the effect of boundary layer separation from the sidewalls (Figure 3.1(a)). The depth increase and flow separation are important characteristics of expansion flow. The flow characteristics are complex and are difficult to capture by using mathematical models that use the rigid-lid approximation or 2-D simplification.

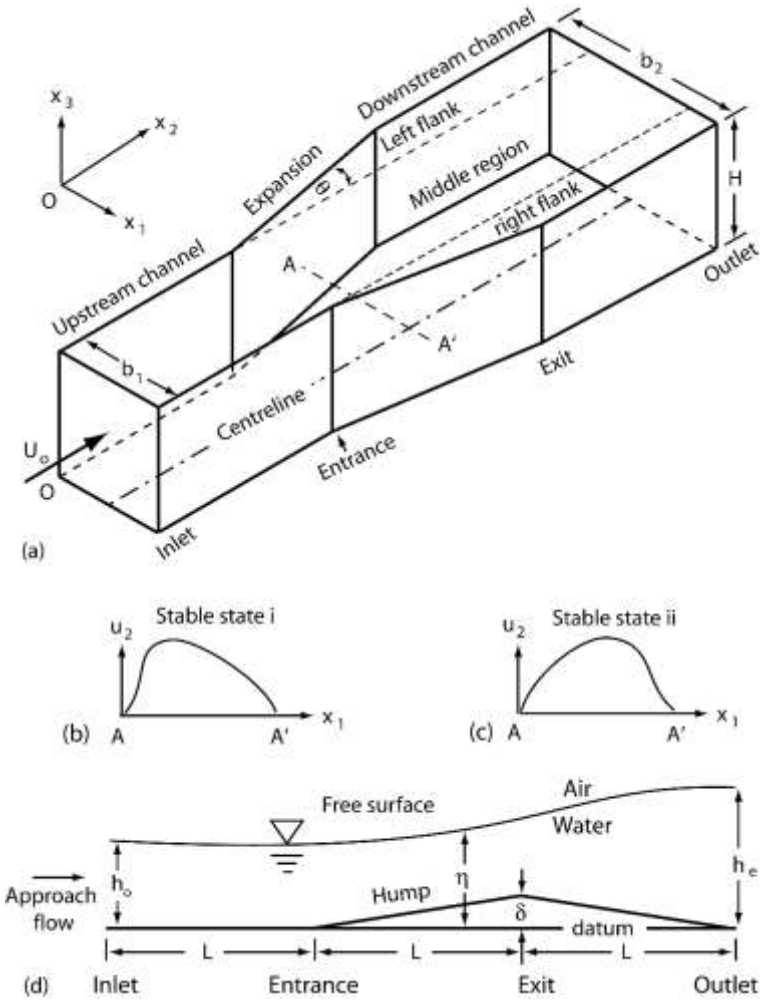

Figure 3.1 (a) 3-D view of symmetrical geometry of a straight-wall expansion about its centerline; (b) and (c) transverse profiles of the $x_2$velocity component u_2; (d) elevation view of the channel with a hump at the channel-bottom

In the following, Section 3.2 describes the methods for two-phase Large Eddy Simulation (LES) of 3-D TBF in the model channel (Figure 3.1(a)). Section 3.3 presents simulation results of the flow field in the flat-bottom case (Figure 3.1(d), $\delta = 0$) as well as in the case of a hump ($\delta > 0$) fitted at the bottom, along with a comparison of the results with experimental data. Section 3.4 discusses eddy behavior, velocity shear and pressure distribution. Section V draws conclusions.

3.2 Methods

3.2.1 Model equations and boundary conditions

Consider two-phase incompressible viscous flow, with air as the gas phase and water as the liquid phase, which are immiscible. The density of air-water mixture is calculated as the volume-weighted average of densities $\rho = \alpha_1\rho_1 + \alpha_2\rho_2$, where α is the volume fraction, and the subscripts 1 and 2, respectively, refer to air and water; $\alpha_1 + \alpha_2 = 1$. The viscosity of the mixture is calculated as $\upsilon = \alpha_1\upsilon_1 + \alpha_2\upsilon_2$. The momentum equation and continuity equation describe the motion of the mixture. Using LES technique, the finite volume method implicitly yields filtered equations

$$\partial u_i/\partial t + \partial(u_i u_j)/\partial x_j = -\rho^{-1}\partial p/\partial x_i + \partial(\upsilon\partial u_i/\partial x_j + \tau_{ij})/\partial x_j + g_i \quad (3.1a)$$

$$\partial u_j/\partial x_j = 0 \quad (3.2b)$$

where u_i is the resolvable-scale filtered velocity component in x_i-direction (i = 1, 2, 3 for the transverse, longitudinal and vertical directions, respectively); t is time; p is the resolvable-scale pressure; τ_{ij} is the subgrid scale stress; g_i is the gravitational acceleration ($g_1 = g_2 = 0, g_3 = -9.81\ \mathrm{m/s^2}$). The motion of large eddies is computed. Subgrid-scale eddies smaller than the mesh size Δx_i need to be modeled.

In Eq. 3.1, τ_{ij} allows for the effect of unresolved velocity fluctuations on the resolved motion, given by $\tau_{ij} = 2\rho^{-1}\mu_t S_{ij}$, where $\mu_t = \rho L_s^2|S|$; $|S| = \sqrt{2S_{ij}S_{ij}}$; S_{ij} is the resolved strain rate; μ_t is the subgrid-scale turbulent viscosity (Lilly, 1966; Smagorinsky, 1963); L_s is the mixing length. L_s was estimated as the lesser of two products: a) $C_s(\Delta x_1\Delta x_2\Delta x_3)^{1/3}$ where C_s is the Smagorinsky coefficient, b) the product of the von Karman constant and the distance to the closest wall. Here, $\Delta = (\Delta x_1\Delta x_2\Delta x_3)^{1/3}$ is the local grid scale. This is the largest scale of unresolved turbulence, interacting the most actively with the resolved motion (Rodi et al., 2013).

The dynamic Smagorinsky-Lilly model (Germano et al., 1991; Lilly, 1992) was used to calculate C_s and hence μ_t as follows. Let $\hat{\Delta} = 2\Delta$ denote a test filter. The test filtered subgrid-scale (SGS) stress tensor, T_{ij}, is modeled as $T_{ij} = 2C\hat{\Delta}^2|\hat{S}|\hat{S}_{ij}$, where the symbol $\widehat{\ }$ means a test filtered level operation, and C is a coefficient. The grid filtered SGS stress tensor, t_{ij}, is modeled in the same way $t_{ij} = 2C\Delta^2|S|S_{ij}$. The coefficient C is solved from $C = L_{ij}M_{ij}/(M_{ij}M_{ij})$, where $L_{ij} = T_{ij} - t_{ij}$ and $M_{ij} = 2(\hat{\Delta}^2|\hat{S}|\hat{S}_{ij} - \Delta^2|S|S_{ij})$. The Smagorinsky coefficient is computed from $C_s = \sqrt{C}$, using information provided by the resolved scales of motions. To avoid numerical instability, negative values of the eddy viscosity are truncated to zero. The dynamic Smagorinsky-Lilly model has been successfully used to study different types of turbulent flows. Recent examples of studies include turbulent flows around cylinders (Abdelhady & Wood, 2021; Islam & Mohany, n.d.; Nikoo et al., 2018; Shang et al., 2019), a hydrofoil (Long et al., 2019) and an in-stream deflector (Zhan et al., 2019), flows in a T-junction (Georgiou & Papalexandris, 2017) and pipe bend (He et al., 2021), and two-phase turbulent flow (Cheng et al., 2018).

Turbulent flow entered the channel (Figure 3.1(a)) at the inlet and left at the outlet. The channel had four types of boundaries: inlet; outlet; solid walls (the bottom and sidewalls); top opening (at $x_3 = H$). At the inlet, the mean water velocity U_o and depth h_o were specified (Figure 3.1(a), 3.1(d)). A fluctuating vorticity field was superimposed on the mean flow, using the 2-D vortex method (Mathey et al., 2006), to allow for the effect of background turbulence on TBF. The relative

turbulence intensity $T' = 100(2k/3U_o^2)^{1/2}$, where k is turbulence kinetic energy, was assumed to be 5% (literature value). The eddy viscosity ratio v_t/v was 10. At the top opening exposed to the atmosphere, the resolvable scale pressure was $p = 0$. Note that the focus of this research was on the influence of initial condition on bistability. Thus, the inlet flow condition was kept as simple as possible. Note that a cyclic condition cannot be applied between the inlet and outlet because of their different cross-sectional shapes and different number of nodes.

In Figure 3.1, the linear dimensions of the model channel are: b_1 = 0.1711 m; b_2= 0.2893 m; L = 0.3048 m; δ = 0.0127 m; H = 0.1904 m. When δ = 0, the channel-bottom is flat; H = 0.2045 m. The portion of the channel $0 < x_1 < b_1$ is referred to as the middle region; the portion $x_1 < 0$ and $x_2 > L$ the left flank; the portion $x_1 > b_1$ and $x_2 > L$ the right flank (to an observer facing downstream). The hump is an isosceles triangle, with a height of δ (5 to 10% of the approach flow depth) and a base of 2L, located at the channel bottom. The hump is uniform in the x_1 direction.

3.2.2 Simulation setup and solution procedures

Model simulations matched available experiments (Najafi-Nejad-Nasser & Li, 2015) in expansion geometry (Figure 3.1) and hydraulic conditions. Above the free surface, the thickness of an air layer was 10% of the maximum flow depth in the experiments, sufficient to capture spatially and temporally varying free surface η and to avoid possible numerical instability and/or accuracy issues. It is crucial to accurately compute η in multi-phase simulations of open-channel flow.

LES mesh of hexahedrons covered the channel (Figure 3.1(a)); the resolutions were refined near the bottom and sidewalls with 41 inflation layers. The first layer off a wall had the dimensionless wall distance $y^+ \equiv yu_*/v_2 = 1$, where y is the distance to the wall, $u_* \equiv \sqrt{\tau_b/\rho_2}$ is the friction velocity, τ_b is the bottom shear stress; therefore, the viscous sublayer was resolved. The transition of spacing between adjacent layers was smooth, with a growth rate limited to 1.1. The mesh was also refined for the free surface region $h_o < x_3 < h_e$ itself (Figure 3.1(d)) and its adjacent regions. The mesh was not exactly symmetric about the channel centerline because the channel width did not divide evenly into the cell size chosen for generating the mesh, which inevitably produced a remainder. Some LES studies used $y^+ = 4$ for near-wall mesh refinement (Tokyay & Sinha, 2020). Others used uniform Cartesian mesh, along with a wall function, and avoid refinement (Ottolenghi et al., 2020; Z. Xie et al., 2013).

The process of mesh generation is as follows: First, the outlet plane of the model channel (Figure 3.1(a)) was discretized into squares. Second, the regions near the channel-bottom and sidewalls in this plane were refined. Third, the mesh in this plane was swept toward the inlet plane. Lastly, the body of influence was used to refine the water-surface region. The hexahedron sizes of mesh were determined using Zang's (1991) guidelines about LES mesh: In the wall-normal direction, there is at least one node in the interval $0 < y^+ < 1$ and at least three nodes in the interval $0 < y^+ < 10$. In the streamwise and spanwise directions, the sizes fulfill the requirements $\Delta x_2^+ < 80$ and $\Delta x_1^+ < 30$, where $x_i^+ = x_i u_*/v$ for $i = 1, 2$. Take M2 mesh (Table 3.1) as an example. In the streamwise direction, Δx_2^+ was 36. In the wall-normal directions (Δx_1^+ and Δx_3^+), where the viscous sublayer was directly resolved, the first node off the wall was situated at $y^+ = 0.5$, the corresponding normalized distances being x_1/h_o = 3.1× 10^{-4} and x_3/h_o = 3.1× 10^{-4}; further, ten nodes were placed on the interval $0 < y^+ < 10$. There was a progressive refinement of sizes for the region from the wall to the interior by means of inflation layers until $\Delta x_1^+ = \Delta x_3^+ = 27$. The growth rate

of sizes was kept within 1.1. Table 3.1 lists the mesh in terms of wall units based on the maximum friction velocity from LES output. It is worth mentioning that all the LES mesh in this study has a low skewness, having an average value below 0.3 and a maximum value below 0.9, and thus the mesh quality is acceptable to maintain numerical accuracy and stability.

Variables are stored at the cell centroid. Their interfacial values are estimated. The least square cell-based method solves variable gradients on the cell faces. In the discretization of model equations, the bounded central differencing scheme gives the face values of most variables. The PRESTO! Scheme calculates the face values of p. For temporal development, the bounded 2nd-order implicit method integrates the equations over a time step Δt. The SIMPLE algorithm solves the equations in a pressure-velocity coupling manner and iterates until the convergence criterion of 10^{-6} or a maximum of 120 iterations per Δt is reached. The volume of fluid method, coupled with the level-set method (Sethian & Osher, 1987; Yue et al., 2005), reliably tracks the position of η using the criterion $\alpha_2 = 0.5$. Details about PRESTO! and SIMPLE can be found in the literature (Patankar, 2018).

Table 3.1 Summary of LES runs. The discharge is Q = 11.8 L/s for runs H8, H9 and H10, and Q = 10.23 L/s for the other runs. Computed values of the energy coefficient α and momentum coefficient β (Chow, 1959) are for the expansion exit ($x_2 = 2L$)

LES run	h_o (cm)	h_e (cm)	U_o (cm/s)	Δt (s)	$(\Delta x_1, \Delta x_2, \Delta x_3)$ (wall unit)	Re	Fr	Bottom condition	Initial condition	α	β	u_*/U_o mean $\pm$ std
M1	18.57	18.81	32.2	0.006	(33, 45, 33)	59759	0.24	Flat	i	-	-	-
M2	18.57	18.81	32.2	0.006	(27, 36, 27)	59759	0.24	Flat	i	1.57	1.22	0.026±0.006
M3	18.57	18.81	32.2	0.006	(20, 27, 20)	59759	0.24	Flat	i	-	-	-
M4	18.57	18.81	32.2	0.006	(14, 18, 14)	59759	0.24	Flat	i	-	-	-
M5	18.57	18.81	32.2	0.006	(11, 15, 11)	59759	0.24	Flat	i	-	-	-
M6	18.57	18.81	32.2	0.006	(10, 13, 10)	59759	0.24	Flat	i	-	-	-
T4	18.57	18.81	32.2	0.008	(27, 36, 27)	59759	0.24	Flat	i	-	-	-
T5	18.57	18.81	32.2	0.004	(27, 36, 27)	59759	0.24	Flat	i	-	-	-
F6	18.57	18.81	32.2	0.006	(27, 36, 27)	59759	0.24	Flat	ii	1.67	1.27	0.027±0.006
F7	18.57	18.81	32.2	0.006	(33, 44, 33)	59759	0.24	Flat	iii	1.55	1.21	0.027±0.006
H8	17.27	17.67	39.9	0.004	(33, 44, 33)	68966	0.31	Hump	i	1.33	1.13	0.021±0.006
H9	17.27	17.67	39.9	0.004	(33, 44, 33)	68966	0.31	Hump	ii	1.33	1.13	0.020±0.005
H10	17.27	17.67	39.9	0.004	(27, 36, 27)	68966	0.31	Hump	iii	1.32	1.12	0.021±0.005

Note: The Reynolds number is Re = $U_o h_o/\nu_2$. The Froude number is Fr = $U_o/\sqrt{g h_o}$. The mean values and standard deviations are for the channel-bottom in $2 < x_2/L < 2.75$. The wall units are based on the maximum friction velocity from the LES output.

3.2.3 Initial conditions

Table 3.1 lists ten LES runs (M1–H10) of turbulent subcritical flow. The time step used satisfies the Courant-Friedrichs-Lewy criterion for numerical stability (Courant et al., 1928). The flow history or initial conditions for the runs were specified in one of three different ways:

(1) Stagnant water ($u_i = 0$) in the left flank (Figure 3.1(a)); the middle region and right flank having water velocity $u_2 > 0$ and $u_1 = u_3 = 0$, where u_2 was uniform at a given cross-section (x_2 = constant) and satisfied $\iint u_2 dx_1 dx_3 = Q$. Here, Q is the flowrate from experiments (Najafi-Nejad-Nasser & Li, 2015). The free surface η rose linearly along the expansion length, from $\eta = h_o$ at $x_2 = L$ to $\eta = h_e$ at $x_2 = 2L$; $\eta = h_o$ for $x_2 < L$; $\eta = h_e$ for $x_2 > 2L$. η was uniform in the x_1 direction. The pressure p was hydrostatic pressure

below the free surface ($x_3 < \eta$); $p = 0$ and $u_i = 0$ above ($x_3 > \eta$). This set of initial conditions is labeled as 'i' in Table 3.1.

(2) Stagnant water in the right flank; the middle region and left flank having water velocity in the x_2 direction. Other remarks are similar to those given in initial condition i. This set of initial conditions is labeled as 'ii' in Table 3.1.

(3) Stagnant water in both the left and right flanks; the middle region having water velocity in the x_2 direction. Other remarks are similar to those given in initial condition i. This set of initial conditions is labeled as 'iii' in Table 3.1, which is included for completeness.

The initial conditions i and ii are contrary conditions (Figure 3.2). The condition i/ii mimics the flow condition at the time when streamlines into the left/right flank remain blocked during a flume experiment. In a natural expansion, local turbulent eddies or disturbances can sporadically cause a one-sided blockage for a certain amount of time. The initial condition can be interpreted as a historical scenario of flow. Does the historical scenario connect to future ones across time following the relaxation of blockage? The LES runs (Table 3.1) help address the question of how initial conditions affect the flow states. This question has rarely been addressed before.

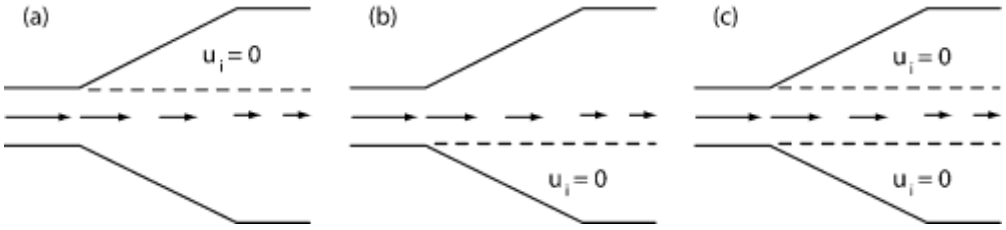

Figure 3.2 Initial conditions: (a) initial condition i; (b) initial condition ii; (c) initial condition iii

3.2.4 Ensemble average

The physical length of expansion and the flow velocity approaching the expansion are two of the most important parameters in the design of expansions. The associated advection time scale is

$$T = L/U_o \tag{3.2}$$

T is therefore of central importance in the analysis of LES output. The LES runs each commenced from initial conditions i, ii or iii (Table 3.1, Figure 3.2). Each run allowed a spin-up time period $T_s = 37.5T$, and continued for another time period T_o for output ($T_o > T$). The large T_s permitted flow development. Subsequent computations for output predicted n snapshots of p, u_i and η on the mesh, at an output sampling frequency $f = 1/\Delta t$. The ensemble averages of velocity $\bar{u}_i$, pressure $\bar{p}$ and free surface elevation $\bar{\eta}$ at a given node were obtained by

$$\bar{u}_i = \sum u_i/n\,;\ \bar{p} = \sum p/n\,;\ \bar{\eta} = \sum \eta/n \tag{3.3}$$

The horizontal velocity is given by $\boldsymbol{u} = \bar{u}_1\hat{\boldsymbol{x}}_1 + \bar{u}_2\hat{\boldsymbol{x}}_2$, where $\hat{\boldsymbol{x}}_i$ is a unit vector in the x_i direction.

The determination of states of bistable flow by ensemble average requires a large enough number of snapshots, satisfying

$$n/f > T \tag{3.4}$$

On the other hand, the case $n/f = T$ may be considered as a benchmark case, which is of interest and relevance to the engineering design.

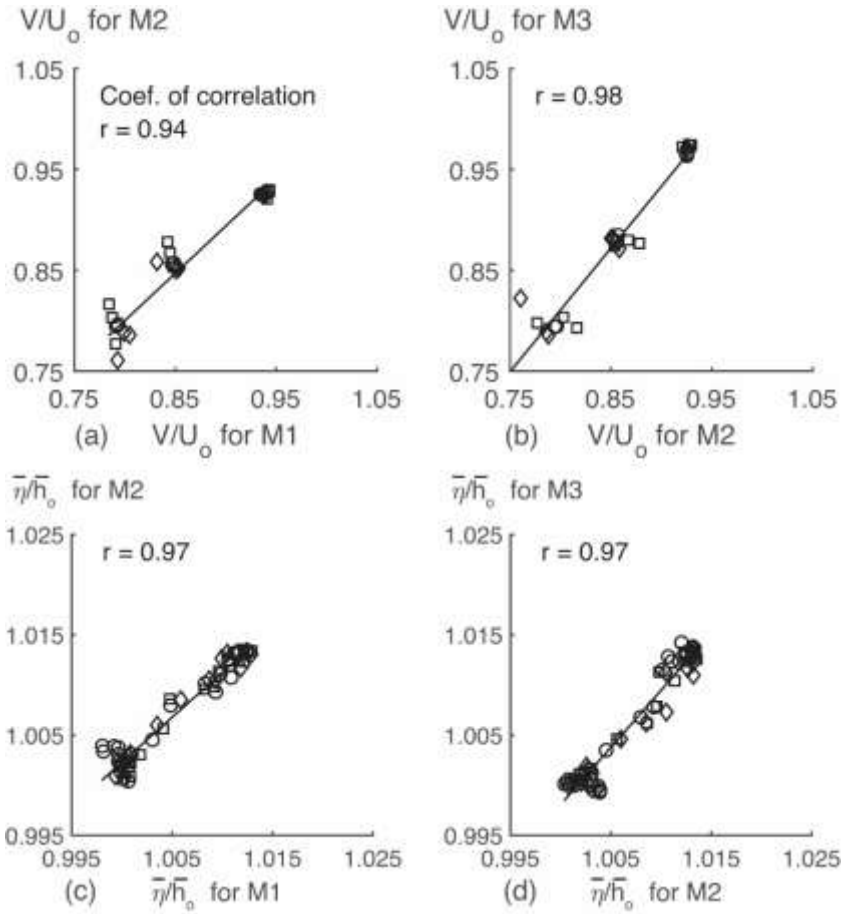

Figure 3.3 Comparison of predicted $V = (\bar{u}_1^2 + \bar{u}_2^2 + \bar{u}_3^2)^{1/2}$and $\bar{\eta}$ values: (a) and (c) between M1 and M2; (b) and (d) between M2 and M3. The data points are from locations in three selected planes at x_1/b_1= 0.25 (□), 0.5 (○), and 0.75 (◊) m. The comparison is not to be interpreted as mesh independence of LES results

3.2.5 Choice of mesh and time step

M1, M2 and M3 used the same simulation conditions, except the mesh size, Δx_i, being progressively finer for the three runs. Δx_i decreases by 20% from M1 to M2 and further by 25% from M2 to M3, and correspondingly the number of computing nodes increases from 1.59×10^6 for M1 to 2.56×10^6 for M2 and to 4.96×10^6 for M3. No change was made to the aspect ratio of mesh resolutions. The number of inflation layers for near-wall regions was adjusted among the runs, being 43, 41 and 38, respectively, in order to achieve smooth transition of adjacent cells. The number of computing nodes was 2.65×10^6 for H8, H9 and H10.

The choice of mesh aimed to directly compute large energy-carrying turbulent structures. Unresolved small eddies were modelled through μ_t, which inevitably involved some uncertainties. Reducing the local grid scale will help reduce the uncertainties but will increase computing costs. A need exists to achieve a balance between computing costs and computational result consistency. As the first order approximation, this study chose average velocity and water surface elevation variables for assessment of results consistency. Between M2 and M1 and between M2 and M3, the maximum relative difference of average velocities and water surface elevations at a series of

selected locations was as small as 4.6 % (Figure 3.3). As far as the chosen variables are concerned, further refinement from the M2 mesh resolutions was not necessary. This justified using the M2 mesh in subsequent runs. T4, M2 and T5 used the same conditions, except Δt, being progressively smaller. These three runs produced consistent average velocities and water surface elevations. Between M2 and T5, the maximum difference of the average values was 2.6 % (Figure 3.4). It is suitable to use the M2 mesh resolutions and time step $\Delta t \leq 0.006$ s for subsequent runs (F6–H10). Higher order statistics of turbulence are beyond the scope of this study. They differ among the runs.

This study used mesh cells having non-uniform spacing while providing acceptable resolutions to perform LES, as discussed earlier. Some previous studies (Baggett et al., 1997; Chapman, 1979; H. Choi & Moin, 2012; Y. Long et al., 2019; Yang & Griffin, 2021) estimate the total number of uniformly spaced cells from the Reynolds number, which may be based on the friction velocity. In practice, it is wasteful to use uniformly spaced cells for a model channel with the sub-region where the dissipation is small, and in some cases, the use of non-uniformly spaced mesh cells can reduce the total number of cells needed by a factor of 8.1×10^3, as stated in Wilcox (2006).

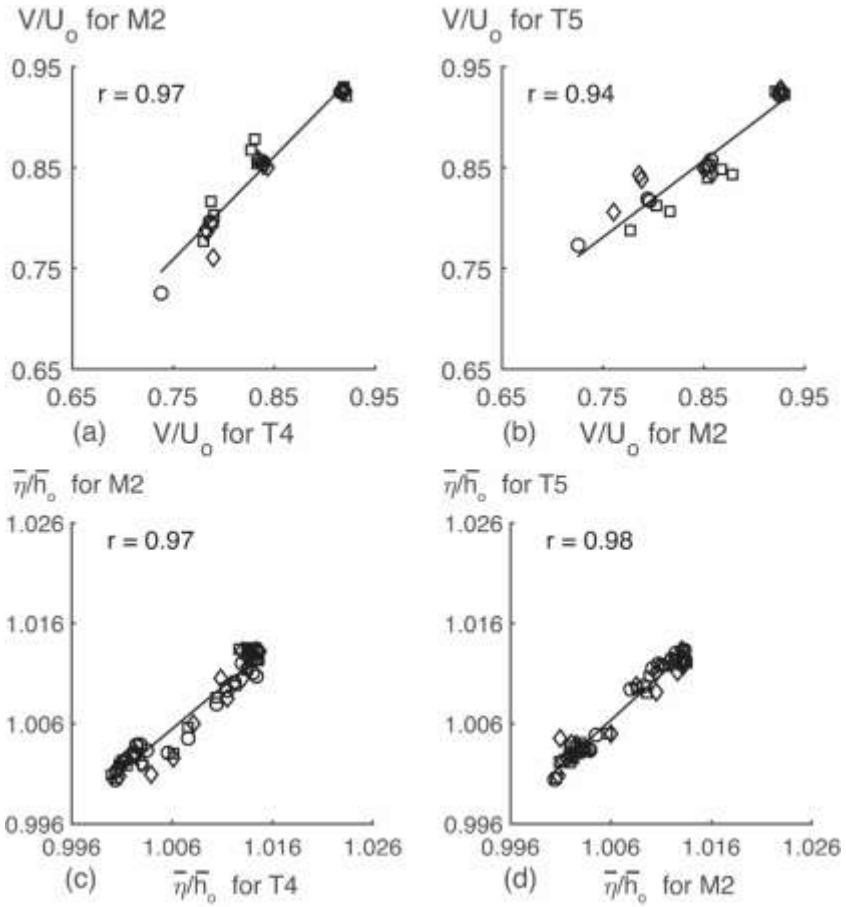

Figure 3.4 Comparison of predicted $V = (\bar{u}_1^2 + \bar{u}_2^2 + \bar{u}_3^2)^{1/2}$and $\bar{\eta}$ values: (a) and (c) between T4 and M2; (b) and (d) between M2 and T5. The data points are from locations in three selected planes at x_1/b_1= 0.25 (□), 0.5 (○), and 0.75 (◊) m

3.3 Results

3.3.1 Ensemble average of bistable flow field

In order to determine the states of bistable flow (Figures 3.1(b), 3.1(c)), a large number of snapshots of the instantaneous flow field from LES following a spin-up time period of 37.5T (Eq. 3.2) were predicted. Take Run M2 (Table 3.1) as an example. M2 used the initial condition i (Figure 3.2(a)). The time scale of importance (Eq. 3.2) is $T = 0.96$ s, the spin-up time is $T_s = 36$ s, and the output data sampling frequency is $f = 167$ Hz. The velocity field averaged over nine increasing snapshots n = 20 to 640 (Eq. 3.3) is plotted in Figures 3.5(a)–3.5(i). All nine ensemble averages show two striking flow features: a) large spatial variations in velocities in the left and the right flanks; b) asymmetrical patterns about the channel centerline and between the two flanks (Figure 3.1(a)). This is regardless of how many snapshots used for averaging. The question is how long the time span of averaging needs to be in order to produce a stable quasi-equilibrium state.

To demonstrate the choice of the number of snapshots after the spin-up time period T_s for averaging, time series of instantaneous velocities at nine selected positions in the expansion are shown in Figures 3.6(a)–3.6(c), 3.7(a)–3.7(c) and 3.8(a)–3.8(c) for M2. As expected, the instantaneous velocities from LES fluctuated in time. The span of sample time was 6.25T, from t = 36 to 42 s at a time interval $\Delta t = 0.006$ s, i.e., the time series each consist of a total of 1000 data points. The fluctuations were larger in amplitude in the left flank (Figures 3.6(a)–3.6(c)) than in the right flank (Figures 3.8(a)–3.8(c)). The cumulative averages of the instantaneous velocities are shown in Figures 3.6(d)–3.6(f), 3.7(d)–3.7(f) and 3.8(d)–3.8(f). Take as an example t = 39 s. The cumulative average of $\bar{u}_1$ was obtained by taking the average of 500 instantaneous u_1 values (Eq. 3.3, n = 500) from t = 36 to 39 s at $\Delta t = 0.006$ s. The cumulative averages changed very little around $n = 500$ or larger and display asymptotical behaviour. Thus, it is acceptable to use 500 snapshots of instantaneous quantities for averaging; this corresponds to a time span of 3.125T (or 3 s). For convenience, 480 snapshots (a time span of 3T or 2.88 s) after the spin-up time period of 37.5T (or 36 s) are used for averaging.

It is further verified that the time span of 3T (or 2.88 s) for averaging satisfies the condition that two flow quantities separated by this time scale are virtually uncorrelated. This condition means that a time span is sufficiently long and suitable for averaging (Cheng et al., 2018). For the sample time series (Figures 3.6(a)–3.6(c), 3.7(a)–3.7(c) and 3.8(a)–3.8(c)), values of the autocorrelation function r_{k}, for time lag k (Box et al., 2015) are calculated and plotted in Figure 3.9. For a given position (x_1, x_2, x_3), the function measures the correlation between the univariate time series u_i at time t and u_i at time $t + k$ where k = 0, ..., 3 s (or 3.125T). The function has a value of unity at zero time lag because the time series of velocity data is perfectly correlated to itself, and then decays as the time lag increases from zero. As the time lag further increases, the function becomes bounded, having low values. Specifically, for $k \geq 2.88$ s, $|r_k| < 0.25$, and thus low values of r_{k} mean that the instantaneous velocities separated by 2.88 s (or 3T) are not correlated. This confirms that the time span of 3T (or 480 snapshots) are sufficiently long for averaging.

Flow variabilities or eddy activities in the expansion are the top concern from the perspective of hydraulic efficiency. Which of the ensemble averages in Figures 3.5(a)–3.5(i) (in other words, how many snapshots used for averaging) exhibits the highest level of variabilities? Take the left flank of the expansion (Figure 3.1(a), $x_1 \leq 0$; $L \leq x_2 \leq 2L$) as an example to investigate. In Figures 3.5(a)–3.5(f), the ensemble averages over 240 snapshots or less ($n\Delta t \leq 1.5T$) exhibited temporal

fluctuations in flow patterns. The spatial distributions of $\bar{u}_2$ values (Eq. 3.3) had temporally fluctuating standard deviations between 0.1141 m/s for n = 20 ($20\Delta t = T/8$) and 0.1074 m/s for n = 240 ($240\Delta t = 1.5T$).

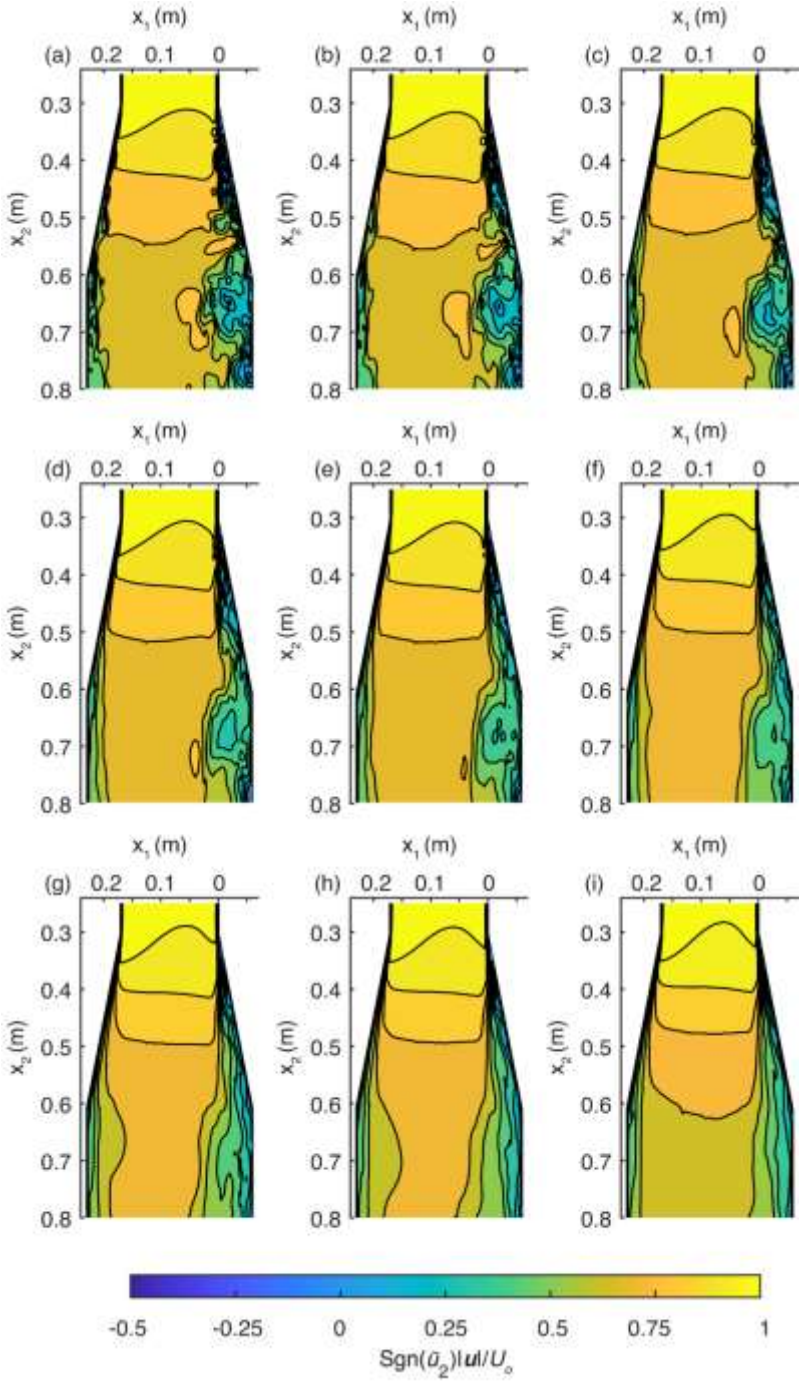

Figure 3.5 Distributions of ensemble-averaged horizontal velocity $\boldsymbol{u}$ at elevation $x_3 = 0.48h_o$ for M2. The number of snapshots n used for averaging in Eq. 3.3 is: (a) 20; (b) 40; (c) 80; (d) 120; (e) 160; (f) 240; (g) 320; (h) 480; (i) 640. Reversed flow occupied the areas of negative contour values

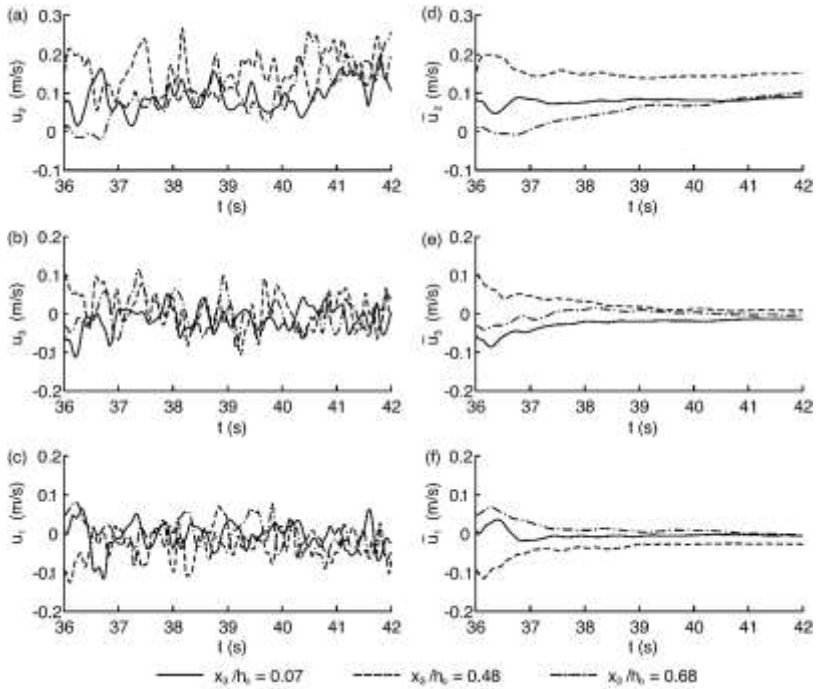

Figure 3.6 Time series of instantaneous velocity components (panels a, b and c), and cumulatively averaged velocity components (panels d, e and f). The horizontal coordinates are $(x_1/b_1, x_2/L) = (-0.157, 1.8)$, in the left flank

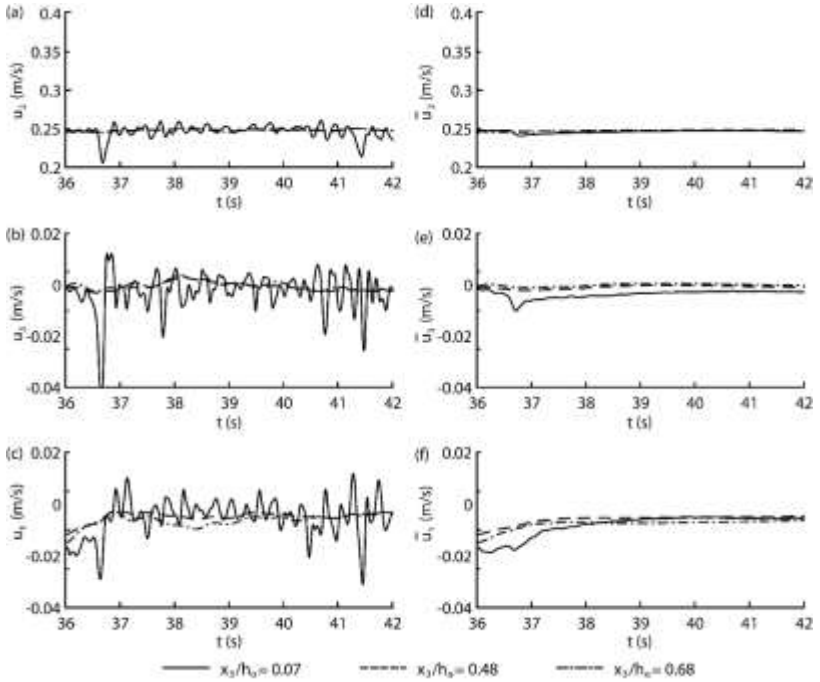

Figure 3.7 Time series of instantaneous velocity components (panels a, b and c), and cumulatively averaged velocity components (panels d, e and f). The horizontal coordinates are $(x_1/b_1, x_2/L) = (0.49, 1.8)$, near the channel centerline. Some curves overlap each other

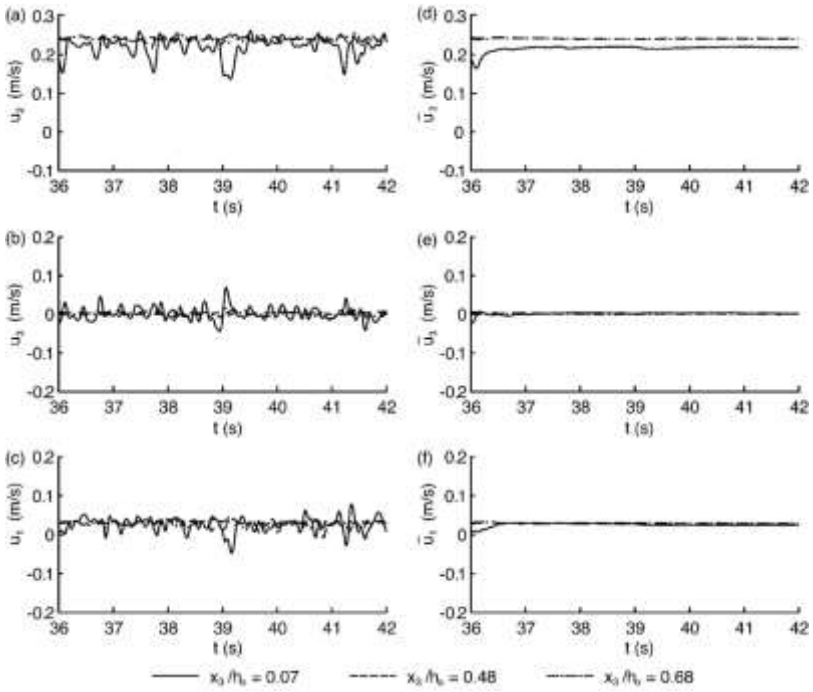

Figure 3.8 Time series of instantaneous velocity components (panels a, b and c), and cumulatively averaged velocity components (panels d, e and f). The horizontal coordinates are $(x_1/b_1, x_2/L) = (1.07, 1.8)$, in the right flank. Some curves overlap each other

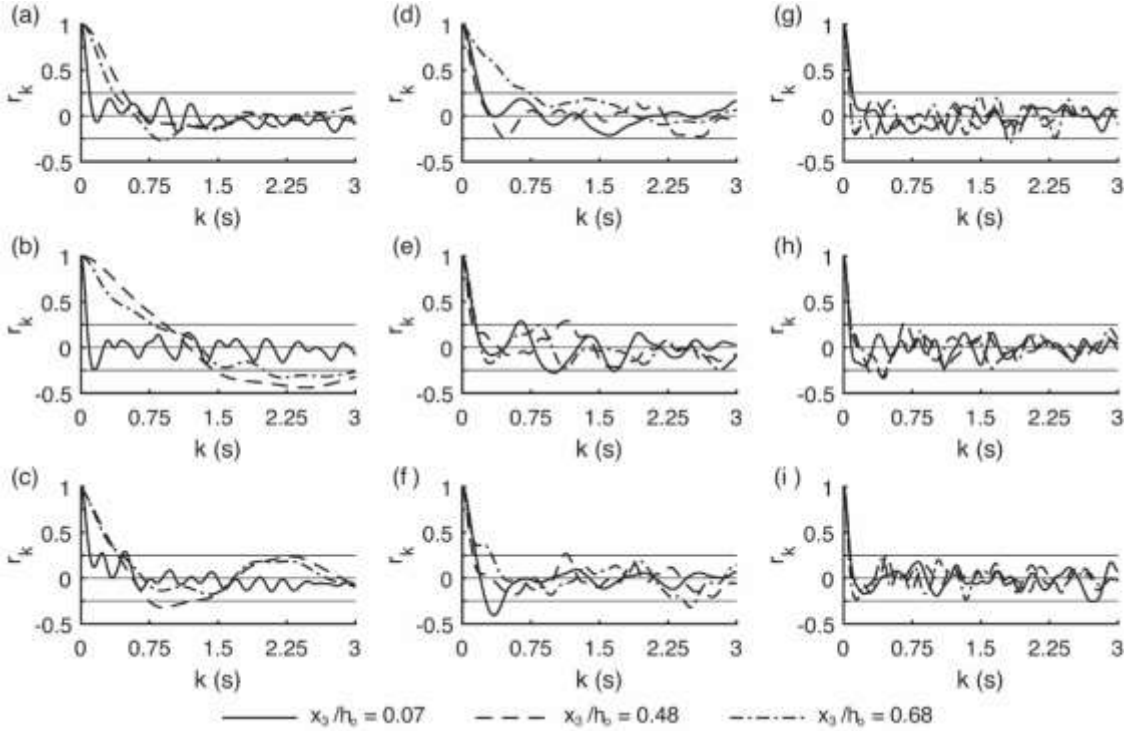

Figure 3.9 Autocorrelation function r_k for time lag k: (a–c) corresponds to Figures 3.6(a)–3.6(c); (d–f) corresponds to Figures 3.7(a)–3.7(c); (g–i) corresponds to Figures 3.8(a)–3.8(c), respectively

In Figure 3.5(g), the ensemble average over 320 snapshots ($n\Delta t = 2T$) manifested some levels of flow variabilities. The distribution of $\bar{u}_2$ values had standard deviation (equal to 0.1076 m/s or $0.334U_o$) among the nine ensemble averages, i.e., the ensemble average in Figure 3.5(h) displayed minimal level of eddy activities. The distribution of $\bar{u}_2$ values had a median value of $0.71U_o$. There were some velocity vectors of reversed flow, caused by flow separation. The distribution of $\bar{u}_1$ values (Eq. 3.3) had a standard deviation of 0.0135 m/s and a near zero median value. Approximately an equal number of velocity vectors pointed in the positive x_1-direction (away from the sidewall) and in the negative x_1-directions (toward the sidewall).

In Figure 3.5(h), the averaged flow field over the time span from t = 36 to 38.8 s shows globally asymmetrical patterns, and is taken as having reached a stable equilibrium state of ensemble average flow. Averaging over a longer time span (Figure 3.5(i)) is not necessary. For this reason, the focus of discussion will be on ensemble average over 480 snapshots. Note that cross-sections in the expansion differ in shape and area, and therefore one should not take averages of velocities and pressure over the cross sections.

Runs M2 and H8 (Table 3.1) started from the initial condition i (Figure 3.2(a)) and yielded snapshots of u_i, p and η distributions. The ensemble average of the snapshots is referred to as flow state i. Runs F6 and H9 (Table 3.1) started from initial condition ii (Figure 3.2(b)), and the ensemble average produced flow state ii. Since M2 and F6 differ only in initial conditions, a comparison of the flow field between them will reveal the influence of flow history on the flow state.

An example of flow state i from M2 is described below: In Figures 3.10(a), 3.10(c), and 3.10(e), distributions of $\boldsymbol{u}$ at the free surface, at the middle depth and near the bottom are plotted. The free surface $\bar{\eta}$ varied in the channel. Contours of normalized $|\boldsymbol{u}|$ are combined to the $\boldsymbol{u}$ directions. For a given location, the sign function Sgn($\bar{u}_2$) assigns a plus (minus) sign to the magnitude if $\bar{u}_2 > 0$ ($\bar{u}_2 < 0$). Thus, a positive magnitude means water flowing towards the outlet, whereas a negative magnitude means towards the inlet or reversed flow. The main characteristics of flow state i are: 1) A core of strong flow occurred in the expansion. The strongest velocity had a magnitude of $+1.05U_o$. The strong flow was asymmetrical about the centerline, deflecting to the right; 2) flow separation occurred along both expansion sidewalls and triggered eddies in both flanks. The eddies had larger structures and reverse flow was more significant on the left than the right. The reverse flow had a maximum magnitude of almost $-0.35U_o$; 3) in the downstream channel, flow separation ceased to exist along the right sidewall but persisted along the left (the initially stagnant left flank). In the upstream channel, the longitudinal flow velocity was zero at the solid wall surface and increased rapidly with normal distance. The velocities were the strongest near the free surface (Figure 3.10(a)) and the weakest near the bottom (Figure 3.10(e)). The flows near the surface and bottom had small pockets of strong velocities in the expansion and nearby regions. The flow had complex 3-D structures. The deflection of primary flow direction is the most significant at the mid depth.

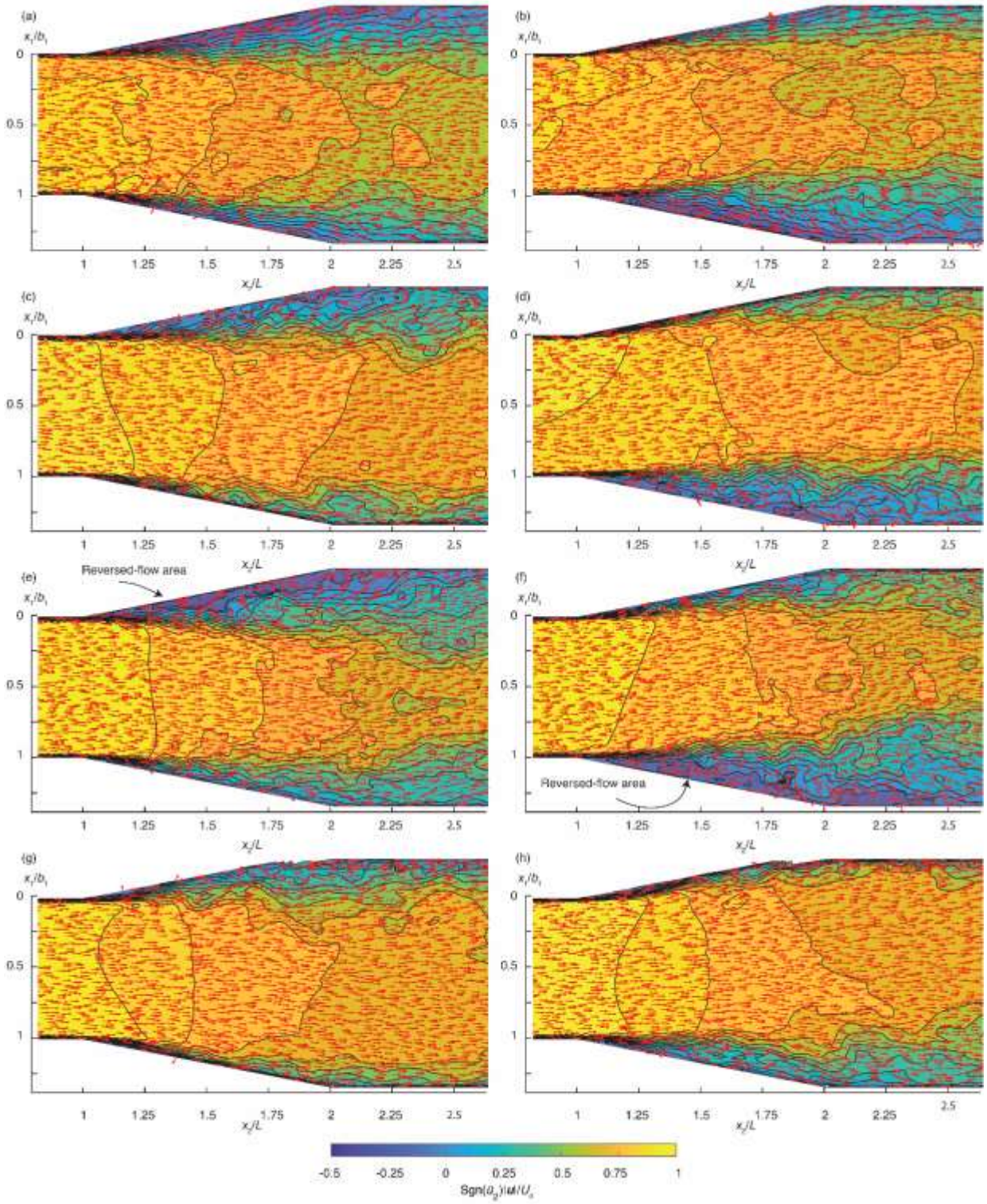

Figure 3.10 Distributions of $\boldsymbol{u}$ at elevations: (a) $x_3 = \eta$ for M2; (b) $x_3 = \eta$ for F6; (c) $x_3 = 0.48h_o$ for M2; (d) $x_3 = 0.48h_o$ for F6; (e) $x_3 = 0.07h_o$ for M2; (f) $x_3 = 0.07h_o$ for F6; (g) $x_3 = 0.48h_o$ for H8; (h) $x_3 = 0.48h_o$ for H9. Flow reversal occupied the areas of negative contour values

An example of flow state ii from F6 is illustrated in Figures 3.10(b), 3.10(d) and 3.10(f). Flow state ii featured a core of strong flow in the expansion, flow separation along both expanding sidewalls, eddies, and flow reversal is very strong in the left flank. Flow state ii shared similarities with flow state i. However, there were important differences between them. In flow state ii, the core flow deflected to the left, as opposed to the right in flow state i. The eddies had larger structures on the right than the left. Flow separation and reversal were persistent along the right sidewall of the downstream channel. All these directions and sides were just opposite to what occurred in flow state i. Flow states i and ii were virtually a mirror image of each other, meaning that the expansion flow was bistable.

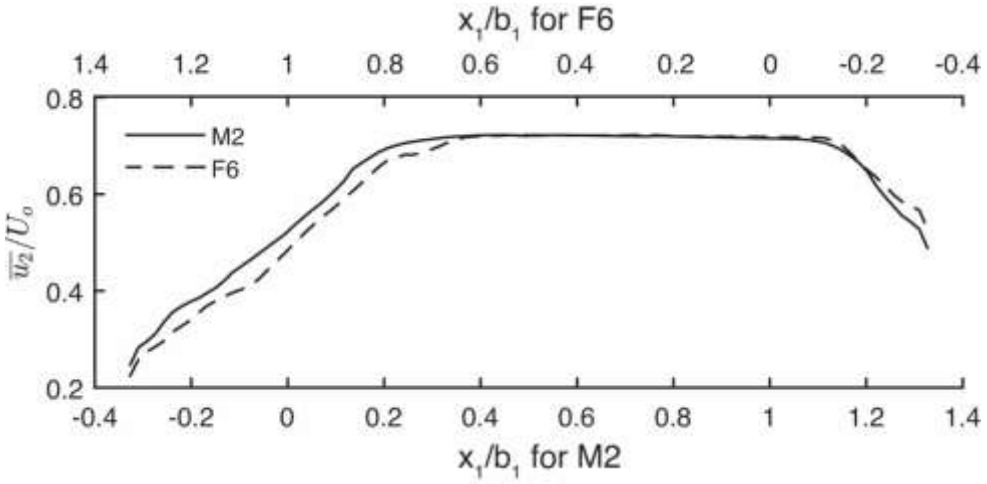

Figure 3.11 Comparison of lateral profiles of temporally and spatially averaged streamwise velocity between M2 and F6. The root mean square error is 0.008 m/s compared to a peak velocity of 0.2324 m/s. The correlation coefficient is 0.99

Runs using the initial condition i and ii (e.g. M2 vs. F6) need not to produce mirror-image flow structures across the channel width at fixed coordinates (x_2, x_3), when only time average is applied to the instantaneous flow quantities (e.g. Figure 3.10(c) vs 3.10(d)). This is for a number of reasons. On the one hand, there are eddy structures forming in the expansion, and they evolve while moving toward downstream. On the other hand, the flow field is three-dimensional, with interacting motions of eddies between different elevations. Further applying spatial average results in mirror-image flow structures between the runs, as illustrated by the example in Figure 3.11, where the time averaging was over 2.88 s (or 480 snapshots), and spatial averaging was over $2.25L \leq x_2 < 2.75L$ and between $x_3 = 0.48h_o$ and $0.68h_o$. It is a common practice that both time and space (often in multi-directions) averages are applied to LES output for flow statistics (Cheng et al., 2018; Mokhtarpoor & Heinz, 2017; Monti et al., 2019; Xie et al., 2013; Yan et al., 2017).

3.3.2 Influence of a hump on the flow field

How does TBF in an expansion respond to the presence of a hump at the bottom (Figure 3.1(d))? The bottom had a hump for H8, whereas it was flat for M2, which was the main difference in setup between them. Other differences were only of minor importance and were for the sake of matching experiments (Najafi-Nejad-Nasser & Li, 2015). Similar remarks apply to F6 versus H9.

As an example, $\boldsymbol{u}$ distributions at the middle depth for H8 and H9 are plotted in Figures 3.10(g) and 3.10(h). The distributions were representative of those in a large range of depths, except for flow details near the sidewalls. The distributions in Figure 3.10(g) differed from those in Figure 3.10(c) due to the influence of the hump. The most important difference was the extent of flow reversal. In Figure 3.10(g), flow reversal occupied about 0.93% of the expansion area within the left flank, compared to 10.27% in Figure 3.10(c). This was a moderate drop. In the expansion within the right flank, there was almost no flow reversal at the mid-depth (Figure 3.10(g)) and other depths. Near the bottom, the drop was particularly significant, from 37.89% within the left flank for M2 (Figure 3.10(e)) to 4.57 % for H8. In the upper column, the drop was particularly significant, from 22.45 % within the left flank for M2 to 0.94 % for H8.

For F6, flow reversal occupied a large percentage of the right flank, particularly near the bottom (Figure 3.10(f)). For H9, the hump reduced reversal areas in most horizontal planes. For example, the percentage dropped from 24.33% in Figure 3.10(d) to 1.65% in Figure 3.10(h) within the expansion portion of the right flank. The humps for H8 and H9 achieved about the same reduction to flow reversal areas.

With the hump (Figures 3.10(g), 3.10(h)), the surface velocities near the sidewalls were less strong, compared to without a hump (Figures 3.10(a), 3.10(b)). In some upper horizontal planes, the hump shifted the locations of some strong velocities and created more uniform flow across the channel width. The hump accelerated the middle-depth flow and enhanced uniformity (Figs 3.10(g), 3.10(h)). It increased the effective width of flow towards downstream, compared to without a hump. It also accelerated near-bottom flow upon approaching the crest ($x_2 = 2L$), where the flow experienced vertical contraction. Downstream of the crest, the velocities weakened due to the proximity to the crest surface and vertical expansion. Vertical contraction and expansion caused vertical motions; streamlines terminated in one horizontal plane and emerged in adjacent ones. Further downstream, the flow recovered to some extent. The flow field for F7 differed from those for M2 and F6 in details. Likewise, the flow field for H10 differed from those for H8 and H9.

3.3.3 Data comparison

Pressures at 25 locations in the expansion were extracted from the F6 results and compared with measurements from an experiment without a hump (Najafi-Nejad-Nasser & Li, 2015) (Figure 3.12(a)). The measurements were from an array of 20 pressure taps at the left sidewall and five taps at the bottom along the centerline. The five locations are at: x_2/L = 1.291, 1.541, 1.708, 1.875 and 1.97; $0 \leq x_3/h_o < 0.9$. In Figures 3.12(a) and 3.12(b), $\bar{p}_o$ is the reference pressure at (x_1/b_1, x_2/L, x_3/h_o) = (0.5, 2, 0). The computed $\bar{\eta}$ values for F6 at x_2/L = 1, 2 and the five above-mentioned locations in between are compared with measurements from an experiment without a hump in Figure 3.12(c). It is not known whether the experimental flow was at flow state i or ii. The root-mean-square errors of the computed $\bar{\eta}$ values from the measurements are negligible (Figures 3.12(c)). The comparisons are good.

Similarly, the computed pressures at 25 locations for H8 are compared with measurements from an experiment with a hump (Najafi-Nejad-Nasser & Li, 2015) in Figure 3.12(b). The computed and measured $\bar{\eta}$ values at x_2/L = 1, 2 and the five above-mentioned locations in between are compared with experimental measurements in Figure 3.12(d). The comparisons are satisfactory. The root-mean-square errors of the computed $\bar{\eta}$ values are as small as 0.29%.

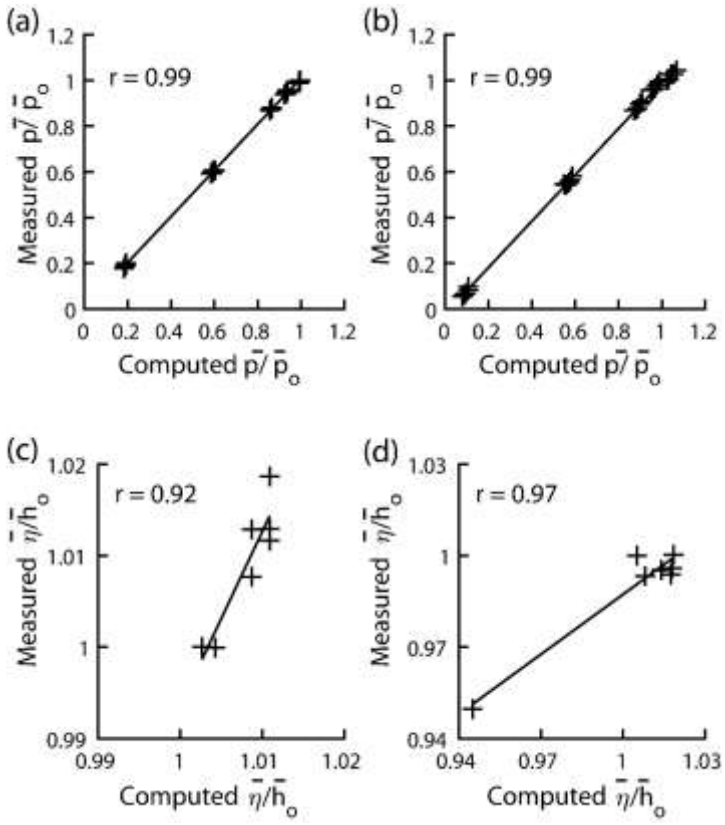

Figure 3.12 Comparisons of computed pressures $\bar{p}$ and water-surface position $\bar{\eta}$ for F6 with measurements at selected locations (panels a and c); comparisons of computed pressures $\bar{p}$ and water-surface position $\bar{\eta}$ for H8 with measurements at selected locations (panels b and d). The reference pressure is $\bar{p}_o$ = 1843 and 1561 Pa in (a) and (b), respectively. r is the correlation coefficient

3.3.4 Influence of outlet boundary condition

An additional LES run (M2P) was performed to assess the influence of outlet boundary condition on bistability. This run used the same conditions as M2 (Table 3.1), except that M2P implemented a numerical beach. M2P produced classical boundary-layer profiles of turbulence quantities before the expansion (Figure 3.13). However, it did not cause significant changes to the key features of bistable flows shown in Figure 3.10.

In M2P, the vicinity of pressure outlet (Figure 3.1(a)) was treated as a boundary zone, where a sink term (Park et al., 1999; Perić & Abdel-Maksoud, 2016) was added to Eq. 3.1. This term damps outgoing waves (if any) in the zone, and thus effectively avoids numerical wave reflection by the outlet. Examples of instantaneous water-surface profiles are plotted in Figure 3.14. In the entire channel, no waves had an amplitude larger than Δx_3, true for all the runs in Table 3.1. Small waves existed, having a wavelength exceeding $20\,\Delta x_2$ (Figure 3.14). Thus, the wave steepness (amplitude/wavelength) was very small ($< 3.75 \times 10^{-2}$). Besides, no waves rapidly fluctuated at time scale comparable to the time step Δt. The fact that the water surface profiles overlapped between runs M2 and M2 with damping (Figure 3.14) means no concerns of significant wave reflection from the outlet.

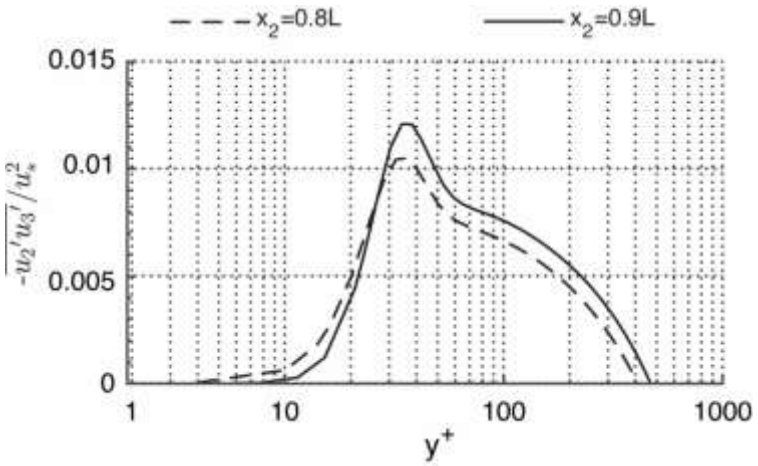

Figure 3.13 Vertical profile of turbulent shear stress at x_1/b_1 = 0.5, averaged over 0.3T after t > 42T for M2P. The global value (0.009 m/s) of u_* was used for normalization

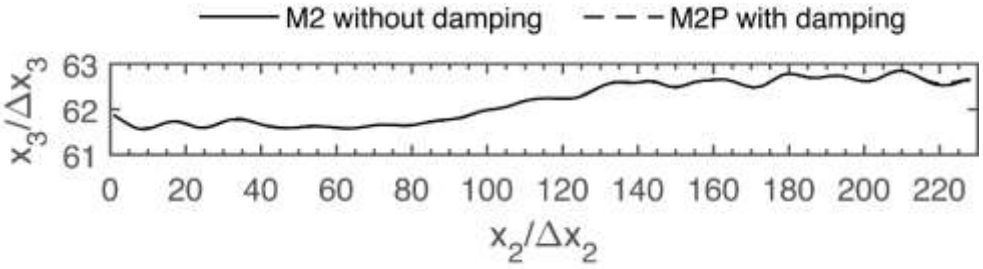

Figure 3.14 Instantaneous water-surface profiles along the channel centerline at t/T = 42. The two curves virtually overlap

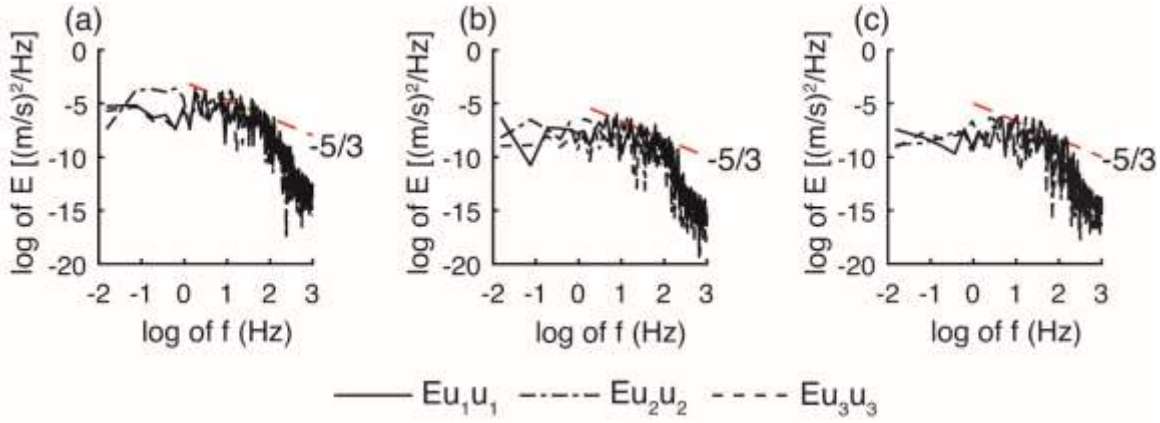

Figure 3.15 Velocity spectral densities for the u_1 component ($E_{u_1u_1}$), u_2 component ($E_{u_2u_2}$), and u_3 component ($E_{u_3u_3}$) at three selected ($x_1/b_1, x_2/L, x_3/h_o$) locations: (a) (1.07, 1.8, 0.07), (b) (1.07, 1.8, 0.48), and (c) (1.07, 1.8, 0.68). The results are for M2

The spectral distributions of instantaneous velocities can be obtained from a Fourier analysis of the fluctuating turbulent velocities. Time series of the velocities (u_1, u_2, u_3) at a series of locations were extracted from the LES predictions. The data were transformed from time domain to frequency domain. As output, examples of velocity spectral densities (or spectral functions) at

three selected locations are plotted in Figure 3.15. These functions show a typical velocity spectrum for a turbulent flow (Wilcox, 2006). In particular, there exists the inertial subrange, rather following the well-established Kolmogorov $-5/3$ law, and a cascade process or a transfer of the turbulence kinetic energy from larger eddies (lower frequency) to smaller eddies (higher frequency) as the turbulence decays. This study properly resolves a spectrum of scales and reproduces the law.

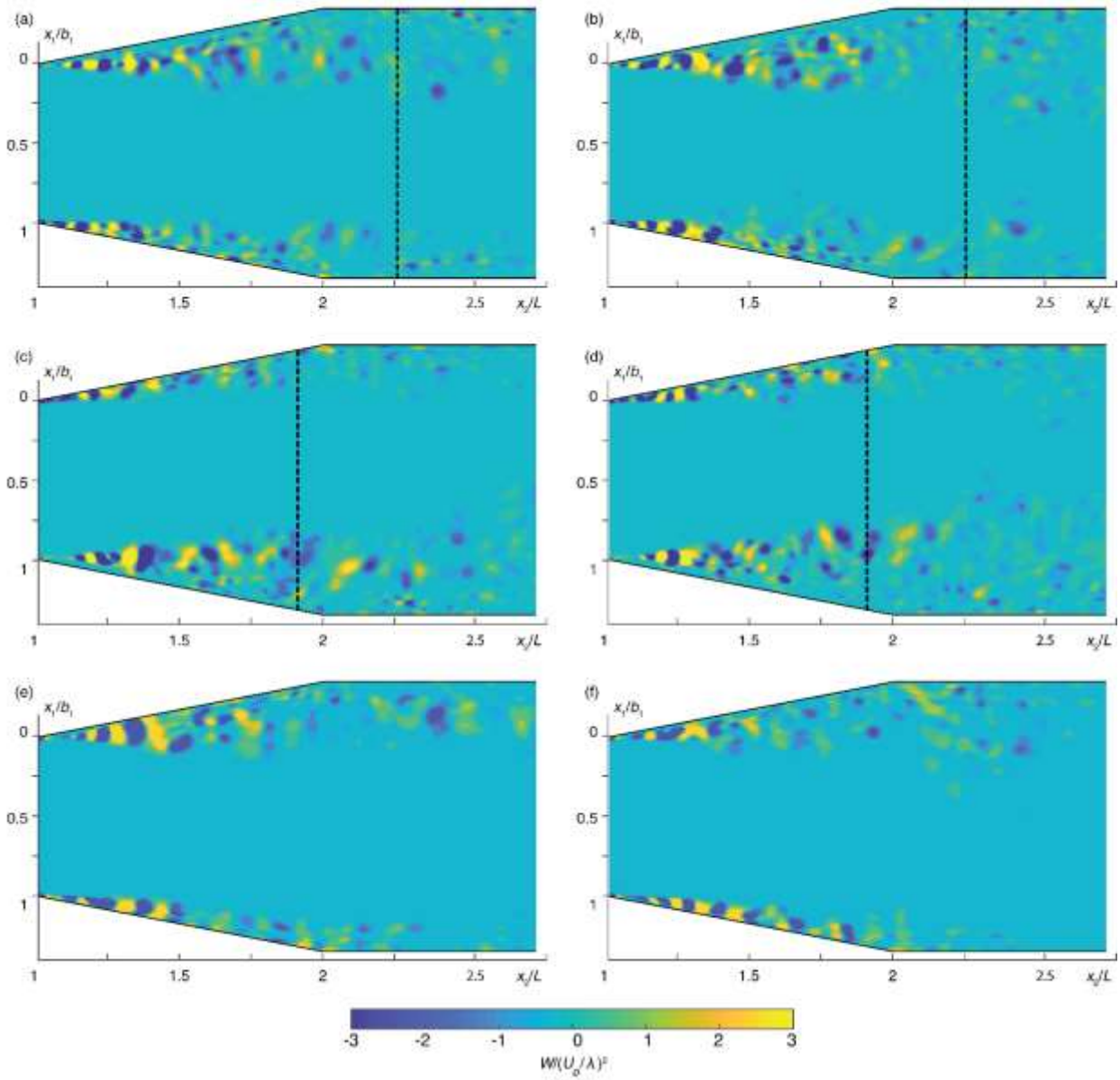

Figure 3.16 Horizontal planes near the middle depth x_3 = 0.09 m (left panels) and the near bottom $x_3 = 2\delta$ (right panels), showing rotation-dominated areas (eddy cores) and strain-dominated areas: (a) and (b) for M2; (c) and (d) for F6; (e) and (f) for H8. The w values in (a) to (f) have standard deviations σ_w = 7.7, 7.8, 8.4, 7.4, 13.9, and 13.4 (s^{-2}), respectively

3.4 Discussion

3.4.1 Asymmetric distributions of eddies as bistability indicator

The motion of a fluid can be decomposed into linear deformation, angular deformation and eddy rotation. The Okubo-Weiss parameter, *w*, is used to quantitatively identify and trace persistent turbulent eddies in the expansion and downstream channel. *w* is expressed as $w = s_n^2 + s_s^2 - \omega_3^2$, where the normal strain component is $s_n = \partial\bar{u}_2/\partial x_2 - \partial\bar{u}_1/\partial x_1$; the shear strain component is $s_s = \partial\bar{u}_1/\partial x_2 + \partial\bar{u}_2/\partial x_1$; the relative vorticity is $\omega_3 = \partial\bar{u}_1/\partial x_2 - \partial\bar{u}_2/\partial x_1$. Rotation-dominated areas (or eddies) are areas of $w < -w_o$, where w_o is a certain threshold. The cores of eddies are located in local minima of negative *w* values; they exhibit large vorticity and strong circulation density of the velocity field. Strain-dominated areas are areas of $w > w_o$. Areas of $-w_o \le w \le w_o$ have background vorticity and strain. The threshold is taken to be $w_o = 0.2\sigma_w$ (Isern-Fontanet et al., 2004), where σ_w is the standard deviation of *w* values in the flow area of interest.

Examples of *w* contours are shown in Figure 3.16. Values of *w* have been normalized by $(U_o/\lambda)^2$, where λ is an eddy length scale, taken to be $3(\Delta x_1 \Delta x_2 \Delta x_3)^{1/3}$ or ($\lambda \approx 0.01\ m$). Eddies larger than λ can be discerned from the computed flow field. The Reynolds number based on U_o and λ equals 3220 for runs with a flat bottom and 3990 for runs with a hump. For M2, a string of alternating eddy and strain pockets appear along the left- and the right-side of the channel at the middle depth (Figure 3.16(a)). Eddies and strains are local-scale flow features. The string on the left side traces a meandering path, whose cross-stream amplitude increases as eddy patterns develop towards downstream. These patterns are coherent turbulence structures at length scales comparable to half-expanding-width $(b_2 - b_1)/2$ (Figure 3.1(a)). The pattern development is accompanied by weakening of local rotations. The string on the right side virtually hugs the sidewall, with little cross-stream shifting of eddy positions. The above discussion is also pertinent to the eddy and strain distributions in a near-bottom horizontal plane (Figure 3.16(b)). Between F6 and M2, the distributions resemble a mirror image of each other, as seen by comparing Figure 3.16(c) to 3.16(a), and Figure 3.16(d) to 3.16(b), which demonstrates bistability. Comparisons of Figures 3.16(e)–(f) (for H8) to Figures 3.16(a)–(b) (for M2) show an example of a hump can effectively suppress the development of meandering structures and of eddies associated with wall friction forces. This is also true for the hump in H9.

3.4.2 Effect of shear instability on bistability

Why the influence of the initial conditions used did not die out? Plausible explanations are outlined below, using M2 as an example. On the right side of the expansion (Figure 3.1(a)), turbulence is generated near the right sidewall by wall friction forces, upon commencement of the run. However, on the left side, turbulence is generated in the interface plane $x_1 = 0$ and $x_2 > L$ (Figure 3.1(a)) by velocity shear ($\bar{u}_2 > 0$ for $x_1 > 0$; $\bar{u}_2 = 0$ for $x_1 < 0$). Friction forces and velocity differences are two mechanisms for turbulence generation (Hinze, 1959). Kelvin-Helmholtz instability can occur and result in turbulent eddies along the interface. These eddies are stronger than those induced by friction forces near the right sidewall (Figures 3.10(a), 3.10(c), and 3.10(e)).

An example of evidence of instability-triggered eddy motions is given through analyzing sample lateral profiles of $\bar{u}_2$ velocity (Eq. 3.3), extracted from the results for M2 and F6. For M2 (initial condition i), the eddy motions cause mixing of momentum, smear out a sudden change of initial values of $\bar{u}_2$ across the interface, and produce lateral profiles of continuously varying $\bar{u}_2$. Also,

the second-order derivative of $\bar{u}_2$ (Figures 3.17(a), 3.17(b)) have points of inflection, where $\partial^2\bar{u}_2/\partial x_1^2 = 0$ and changes its sign. In the limit of negligible viscous effect, such $\bar{u}_2$ profiles satisfy Rayleigh's necessary condition for instability (Drazin & Howard, 1966). When perturbed by small disturbances, the velocity profiles may be unstable. The disturbances will draw energy from the mean flow and turbulent eddies will grow. This scenario is more likely to occur in the left than the right flank (Figure 3.1(a)) because the profiles have more points of inflection in the left portion. In contrast, for F6 (initial condition ii), instability-triggered eddy motions are more likely to occur in the right than the left flank, as the $\bar{u}_2$ profiles have more points of inflection in the right portion (Figs 3.17(c), 3.17(d)). The above discussion is applicable to the expansion as well as the downstream channel.

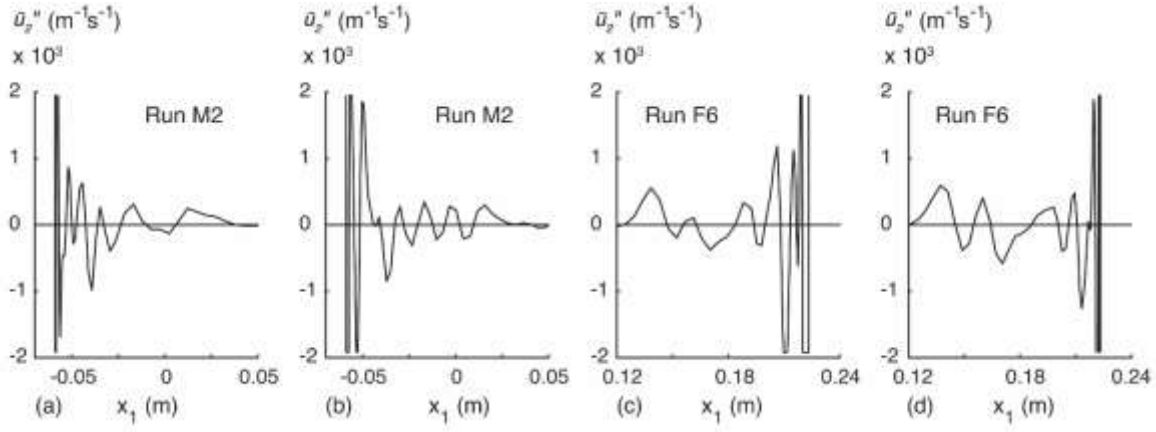

Figure 3.17 Values of $\bar{u}_2'' = \partial^2\bar{u}_2/\partial x_1^2$. Points on the $\bar{u}_2$ profiles, at which $\bar{u}_2''$ equals zero and changes sign, are a point of inflection. The (x_2, x_3) locations of panels (a)–(d) are marked in Figs 3.16(a)–3.16(d) (dashed lines), respectively. Data points of $|\bar{u}_2''| > 2000$ have been truncated and connected for visual clarity

Lateral profiles of $\bar{u}_2$ for H8 have less points of inflection than for M2 at the same (x_2, x_3) coordinates, meaning the hump effectively suppresses eddy motions triggered by instability as well as those induced by wall friction forces. The same effect is seen by comparing $\bar{u}_2$ profiles between H9 and F6. A previous study of TBF in a shallow, rectangular reservoir formulated a shape parameter from the flow domain geometry as the criterion to determine bistability (Dewals et al., 2012). This study has demonstrated a new bistability mechanism, i.e. the dominance of persistent eddy motions triggered by shear instability over those due to wall friction forces. This differs from wake bistability.

3.4.3 Pressure gradient and non-uniformity in bistable flow

TBF contains significant turbulent velocities, which affect the values of $\bar{p}$ and hence the pressure gradient $\nabla\bar{p}$ (Hinze, 1959). The horizontal component $\nabla_h\bar{p}$ of $\nabla\bar{p}$ is of particular interest. This component is small (compared to the vertical component) but critical to bistable flow in an expansion. An example of $\nabla_h\bar{p}$ is shown in Figure 3.18. For F6 (Figure 3.18(a)), pockets of an adverse pressure gradient ($\partial\bar{p}/x_2 > 0$) appeared along both the left- and the right-side of the channel, where the vectors point in the positive x_2-direction, and the magnitudes are local maxima. Such pressure distributions decelerate or even reverse local flow velocities, and are partly responsible for triggering and maintaining turbulent eddies (Figure 3.16(d)). The distributions of vectors and contours for M2 are more or less a mirror image of those in Figure 3.18(a). The

magnitude of $\nabla_h \bar{p}$ can be reduced by fitting a hump at the bottom, as seen from comparing Figure 3.18(b) for H9 to Figure 3.18(a) for F6. The hump reduces local maxima.

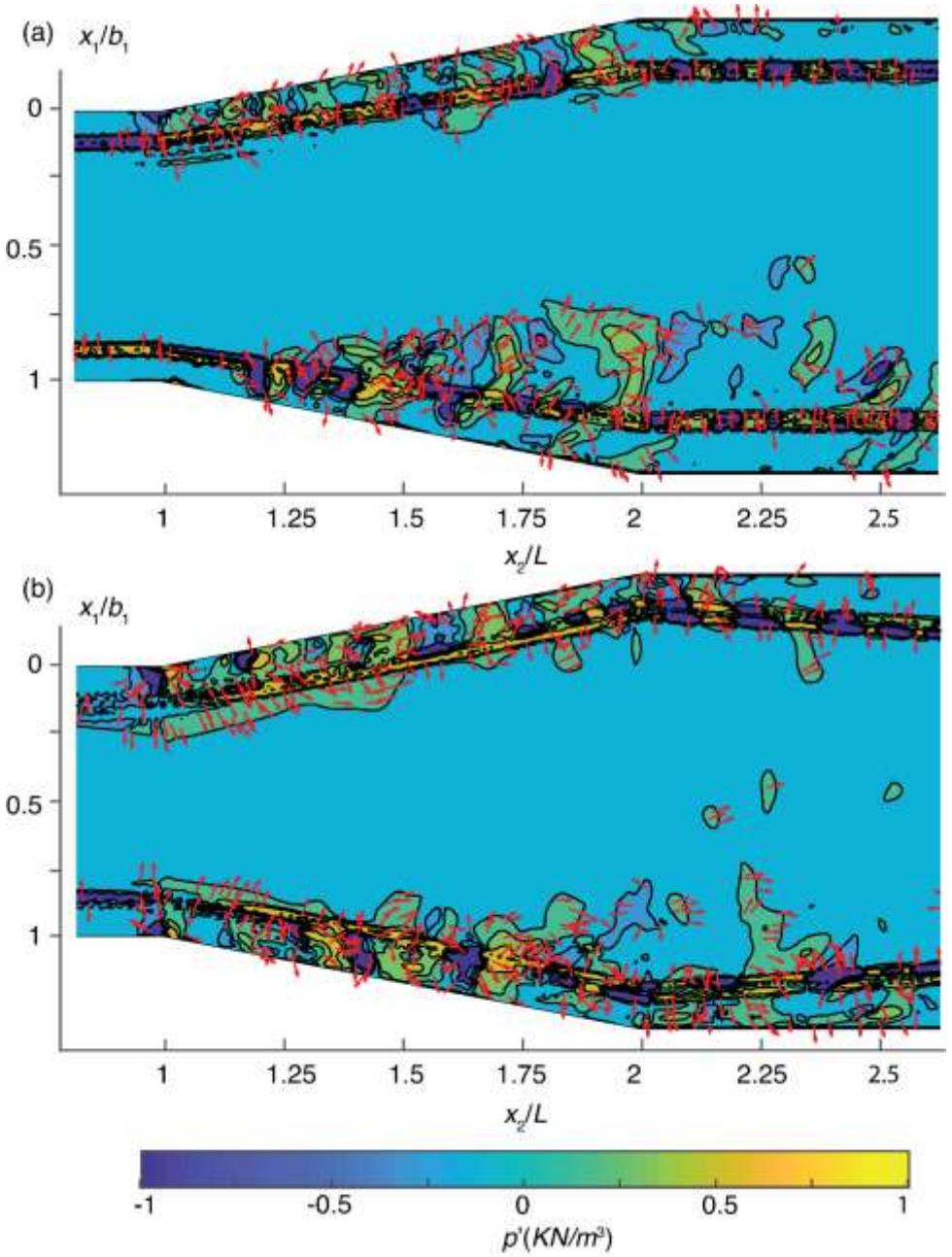

Figure 3.18 Horizontal planes at $x_3 = 2\delta$, showing $\nabla_h \bar{p}$ for: (a) F6; (b) H9. The vectors show the direction of $\nabla_h \bar{p}$. The contours show its magnitude; positive contour values mean $\partial \bar{p}/\partial x_2 > 0$, whereas negative contour values mean $\partial \bar{p}/\partial x_2 < 0$. The definition of p' is $p' = Sng(\partial \bar{p}/\partial x_2)|\nabla_h \bar{p}|$. For clarity, vectors with a magnitude smaller than 0.15 kN/m^3 are not shown

$\partial \bar{p}/x_1 \neq 0$ has implications to the practice of measuring pressures in TBF. The $\bar{p}$ values vary along a straight line at fixed (x_2, x_3) coordinates (Figures 3.16(a)–3.16(d), dashed lines). It is insufficient to measure the pressure at one point using a pressure tap at the sidewall; the pressure reading does

not accurately represent the distribution of pressures along the line. The $\bar{p}$ values varied along the dashed lines (Figure 3.16) by 9–15 Pa. The variations can be quite significant at prototype scales.

In a horizontal plane, pockets of relatively large pressures developed on one side of the channel force the main flow to deflect from the centerline towards the other side; the result is a forced acceleration, the development of a low-pressure region, and hence the suppression of flow separation. Nevertheless, the centrifugal force developed from the deflected streamline curvature tends to pull back the flow towards the centerline. A transition from one stable flow state to the other can be forced by obstructing/disturbing the fast-flowing streamlines on the low-pressure side for a sustained period of time (e.g. longer than L/U_o). The obstruction/disturbance defines a new initial condition in flow history and affects the subsequent development of the flow field. Disturbances are inevitable in turbulent flow. Background turbulence has little influence on the existence of two flow states and the change of flow states in the expansion, as confirmed by sensitivity runs. They used different turbulence intensities (5%, 10% and 15%) and υ_τ/υ ratios at the inlet, but did not yield significantly different flow in the expansion.

The boundary shear stress is not uniform along channel boundaries (Chow, 1959). Different stable states of TBF aggravate non-uniformity. On one side of the expansion, if τ_b due to recurring eddies exceeds a certain threshold, bed sediments will be eroded in erodible channels. On the other side, bistability intensifies near-wall velocities, enlarges the wall shear stresses, and hence increases the risk of bank erosion. Thus, it is of practical importance to be able to control bistability. The current practice in the design of expansions has assumed uniform flow without separation. Separation reduces the hydraulic efficiency. As an attempt to control separation, one may put a limit on θ (Figure 3.1(a)). However, for given b_1 and b_2 values, a smaller θ leads to a longer expansion. It is often not feasible to accommodate a large L due to practical constraints and/or high costs. Besides, limiting θ does not address the issue of bistability. This research has contributed to an improved understanding of the characteristics of TBF and offers an unconventional idea for turbulence control. The momentum coefficient β and energy coefficient α are an indicator of flow uniformity (Chow, 1959). The α, β and u_* values are listed in Table 3.1. Expansions with a hump (H8 and H9) improve flow uniformity, compared to those without a hump (M2 and F6). The hump in the expansion causes the flow to accelerate, neutralizes the expanding width's tendency of inducing an adverse pressure gradient, and thus prevents flow separation (Najafi-Nejad-Nasser & Li, 2015). The hump reduces the friction velocity.

3.5 Summary and conclusions

This research investigates turbulent bistable flow in an open-channel expansion using two-phase Large Eddy Simulation. The simulated pressure distribution and free-surface position compare well with experimental data. The simulation results show that two stable flow states can possibly exist in the expansion, for a given flow approaching the expansion. The flow history dictates which of the two states will occur. The flow history is imposed as initial conditions in simulations. This finding contradicts the traditional practice in turbulent flow computations, which prescribes an initial state of rest or motion and integrates model equations over time long enough, until the so-called transient influence of the prescribed initial condition dies out, and the subsequent flow field becomes independent of the condition.

The two stable flow states differ substantially in eddy size, core rotation strength, flow reversal, and the extent of flow separation between the opposing sides about the channel centerline. The two flow states are virtually a mirror image of each other, in terms of velocity and pressure-gradient distributions as well as eddy rotation conditions. This demonstrates bistability. Its occurrence is due to the dominance of eddy motions triggered by shear instability over those due to wall friction forces.

In the turbulent bistable flow, the horizontal gradient of the ensemble average pressure field and hence the values of ensemble average pressure are not constant along a transverse straight line in a horizontal plane. It will not suffice to measure the pressure at one point using a pressure tap at the sidewall and use the pressure reading to represent the pressure distribution along the line.

Bistability reduces the hydraulic efficiency of an expansion. Fitting a simple hump at the expansion bottom helps suppress bistability. The presence of the hump effectively reduces flow reversal, separation and eddy motions, compared to the case of a flat-bottom expansion. The hump improves flow uniformity and hence hydraulic efficiency. The hump breaks the interaction between eddies triggered by shear instabilities and those induced by wall-friction forces, with beneficial effects on open-channel stability.

Further studies should consider different types of expansions and investigate the optimal dimension and location of humps. Also, it is worth investigating the evolution of turbulent bistable flow states, the transition between them, and higher order statistics of turbulence.

4 Hydraulic jump and choking of flow in pipe with a change of slope[2]

4.1 Background

The hydraulic jump is a phenomenon whereby the flow transfers abruptly from the supercritical to the subcritical condition. This phenomenon can occur in sewer pipes (Stahl & Hager, 1999) and stilling basins (Wu et al., 2018), and downstream of overflow, underflow and drop structures (De Padova et al., 2013; Qian et al., 2021). Most studies of the phenomenon focus on the dissipation of flow energy for the control of erosion downstream of hydraulic structures. Some studies aim at reducing the uplift pressure on a stilling basin structure (Li et al., 2015), raising water levels in an irrigation channel and other water conveyance channels, positioning gaging stations, enhancing the mixing of chemicals in water and wastewater treatment plants, and aerating water bodies. The phenomenon has been studied extensively for the above-mentioned applications.

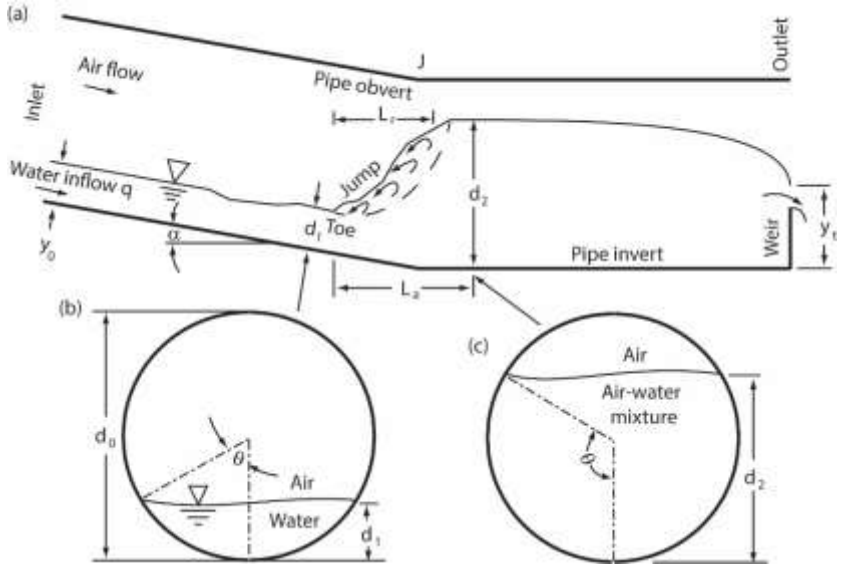

Figure 4.1 Definition diagram of hydraulic jump in a circular pipe with a change of slope: (a) elevation view in the pipe invert-obvert plane; (b) cross-sectional view before the jump; (c) cross-sectional view after the jump

The new context of this study is that there are an increasing number of cases where: a) new urban drainage pipes are laid on steep terrain, b) the actual flow rates in existing sloping pipes exceed the design flow rates due to intensified rainfalls or increasing domestic and industrial discharges, and c) the aging of existing pipes has reduced the pipe capacity to carry the design flow rates. Under such conditions, a hydraulic jump may form somewhere in a partially full pipe (Figure 4.1) and the pipe may flow full downstream of the jump. This may choke the downstream pipe and cause a poor drainage and thus aggregate costly urban floods. There are very limited studies of hydraulic jumps in sloping pipes, and the hydrodynamic behaviour of the jumps are poorly understood. This is in contrast to the thoroughly studied classical hydraulic jump (CHJ) on the horizontal floor.

[2] This chapter contains information that was published in Journal of Hydrodynamics: https://doi.org/10.1007/s42241-023-0090-3

The hydraulic jump in a sloping pipe is influenced by the weight of water contained in the jump itself and by pipe wall friction. A steep slope can lead to non-hydrostatic pressure distribution. Air flows above water, and air entrainment further complicates the problem. Such complications are not dealt with in previous studies of CHJs. The studies simplify the jumps as one-phase flow and reveal only basic characteristics. For example, the jumps are of several distinct types, depending on the Froude number Fr_1 of the approach flow. The ratio of the initial depth d_1 to the sequent depth d_2, roller length L_r and jump length are expressed as a function of Fr_1. For the particular case of rectangular channels, d_2/d_1 is given by the Bélanger equation. This ratio is smaller than given by the equation when friction is considered. L_r is larger at higher Fr_1.

Even a simple jump on horizontal floor has complex internal structures. There is a zone of rollers, bounded by the free surface and a line drawn through points of zero longitudinal velocity (Mignot & Cienfuegos, 2011). In this zone, negative velocities can reach 0.6 times the cross-sectional mean velocity of the approach flow (Zhang et al., 2013). Vorticity begins to develop at the jump toe due to strong shear (Witt et al., 2018) and slowly decays downstream. Turbulence is significant in the shear layer (Mignot & Cienfuegos, 2011). Such structures cannot be adequately treated using the analytical approach. This research takes the numerical approach.

The region of hydraulic jump typically comprises air pockets within water and water droplets surrounded by air. The distribution of void fractions, bubble count rate and size distribution, and air-water interface statistics are of relevance. Local maxima of void fraction indicate the shear layer and decrease with increasing distance from the toe as the shear layer expands. Thus, one needs a two-phase model in order to simulate jumps.

Limited studies deal with jumps in a circular pipe. The filling ratio d_1/d_0 and Fr_1 dictate the types of jumps that form (Stahl & Hager, 1999). The ratio d_2/d_1 has been obtained using several methods: data fitting (Stahl & Hager, 1999), Newton-Raphson iterations and analytical solutions. Some studies focus on air movement in circular conduits (Qian et al., 2017) and hydropower conduits (Li et al., 2022). Air entrainment in sewers has implications for odor problems, negative pressure, blowback, and supersaturated total dissolved oxygen. Previous studies of air entrainment provide empirical expressions of aeration efficiency (Tuna et al., 2014). The influence of slope is absent from the studies. When the influence is considered, studies limit to rectangular channels (Ohtsu & Yasuda, 1991). The case of circular conduits has rarely been explored.

Hydraulic jumps feature turbulence and contain air bubbles. The toe oscillates to a larger extent at higher Fr_1 (Zhang et al., 2013). The free surface fluctuates. Waves propagate downstream. Numerical models must capture the instantaneous fluctuation, without the reflection of waves from downstream. Some instruments like an acoustic Doppler velocimetry are suitable only for jumps at low Fr_1 and in zones of low void ratio (Liu et al., 2004). Due to the presence of bubbles and surface fluctuation, a laser Doppler velocimetry and a particle image velocimetry encounter difficulty in accurately measuring velocities (Jesudhas et al., 2018). Thus, reliable numerical predictions are complementary to uncertain measurements (Mortazavi et al., 2016). Challenges exist in sampling from numerical predictions of instantaneous two-phase flow variables, much like sampling from experimental measurements (Felder & Chanson, 2015).

Numerical models of hydraulic jump should give a complete description of three-dimensional (3-D) turbulent flow. The turbulence is anisotropic (Wang & Murzyn, 2017). The challenges lie in capturing vortex stretching and lengthening (Witt et al., 2018), 3-D oscillations (Jesudhas et al., 2018) and air entrainment. Some researchers used the Reynolds-averaged Navier-Stokes (RANS) equations with a turbulence closure scheme or combined a RANS model with Smoothed Particle Hydrodynamics (De Padova & Mossa, 2021). RANS models cannot reproduce the instantaneous flow and anisotropic turbulence (Jesudhas et al., 2018, 2020). One needs sophisticated techniques such as Large Eddy simulation (LES) and Direct Numerical Simulation (Carvalho et al., 2008).

Jesudha et al. (Jesudhas et al., 2018) simulated CHJ using Detached Eddy Simulation (DES). The results included mean and maximum velocities, free surface profiles, root-mean-square velocities, Reynolds shear stresses, turbulence kinetic energy, and vorticity. Jesudha et al. (Jesudhas et al., 2020) performed DES of a submerged jump. DES produces the internal turbulence structure of a jump but does not resolve near-wall regions. Mortazavi et al. (2016) carried out DNS of air entrainment and bubble motions of a jump. Their focus was on wave breaking. They treated the bottom as a slippery wall. This treatment ignores the influence of the wall boundary layer on air entrainment (Takahashi & Ohtsu, 2017). Hydraulic jumps have flow structures interacting with other features like the wall boundary layer. The boundary layer even viscous sublayer should be resolved. The purpose of this study is to achieve an improved understanding of hydraulic jump behaviour driven by pipe discharge and slope. Hydraulic jumps in a circular pipe with a change of slope are computed by means of 3-D wall-resolved LES.

4.2 Method

4.2.1 Governing equations of two-phase flow

Consider a two-phase incompressible flow of a mixture of air and water (Figure 4.1). The air as the gas phase and water as the liquid phase are immersible. The instantaneous motions in three dimensions (3-D) of the fluid mixture were obtained by means of LES. The governing continuity and momentum equations are given by

$$\frac{\partial u_j}{\partial x_j} = 0 \tag{4.3}$$

$$\rho \frac{\partial u_i}{\partial t} + \rho \frac{\partial (u_i u_j)}{\partial x_j} = -\frac{\partial p}{\partial x_i} + \frac{\partial \Gamma_{ij}}{\partial x_j} + \rho g_i \tag{4.2}$$

where u_j is the instantaneous velocity component in the x_j direction ($j = 1,2,3$), ρ is the density of the mixture, t is time, p is the instantaneous pressure, Γ_{ij} is shear stress and g_i is the gravitational acceleration. The instantaneous velocity vector is given by $v = u_i \hat{x}_i$, where $\hat{x}_i$ denotes the unit vector in the x_i direction.

The density and viscosity of the mixture were calculated as volume-weighted averages: $\rho = \rho_1 \alpha_1 + \rho_2 \alpha_2$ and $\mu = \mu_1 \alpha_1 + \mu_2 \alpha_2$, where the subscripts 1 and 2 refer to the gas phase and liquid phase, respectively, α_1 is the air volume fraction (AVF) and α_2 is the water volume fraction (WVF). For any computational cell, $\alpha_1 + \alpha_2 = 1$. The free surface is tracked by combing the volume of fluid method with level set equations. Zeng and Li (2022) demonstrated the effectiveness of the combination to calculate interface curvatures and surface tension forces. The combination accurately tracks the free surface of CHJ (Mortazavi et al., 2016) and a wedge-shaped

jump near a surface-piercing foil (Li et al., 2021). The shear stress Γ_{ij} is the sum of molecular-viscosity-induced shear stress $\mu\partial u_i/\partial x_j$ and turbulence-induced shear stress τ_{ij}.

The formulations discussed above are pertinent to the phenomenon of hydraulic jump. This phenomenon features complex internal flow structures, violent turbulence, instantaneous fluctuation, and substantial air entrainment. This study considers the influence of gravity and the concentration of air, both of which are absent from the study of CHJs. Applying the finite volume methods to Eqs. 4.1 and 4.2 implicitly yields filtered equations for the resolvable-scale filtered velocity and pressure. The motions of large eddies are computed. Sub-grid-scale eddies smaller than the LES mesh size Δx_i need to be modelled. The sub-grid-scale stress τ_{ij} is an extra unknown tensor in the filtered momentum equation. This stress allows for the effect of unresolved velocity fluctuation on the resolved motion and needs to be computed using a turbulence closure model.

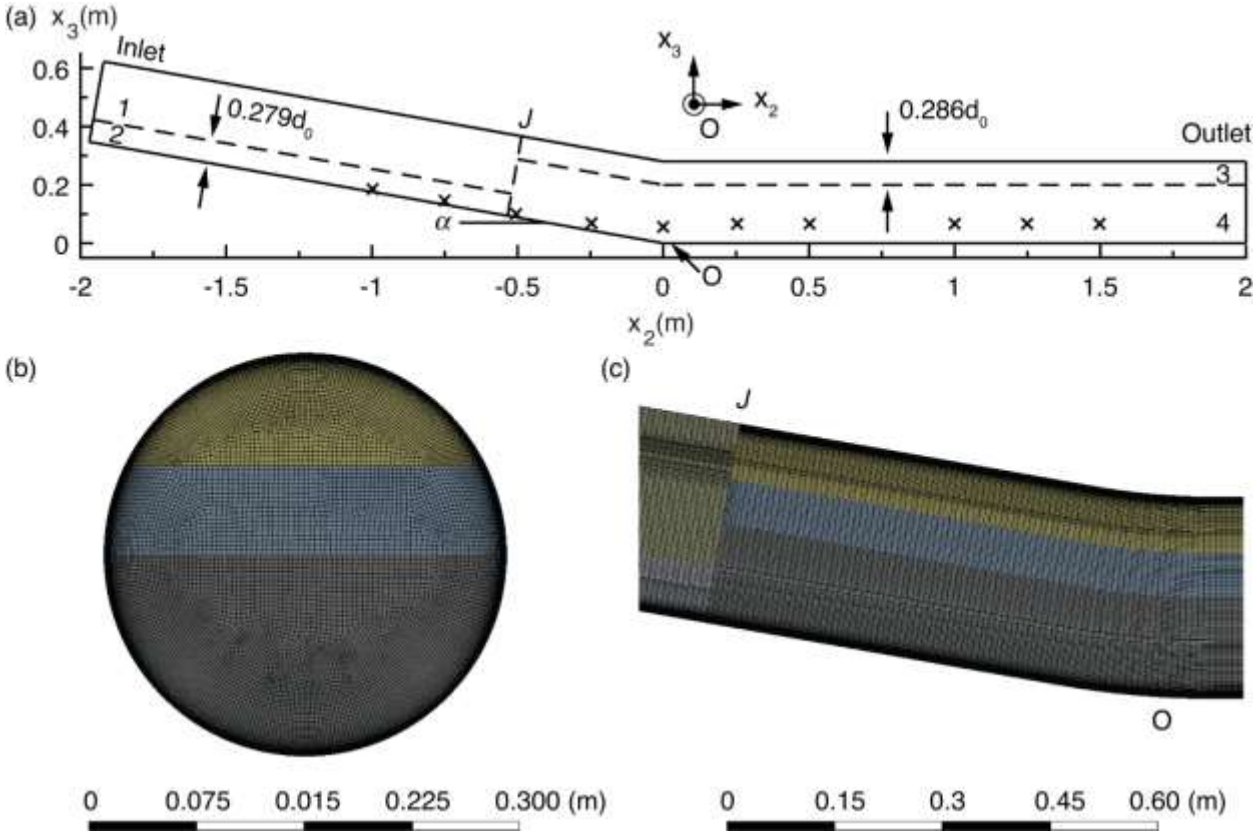

an

Figure 4.2 (a) Elevation view of the model domain, divided by the dashed lines into four zones for mesh generation and initialisation of LES, (b) Computational cells at a pipe cross-section, (c) Elevation view of a portion of the LES mesh. The mesh was used for runs B1 and Q2–Q6

4.2.2 Turbulence closure model

The dynamic Smagorinsky-Lilly model (Lilly, 1992) provides turbulence closure, which involves subgrid-scale turbulent viscosity μ_t and resolved scale strain rate S_{ij}. The shear stress due to turbulence is given by

$$\tau_{ij} = 2\mu_t S_{ij} \tag{4.3}$$

where $\mu_t = \rho L_s^2 |S|$, $|S| = \sqrt{2S_{ij}S_{ij}}$ and L_s is the mixing length. L_s was estimated as the lesser of two products:

(1) $C_s\Delta$, where C_s is the Smagorinsky coefficient, $\Delta = (\Delta x_1 \Delta x_2 \Delta x_3)^{1/3}$ is the local grid scale, and Δx_i is the local mesh size in the x_i direction
(2) The product of the von Karman constant and the distance to the closest wall. This is the largest scale of unresolved turbulence, interacting the most actively with the resolved motion.

The dynamic Smagorinsky-Lilly model determines the value of C_s as follows. Let $\hat{\Delta} = 2\Delta$ denote a test filter. The shear stress in Eq. 4.2 is replaced by the test filtered subgrid-scale (SGS) stress tensor $T_{ij} = 2C\hat{\rho}\widehat{\Delta}^2|\hat{S}|\hat{S}_{ij}$, where the symbol $\widehat{\ }$ means a test filtered level operation and C is a coefficient. The grid filtered SGS stress tensor, t_{ij}, is modeled in the same way $t_{ij} = 2C\rho\Delta^2|S|S_{ij}$, where C is solved from $C = L_{ij}M_{ij}/M_{ij}M_{ij}$, $L_{ij} = T_{ij} - t_{ij}$ and $M_{ij} = 2(\widehat{\Delta}^2\hat{\rho}|\hat{S}|\hat{S}_{ij} - \Delta^2\rho|S|S_{ij})$. The Smagorinsky coefficient is computed from $C_s = C^{1/2}$, using information provided by the resolved scale motions. To avoid numerical instability, negative values of the eddy viscosity are truncated to zero. The dynamic Smagorinsky-Lilly model has been successfully used to study different types of turbulent flows. Recent examples of studies include pipe bend (He et al., 2021) and two-phase turbulent flow (Zeng & Li, 2022). The dynamic Smagorinsky-Lilly model avoids using a non-universal coefficient C_s, unlike the standard Smagorinsky-Lilly model.

4.2.3 Mesh for LES

The computational domain was divided into four zones (Figure 4.2(a)) to facilitate LES mesh generation and LES initialisation. The normal distance from the pipe invert to the dividing plane for zone 1 is smaller (equal to $0.279d_0$), compared with that from the pipe obvert to the plane (equal to $0.721d_0$) for zone 2, whereas the opposite is true for zone 4, compared with zone 3. The procedures for generating the mesh are as follows. First, the upstream plane of each zone was discretised into squares (Figure 4.2(b)). This plane is at the inlet for zones 1 and 2, and at the "J" location for zones 3 and 4 (Figure 4.2(a)). Then, the near-wall region of this plane was refined by using inflation layers. Next, the mesh in this plane was swept toward the downstream plane of the zone in question (Figure 4.2(c)). Zone 1 is expected to be occupied by purely air flow, which is not the focus of this study. For this reason, the near-wall region of zone 1 was not refined (or no inflation layers added), which avoids an unnecessary increase of computing nodes.

The mesh consisted of hexahedrons. The hexahedron sizes were determined using Zang's (1991) guidelines about LES mesh: In the wall-normal direction, there is at least one node in the interval $0 < y^+ < 1$, where y^+ is the non-dimensional wall distance, and there are at least three nodes in the interval $0 < y^+ < 10$.

For most of the LES runs in Table 4.1, in the streamwise and spanwise directions, the sizes fulfill the Zang's (1991) requirements $\Delta x_2^+ < 80$ and $\Delta x_1^+ < 30$, where $x_i^+ = x_i u_*/\nu$ for $i = 1, 2$ and u_* is the friction velocity. Take run B1 as an example. In the streamwise direction, Δx_2^+ was 57. In the wall-normal directions, where the viscous sublayer was directly resolved, the first node off

the wall was situated at $y^+ = 0.31$, the corresponding normalized distances being $x_1/d_0 = 1.56 \times 10^{-4}$ and $x_3/d_0 = 1.56 \times 10^{-4}$, further, seven nodes were placed on the interval $0 < y^+ < 10$. Cheng et al. (2020) used $y^+ \approx 5$, and reported beneficial mesh refinement in a study of external flow. In this study, there was a progressive refinement of sizes for the region from the wall to the interior by means of inflation layers until $\Delta x_1^+ = \Delta x_3^+ = 21$. The growth rate of sizes was kept within 1.1. Table 4.1 lists the mesh in terms of wall units based on the maximum friction velocity in the downstream pipe from LES output.

The hexahedron sizes for Q3–Q6 do not meet Zang's (1991) requirements: $\Delta x_2^+ < 80$ and $\Delta x_1^+ < 30$. For Q3–Q6, the water inflow at the inlet had a very large velocity u_0 (Table 4.1), resulting in a large friction velocity u_* and causing $\Delta x_2^+ > 80$ and $\Delta x_1^+ > 30$. However, the sizes in the cases sufficiently satisfy Piomelli's (Piomelli, 1993) criteria: $\Delta x_2^+ < 244$ and $\Delta x_1^+ < 77$. This ensures accurate predictions of the 1st and 2nd order statistics of turbulence characteristics. Mesh independence is usually not tested in LES model.

Table 4.1 Conditions of LES runs. The values of the non-dimensional wall distance, y^+, are for the first cell off the wall of the downstream pipe. The Reynolds number Re and Froude number Fr_1 are defined, respectively, as $\mathrm{Re} = Vd_1/\nu_2$ and $\mathrm{Fr}_1 = V/(gD)^{1/2}$, where V is the cross-sectional average velocity just before the jump, D is the hydraulic depth, ν_2 is the viscosity of water and g is gravity. The ratio d_2/d_1 is smaller (by up to 20%) than that from the Belanger equation for the same value of Fr_1

Run ID	u_0/ (m·s^{-1})	q / (L·s^{-1})	α / °	u_*/ (m·s^{-1})	y^+	Δx_2^+	Δx_1^+	Nodes	Re	d_1/d_0	Fr_1	d_2/d_1	L_r/d_2	L_a/d_2
B1	0.705	9.88	10.00	0.007	0.31	57	21	6 867 930	82 833	0.12	4.7	6.07	6.57	7.83
Q2	1.070	15.00	10.00	0.009	0.38	69	26	6 867 930	113 445	0.15	4.3	5.18	5.81	6.94
Q3	1.427	20.00	10.00	0.013	0.57	105	39	6 867 930	142 764	0.18	4.3	4.64	5.14	8.63
Q4	1.784	25.00	10.00	0.019	0.82	150	56	6 867 930	170 670	0.20	4.9	Choking	6.01	6.93
Q5	2.141	30.00	10.00	0.020	0.88	160	60	6 867 930	196 452	0.19	5.2	Choking	5.33	6.35
Q6	2.500	35.00	10.00	0.022	0.96	175	66	6 867 930	225 600	0.18	5.1	Choking	5.18	6.11
S7	0.705	9.88	11.31	0.007	0.29	53	20	6 883 119	79 403	0.11	3.8	6.68	5.59	7.91
S8	0.705	9.88	12.95	0.007	0.29	54	20	6 833 255	86 791	0.09	5.9	8.02	6.07	9.78
S9	0.705	9.88	14.57	0.008	0.36	65	24	6 808 354	87 963	0.08	6.6	9.26	8.04	11.57
S10	0.705	9.88	16.17	0.009	0.38	70	21	6 776 134	89 707	0.10	6.9	7.30	8.16	10.18
H11	1.510	21.74	0	0.013	0.41	127	63	3 810 000	128 295	0.36	1.9	2.09	2.75	5.72
H12	1.730	17.70	0	0.011	0.35	109	54	3 810 000	114 172	0.28	2.4	2.57	2.98	6.03
H13	1.730	11.75	0	0.008	0.27	84	42	3 810 000	85 318	0.21	2.8	2.94	3.38	6.73
H14	2.040	13.90	0	0.010	0.33	102	51	3 810 000	101 649	0.21	3.5	3.57	3.86	7.16
H15	2.630	17.78	0	0.015	0.49	151	75	3 810 000	128 010	0.22	4.1	4.23	4.28	8.39

The skewness of mesh is the key indicator of the mesh quality. The lower the average skewness, the better the mesh quality. The mesh generated for each of the LES runs (Table 3.1) had an average skewness below 0.1, meaning that the difference between the shape of the cell and the shape of an equilateral cell of equivalent volume is small and the mesh properly preserves numerical accuracy and stability. The mesh had a maximum skewness of about 0.7. A general rule is that the maximum skewness of mesh is below 0.95 and the average skewness is below 0.33. The generated mesh in this study clearly satisfies this rule.

4.2.4 Conditions at boundaries

The computational model domain (Figure 4.2(a)) has the following boundaries: (1) The inlet, as a lateral open boundary at upstream, (2) The outlet, as a lateral open boundary at downstream and (3) pipe walls, as a solid boundary. The conditions imposed at these boundaries are described below:

(1) At the inlet, the circular section was divided by a horizontal chord (free water surface) into a minor segment below the chord (for inflow of water) and a major segment above (for air flow). The inflow of water had a prescribed depth $y_0 = 0.279d_0$, where d_0 is the pipe diameter, the corresponding angle being $\theta_0 = 63.7°$. The inflow had a prescribed uniform velocity u_0 and thus a flow rate $q = u_0(2\theta_0 - sin\,2\,\theta_0)d_0^2/8$. The prescribed conditions of inflow for LES (Table 4.1) match Qian et al.'s (2017) experiments in depth, flow rate, and pipe diameter ($d_0 = 0.28$ m). This allows a comparison of LES results with experimental data, which is one of the reasons for the zone division as shown in Figure 4.2(a).

    Turbulence was superimposed on the uniform velocity at the inlet, using the 2-D vortex method (Mathey et al., 2006). This method generates fluctuating vorticity and allows for the effect of background turbulence on the behaviour of hydraulic jumps. The method requires input of the relative turbulence intensity $T' = 100(2k/3u_0^2)^{1/2}$, where k is the turbulence kinetic energy. In this study, the intensity was set to 5%, and the ratio of the turbulent eddy viscosity to viscosity of water, ν_τ/ν_2, was set to 10. The vortex method has been used successfully in LES of turbulent flows of air around buildings (Zheng et al., 2020) and an air-water mixture in an open channel (Zeng & Li, 2022).

    The major segment of the inlet section above the free water surface was treated as a pressure outlet. In other words, the relative pressure was set to zero, and thus air was allowed to freely enter or leave the computational model domain.

(2) At the outlet, a weir acted as a downstream control (Figure 4.1(a)). The height of the weir was adjusted so as to produce subcritical flow in the vicinity and, more importantly, the required depth d_2 to form a hydraulic jump. The requirement is that d_1 and d_2 are conjugate depths. The height was set to $d_0/2$ for LES, in consistency with Qian et al.'s (2017) experiments. For the LES runs (Table 4.1), the relative pressure of the overflow above the weir was set to zero at the outlet, through which both air and water were allowed to freely pass. The position of the water surface at the outlet was free to adjust.

(3) At the pipe walls, non-slippery wall condition was imposed.

4.2.5 Initial conditions

The LES initialisations were facilitated by the division of the model domain into four zones (Figure 4.2(a)). In the pipe invert-obvert plane, the division into $0.286d_0$ for zone 3 and $0.714d_0$ for zone 4 was estimated from the water surface elevations of Qian et al.'s (2017) experiments. As initial conditions, all cells in zones 1 and 3 were filled with air (or $\alpha_1 = 1$ and $\alpha_2 = 0$), whereas all cells in zones 2 and 4 were filled with water (or $\alpha_1 = 0$ and $\alpha_2 = 1$). The water flows in zones 2 and 4 each had uniform velocities, calculated on the basis of continuity. For example, for run Q2 (Table 4.1), the longitudinal (parallel to the pipe invert) velocity u_p was 1.070 m/s in zone 2, giving $u_2 = u_p\,cos\,\alpha = 1.054$ m/s and $u_3 = u_p\,sin\,\alpha = -0.186$ m/s to all the cells in zone 2, and u_p was 0.319 m/s in zone 4, giving $u_2 = 0.314$ m/s for $x_2 < 0$, $u_2 = 0.319$ m/s for $x_2 > 0$, $u_3 =$

-0.055 m/s for $x_2 < 0$ and $u_3 = 0$ m/s for $x_2 > 0$ to all the cells in zone 4. Both zones had zero velocity in the x_1 direction. In zones 1 and 3, the air had zero velocities.

The distributions of initial pressures were hydrostatic in the entire domain for all the LES runs. Each of the LES runs (Table 4.1) allowed a spin-up period of model time, which was sufficiently long for the influence of the given initial conditions on the instantaneous flow to diminish. The aforementioned way for initializations helped shorten the spin-up period. Subsequent computations produced snapshots of instantaneous velocity and pressure distributions useful for ensemble averages of hydraulic jump properties.

At the interface of zones 1 and 3, initially there was a water-level difference of $0.435d_0$ (Figure 4.2(a)). This difference gave a maximum theoretical velocity $\sqrt{0.870d_0g}$, being smaller than the inlet velocity u_0 for runs Q6 and H15 (Table 4.1). The time step was chosen such that it was sufficiently small to handle the larger u_0 without any divergence problem. The same time step was sufficient to handle the initial discontinuity. The discontinuity was smeared out as iterations proceeded.

4.2.6 LES runs

Ten LES runs were performed under the conditions summarised in Table 4.1. These include a prescribed depth of water inflow, y_0, at the inlet, the cross-sectional average water velocity, u_0, at the inlet, and the slope angle, α, of the upstream pipe (Figure 4.2(a)). The prescribed y_0 and u_0 gave a water flow area of $A_0 = 0.014$ m^2. The flow rate of $q = u_0A_0$ entering the inlet into the pipe matched the experiment of Qian et al. (2017). The value of y_0 was 0.078 m, and the ratio of y_0 to the pipe diameter, d_0, was $y_0/d_0 = 0.279$ for all the runs.

The LES runs used a time step of $\Delta t = 0.01$ s. This time step satisfies the Courant-Friedrichs-Lewy criterion for numerical stability. Take run B1 as an example. The streamwise mesh size was $\Delta x_2 = 0.008$ m, the cross-sectional average velocity at the inlet was $u_0 = 0.705$ m/s, and thus the Courant number was $C = u_0\Delta t/\Delta x_2 = 0.88$. The Courant number had an average value below 1.3 over the entire computational domain. It reached 13 in a very limited number of cells. Using the SIMPLE algorithm, the governing equations were solved in a pressure-velocity coupling manner. Iterations continued until the convergence criterion of 10^{-6} or a maximum of 120 iterations per time step was reached. The LES runs encountered no issues of divergence in the computations.

Run B1 was intended for validating LES predictions using available observations (2017). Q2–Q6 quantified the influence of an increasing discharge. S7–S10 explored the influence of an increasing slope. H11–H15 matched the experiments of hydraulic jump in a horizontal pipe of Stahl and Hager (1999), allowing data comparison. For H11–H15, the pipe had a diameter of $d_0 = 0.24$ m and a total length of $L = 6$ m. The height of the weir was adjusted to control the location of jump. The mesh was generated following the same procedures as the other runs. The resolutions were coarser (being 0.005 m, 0.010 m and 0.005 m in the x_1, x_2 and x_3, respectively), but satisfied the criteria of Piomelli (1993).

The computations were performed using 32-core nodes on the High-Performance Computing Facility of Concordia University. The LES runs (e.g., B1) took up to 636 hours of computing time to complete.

4.3 Results

4.3.1 Instantaneous flow field and cumulative average

Each LES run (Table 4.1) predicted instantaneous values of u_j, p, α_1 and α_2 in the domain between the inlet and outlet (Figure 4.1). The instantaneous values all fluctuated. As expected, the fluctuation was relatively profound in the region of hydraulic jump. The upper boundary of this region was identified as a topological surface (a 2-D manifold) using threshold values of $\alpha_2 = 0.45-0.55$. Examples of snapshots of the surface at different model times are plotted as the isosurface $\alpha_2 = 0.50$ (a 3-D surface representation of points with equal values) in Figures 4.3(a)–4.3(c). It is shown that the instantaneous free surface fluctuated vividly in space as well as in time, and the fluctuations were much stronger in the region of hydraulic jump than outside. One can roughly locate the jump, in the presence of turbulent eddies, wavy patterns, and characteristic details different from one timestep to another. The jump length L_a passed through the change of pipe slope. Individual snapshots of instantaneous flow, separated by a sufficiently large time lag between, are uncorrelated with each other. This can be confirmed by an autocorrelation analysis.

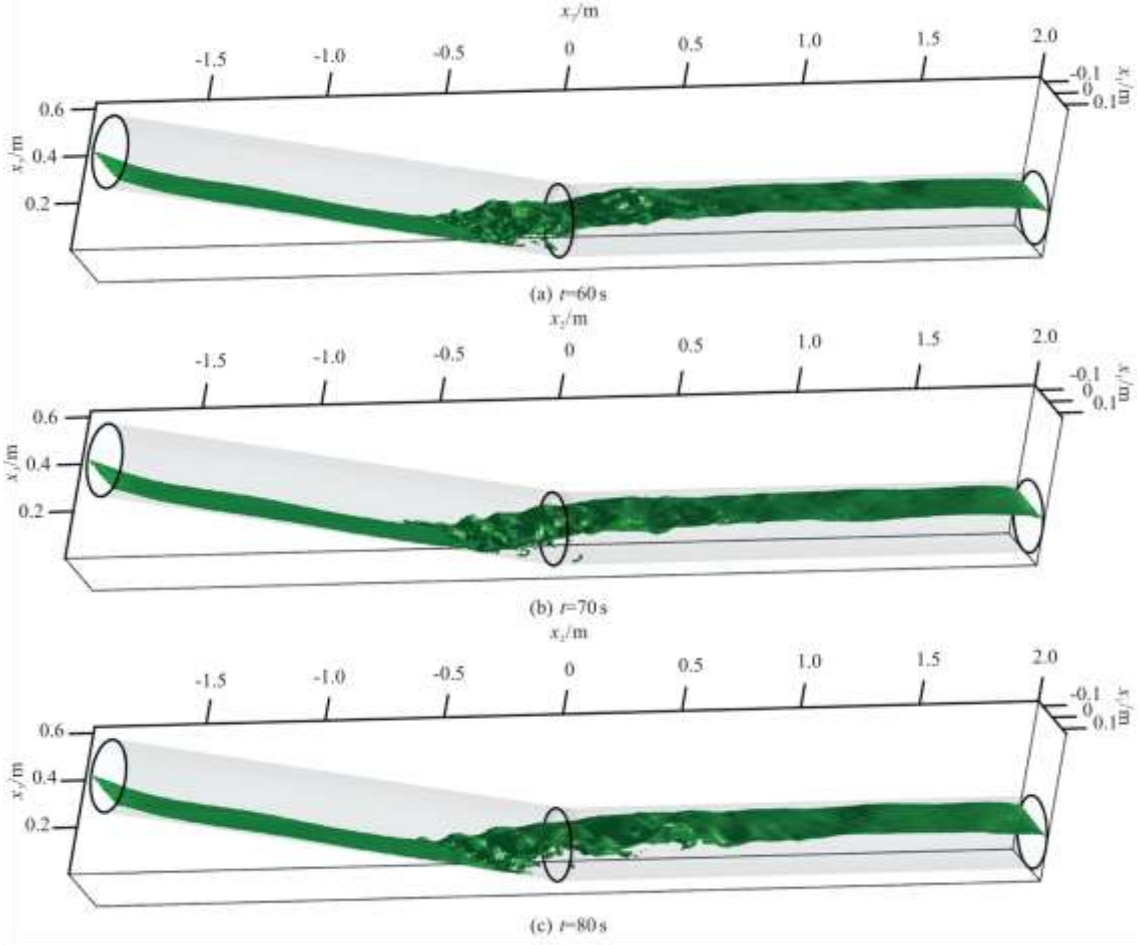

Figure 4.3 3-D view of the isosurface of α_2 = 0.5 at model times for run B1 (Table 4.1)

To demonstrate the fluctuation, examples of u_j time series are plotted in Figures 4.4(a)–4.4(d) for four selected locations in the region of hydraulic jump (Figure 4.2(a)). In Figure 4.4, the model time t covered a duration of 20 s (after a spin-up of 60 s) and was normalised by the time scale t_f associated with the fluctuation frequencies of energy-bearing eddies that are larger than those in the inertial subrange. For the LES runs in Table 4.1, t_f had a maximum value of about 1 s, and this value was used for normalisation.

The velocity u_2 is the primary flow. From the inlet down to $x_2 = -0.25$ m on the slope (Figure 4.2(a)), u_2 was always positive. Although the primary flow fluctuated in magnitude with time, its direction pointed always downstream. In Figure 4.4(a) for $x_2 = -0.25$ m, u_2 fluctuated between $0.83u_0$ and $3.94u_0$ around a mean of $3.33u_0$, meaning a substantial increase from the inlet velocity u_0 (Table 4.1). In Figures 4.4(b) – 4.4(d) for other three locations $x_2 = 0$ m, 0.25 m and 0.50 m (Figure 4.2(a)), u_2 fluctuated between positive and negative values. The fluctuation of u_2 at $x_2 = 0\ m$ (Figure 4.4(b)) was in the largest range $-0.95u_0 < u_2 < 3.82u_0$ among the ten locations marked in Figure 4.2(a). In Figure 4(d), the u_2 time series had a mean dropping to $0.35u_0$, as a result of an expanding water flow area after the hydraulic jump.

The velocities u_1 and u_3 are the secondary flow. In Figures 4.4(a)–4.4(d) for four locations in the region of hydraulic jump, the spanwise component u_1 fluctuated between positive and negative values. In Figure 4.4(b) for $x_2 = 0$ m, the values of u_1 ranged from $-1.89u_0$ to $1.94u_0$, which was the largest fluctuation among the ten locations (Figure 4.2(a)). Also, the u_1 time series had the largest mean, equal to $0.20u_0$. Upstream of $x_2 < -0.25$ m and downstream of $x_2 > 0.50$ m, u_1 time series had a smaller mean, on the magnitude of $O(10^{-3})$ m/s. In the vertical direction, in Figure 4.4(a) for $x_2 = -0.25$ m, the time series of u_3 contained positive values, meaning that there were upward motions even at this down slope location (Figure 4.2(a)). In Figures 4.4(a)–4.4(d) for four locations, the values of u_3 fluctuated between positive and negative values. In Figure 4.4(c) for $x_2 = 0.25$ m, the fluctuation ranged from $-1.36u_0$ to $1.58u_0$, being the strongest among the ten locations (Figure 4.2(a)). The u_3 time series had a negative mean at all the locations and ranged from –0.08 m/s to –0.01 m/s at $x_2 \geq 0$.

The root mean square deviation (RMSD) indicates the degree of fluctuation around the mean. The primary flow had larger RMSDs than the secondary flow and larger RMSDs in the sloping pipe than the horizonal pipe.

The accumulatively (forward) averaged velocity was calculated as

$$\langle u_j \rangle = T^{-1} \int_{t_0}^{t_0+T} u_j \, dt \tag{4.4}$$

where T is a time duration elapsed following the spin-up time period t_0. Examples of $\langle u_j \rangle$ are plotted in Figures 4.4(e)–4.4(h) for four locations (Figure 4.2(a)). Note that $t_f = 1\ s$. Take as an example $t = 70$ s in Figure 4.4(e). The velocity $\langle u_j \rangle$ was obtained by taking the average of 1 000 instantaneous u_j values from $t = 60$ s to 70 s at an interval $\Delta t = 0.01$ s. At $t = 70$ s, $\langle u_j \rangle$ changed very little. In fact, all the velocity curves in Figures 4.4(e)–4.4(h) became asymptotically horizontal after $T = 5$ s. As a conservative choice, this study used $T = 10$ s for ensemble averaging of flow variables.

The velocity spectral density E for the u_j time series in Figures 4.4(a)–4.4(d) was plotted in Figure 4.5. The spectrum shows the existence of energy containing eddies and the inertial subrange, well captured in the predicted instantaneous flow field. The predicted energy cascade satisfies the well-known Kolmogorov −5/3 law. This insightfully confirms the quality of the predictions. It is worth mentioning that refinement of LES mesh may modify the slope (Cheng et al., 2020).

4.3.2 Ensemble average of instantaneous flow

The ensemble average of instantaneous flow properties has practical applications. The instantaneous velocity u_j, pressure p, and WVF α_2 were sampled from the output of each LES runs (Table 4.1). Data sampling started after the spin-up period of time (or $t > t_0$) and the sampling frequency was 100 Hz. For a given location (x_1, x_2, x_3), the ensemble averages of the instantaneous variables are calculated as:

$$\bar{u}_j = \frac{1}{n}\sum_1^n u_j,\ \bar{p} = \frac{1}{n}\sum_1^n p,\ \bar{\alpha}_1 = \frac{1}{n}\sum_1^n \alpha_1,\ \bar{\alpha}_2 = \frac{1}{n}\sum_1^n \alpha_2 \tag{4.5}$$

where n is the number of ensembles, chosen to be $n = 1\ 000$. The corresponding time duration was $t_n = 10$ s. This choice is justified on the following grounds:

(1) $t_n > t_f$ by an order of magnitude.
(2) t_n is 3–15 times the advection time scale t_a. For each LES run, t_a was estimated from the aeration length L_a and inlet velocity as $t_a = L_a/u_0$. Note that $L_a > L_r$ (Stahl & Hager, 1999). For the LES runs, the distributions of $\bar{\alpha}_2$ showed $1.50\ \text{m} < L_a < 2.25\ \text{m}$, u_0 ranged from 0.7 m/s to 2.5 m/s. Estimates of t_a were 0.68 s−3.19 s, and thus, $t_n > t_a$.
(3) The cumulatively averaged velocities shown in Figures 4.4(e)–4.4(h) support the choice of $t_n = 10$ s.
(4) The sufficiency of $t_n = 10$ s is manifested in the autocorrelation function (Figure 4.6).

The suitability of using $t_n = 10$ s was further confirmed by evaluating the autocorrelation function r_k for time lag k (Box et al., 2015). The values of r_k are plotted in Figures 4.6(a)–4.6(d), which correspond to the sample time series in Figures 4.4(a)–4.4(d), respectively. If two quantities separated by a timescale are virtually uncorrelated, the selected number of ensembles n is sufficient and suitable for averaging (Cheng et al., 2018). The function r_k measures the correlation between the univariate time series u_j at time t and u_j at time $t + k$, where k increases from 0 s,···, 10 s. In Figures 4.6(a)–4.6(d) for the four selected locations, the wavy curves fluctuated in wavelength and amplitude, which depend on the direction and location, but the curves had some common features. The function had a value of unity at $k = 0$, because the time series of velocity data was perfectly correlated with itself. The function decayed with increasing k from zero, became bounded by ±0.25 for $k > 1$ s, and then oscillated around zero. The oscillations had peaks and troughs within ±0.15 for $k > 5$ s. These low values of r_k mean that instantaneous velocities separated by a time span of $t_n = 10$ s were uncorrelated. This justifies the use of $t_n = 10\ s$ (or 1 000 ensembles) for averaging. This is comparable with other LES studies (Li et al., 2011).

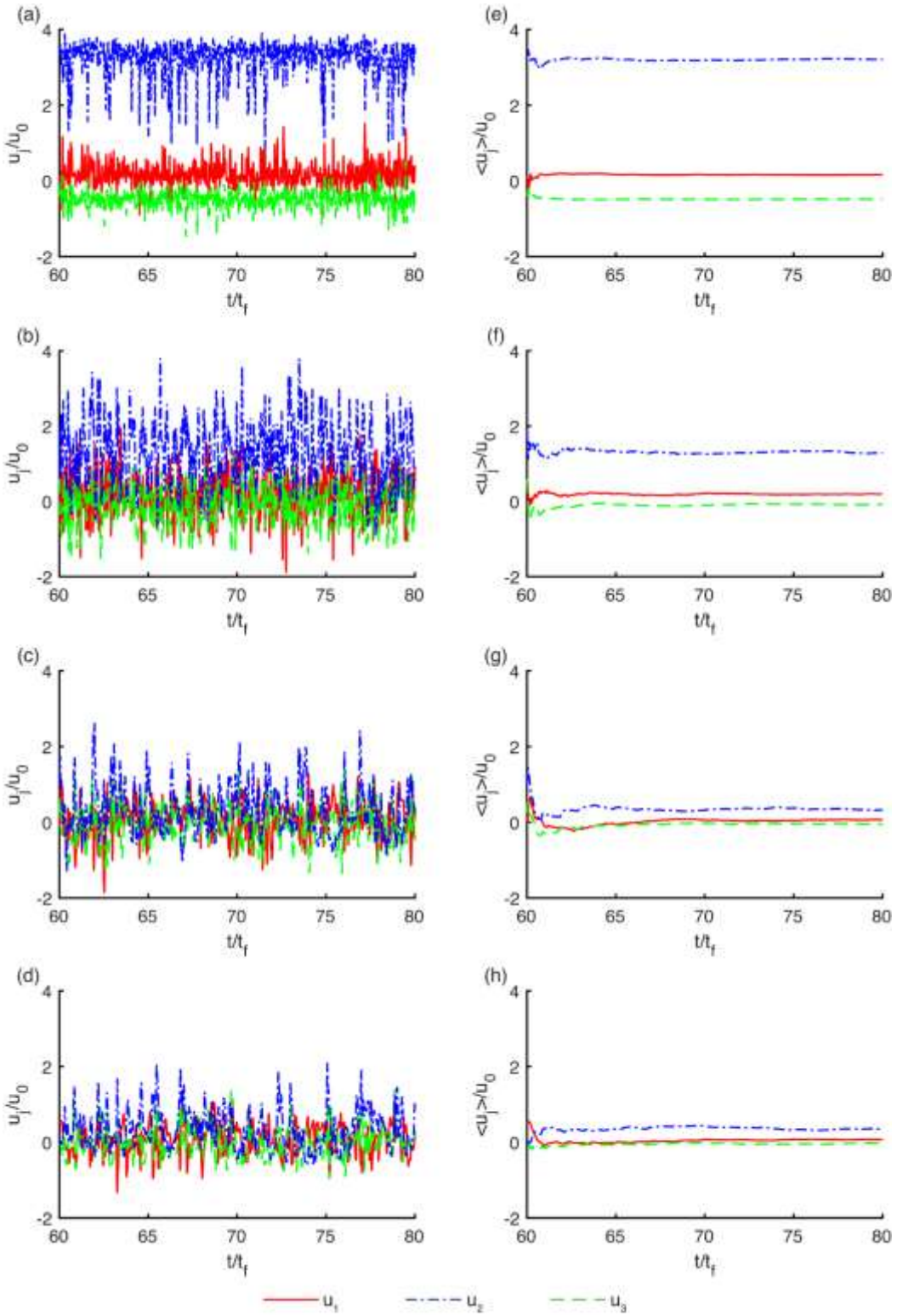

Figure 4.4 Time series of instantaneous velocity u_j and cumulatively averaged velocity $\langle u_j \rangle$ for run B1 (Table 4.1), at four locations whose (x_1, x_2, x_3) coordinates are: (a) and (e) (0, –0.25, 0.07) m, (b) and (f) (0, 0, 0.06) m, (c) and (g) (0, 0.25, 0.07) m, (d) and (h) (0, 0.50, 0.07) m. The locations are marked in Figure 4.2(a)

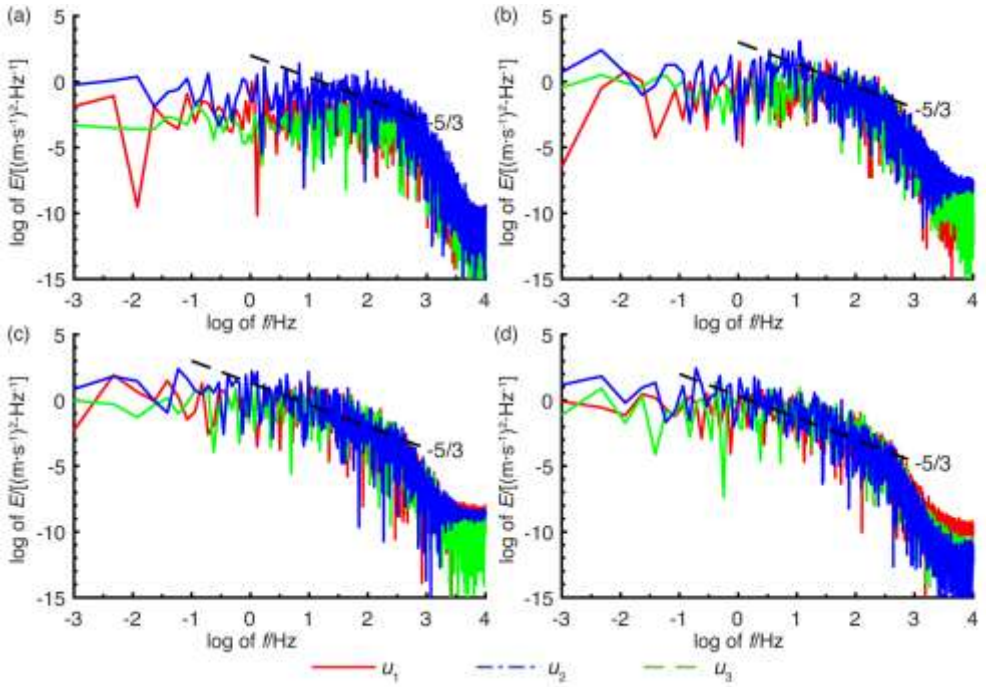

Figure 4.5 Velocity spectral densities $E_{u_j u_j}$ for the u_j component. Panels a–d correspond to Figures 4.4(a)–4.4(d), respectively

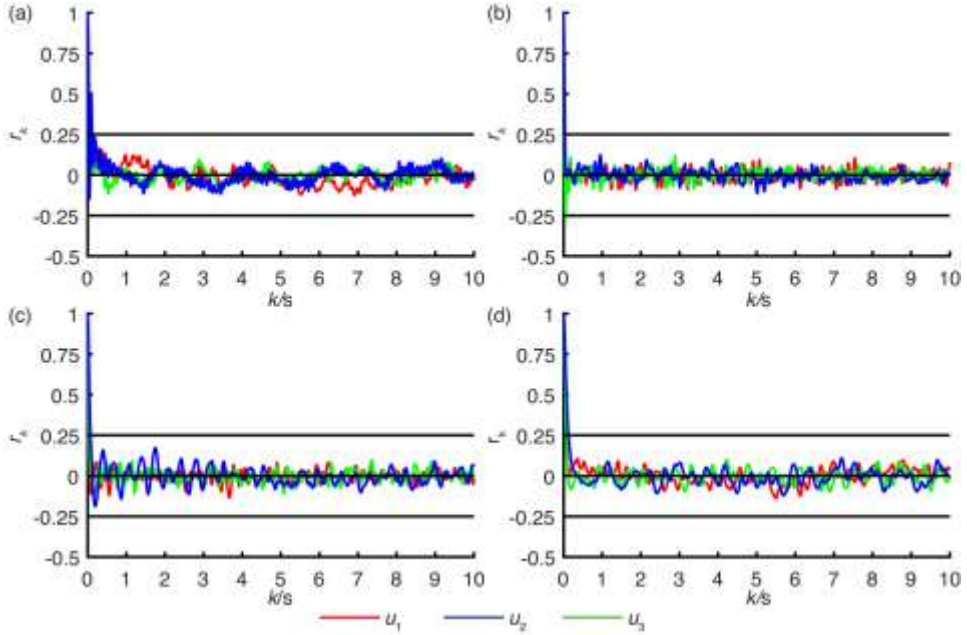

Figure 4.6 Autocorrelation function r_k for time lag k: (a)–(d) correspond to Figures 4.4(a)–4.4(d), respectively

Ensembles can come from any different instants over the LES output duration, and the averaging of them gives the expected value of a turbulent variable. This study sampled the unsteady flow results from LES at an equal time interval merely for convenience. In contrast, conventional time averaging typically needs continuous records over a certain time duration and returns the mean.

Its use is limited to steady flow and has the inconvenience of segregating the flow into bulk and turbulent components.

4.3.3 Ensemble average surface profile of hydraulic jump

The ensemble average of the free-surface position was traced using contours of WVF (Eq. 4.5), with $\bar{\alpha}_2 = 0.50$ on the surface and $\bar{\alpha}_2 < 0.50$ above. An example of ensemble average free surface profiles in the central plane ($x_1 = 0$ m) is shown by a contour line of $\bar{\alpha}_2 = 0.50$ in Figure 4.7 for B1 (Table 4.1). This profile started from the inlet, ran virtually parallel with the pipe invert, dropped to the lowest level (with a flow depth of 0.03 m) at $x_2 = -0.36$ m, and rose suddenly before levelling off at $x_2 \approx 0.84$ m. In this example, the computed free surface profile compared reasonably well with available experimental data (Figure 4.7), with a small root mean square error of 0.013 m.

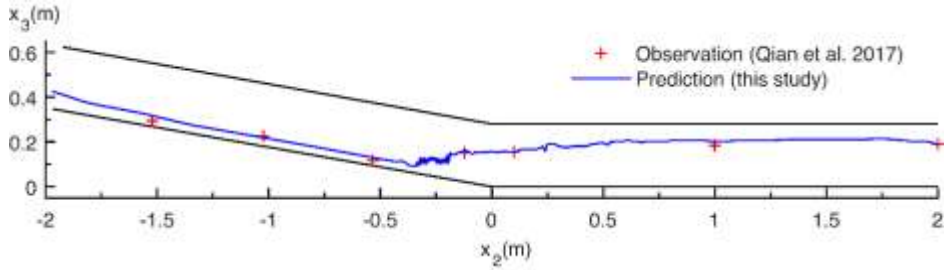

Figure 4.7 Central plane $x_1 = 0$, showing the ensemble average free surface profile for run B1 (Table 4.1)

The free surface profile in Figure 4.7 showed a hydraulic jump with a well-defined toe located in the sloping pipe. The downstream end of the jump in the horizonal pipe was not as apparent but could be located by using multi-level contours of $\bar{\alpha}_2$. In Figures 4.8(a)–4.8(e), an elongated region of $0.25 < \bar{\alpha}_2 < 0.75$ signified a substantial aeration of water flow by air entrained from above the water surface. The longitudinal length of this region is taken as the aeration length, L_a, in this study. For run B1 (Table 4.1), the aeration region extended from x_2 =–0.54 m to 1.02 m, giving a value of $L_a = 1.569$ m. The downstream end of a jump as a two-phase flow was well-defined in this way, and thus L_a could be determined without ambiguousness for any other run (Figures 4.8(b)–4.8(e)).

In Figure 4.8(a), water ($\bar{\alpha}_2 > 0.99$) flowed down-slope as a wall jet hugging the invert of the sloping pipe and penetrating to the downstream end of the slope. The interface between the gas phase above and liquid phase below was sharp. Below this interface, the depth of flow section, d, was not uniform but remained a filling ratio as small as $d/d_0 = 0.122$ and the flow was supercritical before the toe. Downstream, a hydraulic jump developed, the region contained an air-water mixture, and wavy contour of $\bar{\alpha}_2$ reflected turbulence and resultant air entrainment. Further downstream, the air-water interface was less sharp, compared to upstream of the jump. It would be practical to take where the contours of $\bar{\alpha}_2 = 0.25$, 0.50 and 0.75 just collapse into a single line as the downstream end of L_a.

The discharge q was 9.88 L/s in Figure 4.8(a) for B1; it increased by 52% in Figure 4.8(b) and 100% in Figure 4.8(c) for two other runs (Table 4.1). The result was that the wall jet penetrated further downstream; the toe position shifted progressively downstream, although it remained on

the slope; the aeration length, and both the initial and sequent depths became larger. A further increase of q to 25, 30 and 35 L/s for Q4–Q6, without increasing the height of the weir (Figure 4.1(a)), produced an ill-defined or incomplete jump.

Among B1, S7 and S8, the slope angle α increased gradually from 10° to 11.30° and to 12.95°. These increases resulted in a slight downslope shift in the toe, but the downstream end of the jump moved noticeably downstream (Figures 4.8(a), 4.8(d), 4.8(e)). The sequent depth was not very sensitive to the increasing α, but the aeration length was. An increase of α from 11.30° to 12.95° caused L_a to increase by 0.37 m and enhanced air entrainment and the degree of air-water mixing in the hydraulic jump.

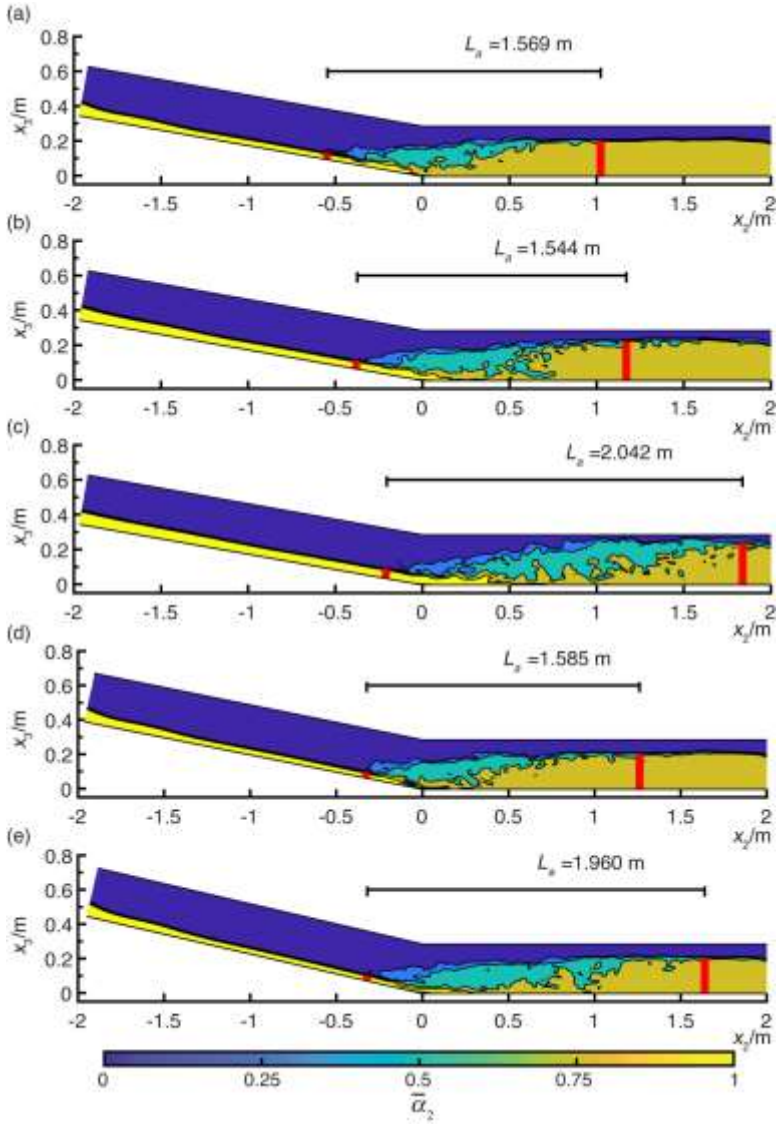

Figure 4.8 Central plane $x_1 = 0$, showing contours of $\bar{\alpha}_2$ for runs: (a) B1; (b) Q2; (c) Q3; (d) S7; (e) S8

4.3.4 Vertical structure of ensemble averaged velocity

A total of 19 cross sections (CS1–CS19) was selected to analyse the ensemble average invert-parallel velocity u_p. Its variation with normal distance from the invert is plotted in Figure 4.9 for CS8–CS17, which intersect the invert at a right angle at $x_2 = -0.43$ m, -0.24 m, -0.05 m, 0.20 m, 0.40 m,···, 1.40 m. Upstream of the jump toe, u_p varied little (uniform below the free surface), except in a thin boundary layer next to the invert, but the flow accelerated down the slope. In Figure 4.9(a), the uniform u_p accelerated from 1.25 m/s at CS1 to 2.53 m/s downstream at CS9. Further downstream, the mean velocity below the free surface started to decelerate due to an expanding depth. The region of jump showed strong velocities near the invert, relatively weak velocities just beneath the free surface, and a wavy change of velocities in between. The velocities just underneath were close to zero and even negative (e.g., –0.32 m/s at CS10). Negative velocities occurred at CS10–CS14, which did not necessarily occur at the surface.

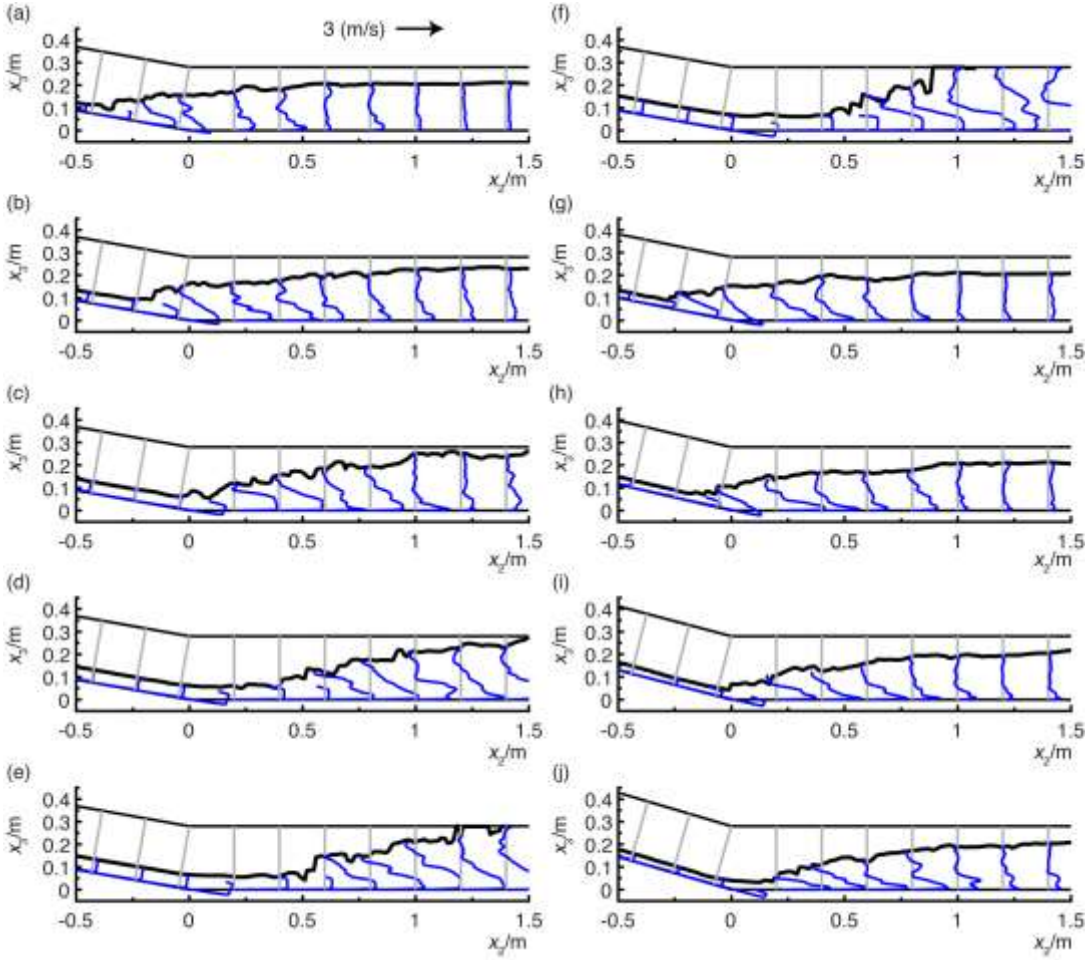

Figure 4.9 Profiles of invert-parallel velocity u_p at ten x_2 locations in the central plane $x_1 = 0$ for runs: (a) B1; (b)–(f) Q2–Q6; (g)–(j) S7–S10. The black curve is the free surface

The strong velocities near the invert in Figure 4.9 were a core jet. It resembles the wall jet observed from experiments of sluice gate flow and predicted from DES (Jesudhas et al., 2018). Both jets were accompanied by a jump. The peak velocity, v_0, of the core jet tended to decay in the downstream direction. The decay was not monotonical. In Figure 4.9(a), for instance, v_0 decreased

to 0.40 m/s at CS13, increased to 0.86 m/s at CS14, decreased to 0.34 m/s at CS15, and increased again to 0.41 m/s at CS16. The tendency of decay was consistent with the observations of Ohtsu and Yasuda (1991), who attributed the decay to the effect of surface rollers in the D-jump. Downstream of the aeration length, u_p showed spatially uniform rather than jet patterns. At CS18, the uniform velocity was about $0.5u_0$. To the best of our knowledge, the results discussed above are new.

The above discussion is also valid at increasing discharge in Figures 4.9(b)–4.9(f) for Q2–Q6 and at increasing slope in Figures 4.9(g)–4.9(j) for S7 to S10, except the additional feature of choking of flow in Figures 4.9(d)–4.9(f) for Q4–Q6. An increase in discharge caused the core jet to develop further downstream and even to reach the outlet for Q4–Q6. In this case, there were no profiles of uniform velocities. The maximum reversal flow velocities were not sensitive to increasing discharge; they occurred below the abruptly changing surface of hydraulic jump. An increase in slope (B1, S7 and S8) intensified the supercritical flow down the slope and advanced the flow further downstream. Nevertheless, among S8 to S10, the advancement was not really significant, with the maximum flow velocities all near CS11.

In Figure 4.9(a), the local maximum velocity occurred at the surface upstream of CS9, below the surface at CS9, and in the core jet at CS10–CS12 and CS14. Reverse flow velocities began at CS10, with negative values. The strongest reverse flow occurred at the water surface at CS10 and CS11 and somewhere below the surface at CS12–CS14. At CS13, the local maximum velocity was near the surface rather than in core jet. The maximum velocity occurred near the invert at CS15, near the water surface at CS17 and CS19, somewhere in the fluid column at CS18, near the invert at CS16. The global maximum flow velocity occurred near the invert.

4.3.5 Cross-sectional distribution of air volume fraction

The distributions of $\bar{\alpha}_1$ (Eq. 4.5) at a series of cross sections are shown as contours in Figure 4.10 for B1. The upper edge of the contour region was the free surface with $\bar{\alpha}_1 = 50\%$. A number of observations are made from Figure 4.10:

(1) The surface rose from upstream (Figure 4.10(a)) to downstream (Figure 4.10(f)). A hydraulic jump began at the toe section (Figure 4.10(a)) and developed downstream.
(2) At the toe section, the surface was virtually flat, and $\bar{\alpha}_1$ decreased rapidly immediately below the surface. The incoming core jet allowed little air entrainment.
(3) Air entrainment from above the free surface initiated at the next CS (Figure 4.10(b)) and grew in the next few CSs (Figures 4.10(c)–4.10(f)). The shape of the surface and patterns of $\bar{\alpha}_1$ distributions became increasingly irregular. The core jet maintained a local area of low $\bar{\alpha}_1$ around the invert.
(4) Further downstream, the surface became flat. The $\bar{\alpha}_1$ distributions below became nearly uniform (Figure 4.10).

These features are seen from the results for the other LES runs (Table 4.1).

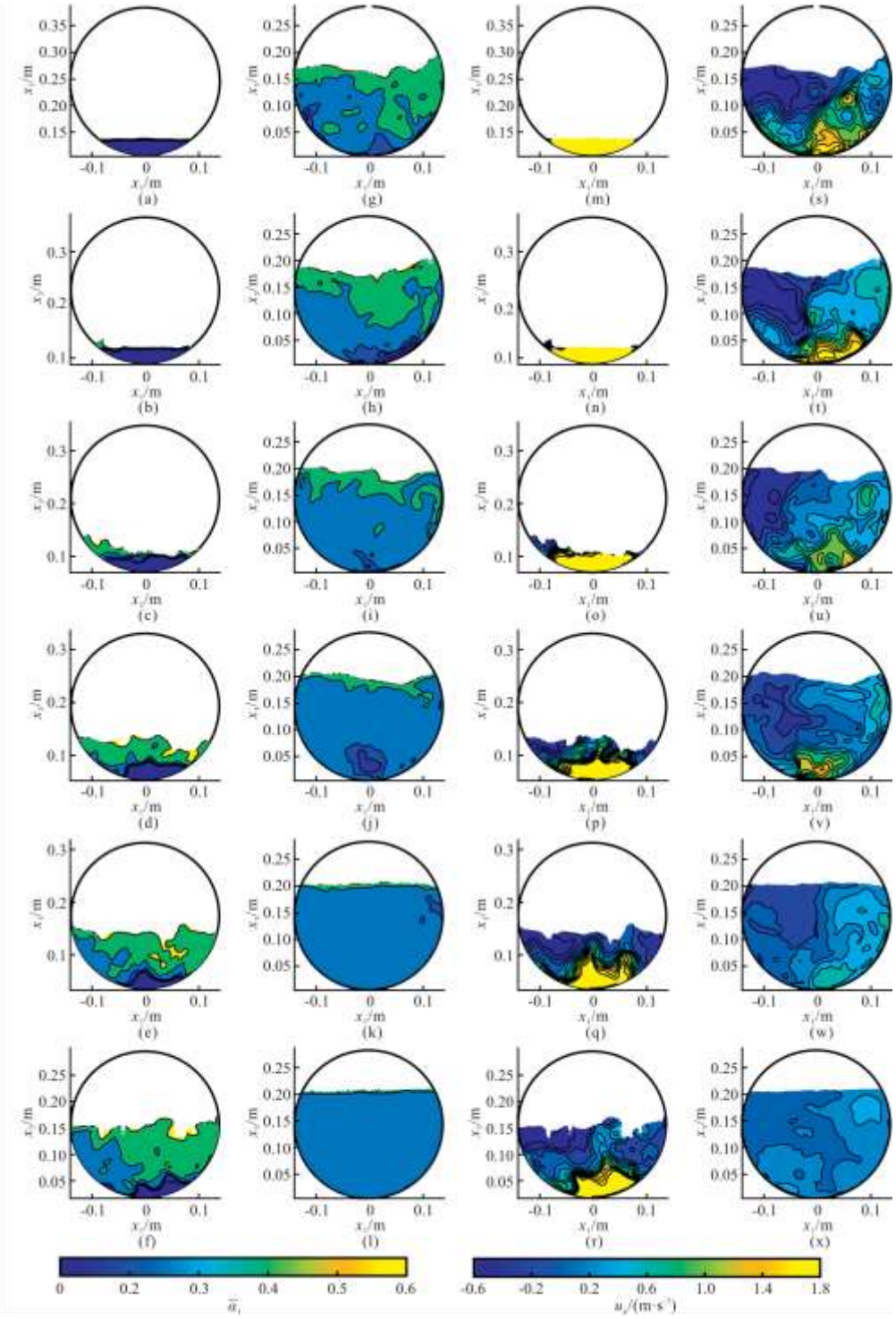

Figure 4.10 Pipe CSs, showing the contours of: (a)–(l) $\bar{\alpha}_1$, (m)–(x) u_p. The results are ensemble averages for B1. For 12 panels (a)–(l) and (m)–(x), respectively, x_2 =−0.56 m, −0.46 m,···, −0.06 m, 0.05 m, 0.15 m, 0.25 m, 0.45 m, 0.75 m, 1.05 m

The maximum depth below the free surface (or the minimum height h_{min} above the invert) reached by aeration is of interest in two-phase flow. Without losing generality, a specific value $\bar{\alpha}_1 = 15\%$

was used for discussion. This percentage may occur at multiple locations along a normal line in the central plane. For B1, upstream of $x_2 = -0.55$ m (Figure 4.8(a)), the location of $\bar{\alpha}_1 = 15\%$ was close to the surface, with negligible AVF below. The minimum height dropped from $h_{min} = 0.037$ m at $x_2 = -0.19$ m to 0.001 m at $x_2 = 0.40$ m. Further downstream, the locations of $\bar{\alpha}_1 = 0.15$ were generally near the invert, except at $x_2 = 1.20$ m where $h_{min} = 0.033$ m. At $x_2 = 1.60$ m, 1.8 m close to the weir, $h_{min} = 0.002$ m. After the jump ended, the maximum AVF was $\bar{\alpha}_1 = 0.15$ below the free surface.

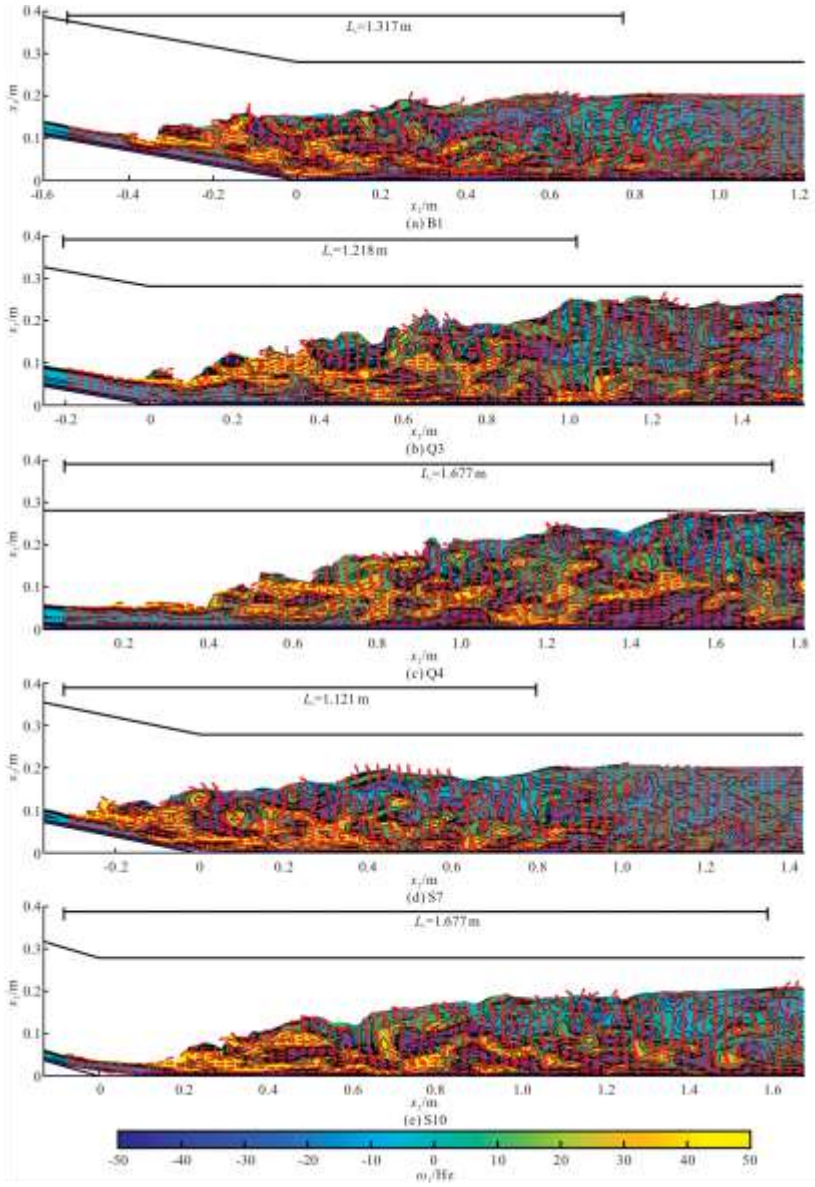

Figure 4.11 Central plane $x_1 = 0$, showing ensemble average velocity $\boldsymbol{u}/|\boldsymbol{u}|$ (normalised vectors) and vorticity (contours) for LES runs. The upper edge of the vector region is the free surface ($\bar{\alpha}_2 = 0.5$). For clarity, some densely populated vectors have been skipped

For the other runs (Table 4.1), similar features are observed from the LES results. In the case where choking of flow occurred more intense fluctuations in $\bar{\alpha}_1$ are seen in the incomplete jump, e.g., at $x_2 = 0.60$ m (for Q4), at $x_2 = 1.40$ m (for Q5) and at $x_2 = 1.20$ m (for Q6). The upstream end of the pressured flow region moved upstream at increasing flow rates for the three runs (Table 4.1).

4.3.6 Velocity vector and vorticity fields

The velocity vector $\boldsymbol{u} = \langle \bar{u}_2, \bar{u}_3 \rangle$ and vorticity $\omega_1 = \nabla \times \boldsymbol{u}$ in the central plane are plotted in Figure 4.11. The vector field helped demarcate the zone of rollers and roller length L_r. The downstream end of the zone was identified by closely examining the vectors near the free surface. In Figures 4.11(a)–4.11(e), each LES run predicted a bottom flow along the invert, carrying fluid downstream. A portion of this bottom flow was a core jet. In Figures 4.10(m)–4.10(t), the jets extended a certain distance $\tilde{x} = (x_2 - x_{2r})/L_a$, where x_{2r} is the x_2 coordinate of the jump toe. Take B1 as an example. This distance was $\tilde{x} \approx 0.60$. The fluid carried by the jets moved much faster than the surrounding and overlying fluid, giving rise to a shear layer, and shear-induced turbulent mixing caused an outward transmission of momentum from the core. Note that the core jet differs from the shear layer in CHJs.

The portion of the free surface bounded by the toe and by the point that separated vectors in the reverse (or negative x_2) direction at upstream from vectors in the positive x_2 direction at downstream, was identified. The x_2-direction distance between the toe and this point gives L_r. In Figure 4.11(a) for B1, $L_r = 6.57d_2$, compared with $L_a = 7.83d_2$. Values of L_r/d_2 and L_a/d_2 are summarised in Table 4.1. From Figure 4.11(a), a number of observations are made:

(1) Below the free surface was a layer of reverse flow, with thickness varying with $\tilde{x}$. Eddy motions prevailed. Below this layer, velocity vectors pointed generally downstream, as was the case in the entire flow depth downstream of the jump.
(2) The vorticity ranged from –50 Hz to 50 Hz, compared to $u_0/y_0 \approx 9$ Hz. The negative extreme vorticity occurred in the zone underneath the core jet. This zone had a wavy boundary and a varying thickness along the invert. The vorticity above the jet weakened with distance downstream.
(3) Upstream of $\tilde{x} = 0.30$, the zone away from the invert had weak vorticity.
(4) The zone immediately above the core jet had positive extreme vorticity. There were small, elongated pockets of clockwise (CW) rotation ($\omega_1 < 0$) near the free surface at $\tilde{x} \approx 0.16$ and in the middle depth at $\tilde{x} \approx 0.54$.
(5) In $0.30 < \tilde{x} < 0.50$, longer, elongated pockets of $\omega_1 > 0$ extended from the free surface and broke downstream. Below the surface, in the upper fluid column, there were alternating zones of CW rotations and counter-clockwise (CCW) rotations ($\omega_1 > 0$). In the lower fluid column but away from the invert, CCW rotations dominated, with very few pockets of CW rotations.
(6) In $0.50 < \tilde{x} < 0.73$, the upper half of fluid column displayed $\omega_1 < 0$, whereas the lower half showed $\omega_1 > 0$ but with more small pockets of $\omega_1 < 0$.
(7) In $0.73 < \tilde{x} < 0.90$, large pockets of alternating $\omega_1 < 0$ and $\omega_1 > 0$ appeared in the upper fluid column, whereas small pockets of alternating vorticities in the lower column. Further downstream, vorticity was weak.

The above-mentioned vorticity features apply to the central plane. The 3-D vorticity was much more complicated.

At increasing q (Table 4.1, B1, Q2, Q3), the above-mentioned flow features had larger dimensions and shifted downstream. Within a small distance $\tilde{x}$, $\omega_1 > 0$ above the core jet, a few small pockets of $\omega_1 < 0$ appeared near the free surface and in the middle depth (e.g., at $\tilde{x} \approx 0.20$ in Figure 4.11(b) for Q3). Downstream of $\tilde{x} \approx 0.24$ for Q2 and of $\tilde{x} \approx 0.30$ for Q3, the zones of $\omega_1 < 0$ gradually enlarged in the upper fluid column and dispersed into the lower column (Figure 4.11(b) for Q3), the zones extended downstream up to $\tilde{x} \approx 0.90$ for Q2 and $\tilde{x} \approx 0.60$ for Q3. In these $\tilde{x}$ ranges, the free surface region showed reverse flow, whereas the lower fluid column showed flow toward downstream (with $\omega_1 > 0$). Downstream of $\tilde{x} \approx 0.97$ for Q2 and $\tilde{x} \approx 0.67$ for Q3, ω_1 was small, and velocity vectors gradually became horizontal. Runs Q4–Q6 produced an incomplete hydraulic jump, with choked flow; the upper fluid column had $\omega_1 < 0$, whereas the lower column had $\omega_1 > 0$. However, alternating vorticity pockets existed in both the upper and lower columns, but the alternations were more frequent and chaotic in the upper column.

At an increasing slope (Figure 4.1(a), B1, S7–S10 in Table 4.1), the zone of $\omega_1 > 0$ near the invert after the jump toe enlarged significantly. In Figure 4.11(e) (for S10), in the lower fluid column, there were elongated pockets of $\omega_1 < 0$ of much larger magnitude than in Figures 4.11(a), 11(d) (for B1 and S7), and it took a longer distance for the velocity vectors to become horizonal. Other flow characteristics for Q2–S10 are similar to those for B1.

4.4 Discussion

4.4.1 Data comparison

The spectrum of predicted instantaneous velocity has been shown to be consistent with the Kolmogorov $-5/3$ law (Figure 4.5), meaning that the mesh properly resolves instantaneous turbulent eddies of different sizes and the turbulence closure scheme is realistic. The profile of the ensemble average free surface compares well with available observations (Figure 4.7), indicating that the ensemble average is valid. This section further provides data comparison.

Table 4.2 Comparison of flow depth and velocities between laboratory observations and LES predictions

(x_1, x_2) / m	d/d_0		$\langle \bar{u}_2 \rangle / u_0$		x_2/ m	U_2/u_0	
	Observation	Predicted	Observation	Predicted		Observation	Predicted
(0, −1.03)	0.16	0.13	-	-	−1.03	2.28	2.02
(0, −0.54)	0.08	0.13	-	-	−0.54	6.56	2.25
(0, −0.13)	0.46	0.50	-	-	−0.13	0.51	0.49
(0, 0.10)	0.56	0.56	-	-	0.10	0.40	0.33
(0, 0.99)	0.66	0.72	0.77	0.74	0.99	0.33	0.22

Run B1 (Table 4.1) in this study matches a laboratory experiment of a two-phase flow in Qian et al. (2017). Table 4.2 compares the predicted flow depth d (below the free surface), vertically averaged velocity $\langle \bar{u}_2 \rangle = \int \bar{u}_2 \mathrm{d}x_3$ (above the free surface), and cross-sectionally averaged velocity $U_2 = \iint \bar{u}_2 \, \mathrm{d}x_1 \mathrm{d}x_3$ (below the free surface) from this study, with observations from Qian et al. (2017). The observed values of U_2 are obtained by dividing the water discharge by the water flow area below the free surface, assuming that the free surface is uniform in the x_1 direction.

The five locations listed in Table 4.2 are within the LES domain well away from the inlet and outlet (Figure 4.1). Two of them ($x_2 = -0.13$ m, 0.10 m) are inside the region of hydraulic jump. For these two locations, the average relative errors are about 4% for the predicted depth ratio d/d_0 and 10% for the predicted cross-sectionally averaged velocity U_2/u_0. These error percentages are considered to meet the expectation, given the flow fluctuation (Figure 4.4). At the toe and upstream in the supercritical region ($x_2 \leq -0.54$ m), the comparisons are poor.

The predicted air flow velocity is reasonable, the relative error being below 4%. This reflects the physical condition that the free surface motion induces air movement above and the liquid phase transfers momentum to the gas phase. This transfer is significant because of the much higher density of water than that of air. RANS models typically introduce a source/sink term to allow for the transfer, which contains uncertain empirical constants.

The LES runs H11–H15 (Table 4.1) match the experiments of Stahl and Hager (1999). Based on the experimental data, they express the initial-sequent depth ratio, roller length, and aeration length as $d_2/d_1 = 1.16Fr_1^{0.85}$, $L_r/d_2 = Fr_1^{0.5}$ and $L_a/d_2 = 4Fr_1^{0.5}$. The predicted values of d_2/d_1, L_r and L_a from this study are compared with the values from Stahl and Hager (1999) in Figure 4.12. The relative errors in the predicted depth ratio are below 5% for runs H11–13, 7% for H14 and below 10% for H15, the relative errors in the predicted roller length are below 6% for all the five runs, and the relative errors in the predicted aeration length are below 4%. These percentages of errors are acceptable. For H15, the relatively large error in d_2/d_1 is possibly due to the high sequent depth downstream.

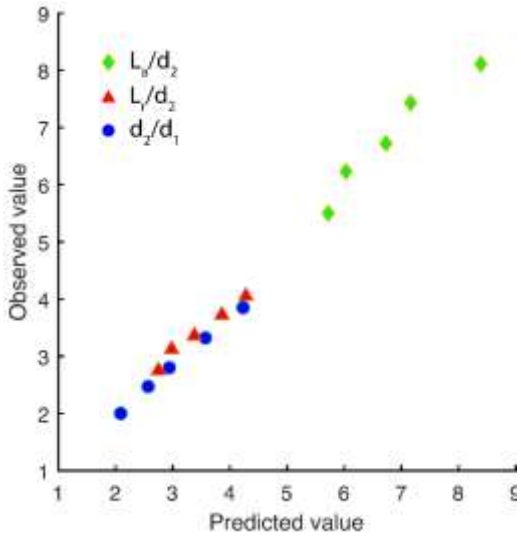

Figure 4.12 Comparison of predicted values of d_2/d_1 (blue), L_r/d_2 (red) and L_a/d_2 (green) from this study with observation (Stahl & Hager, 1999)

4.4.2 Okubo-Weiss parameter for delineating hydraulic jump

The difficulty of pinpointing the downstream end of a jump has been long recognised. So far researchers have relied on visually inspecting the flow field, which is inefficient. The jump dimensions so obtained may contain significant errors. This study proposes using the Okubo-Weiss parameter w as a new way to delineate the region of hydraulic jump. The theoretical base is that fluid motions can be decomposed into linear deformation, angular deformation and eddy rotation.

The parameter is given as $w = s_n^2 + s_s^2 - \omega_1^2$, where s_n is the normal strain component ($s_n = \partial\bar{u}_2/\partial x_2 - \partial\bar{u}_3/\partial x_3$), s_s is the shear strain component ($s_n = \partial\bar{u}_3/\partial x_2 - \partial\bar{u}_2/\partial x_3$). Rotation-dominated zones (or eddies) are zones of $w < -w_o$, where w_o is a certain threshold. The cores of eddies are located in local minima of negative w values; they exhibit large vorticity and strong circulation density of the velocity field. Strain-dominated zones are zones of $w > w_o$. Zones of $-w_o < w < w_o$ have background vorticity and strain. This study uses the threshold $w_o = 0.2\sigma_w$ (Isern-Fontanet et al., 2004), where σ_w is the standard deviation of w values in the target flow zone.

Examples of w contours are plotted in Figure 4.13 for the same central plane as u and ω_1 in Figure 4.11. The values of w have been normalized by $W_n = (u_0/\lambda)^2$, where λ is an eddy length scale, taken to be $3(\Delta x_1 \Delta x_2 \Delta x_3)^{1/3}$ or ($\lambda \approx 0.012\ m$). Eddies larger than λ can be discerned from the computed flow field. The Reynolds number based on u_0 and λ equals 8 484. The parameter quantitatively identifies and traces persistent turbulent eddies in the central plane of the hydraulic jump. Calculations of w can be done for any other vertical planes.

Eddies and strains are local-scale flow features. The w contours (Figure 4.13) coincide with zones of strong vorticity (Figure 4.11), but zones of weak vorticity (e.g., zones outside aeration length) are filtered out from Figure 4.13 as background vorticity and strain. The strong alternating eddy and strain pockets in Figure 4.13 (yellow and blue zones) exhibit the same patterns of rotations as in Figure 4.11 (gold zones). Take B1 as an example. Strong alternating eddy and strain pockets almost fill the region -0.40 m $< x_2 < 0.40$ m (Figure 4.13(a)). Further downstream throughout to the downstream end of roller length (as identified in Figure 4.11(a)), strong, dispersed alternating eddy and strain pockets show up near the invert, only a few sparse weak eddy and strain pockets appear in the upper fluid column.

Contours of w clearly indicate the region of coherent turbulent activities in a hydraulic jump. From Figure 4.13(a) (for B1), there is no difficulty to tell that this region starts upstream from $x_2 = -0.40$ m, and it ends downstream at $x_2 = 0.80$ m at the invert whereas at $x_2 = 0.50$ m at the free surface. Downstream of $x_2 = 0.50$ m, there are no strong eddy and strain pockets near the surface. Without ambiguity, the aeration length is 0.9 m (from $x_2 =$ –0.40 m to 0.50 m). The other cases shown in Figure 4.13 support the discussion above. In conclusion, this study presents a quantitative approach to delineating the region of hydraulic jump, complementary to the traditional qualitative approach requiring visual inspections of the flow field or free surface profiles.

It is also convenient to use the Okubo-Weiss parameter to delineate the 3-D region of hydraulic jump (Figure 4.14). In Figure 4.14, isosurfaces of instantaneous w values reveal the longitudinal and lateral variations of hydraulic jump features. Unlike in CHJ on horizontal floor, in a circular pipe, the lateral variations are an important aspect of jump structures. As expected, the instantaneous values of the parameter (Figure 4.14) vary much more greatly than the ensemble average values (Figure 4.13). The instantaneous flow (Figure 4.14) contains stronger alternating eddies and strain pockets within the hydraulic jump length than outside, as is the case for the ensemble average flow (Figure 4.13). The parameter has instantaneous maxima/minima seven times the ensemble average maxima/minima. With the features shown in Figure 4.13 or 4.14, one can possibly delineate the region of hydraulic jump with good accuracy.

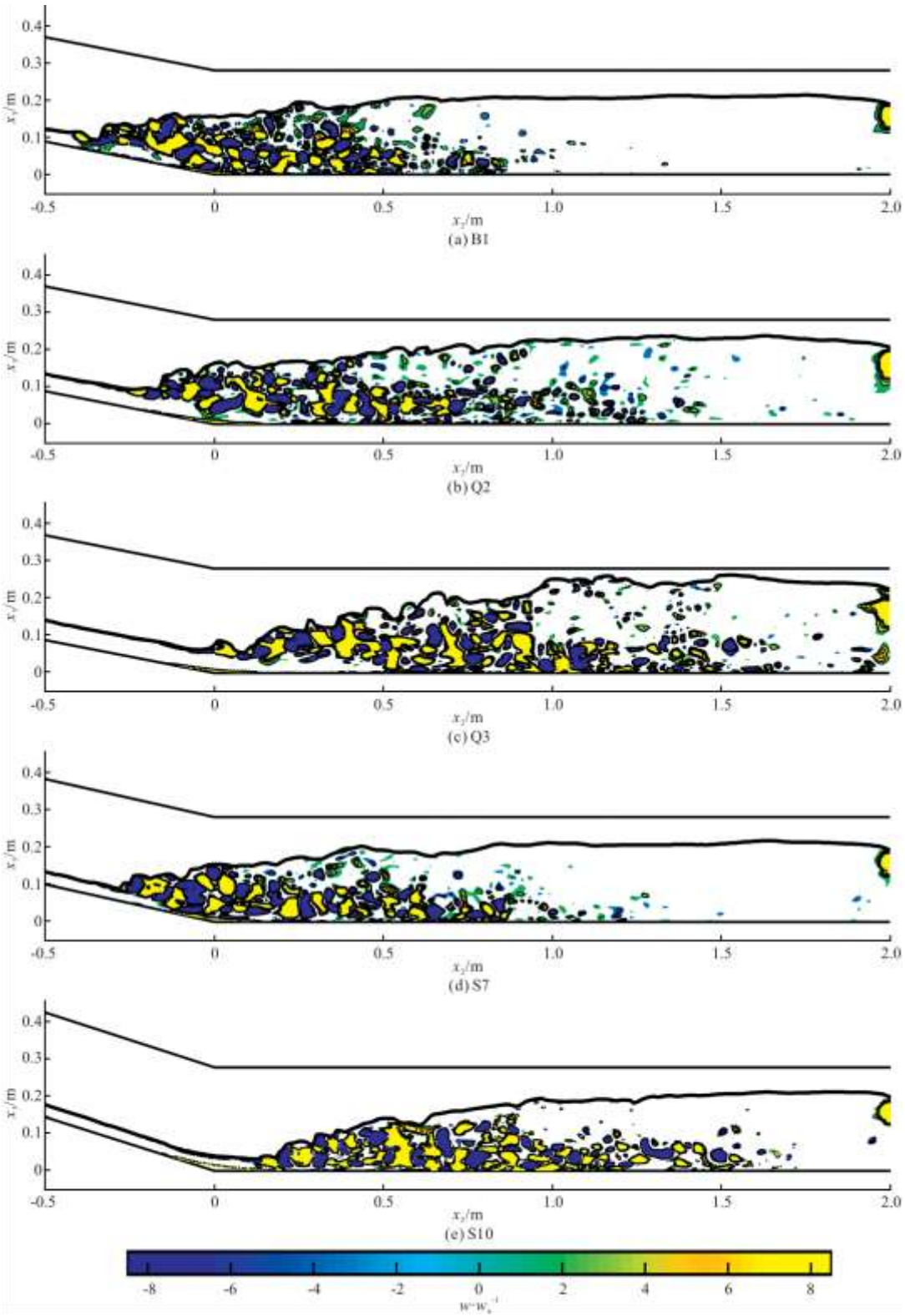

Figure 4.13 Central plane $x_1 = 0$, showing contours of w for runs: (a) B1; (b) Q2; (c) Q3; (d) S7; (e) S10. The black curve in each panel marks the position of the free surface

4.4.3 Influence parameters and modelling improvement

The Froude number Fr_1 (Table 4.1) is a key parameter in the analysis of hydraulic jumps. Fr_1 has to be prescribed as input to hydraulic designs and to most empirical formulae of hydraulic jump. This is difficult in the case of sloping pipes. The reason is that one has no a priori knowledge about Fr_1. Fr_1 is part of the solution to the hydraulic jump problem. From B1 to Q2 throughout Q6, the discharge q monotonically increases, but the resulting value of Fr_1 goes up and down (Table 4.1), depending on whether the resultant change of V outweighs that of D or vice versa. For example, when q increases from 9.88 L/s for B1 by about 50% for Q2, the increase of D outweighs that of V in terms of influence on Fr_1. This explains the reduced aeration lengths from B1 to Q2. It appears that an increasing q causes the jump toe to shift down the slope and even to the horizontal pipe.

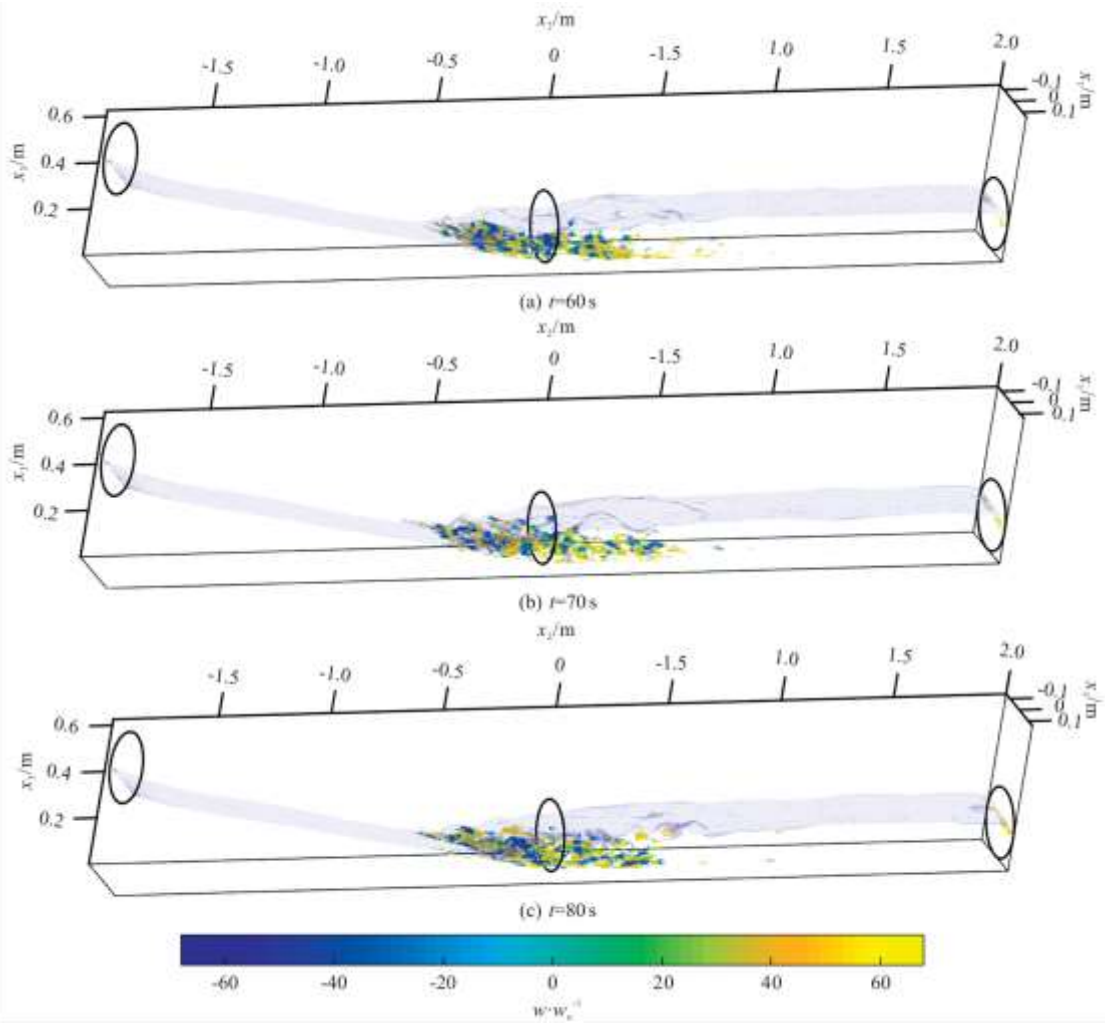

Figure 4.14 3-D distribution of instantaneous Okubo-Weiss parameter values at model times for B1

The jump can start in the sloping or the horizontal pipe. The influence of slope is non-trivial. First, the weight of fluid contained in the jump volume itself depends on the length of jump. This length cannot be determined easily by theory. For this reason, no data fitting, empirical relationship, and analytical expression can yield a fully predictive model of hydraulic jumps. Second, the weight resolved down the slope, which influences the balance of forces in the momentum principle,

depends on the steepness of the slope. Compared with the range of L_r/d_2 values (Table 4.1) from this study, the approximation $L_r/d_2 = 4.5$ suggested in Edwards et al. (2018), Montes (1998) would lead to an underestimate of L_r for a given Fr_1.

A further complication is that the jump can be incomplete, as is the case for Q4–Q6, with a compressed roller length. This poses the practical problem of choked flow in drainage sewers. The study of Gargano and Hager (2002) on choking by undular jump leads to the recommendation of maintaining either definitely subcritical or supercritical flow along the entire pipe in order to avoid a transfer of flow condition. However, a transfer is more likely to happen than not in sloping pipes. The study of the influence of slope on choking by Wang and Li (2018) considers an infinitely long pipe. In reality, pipes have a finite length with a changing slope. A larger slope tends to yield a higher value of Fr_1, limited to runs S7–S10 (Table 4.1). This can be explained using the uniform flow theory as a first-order approximation, which gives V (Table 4.1) proportional to the square root of the slope. When the slope exceeds a certain threshold and when a hydraulic jump forms, it forms in the horizontal pipe and a large roller length (runs S9 and S10).

The circular shape of pipes represents a particular influence on not only the hydraulic radius and velocity but also the vorticity distribution (Figure 4.11). The distribution differs significantly from that in CHJ. The former is 3-D, whereas the latter is 2-D. In CHJ, the ω_1 distribution from the horizontal floor to the free surface is simple (Zhang et al., 2013): At a given x_2 coordinate, $\omega_1 < 0$ from the floor through a wall boundary layer, $\omega_1 = 0$ at the peak of the wall jet, and $\omega_1 > 0$ from the peak to the roller region's lower bound. In this study, the ω_1 distribution is complex. In the complete jumps (Figures 4.11(a), 4.11(b), 4.11(d) and 4.11(e)), the entire depth is dominated by regions of $\omega_1 > 0$, with only small pockets of $\omega_1 < 0$, although the strength of positive ω_1 drops and the regions shrink downstream. The upper fluid column contains expanding pockets of $\omega_1 < 0$ and alternation of positive and negative ω_1. Incomplete jumps (Figure 4.11(c)) contain regions of intertwined and alternating vorticities of opposite signs in the entire depth below the free surface.

This study presents fully predictive strategies for computing hydraulic jump. The computations accommodate steep gradients of the velocity and pressure fields, and irregular shapes and rapid free-surface fluctuation. This study has contributed to an improved understanding of the 3-D structures of the jump, including the core jet, and of such integral properties of the jump as the lengths of roller and aeration. Predicting the hydraulic jump as a two-phase flow in a circular pipe is an extension of existing solutions of the hydraulic jump as a one-phase flow (e.g., Montes, 1998).

It would be constructive to explore potential gain from refining LES mesh and enhancing turbulence closure. The study of an external cavitating flow by Cheng et al. (2020) shows improved LES results from mesh refinement and a steeper slope than the Kolmogorov $-5/3$ law in energy cascading. The dynamic Smagorinsky-Lilly model provides turbulence closure in this study. Cheng et al. (2020) suggests that the Wall-Adapting Local Eddy-viscosity model slightly improves the LES results of tip-leakage cavity, when compared with the dynamic Smagorinsky-Lilly model. The study of jet interaction by Li et al. (2011) shows that the Dynamic Kinetic energy Subgrid-scale Model outperforms the dynamic Smagorinsky-Lilly model, improving the LES results of mean flow velocity and turbulence intensity. Future study should investigate whether similar

improvement applies to the LES prediction of hydraulic jumps in a circular pipe. This entails detailed measurements, currently not available for the investigation.

Long et al. (2017) demonstrates the influence of mesh resolution on numerical results of velocity distribution and vortex stretching from solving the unsteady Reynolds-averaged Navier-Stokes equations. They have proposed sound procedures and uncertainty estimators for the verification and validation of numerical results. It would be worthwhile to implement the procedures on LES results in future study when detailed measurements become available.

4.5 Summary and conclusions

Hydraulic jumps in circular pipes with changing slopes are computed in this study using LES. The computations treat the jumps as a 3-D two-phase bubbly flow and cover a range of pipe discharge q and slope angle α (Figure 4.1). The dynamic Smagorinsky-Lilly scheme provides turbulence closure. The following conclusions have been reached:

(1) The LES model captures very well the instantaneous flow fluctuation of hydraulic jump (Figure 4.4). The computed instantaneous velocity field displays spectra in consistency with the well-establish Kolmogorov –5/3 law (Figure 4.5), meaning that the LES mesh properly resolves energy-bearing eddies, the inertial subrange, and energy cascading. This success is partly due to the viscous sublayer and near-pipe-wall region being resolved (Figure 4.2(b)).

(2) It is suitable to estimate the time duration needed for ensemble average of the instantaneous flow, using the aeration length as a length scale and the approach flow velocity as a velocity scale. This suitability has been confirmed by evaluations of autocorrelation functions and cumulative averages (Figures 4.4, 4.6). The calculated ensemble averages of initial-to-sequent depth ratio, free-surface position, water and air velocities, roller length and aeration length are acceptable, when compared with available laboratory observations (Table 4.2, Figure 4.12).

(3) Hydraulic jumps in sloping pipes have complex internal structures. The ensemble averaged flow shows a 3-D core jet hugging the pipe invert (Figure 4.10), irregular distributions of vorticity around the jet, wavy vertical profiles of the streamwise velocity (Figure 4.9), and pockets of alternating CW and CCW rotations (Figure 4.11), not seen from classical jumps on horizontal floors or in sloping rectangular channels.

(4) The value of Fr_1 depends on q (for a given α), α (for a given q), and q and α combined. The value is part of solution to the hydraulic jump problem, rather than a prescribed Fr_1. Thus, the jump behaviour driven by q and α are complex. The jumps can be a complete or an incomplete jump and can form in the sloping or the horizontal pipe section (Figure 4.9). The region of jump shows significant secondary flow and streamwise velocities asymmetrical about the vertical plane through the invert.

(5) The reported integral properties of jumps (Table 4.1) are useful to address issues of choked flow by incomplete jumps in sewer pipes. The initial-to-sequent depth ratio is smaller (by up to 20%) than that from the Belanger equation (for the classical jump) for the same Froude number Fr_1 before the jump toe. The roller length of jump as a two-phase flow is larger than that as a one-phase flow ($L_r = 4.5d_2$) suggested in the literature (Montes, 1998).

(6) For the first time, this study proposes using the Okubo-Weiss parameter as a new way to quantitatively delineate the region of hydraulic jump and reveal detailed turbulence

activities such as vortex stretching and lengthening (Figure 4.13). It is more efficient and less ambiguous than traditional visual inspections.

5 Large-eddy simulation of free-surface turbulent flow in a non-prismatic channel[3]

5.1 Background

Open channels need a transition for practical hydraulic engineering applications such as hydro-power generation, water supply, drainage and irrigation. As an example of water supply, water from a lake emerges from a relatively small rectangular concrete channel section and flows through a transition connected to a large trapezoidal earthen channel section. In Figure 5.1, a warped transition provides the needed connection; the channel is non-prismatic or the channel has an inlet and outlet of different shapes and sizes, in contrast to a prismatic channel (Sahu et al., 2014). To reduce construction costs, real transitions have a short length L and a large divergence angle θ. This causes flow separation from sidewalls, turbulent disturbances, free-surface fluctuations, poor hydraulic efficiency, and high risks of earthen-channel erosion.

Traditional studies of channel transitions take the empirical approach, which consider only 1-D time-averaged free-surface flow (Chow, 1959). They ignore 3-D instantaneous turbulent features and fail to achieve optimal hydraulic efficiency and minimise erosion risks. The purpose of this study is to predict the turbulent features by means of two-phase large eddy simulation (LES). The model domain is illustrated in Figure 5.1. The scope of work includes rigorous validations of LES predictions using newly available experimental data and benchmark solutions. These represent unique and new contributions. In the broad sense, this study demonstrates the two-phase LES approach as a modern approach to future hydraulic design, offering a good complement to the experimental approach.

Unlike the Reynolds-averaged equation models that simulate time-averaged flow field, LES provides instantaneous flow field. Knowledge about the instantaneous flow velocity and the associated peak strength is most relevant to addressing channel erosion risks. Previously, some researchers (e.g., Nashta & Garde, 1988) obtained semi-analytical functions for describing transition profiles. Others (Murty Bhallamudi & Hanif Chaudhry, 1992; Rahman & Chaudhry, 1997; Younus & Hanif Chaudhry, 1994) numerically simulated two-dimensional (2-D) depth-averaged flow in expansion. These studies do not produce detailed structures of the flow field or separation features. This is one of the significant gaps addressed by this study.

Compared to other types of transitions (Chow, 1959), the warped transition is a superior choice (USACE, 1991). Its sidewalls are flush with both the upstream and downstream channel sections (Li, 2022). The seamless joints help reduce turbulent disturbances. A few recent studies (Choi et al., 2022; Zeng & Li, 2022) compute instantaneous flows in a straight-wall transition rather than a warped transition.

We address the question of a realistic flow condition at the inlet (Figure 5.1), with required fluctuations in LES. Periodic conditions often used in LES studies (Nikora et al., 2019; Ramos et al., 2019; Xie et al., 2013) are invalid for a non-prismatic channel. However, inlet conditions may be generated using another method such as: precursor method, recycling and rescaling method, or a synthetic method. The 1st method is reportedly most accurate (Tabor & Baba-Ahmadi, 2010), and the 2nd method is effective in producing a fully developed turbulent boundary layer, but both

[3] This chapter contains information from a manuscript submitted to the Journal of Hydroinformatics.

incur high computing costs and can possibly produce a periodicity (Dhamankar et al., 2018). The synthetic methods are a trade-off between computational accuracy and cost. The synthetic methods including spectral synthesiser (SS) and vortex method (VM) have been applied in recent LES studies of one-phase air flow (Antoniou et al., 2017).

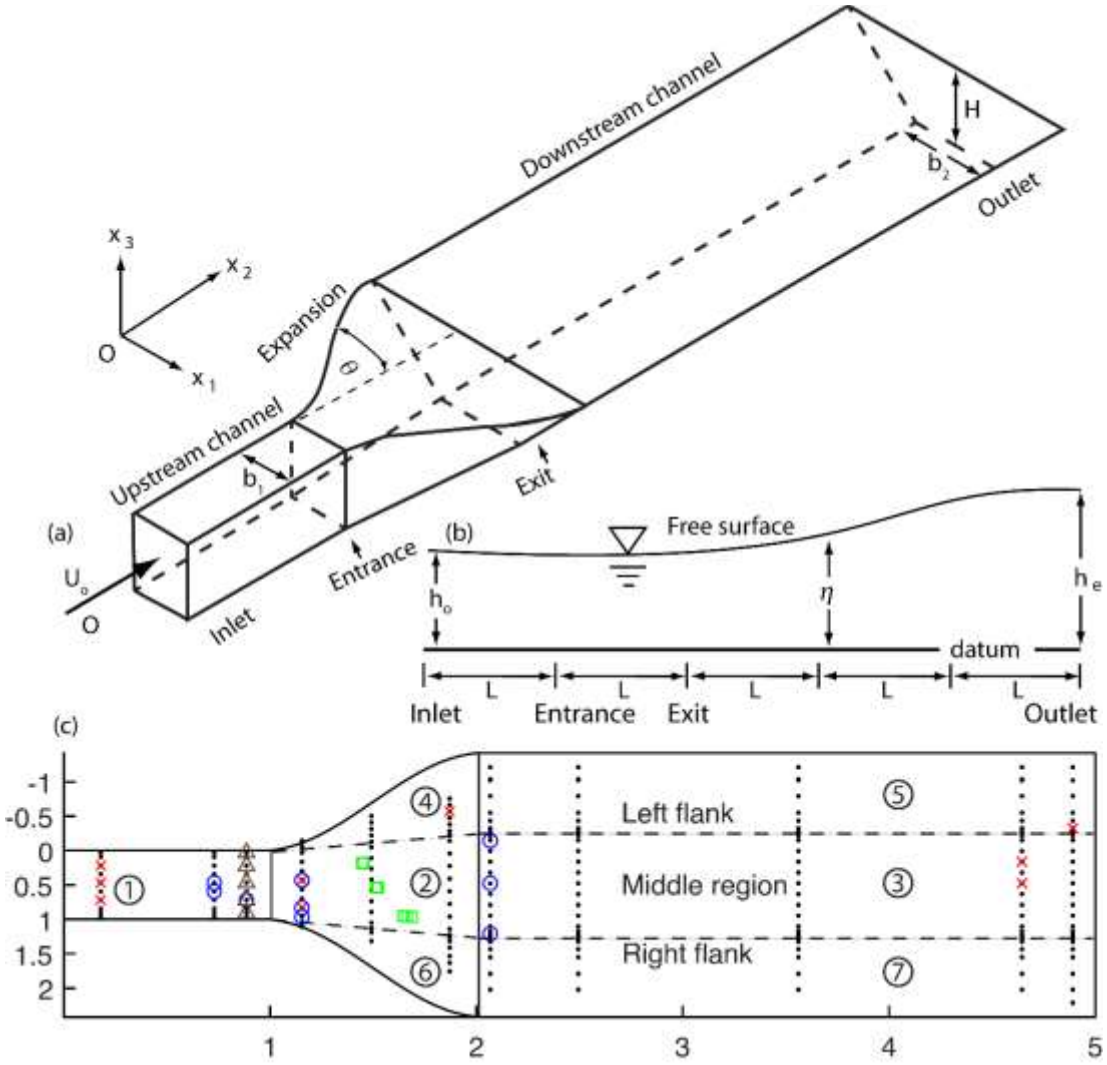

Figure 5.1 LES model channel. (a) 3-D view; (b) elevation view; (c) top view. The channel dimensions are: $b_1 = 0.2032$ m; $b_2 = 0.3048$ m; $H = 0.2607$ m; $h_o = 0.2284$ m; $L = 0.61$ m. The downstream channel section is isosceles trapezoid with side slope of 45°. The green squares mark nine cells: three at $x_3/h_o = 0.83$, three at 0.47, and three at 0.06

We also address the question of possible reflection of surface waves from the outlet (Figure 5.1) and the influence of initial conditions in LES on the flow development. The results from this study include 3-D velocity, vortical motions, and first- and second-order statistics of turbulence.

Few applications of SS and VM have been reported in the literature, and little is known about suitable values for parameters as input to SS and VM. Previously, Liu et al. (2021) applied SS in their study of flow in a rectangular vegetated channel, and Zeng and Li (2022) applied VM in their

investigation of flow choking in a circular partially full pipe. The rectangular channel and circular pipe are prismatic channels. Non-prismatic channels are a new case, where more complicated mechanisms of flow separation, eddy formation and turbulence interaction are involved. This is one important difference of this study from the previous studies. Another important difference of this study is a systematic assessment of proper parameters in SS and VM and their values. The contributions from this study include improved strategies for computing open-channel turbulence and for visualising and analysing the computational results, with relevance to practical applications. The contributions will be discussed later in this study.

5.2 Method

5.2.1 Model equations

We considered an incompressible flow of an air-water mixture, with air above the free surface and water below. The position of the free-surface was tracked using the volume of fluid method. The density, ρ, of the mixture was calculated based on the volume fraction, α, as $\rho = \alpha_1\rho_1 + \alpha_2\rho_2$, where the subscripts 1 and 2 refer to air and water, respectively. For a given cell, $\alpha_1 + \alpha_2 = 1$. The viscosity, υ, of the mixture was calculated as $\upsilon = \alpha_1\upsilon_1 + \alpha_2\upsilon_2$.

LES used filtered equations of momentum and continuity:

$$\partial u_i/\partial t + \partial(u_i u_j)/\partial x_j = -\rho^{-1}\partial p/\partial x_i + \partial(\upsilon\partial u_i/\partial x_j - \tau_{ij})/\partial x_j + g_i \quad (5.1)$$

$$\partial u_i/\partial x_i = 0 \quad (5.2)$$

where u_i is the resolvable-scale filtered velocity component in the x_i-direction (i = 1, 2, 3); t is time; p is the resolvable-scale pressure; τ_{ij} is the SGS stress; g_i is the gravitational acceleration. LES computes the exact motion of large eddies and models SGS eddies smaller than the mesh size Δx_i.

5.2.2 Turbulence closure models

The term τ_{ij} accounts for the effect of unresolved velocity fluctuations on the resolved motion. It is related to the resolved strain rate, S_{ij}, through eddy viscosity, μ_t, as

$$\tau_{ij} = -2\rho^{-1}\mu_t S_{ij} + \frac{1}{3}\tau_{kk}\delta_{ij} \quad (5.3)$$

where τ_{kk} is the isotropic part of the SGS stress, not modelled but added to the filtered static pressure term. We assess three SGS stress models for μ_t: dynamic Smagorinsky-Lilly (DSM) model (Germano et al., 1991); wall-adapting local eddy-viscosity (WALE) model (Nicoud & Ducros, 1999); dynamic kinetic energy (DKE) SGS model (Kim & Menon, 1997). The 1st and 2nd models predict the behaviour of μ_t correctly near a solid surface, without using empirical damping functions, whereas the 3rd model takes the specified filter width, Δ_f, as the relevant length scale. The standard Smagorinsky SGS stress model has been previously used in LES studies of free surface flow (Cataño-Lopera et al., 2017), where the eddy viscosity coefficient is set as a constant. This is unrealistic for strongly separated flow. Therefore, we do not consider the standard model.

5.2.3 Boundary conditions

We assess three ways to specify the inlet condition for the distribution of mean-inflow velocity v_o:

(1) 1/7th power-law (Table 5.1, labelled as '1/7')
(2) 1/14th power-law (labelled as '1/14')
(3) mapped 3-D velocity from the laboratory measurements (labelled as 'EXP').

The measurements were made from 70 points in the plane $x_2/L = 0.179$ (Figure 5.1). Inlet turbulent fluctuations (ITF) are usually needed for the superimposition to v_o. We assess two ways to meet this need: using SS to generate ITF from a total of 100 Fourier harmonics; using 2-D VM to superimpose a fluctuating vorticity field from a total of 190 vortices. In both, either the turbulence intensity T' and the eddy-to-molecular viscosity ratio v_t/v, T' and the length scale l, T' and the hydraulic diameter D, or TKE k and turbulent dissipation rate ϵ were supplied. Estimation from the measurements (Ramamurthy et al., 2017) from two planes ($x_2/L = 0.729$ and 0.885) gave $T' = 7.7$; $l = 0.2284$ m; $D = 0.2813$ m. A Reynolds-averaged simulation suggested $T' = 2.5$.

We assess two ways to specify outlet condition:

(1) pressure outlet $p = 0$, with the flow depth equal to 0.2371 m

(2) pressure outlet, in combination with numerical beach technique (NBT) for damping waves (Park et al., 1999).

Other boundary conditions were: $u_j = 0$ on the no-slip bottom and at the no-slip sidewalls. The pressure is zero at the free surface.

Table 5.1 Boundary condition, initial condition (IC) and hydraulic condition for LES runs. All runs have a large Reynolds number (Re= $h_o U_o/v$) and Froude number (Fr= $U_o/\sqrt{gh_o}$) below unity

Run ID	U_o (m/s)	Q (L/s)	L_u/h_o	v_o	ITF	IC	SGS	T'	l or D (m)	Nodes	NBT	Re	Fr	h_r	F_2
T1					VM			5.13			-	111230		-	-
T2					VM			7.7			-	111230		-	-
T3	0.487	22.6	2.67	1/7th	VM	'L'	DSM	11.6	0.2813	3763707	-	111230	0.33	-	-
T4					SS			5.13			-	111230		-	-
T5					SS			7.7			-	111230		-	-
T6					SS			11.6			-	111230		-	-
T7	0.487	22.6	2.67	1/7th	SS	'L'	DSM	7.7	10[a]	3763707	-	111230	0.33	-	-
D1	0.511	23.7[b]	2.67	1/7th	VM	'L'	DSM	7.7	0.2813	3763707	-	116712	0.34	0.74	0.76
D2											Yes	116712	0.34	0.72	0.70
D3	0.602	28.0	8[c]	1/7th	VM	'L'	DSM	7.7	0.2813	4021768	-	137497	0.40	0.73	0.77
D4	0.487	22.6		1/14th							-	111231	0.33	0.54	0.57
D5	0.487	22.6	2.67	1/7th	SS	'N'	DSM	7.7	0.2813	3763707	-	111231	0.33	-	-
D6						'L'					-	111231	0.33	0.69	0.68
E1					VM		DSM	7.7	0.2813		-	109860		0.78	0.77
E2					SS		WALE	2.5	0.2284		-	109860		0.85	0.82
E3					VM		WALE	2.5	0.2284		-	109860		0.82	0.81
E4	0.481	22.3	2.67	EXP	VM	'S'	WALE	2.5	0.2284	3763707	Yes	109860	0.32	0.80	0.78
E5					VM		WALE	7.7	0.2813		-	109860		0.77	0.77
E6					SS		WALE	7.7	0.2813		-	109860		0.84	0.81
E7					VM		DKE	7.7	0.2813		-	109860		0.78	0.78
E8					SS		DKE	7.7	0.2813		-	109860		0.87	0.81
E9	0.481	22.3	8[c]	EXP	VM	'S'	DSM	7.7	0.2813	4021768	-	109860	0.32	0.85	0.84
P1	0.481	22.3	2.67	INS[d]	-	'S'	DSM	-	-	3763707	-	109860	0.32	0.85	0.84
P2				INS[e]	-			-	-		-	109860	0.32	0.88	0.85

[a] Viscosity ratio ($v_t/v = 10$) is used instead of l or D; [b] A larger value is used to compensate lower velocities in sidewall boundary layers; [c] The inlet in Fig 5.1 is moved to $x_2 = -2L$; [d] Inlet instantaneous velocities are constructed from the LES results for E1; [e] Inlet instantaneous velocities are constructed from experimental data.

5.2.4 LES mesh

The model domain (Figure 5.1(a)) was discretised into a mesh of hexahedrons. The regions near the bottom, sidewalls were refined using 30 inflation layers. The first layer off a wall had a wall distance $y^+ \equiv yu_*/\upsilon_2 \leq 1$, where y is the distance to the wall, and u_* is the friction velocity. The mesh resolves the viscous sublayer. The between-layer spacing varied smoothly. The mesh sizes satisfy Zang's (1991) guidelines and/or Piomelli's (1993) criteria. The growth rate of sizes was kept within 1.2. The mesh had a low skewness; the average value is below 0.17 and the maximum below 0.65. With low skewness (Chung, 2002), the mesh quality is good to maintain numerical accuracy and stability.

5.2.5 Initial conditions

We assess three different ways to specify the initial conditions:

(1) The left flank had $u_i = 0$; the middle region and right flank had water velocity $u_2 > 0$ and $u_1 = u_3 = 0$, where u_2 was uniform at x_2 = constant and satisfied $\iint u_2 dx_1 dx_3 = Q$ (Figure 5.1(a)). The free surface η rose linearly along the transition length, from $\eta = h_o$ at $x_2 = L$ to $\eta = h_e$ at $x_2 = 2L$, where h_e is the flow depth at the outlet; $\eta = h_o$ for $x_2 < L$; $\eta = h_e$ for $x_2 > 2L$. η was uniform in the x_1-direction. The pressure p was hydrostatic at $x_3 < \eta$; $p = 0$ and $u_i = 0$ at $x_3 > \eta$. This set of initial conditions is labelled as 'L' in Table 5.1

(2) For the entire channel, u_2 was uniform at a given cross-section (x_2 = constant) and satisfied $\iint u_2 dx_1 dx_3 = Q$. Other remarks are similar to those given in initial condition 'L'. This set of initial conditions is labelled as 'N'

(3) The ensemble averages of $\alpha_1, \alpha_2, p, u_i$ from Run D1 (Table 5.1) were used as initial conditions for runs E1–E8. This set of initial conditions is labelled as 'S'.

5.2.6 LES runs

The time step was $\Delta t = 0.01$ s for all the LES runs (Table 5.1), which satisfies the Courant-Friedrichs-Lewy criterion for numerical stability. The model equations were solved in a pressure-velocity coupling manner, using the SIMPLE algorithm. Iterations continued until the convergence criterion of 10^{-6} or a maximum of 120 iterations per time step was reached. The LES runs were carried out using Ansys FLUENT software (Fluent, 2018) and the outputs were visualized and processed using MATLAB (MathWorks, 2022) scripts.

5.3 Results and discussion

5.3.1 Validation of inlet turbulent fluctuations using experimental data

Runs T1–T3 differed only in turbulence intensity T' as an input to VM (Table 5.1). The middle value of $T' = 7.7$ was an estimate from experimental data (Ramamurthy et al., 2017). The other input to VM was the hydraulic diameter D. The mean-inflow velocity distribution matched the experimental discharge. Runs T4–T6 matched the conditions of runs T1–T3, respectively, but used SS rather than VM. Run T7 matched run T5 but used the viscosity ratio ($\upsilon_t/\upsilon = 10$) rather than D.

Commencing from the initial condition 'L', runs T1–T7 allowed a spin-up time period $t_o = 32.5$ s or $26t_a$, where t_a is the advection time scale $t_a = L/U_o = 1.25$ s, and continued for $2t_a$. From output of instantaneous velocity u_i (Eq. 5.1) over this $2t_a$ period, we calculated the ensemble

average $\bar{u}_i$ and the root-mean-square-deviation (RMSD) Δu_i (defined as $\Delta u_i = \sqrt{\frac{1}{N}\sum(u_i - \bar{u}_i)^2}$), using ensemble size $N = 250$ at a given cell (x_1, x_2, x_3). Vertical profiles of $\bar{u}_i$ and Δu_i for selected (x_1, x_2) locations for runs T2 and T6 are plotted in Figure 5.2. The selected locations are well upstream of the transition, free of influence by intense local instability and thus suitable for testing the suitability of ITF. For run T2, the computed $\bar{u}_2$ profiles correlate well with the experimental data points (Figures 5.2(a)–5.2(e)). The coefficient of correlation was as high as 0.96 (Figure 5.2(b)) and as low as 0.41 (Figure 5.2(e)), and the overall average root-mean-square-error (*RMSE*) was as low as $\delta\bar{u}_2 = 0.07U_o$ for the $\bar{u}_2$ profile in Figure 5.2(c) and as high as $0.19U_o$ for the $\bar{u}_2$ profile in Figure 5.2(e). The computed Δu_2 profiles plot through the data points (Figures 5.2(k)–5.2(o)). Among runs T1–T7 (Table 5.1), the results for run T2 compare the best with the experimental data.

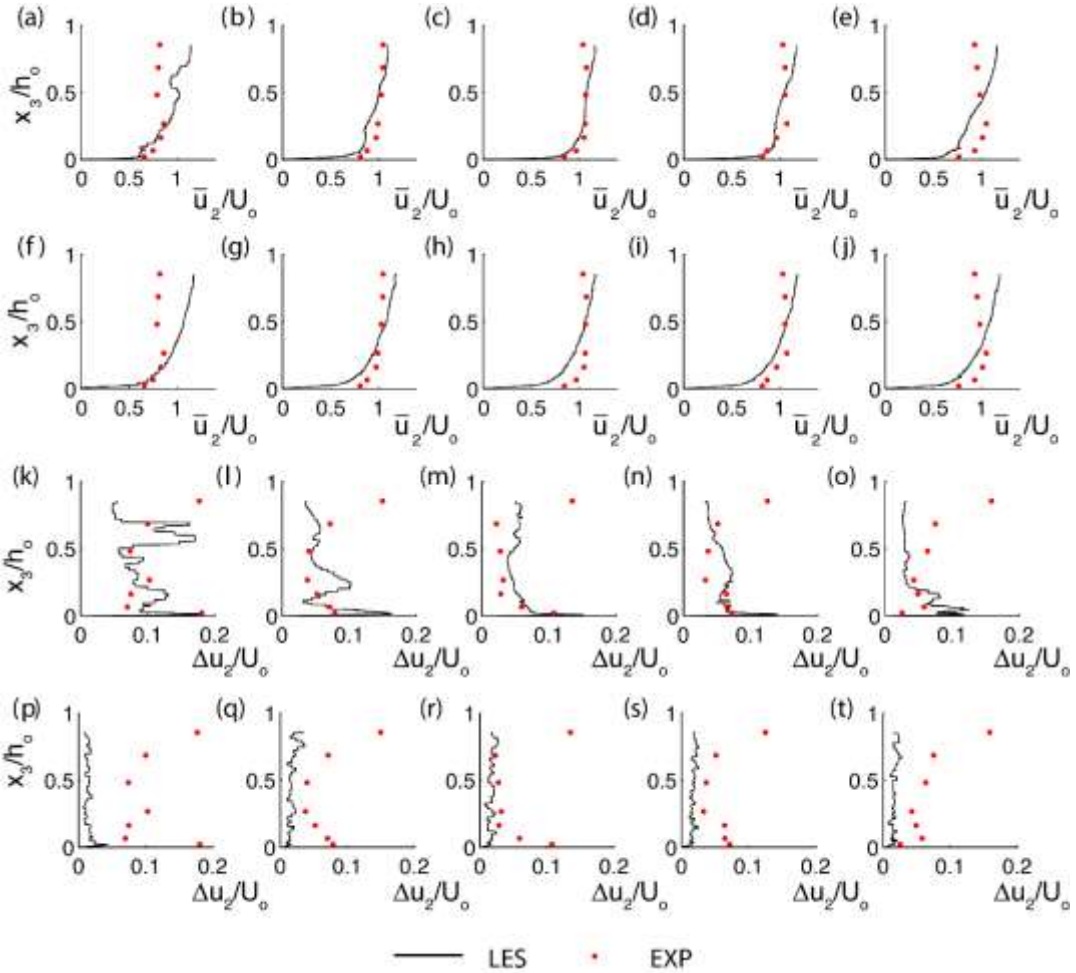

Figure 5.2 Vertical profiles of: (a)–(j) computed $\bar{u}_2$; (k)–(t) computed Δu_2 at five selected locations marked by triangles in Figure 5.1(c). Panels (a)–(e) and (k)–(o) are for run T2. Panels (f)–(j) and (p)–(t) are for run T6. Experimental data points (Ramamurthy et al., 2017) are shown for comparison

Using SS, run T6 produced $\bar{u}_2$ profiles of similar accuracy (Figures 5.2(f)–5.2(j)) as run T2. However, the use of SS surprisingly underpredicted Δu_2 (Figures 5.2(p)–5.2(t)). The turbulence

intensity was actually large for run T6 than run T2 (Table 5.1). Among runs T1–T7, run T6 gave the largest underpredictions of Δu_2. Run T6 has an average $RMSE = 0.21U_o$ for the five selected (x_1, x_2) $\bar{u}_2$ profiles. Among the same seven runs, run T3 gave the lowest value (0.67) for the coefficient of correlation, among the five selected $\bar{u}_2$ profiles. The results for run T7 had similar quality as runs T4–T6. Ai & Mak (2015) reported severe underpredictions by SS compared to VM in their LES study of airflow over a building, without offering validation. We validate the advantage of VM with turbulence intensity ($T' = 7.7$) and hydraulic diameter ($D = 0.2813$ m), and use them for most of the subsequent runs D1–E9 (Table 5.1).

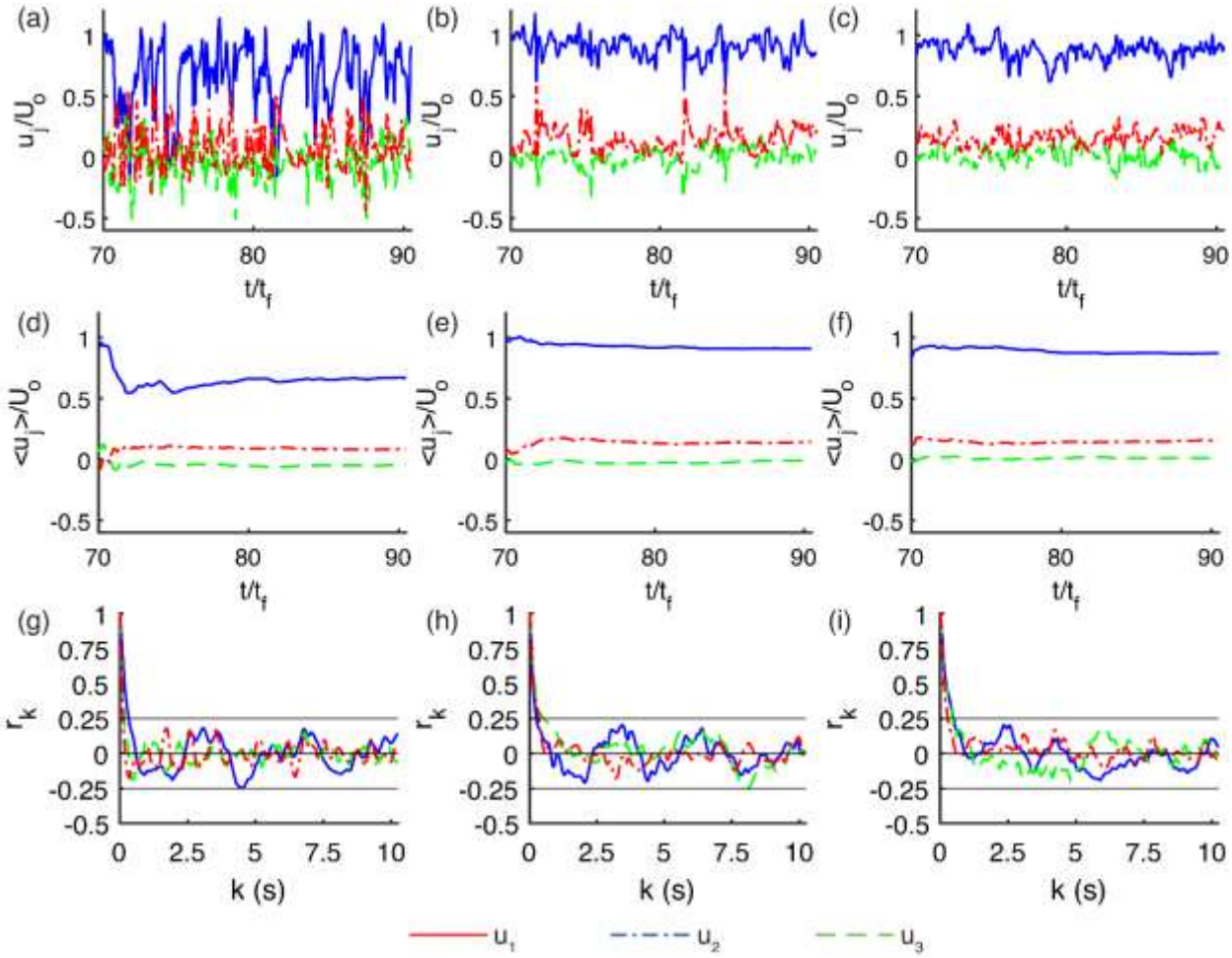

Figure 5.3 (a)–(c) Instantaneous u_j values for run D1 at three selected locations, marked as green squares in Figure 5.1(c); (d)–(f) cumulative average $\langle u_j \rangle$ corresponding to (a)–(c), respectively; (g)–(i) autocorrelation function r_k for time lag k corresponding to (a)–(c), respectively. The coordinates of the locations for panels (a)–(c) are $(x_1/b_1, x_2/L, x_3/h_o)$ = (0.18, 1.44, 0.83), (0.53, 1.51, 0.83), (0.96, 1.66, 0.83)

5.3.2 Instantaneous velocity

Runs D1–P2 output instantaneous u_j, p, and η values, following a spin-up period of $56t_a$ (long enough to ensure fully developed turbulence). As an example, instantaneous u_j values from three selected cells for run D1 are plotted (Figures 5.3(a)–5.3(c)) as a time series. The time was

normalised using t_f, which is a time scale related to the fluctuation frequencies of energy-bearing eddies larger than those in the inertial subrange. The value of t_f was determined from the cut-off frequency indicated by the dashed line in Fig 4(a). The inertial subrange is to the right of this dashed line. The maximum value (about 1 s) of t_f was used for normalisation.

In Figures 5.3(a)–5.3(c), it is shown that the primary flow was stronger than secondary flow, i.e., $|u_2| \gg |u_1|$ and $|u_2| \gg |u_3|$, as expected. The data series of both u_1 and u_3 had a nearly zero mean. The primary flow had a reverse velocity as large as $0.2U_o$. The data series of u_1, u_2 and u_3 all exhibited significant fluctuations; u_2 had larger RMSDs, with a maximum of $0.25U_o$.

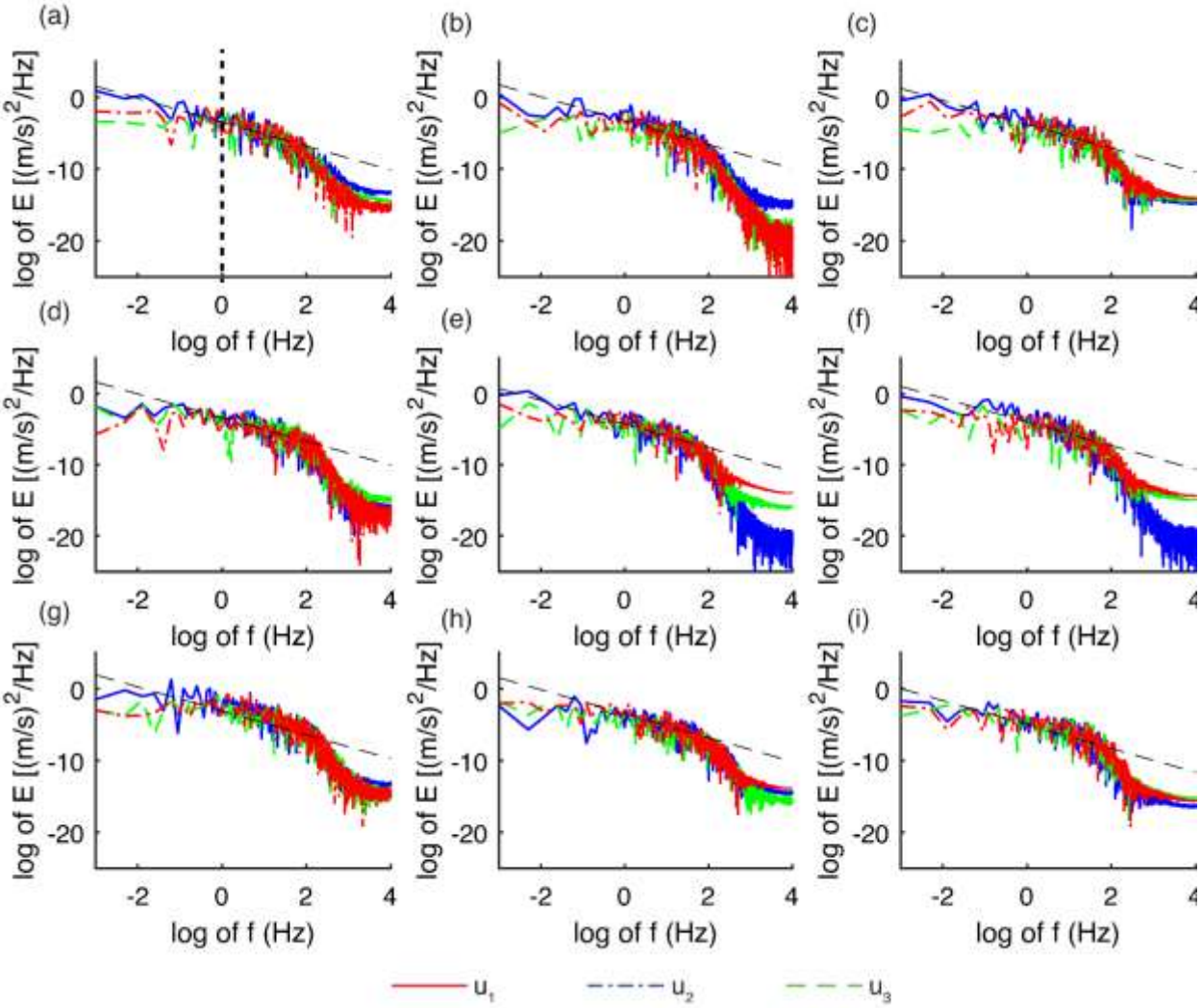

Figure 5.4 Velocity spectral densities $E_{u_iu_i}$ of u_i for run D1 (Table 5.1): (a)–(i) for the nine locations marked as green squares in Figure 5.1(c). Panels (g)–(i) correspond to Figures 5.3(a)–5.3(c), respectively

We examined a near-bed plane and noticed stronger fluctuations near the left sidewall, compared to those at the middle and those near the right sidewall (Figure 5.1(c), green squares). Near the water surface, u_2 near the left sidewall had a mean of $0.64U_0$, much smaller than $0.86U_0$ at the

middle and than $0.83U_0$ near the right sidewall, although the left sidewall location is in a narrower section closer to the transition entrance.

5.3.3 Validation of computed turbulence using a benchmark solution

The Kolmogorov −5/3 law is a well-established spectral distribution of turbulent energy in the inertial subrange (Kolmogorov, 1941). This study used the law as a benchmark solution for validating LES predictions. We extracted data series of instantaneous velocities over a period of 10 s from the predictions for a series of cells and carried out a Fourier analysis of the data series. Examples of output velocity spectral density, E, from the analysis are plotted in Figure 5.4. The distributions show a typical energy spectrum for a turbulent flow, the existence of energy containing eddies and a well-fitted −5/3 slope (dashed lines) in the inertial subrange. We conclude that the LES runs properly resolved a major part of turbulence energy and captured the cascading of energy to smaller eddies.

5.3.4 Data samples from LES output

Averaging instantaneous LES output is needed for practical use of LES results. What is the required minimum length of data series or minimum sample size? We answer this question by evaluating the accumulative average $\langle u_i \rangle$ and the autocorrelation function r_k over a time period T elapsed following a spin-up period t_0. Examples of $\langle u_j \rangle$ are plotted in Figures 5.3(d)–5.3(f). Take as an example t/t_f = 80 in Figure 5.3(d). $\langle u_i \rangle$ was the average of 1000 instantaneous u_i values from t/t_f = 70 to 80. At $t/t_f \geq 80$, $\langle u_j \rangle$ changed very little. This is true for other locations in the model channel. Thus, $10t_f$ or 10 s is suitable for ensemble averaging, corresponding to sample size N = 1000.

We confirmed the suitability by further calculating r_k. Examples of r_k values are plotted in Figures 5.3(g)–5.3(i). If two quantities separated by k are essentially uncorrelated, the selected number of ensembles N is sufficient and suitable for averaging (Box et al., 2015). r_k measures the correlation between the univariate data series u_i at time t and u_i at time $t + k$, where k increases from 0, …, 10 s. The wavy curves (Figures 5.3(g)–5.3(i)) fluctuated in wavelength and amplitude, depending on the direction and location. However, they had some common features $r_k = 1$ at $k = 0$ due to a perfect self-correlation;r_k decayed with increasing k from zero and became bounded by ± 0.25 for $k > 1$ s. The curves oscillated within a range of small values for $k > 5$ s. The oscillations might be associated with the Hurst phenomenon (Dimitriadis et al., 2021; Meneveau & Sreenivasan, 1991; Nordin et al., 1972). These low values of r_k toward $k = 10$ s mean that the instantaneous velocities separated by a 10 s time span were uncorrelated. The preceding discussion served the purpose of confirming the suitability of using 10 s for averaging.

Hereinafter, data sampling from LES output started after the spin-up period (or $t > t_0$) at a sampling frequency $f = 100$ Hz and continued until $N = 1000$. In summary, the sampling time duration is $t_N = 10$ s. This choice is justified on the following grounds: $t_N > t_f$ by an order of magnitude; t_N is 8 times the advection time scale t_a; the cumulative average of velocity supports the choice $t_N = 10$ s; the sufficiency of $t_N = 10$ s is manifested in the autocorrelation function. The ensemble-averaged quantities presented hereinafter use $N = 1000$.

Note that in a large water body, turbulent motions can contain slow oscillations at large scales. To capture such oscillations, the sampling time duration needs to be longer. For example, Soulsby (1980) and Walter et al. (2011) used t_N as long as 8–12 minutes for oceanic motions in order to capture the desired turbulent length scales and obtain quasi-stationary statistics.

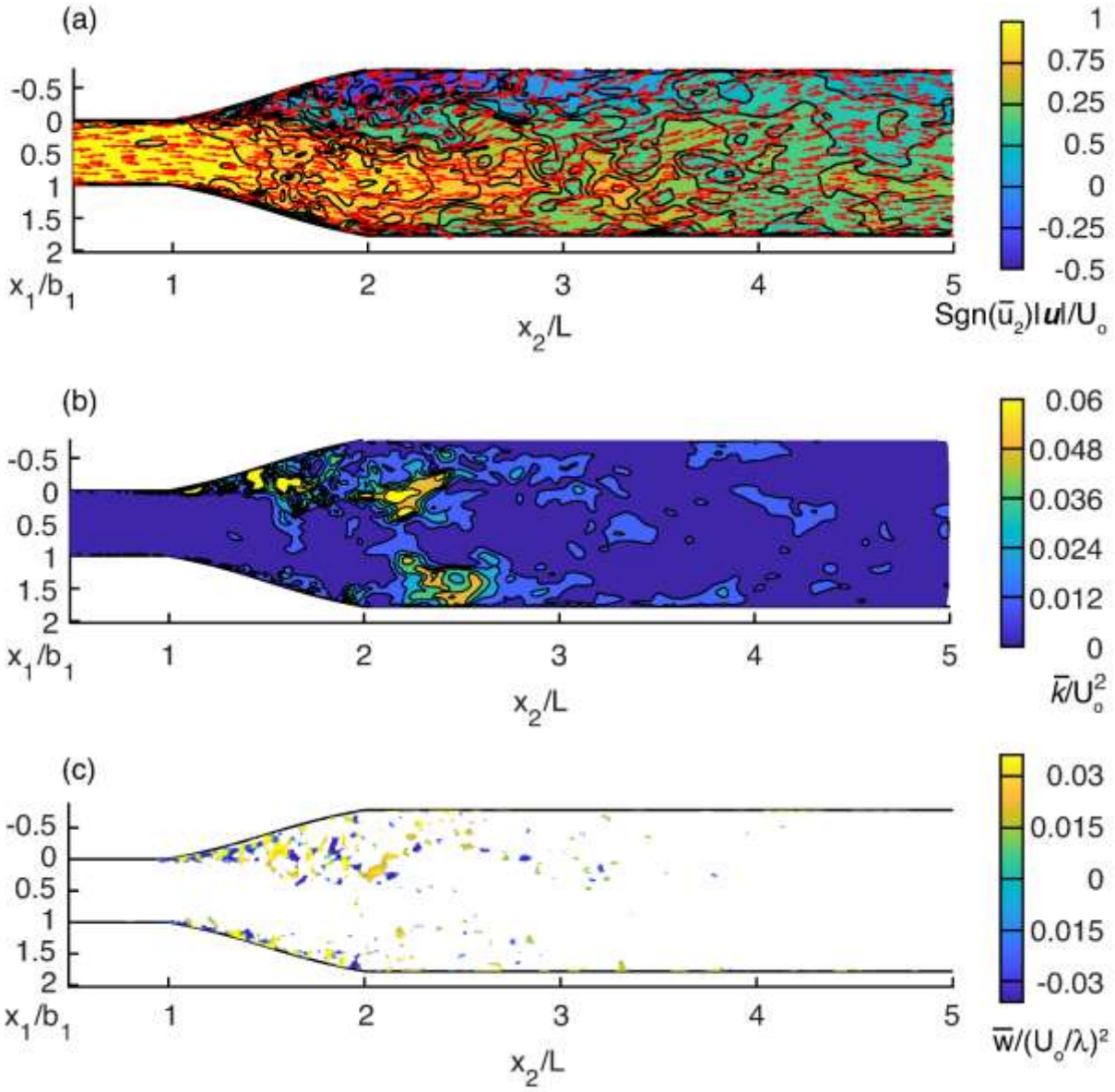

Figure 5.5 Horizontal plane $x_3 = 0.47h_o$, showing the distributions of ensemble-averaged: (a) horizontal velocity vector $\boldsymbol{u}$ for run E1; (b) TKE $\bar{k}$ for D3; (c) Okubo-Weiss parameter $\bar{w}$ for D3

5.3.5 Ensemble-averaged flow field

We investigated the distributions of ensemble-averaged horizontal velocity vector, $\boldsymbol{u}$, by selecting three horizontal planes $x_3/h_o = 0.06, 0.47, 0.83$ (near-bottom, mid-depth, near-surface). In Figure 5.5(a), an example of $\boldsymbol{u}$ distributions, together with contours of normalised $|\boldsymbol{u}|$, is shown. For a given location, the sign function $\mathrm{Sgn}(\bar{u}_2)$ assigns a plus (minus) sign to the magnitude if $\bar{u}_2 > 0$ ($\bar{u}_2 < 0$). A positive (negative) magnitude means flow in the positive (negative) x_2-

direction. Before the entrance ($x_2 < L$), $\bar{u}_2$ was zero at the sidewalls and increased rapidly within a small wall-normal distance. After the entrance ($x_2 > L$), the flow separated, mainly along the left sidewall, having one recirculation zone and persisting a long distance. In the transition, the primary flow had a strong core, deflecting from the centreline to the right (to an observer facing downstream). The strongest velocity magnitude was $|\boldsymbol{u}| = 1.15U_o$. The primary flow velocity was asymmetrical about the channel centreline.

The distributions displayed complex 3-D flow structures. The near-bottom flow had small pockets of strong velocities in the transition and nearby regions. There was a hysteresis of the occurrence of separation; the further away from the water surface, the further to the transition entrance. The near-surface flow separated in the transition along both sidewalls and triggered eddies in both flanks. The reverse flow had a maximum magnitude of $-0.46U_0$.

Extending the upstream section length (from $L_u/h_o = 2.67$ for run D1 to 8 for run D3, Table 5.1) improves the accuracy of first- and second-order statistics of turbulence, as will be demonstrated later. Here, we compared the distributions of ensemble-averaged TKE $\bar{k}$ in the aforementioned three selected horizontal planes. An example of the distributions is shown in Figure 5.5(b). In the transition, compared to near-surface and near-bottom, the mid-depth $\bar{k}$ had large values, with a maximum of $0.11U_o^2$ (Figure 5.5(b)). Large pockets of strong $\bar{k}$ occupied the core of recirculation zones in the left flank. Near the surface, many small pockets of strong $\bar{k}$ flanked a strong-velocity core, within which the magnitude of $\bar{k}$ was relatively weak. Near the bottom, there were pockets of weak magnitude $\bar{k}$ in the two flanks due to the proximity of channel boundaries.

We quantitatively located turbulent eddies using the Okubo-Weiss parameter $\bar{w} = s_n^2 + s_s^2 - \omega_3^2$, where s_n is the normal strain component, s_s is the shear strain component, and ω_3 is the relative vorticity. Horizontal areas of $\bar{w} < -w_o$, where w_o is a certain threshold, are dominated by eddies, with a core in the local minima of $\bar{w} < 0$. The areas exhibit large vorticity and strong circulation density of the velocity field. Areas of $\bar{w} > w_o$ are dominated by strain. Areas of $-w_o \leq \bar{w} \leq w_o$ have background vorticity and strain. We chose $w_o = 0.2\sigma_w$, where σ_w is the standard deviation of $\bar{w}$ values in the flow area. For more details, refer to Zeng and Li (2022).

As an example, contours of normalised $\bar{w}$ for D3 are shown in Figure 5.5(c). The normalisation used an eddy length scale $\lambda = 3(\Delta x_1 \Delta x_2 \Delta x_3)^{1/3} \approx 0.02$ m. Eddies larger than λ can be discerned from the computed flow field. For D3, Re $= 13572$ based on U_o and λ; $\sigma_w = 14, 15, 12$ for the aforementioned three horizontal planes.

In the transition, a string of strong alternating eddy and strain pockets originated near the transition entrance and developed along the left- and the right side of the core of strong velocity (Figure 5.5(a)). These eddies and strains were coherent turbulence structures and local-scale flow features. The string on the left side traced a meandering path, whose cross-stream amplitude increased as eddy patterns developed toward downstream. At the transition exit, the cross-stream amplitude of the eddy patterns had length scales comparable to b_1. The patterns' development was accompanied by the weakening of local rotations.

After the transition, local rotations persisted longer near the surface than near the bottom and diminished at about $x_2/L = 4.8$. The string on the right side virtually hugged the sidewall, with

little cross-stream shifting of eddy positions at the mid-depth (Figure 5.5(c)). This was not the case near the bottom and near the surface, where the cross-stream amplitude increased slightly.

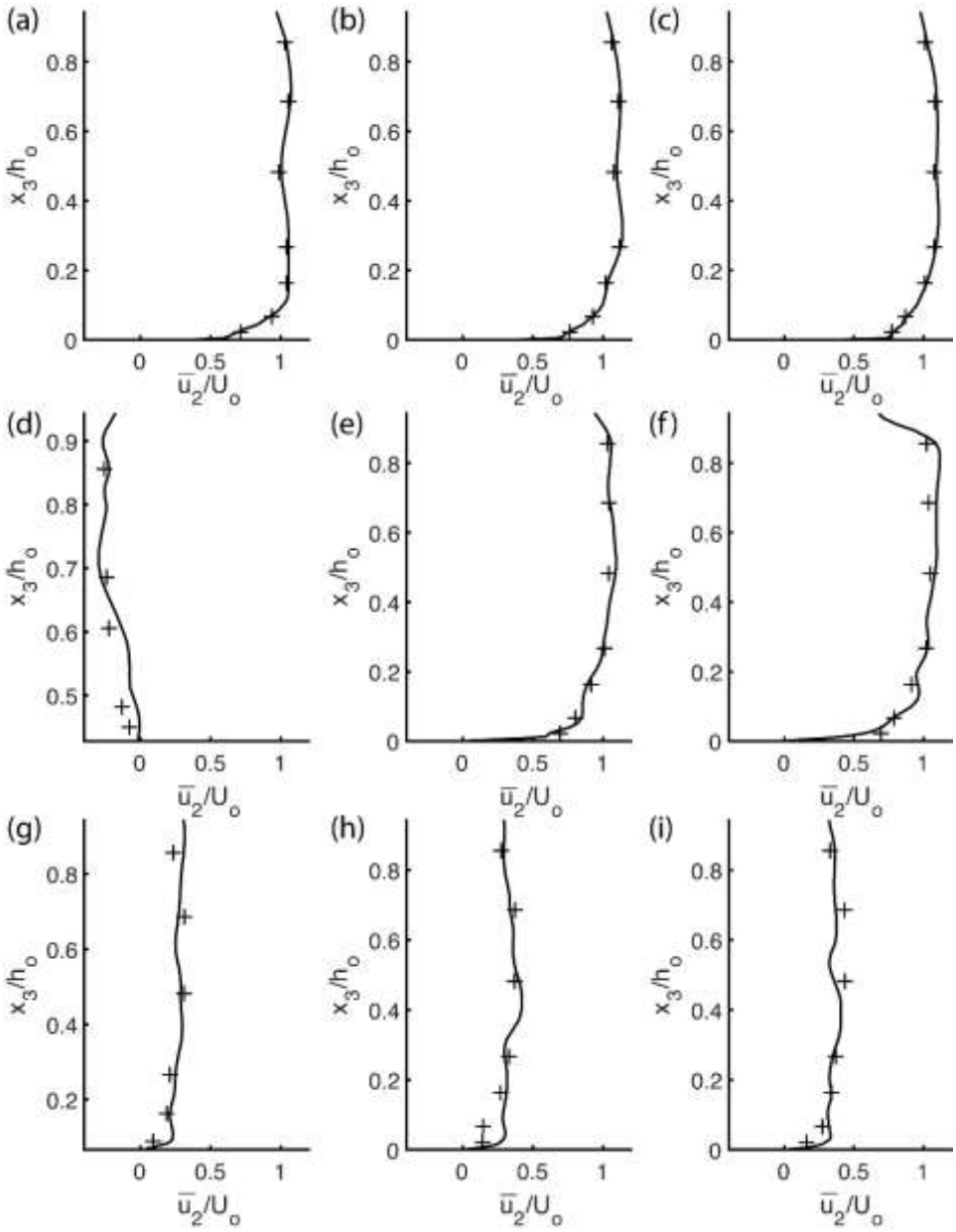

Figure 5.6 Vertical profiles (—) of $\bar{u}_2$ for E1 at: (a)–(i) nine locations, marked by the red multiplication signs in Figure 5.1(c). The data (+) from Ramamurthy *et al.* (2017) are shown for validation

5.3.6 Validations of ensemble-averaged flow using experimental data

Vertical profiles of ensemble average $\bar{u}_2$ from nine (x_1, x_2) locations are plotted in Figure 5.6. The velocities were strong near the surface and decayed toward the bottom. The profiles compared well with experimental data. The computed values correlated well with the experimental values, with the correlation coefficient $r \approx 1$ and a small *RMSE* $\delta\bar{u}_2$. The relative *RMSE* was as small as 0.01 before the transition, about 0.06 in the transition, and below 0.08 after the transition. We accurately

predicted strong reverse flow (Figure 5.6(d)), with a small relative *RMSE* (equal to 0.07). For a large number of locations (Figure 5.1(c), the solid dot symbols), the overall average of the *RMSE* is $0.17U_o$. Some of the profiles (Figure 5.6) show a maximum velocity below the water surface and relatively large variability. The below-surface maximum velocity can be explained by the velocity dip phenomenon (Tominaga et al., 1989). The large variability is due to the transition impact.

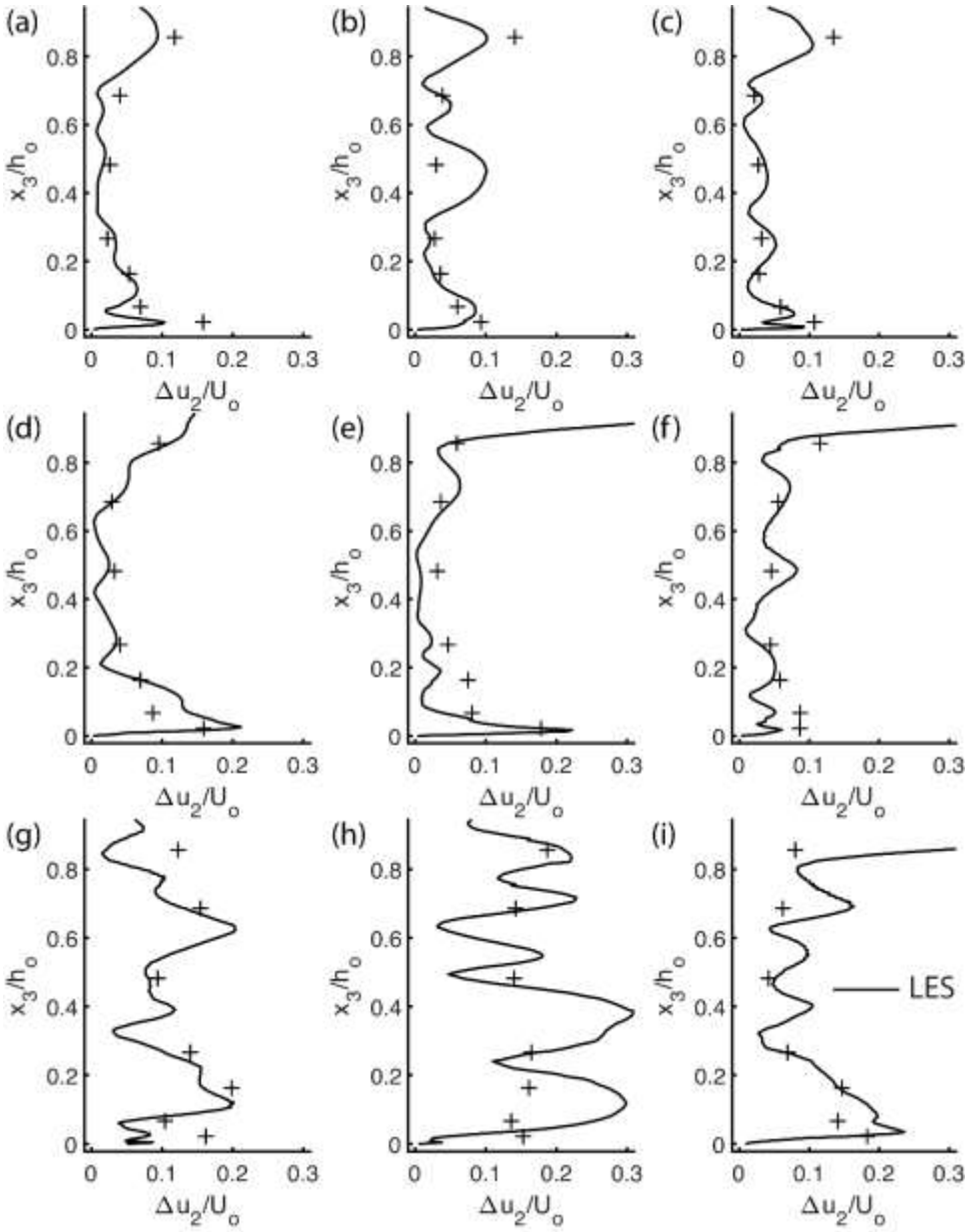

Figure 5.7 Vertical profiles (—) of computed Δu_2 for run E1 at: (a) – (i) nine locations, marked by the blue circles in Figure 5.1(c). The data (+) from (Ramamurthy et al., 2017) are shown for validation

Vertical profiles of Δu_2 from nine locations are shown in Figure 5.7. The computed values of Δu_2 had an acceptable comparison with experimental values. The relative *RMSE* was about 0.08 for

the profiles before the transition (Figures 5.7(a)−5.7(c)). For some locations after the transition, the computed values had relatively large *RMSE*. For example, in Figure 5.7(i), relative *RMSE* was 0.20, but the computed Δu_2 profile showed the same magnitude of fluctuations as the experimental data points. The fluctuations were more profound after the transition (Figures 7(g)–7(i)) than before the transition (Figures 5.7(a)−5.7(c)). This means that the transition contributed to the growth of turbulence and gave rise to very large Δu_2. This is particularly true near the surface in the transition (Figures 5.7(d)−5.7(f)). Overall, the LES results are acceptable in terms of second-order turbulence statistics.

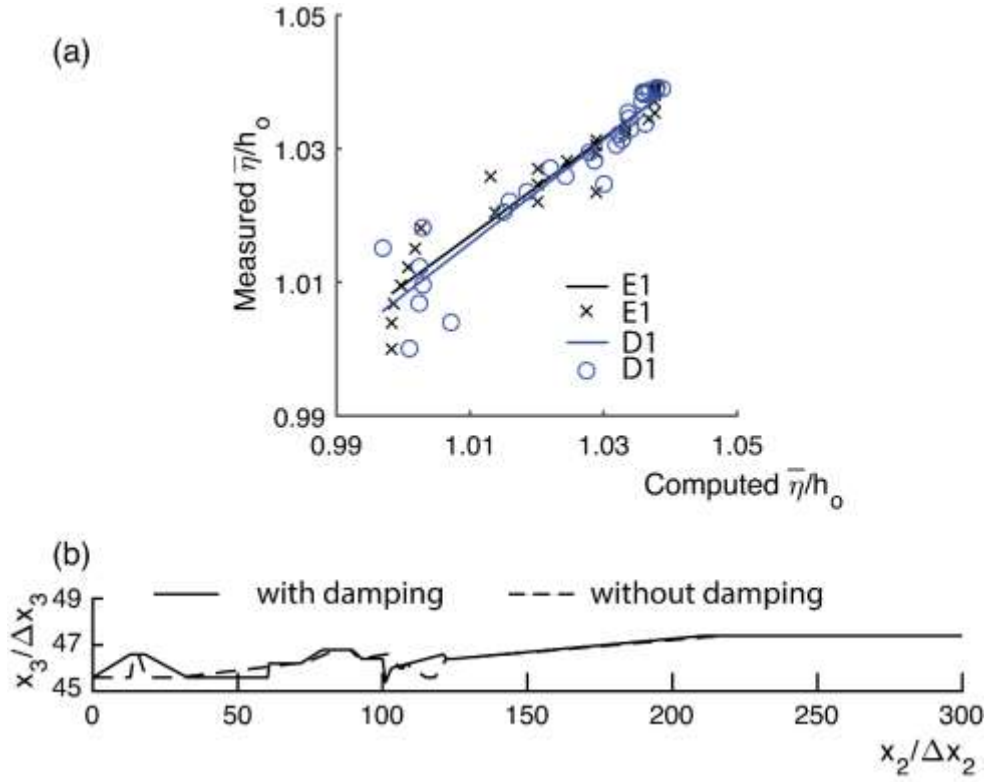

Figure 5.8 (a) Comparison of computed ensemble-averaged free-surface elevations with experimental values at a series of x_2 locations. (b) Comparison of computed instantaneous free-surface profiles along the channel centreline at $t/t_a = 64$ between runs E3 and E4, which are without and with NBT, respectively (Table 5.1)

The ensemble-averaged free-surface positions $\bar{\eta}$ at 30 x_2 locations along the channel centreline for runs E1 and D1 are compared with experimental values in Figure 5.8(a). The relative errors of the computed values for the two runs are below 1.5% and 1.7%. The maximum error occurred near the transition entrance at $x_2/L = 1.16$ for run E1 and at the entrance for run D1. Run D1 used the 1/7th law to give inlet mean-flow condition, whereas run E1 used experimental data (Table 5.1). The computed values correlated well with the experimental values, with the coefficient of correlation $r > 0.9$. All the runs (Table 5.1) gave acceptable values of $\bar{\eta}$.

5.3.7 Discussion of the quality of primary flow predictions

The hit-rate h_r and a factor of two F_2 (Okaze et al., 2021) are useful for assessing the quality of alternative LES setups, parameters, and assigned parametric values. The better the predicted values

of a flow variable compared with measured values, the higher the h_r and F_2 scores. The quality is acceptable (i.e., the prediction is in reasonable agreement with the measurement, which is the goal) if $h_r \geq 2/3$ and $F_2 > 1/2$. A short description of the metrics is given below. Let M_1, M_2, …, M_n denote n measured values of $\bar{u}_2/U_o$ from experiments, and C_1 , C_2 , …, C_n denote the corresponding computed values. The validation metrics are expressed as: $h_r = (\Sigma n_i)/n$, where $n_i = 1$ if $|C_i/M_i - 1| \leq \delta$ or $|C_i - M_i| \leq \omega$ and $n_i = 0$ otherwise, δ is an allowed relative deviation, and ω is an absolute deviation; $F_2 = (\Sigma n_i)/n$, where $n_i = 1$ if $0.5 \leq |C_i/M_i| \leq 2$ and $n_i = 0$ otherwise. According to Schatzmann et al. (2010), $\delta = 0.25$. The threshold ω is 0.20 for $\bar{u}_2$ and 0.06 for Δu_2, as estimated following previous studies. Table 5.1 lists the scores for the runs, which are based on comparisons with 1184 measured values of streamwise velocities, lumped together from the 11 dotted cross sections in Figure 5.1(c). The scores are interpreted as follows:

About initial condition, the uniform u_2 distribution (for run D5) is unsatisfactory because both scores are out of acceptable range. A plausible reason is that the turbulence development is history-dependent, as demonstrated in Zeng and Li (2022). Once established, the flow tends to hug left or right wall, depending on the flow history. In the broad sense, the initial condition used in a LES should reflect the flow history of the experiment in question. Either the initial condition 'L' or 'S' does in this study.

For inlet mean-flow, a 1/14th power-law (for run D4) is unsatisfactory because the h_r score is too low. A 1/7th law (for D3) achieves acceptable scores. In fact, this law is a good approximation of turbulent boundary-layer profiles at high Re, as is the case in this study. Also, the 1/7th law is easier/more efficient to implement than the well-established logarithmic law.

Extending the upstream section length to eight times the depth (for run E9) from 2.67 times (run E1) improves scores. In particular, the extension improves the prediction accuracy of second-order turbulence statistics. It is worth mentioning that the extension increases computational nodes by 7% and computing time by 37% in this study. For similar LES problems of free-surface turbulence, we recommend an adaption length of about eight times the depth, when the inlet conditions reflect the real flow reasonably well. Some previous researchers suggest an adaptation length of three to four times the building height in airflow problems.

VM (for run D1) slightly improves scores over SS (for run D6), when the generated ITF is superimposed on a mean-flow profile (given by e.g., a 1/7th law) that is laterally uniform in the absence of secondary flow and eddy motion. VM generates stronger ITF than SS, for the same values of input parameters (T' and D). VM is more reliable to build secondary eddies and associated rotations, represent secondary flows of Prandtl's second kind, and cause velocity shear. Similar discussion is given in previous LES studies of airflow turbulence (Thordal et al., 2019).

For the first time, this study explores mapping 3-D inlet mean-flow from experimental data. In this new case, SS seems slightly better than VM, as indicated by comparing run E2 to run E3, run E6 to run E5, and run E8 to run E7. Plausible explanations are that the mapped velocity already contains secondary flow eddies, and it becomes less critical or even redundant to add turbulent eddies from VM. The same redundance does not occur to SS because it yields little influence on secondary velocity.

All the three SGS stresses models: DSM, WALE and DKE (for runs E1, E5 and E7) enjoy similar degree of success. This is regardless of whether T' combined with l or with D is used as parameters, as can be seen from comparing run E3 to run E5. The most likely reason is that the mesh for the runs resolves all the important large eddies. The SGS model for smaller eddies has no critical influence on the LES output.

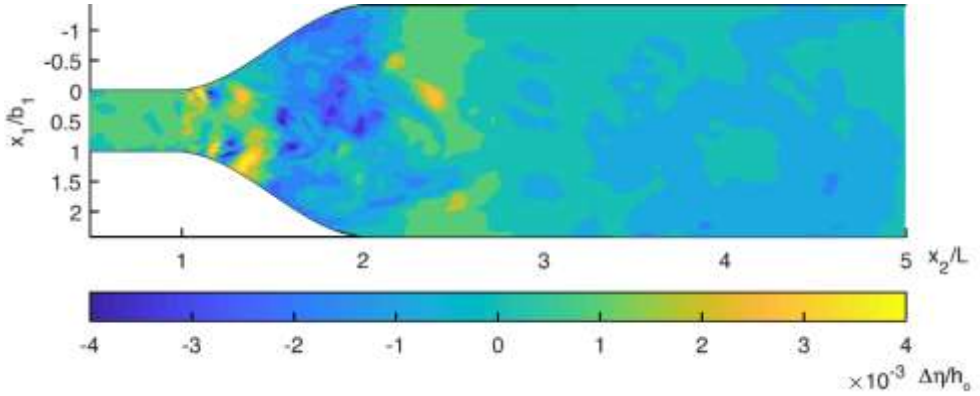

Figure 5.9 Deviation, $\Delta\eta$, of the instantaneous free surface ($\alpha_2 = 0.5$) at $t/t_a = 120$ from the ensemble-averaged free surface over a period of $8t_a$ for run D3

One way to avoid possible wave reflections from the outlet is to implement NBT (for runs D2 and E4). The scores for runs D2 and E4 are close to those for runs D1 and E3. Thus, it is not critical to use NBT. No waves with an amplitude larger than $2\Delta x_3$ appear in the domain (Figure 5.9). Smaller ripples exist before the transition and in the transition. The wavelength is about $30\Delta x_2$. The ripples in the transition are due to a rapidly expanding width. The steepness is very small ($< 3 \times 10^{-2}$). No ripples fluctuate at a time scale comparable to the time step Δt. The free surface overlaps after $x_2/\Delta x_2 > 130$ between runs E3 and E4 (Figure 5.8(b)). Thus, there are no significant reflections, true as well for runs D1 and D2.

It is constructive to discuss the h_r and F_2 scores for cross sections (CSs) in different zones (Figure 5.1(c)). For the three CSs in zone 1 before the transition (Figure 5.1(c)), the scores (> 0.95) are much better for runs E1–E8 than runs D1–D6, due to the fact that runs E1–E8 map inlet mean-flow from 3-D experimental data, preserving the observed flow behaviour before the transition. The scores are not as high just after the transition to some distance downstream ($x_2/L = 2.49$). The influence of the inlet condition on the local flow behaviour weakens and that of separation strengthens, and it is more challenging to accurately predict the behaviour of stronger separated flow.

After the transition, the scores for zones 2, 4 and 6 are good when the upstream section length is eight times the depth (for run D3). The scores change little by using NBT, which is clear from comparing run E4 to run E3 and run D2 to run D1. It is difficult to achieve high scores for zones 4 and 5, where separation is vigorous. The F_2 scores barely pass the acceptable threshold for almost all the runs in Table 5.1. The h_r score is below the acceptable threshold for zone 6 when using 3-D experimental data to give inlet mean-flow and VM to generate fluctuations (for runs E1, E3–E5, and E7).

The recommended length of an upstream channel section of eight times the flow depth has practical implications. In the studies of Nashta and Garde (1988) and Shettar and Murthy (1996), the depths are, respectively, 0.059−0.12 m and 0.05–0.06 m. The corresponding recommended lengths are 0.47−0.96 m and 0.4−0.48 m. In Chow (1959), the flume-to-canal expansion has a depth of 1.15 m, the recommended length being 9.2 m. For a concrete siphon expansion with a design depth of 1.25 m (Hinds, 1928), the recommended length is 10 m. This study provides some guidelines for the practical choice of channel lengths.

5.3.8 Limitation and strategies for improvement

For those runs where SS was used to generate inlet velocity fluctuations, the LES methods give underestimations of RMSD Δu_2 in the upstream channel before the expansion, when compared to measured values on a point-to-point basis. Improvement can be achieved by mapping inlet mean-flow from experimental data of 3-D velocity, combined with VM (for runs E1, E5 and E7). The issue is that such data is often not available in many cases. An alternative is to use a 1/7th power-law together with extended approach section length (for run D3) or a precursor simulation. One limitation is excessively high computing costs. Future work should investigate the influence of varying downstream channel length on LES results.

For improvement, the conditions for run E9 duplicates those for run E1, except that the upstream section length is $3L$ and the flow field from run D3 provides initial condition. Run E9 lasts for $64t_a$. For the precursor run P1, run E1 continues for $64t_a$, with output at each timestep from the plane x_2/L= 0.89 (Figure 5.1(c)). The output gives inlet conditions for run P1 over a period of $64t_a$. The conditions for run P2 differ from those for run P1 in that the instantaneous inlet velocities are reconstructed as

$$u_i = \Delta u_i \times rand(8000, 1) + \bar{u}_i \tag{5.4}$$

where rand is a random function; $\bar{u}_i$ and Δu_i are, respectively, the measured mean velocities and standard deviations from the plane $x_2/L = 0.89$. The reconstruction gives 3-D velocities at each time over a period of $64t_a$. Runs P1 and P2 use instantaneous inlet velocities at each time. Therefore, there is no need to superimpose turbulence. The h_r and F_2 scores of RMSD Δu_2 and $\bar{u}_2$ for runs E9, P1 and P2 are satisfactory for most locations of the LES domain. Note that Eq. 5.4 draws random floating-point numbers from a normal distribution.

5.3.9 New contributions

This study has made unique contributions in two aspects. First, the two-phase flow with a free surface advances from the commonly used rigid-lid approximation. Free-surface variations are important to non-prismatic channel design. Second, the combination of cumulative averaging, autocorrelation and spectrum analysis is an improved method for determining the sample size for ensemble averaging. It avoids trial-and-error and is more efficient and accurate, compared to the traditional method of trying different averaging time.

The Okubo-Weiss parameter is a new alternative to visualize eddy structures. Isosurfaces of $w < -w_0$ represent rotation-dominated regions. The patterns are similar to those using the Q or the λ_2 criterion. However, this parameter has the advantage that w has a definite threshold w_o. Compared to λ_2, w has a physical meaning. For an incompressible flow, $w = 4\lambda_2$ if the vertical velocity is asymptotically small. Distributions of 3-D instantaneous *w* at two different timesteps are illustrated in Figure 5.10, showing strong eddies in the transition. Strong eddy-dominated regions also appear

downstream. The parameter clearly delineates instantaneous coherent structures emerging at the transition entrance and evolving downstream. The structures are particularly relevant to channel erosion assessment. The Q-criterion and λ_2-criterion involve more than one user-defined threshold value.

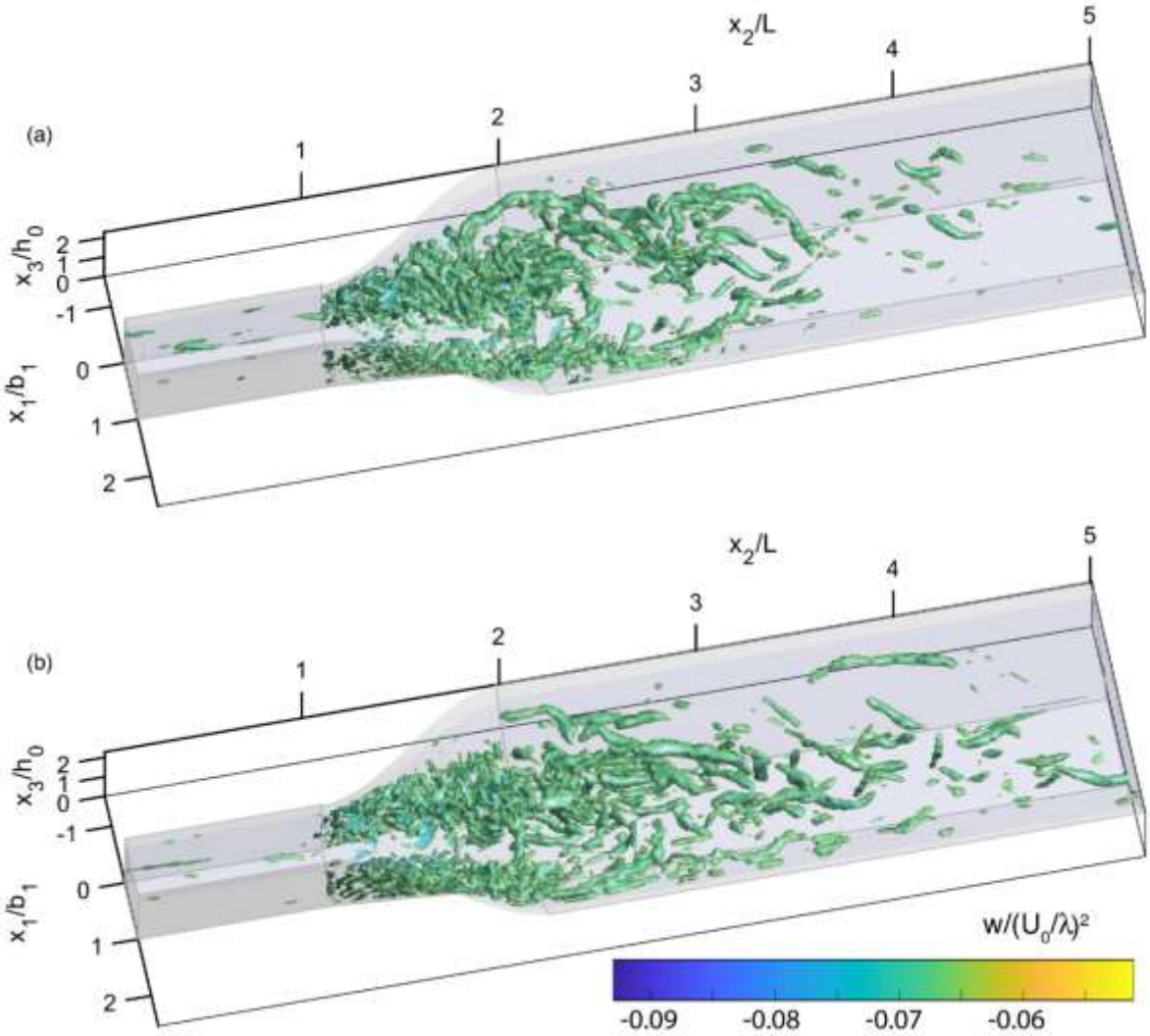

Figure 5.10 Isosurfaces of w for run D3, showing vortex structures at time: a) $t/t_a = 72$; b) $t/t_a = 80$

5.4 Summary and conclusions

In this study two-phase LES of turbulent flow is simulated in a non-prismatic open channel. The significance of this work lies in progressively exploring strategies for LES model setup, selection of proper parameters and parametric value assignments. We validate the LES predictions using experimental data and benchmark solution. The validated strategies can be used to study turbulence under other similar conditions with good accuracy. We show the practical results exerted from this study, which are related to the velocity distributions, spectral distribution of flow energy, and hit-rate for validations in other similar studies.

This study reveals 3-D complex turbulence structures in the non-prismatic channel, as a result of processes mingled together, involving eddy motions translated from upstream and locally generated by asymmetrical separation. It also reveals the influence of flow history on the turbulence development. One implication is that there may be a need to test a subtle approach to specify the initial conditions in a two-phase LES. This newly recognised challenge has not yet received much attention in the literature.

We show that mapping mean velocity distribution from measurements, combined with the spectral synthesiser approach to velocity fluctuations, gives satisfactory inlet conditions. An alternative is a 1/7th power-law, combined with the vortex method. To improve the prediction and control of turbulent behaviour, we recommend to adopt a channel length of eight times the depth of the channel.

For the first time, we report TKE and coherent turbulence structure in a non-prismatic channel. The practical significance is that the former is of relevance to turbulence control and hydraulic efficiency improvements, whereas the latter helps address channel erosion and instability risks.

6 Supplemental material

6.1 Definition of certain parameters

Suppose that for a given cell of the LES model domain, an instantaneous flow variable, z, has N instantaneous values: z_1, z_2, …, z_n, …, z_N. N is known as the sample size. The ensemble average of z is calculated as

$$\bar{z} = \frac{1}{N}\sum_{n=1}^{N} z_n \tag{S1}$$

If Eq. S1 is applied to the velocity component u_i, pressure p, water surface elevation h, or turbulence kinetic energy k, the results will be ensemble averages, denoted by $\bar{u}_i$, $\bar{p}$, $\bar{\eta}$, and $\bar{k}$, respectively.

The root-mean-square-deviation (RMSD) of z is calculated as

$$\Delta z = \sqrt{\frac{1}{N}\sum_{n=1}^{N}(z_n - \bar{z})^2} \tag{S2}$$

where $\bar{z}$ is given in Eq. S1. If Eq. S2 is applied to velocity components, pressure, water surface elevation or turbulence kinetic energy, the results will be RMSDs, denoted by Δu_i, Δp, $\Delta \eta$, and Δk, respectively.

In this study, we distinguish root mean square error (*RMSE*) from RMSD. Suppose that the flow variable, z, has M ensemble-averaged values: $\bar{z}_1$, $\bar{z}_2$, …, $\bar{z}_n$, …, $\bar{z}_M$, from a large eddy simulation, where M may refer to different cells, and that there are M corresponding observed values: O_1, O_2, …, O_m, …, O_M from a laboratory experiment. The *RMSE* is calculated as

$$\delta \bar{z} = \sqrt{\frac{1}{M}\sum_{m=1}^{M}(\bar{z}_m - O_m)^2} \tag{S3}$$

where $\bar{z}_m$ is calculated using Eq. S1. If Eq. S3 is applied to velocity components, pressure, water surface elevation or turbulence kinetic energy, the results will be *RMSE*s, denoted by δu_i, δp, $\delta \eta$, and δk, respectively.

The accumulative average of z is calculated as

$$\langle z \rangle = \frac{1}{T}\int_{t_0}^{t_0+T} z dt \tag{S4}$$

where T is a time duration elapsed following a spin-up period t_0. If Eq. S4 is applied to velocity components, pressure, water surface elevation or turbulence kinetic energy, the results will be accumulative averages, denoted by $\langle u_i \rangle$, $\langle p \rangle$, $\langle \eta \rangle$, and $\langle k \rangle$, respectively.

6.2 Common SGS models and ITF methods

The Smagorinsky-Lilly model (SL), the Wall-Adapting Local Eddy-viscosity Simulation (WALES) model, the Dynamic Smagorinsky model (DSM), and the Dynamic Kinetic Energy (DKE) model are all turbulence closure models used in computational fluid dynamics (CFD) simulations (Pope, 2001; Rodi et al., 2013; Wilcox, 2006).

The SL turbulence model:

- is commonly used as a baseline for other turbulence models.
- assumes eddies are isotropic and that eddy viscosity is proportional to the square of the local strain rate. However, a fixed eddy viscosity can lead to failures in regions where the turbulence is highly anisotropic.
- is not suitable for simulating complex flows that involve significant turbulence interactions, such as those found in flows with large-scale vortices, shocks, or separations.

The WALES Model:
An improvement on the SL model

- accounts for the presence of walls in the simulation domain
- uses a modified version of the Smagorinsky eddy viscosity model that is adapted to the local wall distance.
- provides better accuracy in wall-bounded turbulent flows

The DSM:

- uses a dynamic procedure to calculate the eddy viscosity coefficient
- allows for better accuracy in regions of the flow where the flow is highly anisotropic

The DKE:

- based on the transport equation for the kinetic energy of the turbulent fluctuations
- uses a dynamic procedure to calculate the eddy viscosity coefficient, similar to DSM

The ITF methods SS and VM are introduced further is this section (Mathey et al., 2006; Rodi et al., 2013; Smirnov et al., 2001).
Spectral Synthesizer (SS):

- yields fluctuating velocity components by synthesizing a divergence-free velocity-vector field from the summation of Fourier harmonics
- solves the Navier-Stokes equations in a Eulerian framework
- creates a divergence-free field for homogeneous turbulence and is approximately satisfactory for inhomogeneous turbulence
- uses 100 Fourier harmonics for computation by default
- requires prior knowledge of turbulence intensity, eddy-to-molecular viscosity ratio, length scale, hydraulic diameter, or turbulence kinetic energy and turbulent dissipation rate

Vortex Method (VM):

- produces turbulent fluctuations by superimposing coherent structures of given shape, length and time scales and superimposes a fluctuating vorticity field on the mean flow
- solves the Navier-Stokes equations in a Lagrangian framework
- computes the transverse component of velocity using the Biot-Savart law and the streamwise component based on the influence of the 2-D vortex in the inflow plane through a linear kinematic model
- each vortex has a characteristic time of existence and undergoes a random walk within the plane to add unsteadiness, mimicking coherent turbulent eddies

- provides both temporal and spatial correlations
- uses 190 vortices for computation, which doesn't significantly affect simulation accuracy
- requires prior knowledge of turbulence intensity, eddy-to-molecular viscosity ratio, length scale, hydraulic diameter, or turbulence kinetic energy and turbulent dissipation rate.

6.3 Parameters to characterize the open-channel flow behaviour

A summary of relevant parameters is given in table 6.1.

Table 6.1 Summary of parameters

Parameter	Definition	Application
Energy coefficient α	$\alpha = \rho/2 \int_A V^3 \, dA$, where V cross-sectional average velocity, A is the cross-sectional area	Evaluating the flow uniformity at a cross-section
Momentum coefficient β	$\beta = \rho \int_A V^2 \, dA$, where V cross-sectional average velocity, A is the cross-sectional area	Evaluating the flow uniformity at a cross-section
Reynolds number Re	Re = $U_o h_o / \nu_2$, where ν_2 is the viscosity of water, h_o is the inlet water depth and U_o inlet mean velocity	Characterizing the flow when the viscous force strongly influences the flow
Froude number Fr	Fr = $U_o / \sqrt{g h_o}$, where g is the gravitational acceleration, h_o is the inlet water depth and U_o inlet mean velocity	Characterizing the flow when the gravitational force strongly influences on the flow
Velocity magnitude V	$V = (\bar{u}_1^2 + \bar{u}_2^2 + \bar{u}_3^2)^{1/2}$	Comparing with experimental data at specific locations
Horizontal velocity $\boldsymbol{u}$	$\boldsymbol{u} = \bar{u}_1 \hat{\boldsymbol{x}}_1 + \bar{u}_2 \hat{\boldsymbol{x}}_2$, where $\hat{\boldsymbol{x}}_i$ is a unit vector in the x_i direction	Presenting the velocity contours on a horizontal plane and visualizing the flow reversals
Water surface elevation $\bar{\eta}$	Water surface elevation above the channel bottom	Comparing with experimental data at the channel centreline
Accumulative average $\langle u_i \rangle$	$\langle z \rangle = \frac{1}{T} \int_{t_0}^{t_0+T} z dt$, point velocity u_i is used as 'z' in this thesis	Determining the ensemble-average duration
Autocorrelation r_k	$r_k = \frac{1/T \sum_{t=1}^{T-k} (y_t - \bar{y})(y_{t+k} - \bar{y})}{c_0}$, where c_0 is the sample variance of the time series, y_t and y_{t+k} are time series	Measuring the correlation between univariate time series of stochastic process; this helps determine the ensemble-average duration

Table 6.1 (continued)

Velocity spectral density $E_{u_i u_i}$	Fourier transform of velocities from time domain to frequency domain	Capturing the energy cascade and comparing with the benchmark solution, the $-5/3$ law
Second derivative of streamwise velocity $\bar{u}_2''$	$\bar{u}_2'' = \partial^2 \bar{u}_2 / \partial x_1^2$	Using the Rayleigh's necessary condition to determine the flow shear-instability and the generation mechanism of flow bistability
Okubo-Weiss parameter $\bar{w}$	$\bar{w} = s_n^2 + s_s^2 - \omega_3^2$, where s_n is the normal strain component, s_s is the shear strain component, and ω_3 is the relative vorticity; the 3-D value is obtained by an average over the three dimensions	Visualizing local eddy motions and strain-dominated region
Pressure gradient $\nabla \bar{p}$	$\nabla_h \bar{p}$	Studying the generation mechanism of flow separation — the adverse pressure gradient
Water volume fraction α_2	Contour line of α_2 = 0.5	Visualizing the water surface
	Contour line of α_2 = 0.25, 0.5 and 0.75	Locating the end of the aeration length
Invert-parallel velocity u_p	The velocity that is parallel to the pipe invert and is calculated based on trigonometry	Determining the vertical velocity profiles normal to the pipe invert
Aeration length L_a	The distance from the jump toe to the location where the air volume fraction is negligible	Characteristic aeration length of hydraulic jump
Aeration length L_r	The distance from the jump toe to the location where the last flow reversal locates	Characteristic roller length of hydraulic jump
Air volume fraction α_1	Contour line of α_1 = 0.15	Determining the minimum height above the invert reached by the elevation (the maximum depth below the free surface reached by aeration)
Vorticity ω_1	$\omega_1 = \nabla \times \boldsymbol{u}$	Visualizing the eddy rotations on certain planes

Table 6.1 (continued)

Hit-rate h_r	h_r ($h_r \geq 2/3$): $h_r = (\Sigma n_i)/n$, $n_i = \begin{cases} 1, & if \left\lvert \frac{C_i}{M_i} - 1 \right\rvert \leq \delta \; or \lvert C_i - M_i \rvert \leq \omega \\ 0, & \text{otherwise} \end{cases}$	Validation metrics to judge the consistency between LES results and experimental results and the performance of a LES model setup
Factor-of-two F_2	two F_2 ($F_2 > 1/2$): $F_2 = (\Sigma n_i)/n$, $n_i = \begin{cases} 1, & if\ 0.5 \leq \lvert C_i/M_i \rvert \leq 2 \\ 0, & \text{otherwise} \end{cases}$	Validation metrics to judge the consistency between LES results and experimental results and the performance of a LES model setup
Root-mean-square deviation of velocity Δu_i	$\Delta u_i = \sqrt{\frac{1}{N}\sum (u_i - \bar{u}_i)^2}$	Representing the fluctuation about the ensemble average results
Turbulence kinetic energy	$\bar{k} = 0.5\ (\overline{u_1' u_1'} + \overline{u_2' u_2'} + \overline{u_3' u_3'})$, $\overline{u_i'}$ is the fluctuating component	Relevant to turbulence control and hydraulic efficiency improvements
Deviation, $\Delta\eta$, of the instantaneous free surface from the ensemble-averaged free surface	$\Delta\eta = \eta - \bar{\eta}$	Determining the wave height at the water surface

6.4 Ensemble average VS. conventional time-average

Based on the description of ensemble averaging given in Wilcox (2006, pages 34–35), it is equivalent to making measurements of a turbulent flow quantity in question (e.g., a velocity component or the pressure) from *n* identical experiments. These experiments are repeated with the boundary and initial conditions that differ by small random perturbations.

In our LES run, the source of perturbation in the boundary condition was that random/turbulent fluctuations were superimposed on the prespecified mean flow at the inlet boundary. The 1000 ensembles sampled from the LES output correspond to *n* experiments, which use the same mean flow condition but different turbulent fluctuations.

The perturbation in the initial condition is interpreted as follows: Each of the *n* ensembles was sampled from the LES output. The flow condition just before sampling was the initial condition for the ensemble in question. The initial condition differed from one ensemble to another, because of the turbulent nature of hydraulic jump.

Theoretically, ensembles can be sampled from LES output at random instants, meaning that for ensemble averaging, one needs not to save LES results at consecutive time steps continuously. For the conventional time averaging, one needs to do so; in addition, one needs to distinguish between so-called “slow evolution (bulk flow time scale)” and “rapid fluctuations (turbulent time scale)” of the flow field. The distinguishment is difficult to achieve without uncertainties. In this manuscript, we sampled the LES output at an equal time interval merely for convenience.

In summary, the ensemble averaging gives the expected value of a random (turbulent) variable. It is the most general type of averaging suitable for unsteady turbulent flows. The conventional time averaging integrates the continuous values over a time duration and returns the mean, and its use is limited to steady flows. Therefore, the ensemble averaging is better for applications to LES results. The ensemble averaging avoids the inconvenient and difficult segregation of flow into bulk and turbulent components.

6.5 Rotations VS. strains

Okubo-Weiss parameter gives researchers about eddy-dominated region and strain-dominated region. Rotation and strain are two fundamental aspects of fluid flow. Rotation refers to the spinning or swirling motion of fluid particles, while strain refers to the deformation or elongation of fluid elements. The rotation is important due to the concerns of channel erosion. Meanwhile, the strain is also of importance.

There are two types of strain: Linear strain measures the change in length of a fluid element compared to its original length. Shear strain measures the change in orientation of adjacent molecules as a result of these molecules slipping past each other. Strain is closely related to the concept of stress. The stress is the initial force applied to the material, while the strain is the resulting deformation of the material due to the stress. Stress is typically defined as force per unit area and is categorized into normal stress (acting perpendicular to a surface) and shear stress (acting parallel to a surface) (White, 2009).

Strain-dominated regions play a role in fluid-structure interactions, as they can exert significant forces on structures due to the abrupt changes in velocity. For example, for the water around a ship's hull or the wind loading on a building, fluid strain contributes to the forces exerted on the structure. This impact influences the structural design, stability, and durability of the system. Understanding these factors is crucial for designing and maintaining structures in environments with fluid flow, such as channels, rivers, pipelines, and more.

6.6 More realistic initial condition of TBF investigation

Should a more realistic configuration with presence of turbulent eddies be used as the initial condition for the investigation of TBF? The simple answer is no. During the state of evolution, the differences are limited to some minor features of flow between the flow initial condition i (Chapter 3) and a more realistic condition with recirculation zones. At the state of quasi-equilibrium, the key features (bistability) of the flow are dictated by which of the two sides (i.e., the side to the left and the side to the right of the channel centreline) initiates the asymmetry. It is the contrast in initial flow patterns between the two sides that matters, not the detailed configuration. The use of the simple initial conditions had minimal influence on the bistable flow results presented in this manuscript.

In the experiments, a simple yet effective way to create the contrast in initial flow patterns between the two sides is to place a barrier, blocking the flow on one side, and then to suddenly remove the barrier. Previous researchers (Kline, 1969; Ramamurthy et al., 2017) have demonstrated the effectiveness of this way in their experiments at Stanford University and Concordia University. The expanding width provides the mechanism to maintain the key features. The mechanism at work is that the occurrence of flow separation along one of the sides prevents separation along the other side.

6.7 Scaling up to a realistic scale

The results of the numerical simulation and the related laboratory work can be scaled up to a larger scale using the hydraulic similitude. The use of small models for predicting the behavior of hydraulic structures dates back at least to Leonardo da Vinci. Preliminary model studies include discharge coefficient for a weir, energy dissipation at an outlet structure, energy loss of an intake structure, flood waves and so on.

Similarity between hydraulic models and prototypes may be achieved in three basic forms: geometric similarity, kinematic similarity, and dynamic similarity. There are certain governing laws, such as the Froude number law, Reynolds number law, Weber number law, and manning's equation, that should be satisfied depending on the hydraulic conditions (Hwang et al., 1996).

7 Conclusion and scope of further studies

7.1 Conclusion

This thesis utilizes a two-phase 3-D wall-resolved large eddy simulation (LES) to investigate turbulent expanding flows in non-prismatic hydraulic structures. The simulation geometries include a rectangular straight-wall expansion (Chapter 3), circular pipes with changing slopes (Chapter 4), and a warped open-channel expansion (Chapter 5). In relation to the research questions proposed in Chapter 1, the following answers are provided: The turbulent bistable flow (TBF) has been captured through numerical simulations, and an effective approach to suppressing the TBF and flow asymmetry has been proposed. Flow choking phenomenon in sewer pipes, caused by the hydraulic jump, have been examined under the influence of different discharges and pipe slopes. The location and extent of the relevant hydraulic jump have been accurately predicted. Detailed strategies, employing various combinations of parameters and parametric values, have been explored to create a more vivid inlet boundary condition. This thesis offers practical strategies for determining the number of snapshots required for ensemble average.

After establishing the geometries, mesh grids are generated following well-referenced guidelines. To ensure the accurate prediction of all large eddies and achieve simulation convergence, an assessment of result consistency is conducted by varying mesh sizes and timesteps. This thesis, conducts more detailed investigations concerning boundary conditions, initial conditions, and duration for ensemble average in LES of turbulent expanding flows:

- For the inlet boundary, mapping the mean velocity distribution from measurements, combined with the spectral synthesiser approach to velocity fluctuations, yields satisfactory inlet conditions. An alternative approach involves using a 1/7th power-law profile combined with the vortex method. It is recommended to use an approach channel length of eight times the depth to improve turbulence statistics predictions (Chapter 5). Under the studied hydraulic conditions, there is no significant wave reflection from the outlet. Resolving the viscous sublayer in near-wall regions is crucial for accurately predicting eddy motions.
- The initial conditions of numerical simulations are regarded as the flow history. In experiments, historical scenarios influence the future ones. In numerical simulations, the flow history (initial condition) determines which of the two equilibrium states of the TBF will occur. Even if the simulation lasts for a long time, the prescribed initial condition will not completely diminish (Chapter 3).
- The duration required for ensemble average of the instantaneous flow is thoroughly studied. By using the characteristic length as a length scale (such as the aeration length for a hydraulic jump and the expansion length for an open-channel expansion) and the approach flow velocity as a velocity scale, the resulting advection time scale should be smaller than the duration. The time scale related to the fluctuation frequencies of energy-bearing eddies should also be smaller than the duration. The suitability of the ensemble average duation is further verified through evaluations of autocorrelation functions and cumulative averages.

The calculated results of the simulations have been validated with experimental data using ensemble averages of velocity distribution, pressure distribution, free-surface position, flow depth ratio, air and water velocities, roller length, and aeration length of a hydraulic jump. The results compare well with the experimental data. The computed instantaneous velocity field exhibits spectra consistency with the well-established Kolmogorov –5/3 law. The successful reproduction

of the benchmark solution means that the LES mesh resolves energy-bearing large eddies, the inertial subrange and energy cascading.

This thesis predicts the existence of turbulent flow bistability in open-channel expansions (Chapter 3). The simulations demonstrate that such geometries can have two distinct equilibrium stable states depending on the flow history. The two stable flow states differ substantially in eddy size, core rotation strength, flow reversal, and the extent of flow separation between the opposing sides about the channel centerline. The flow patterns are asymmetrical. The two flow states are virtually a mirror image of each other, in terms of velocity and pressure-gradient distributions as well as eddy rotation conditions. The occurrence is due to the dominance of shear-induced eddy motions over friction-induced eddy motions. In the case of TBF, the horizontal gradient of the ensemble average pressure field shows that ensemble average pressure is not constant along a straight transverse line within a specific horizontal plane. Measuring the pressure using a single pressure tap does not provide a representative value along this line. In reality, there are always disturbances that can trigger the switch of flow separation from one side to the other in the channel expansion.

The hydraulic jumps in circular pipes with changing slopes have complex flow features (Chapter 4), including instantaneous flow fluctuations, a 3-D core jet, irregular distributions of vorticity around the jet, wavy vertical profiles of the streamwise velocity, significant secondary flows, flow asymmetry, and pockets of alternating clockwise and counterclockwise rotations. These differ from those observed in classical jumps on horizontal floors or in sloping rectangular channels. The jump behaviour driven by flow discharge and pipe slope is complex. The Froude number at the toe of the hydraulic jump depends on both flow rate and pipe slope and constitutes part of the solution to the hydraulic jump problem. The jump can be a complete or an incomplete jump and can form in the sloping or the horizontal pipe section. The reported integral properties of the hydraulic jump are useful in addressing issues of choked flow by incomplete jumps in sewer pipes.

This study unveils the complicated 3-D turbulent structures in the non-prismatic warped open-channel expansion (Chapter 5), involving eddy motions translated from upstream and locally generated by asymmetrical separation. Comprehensive strategies are developed for model setup, parameter selection and parametric value assignment. These strategies are developed through comparisons between velocity profiles obtained from simulations and experimental data. To assess the accuracy of a given strategy and assist in the selection process, validation metrics such as root-mean-square-error, hit-rate and factor-of-two are employed.

In terms of practical applications, fitting a hump with a height of 6% the flow depth at the expansion bottom proves beneficial. This hump aids in suppressing flow bistability, enhancing flow uniformity and hydraulic efficiency, as well as reducing flow reversal, separation, and eddy motions. Turbulence kinetic energy and coherent turbulence structure in non-prismatic open channels are important for turbulence control and improving channel stability. The Okubo-Weiss parameter provides detailed turbulence activities such as vortex stretching and lengthening. It is a more efficient and less ambiguous way to quantitatively delineate the region of hydraulic jump compared to traditional visual inspection.

Compared to a prismatic channel, a non-prismatic channel exhibits more complicated flow separation, eddy formation and turbulence interaction, differentiating this thesis from previous

studies of prismatic open-channel turbulence. The LES methods in this research are reliable, efficient, and cost-effective. This LES study offers an attractive complement to physical models, laboratory experiments, and field measurements. The validated strategies in this research can be used to study turbulence under similar conditions with good accuracy.

7.2 List of publications

The following journal articles and conference papers are published as a result of this research work:

Referred journal publications:

Zeng, R., & Li, S. S. (2023). Hydraulic jump and choking of flow in pipe with a change of slope. Journal of Hydrodynamics, 1-23. DOI: 10.1007/s42241-023-0090-3

Zeng, R., & Li, S. S. (2022). Bistability of turbulent flow in open-channel expansion: Characterization and suppression. Physics of Fluids, 34(6), 065106. DOI: 10.1063/5.0089093

Zeng, R., & Li, S. S. (2023). Large-eddy simulation of free-surface turbulent flow in a nonprismatic channel. Journal of Hydroinformatics – IWA. (In review)

Conference proceedings:

Zeng, R., & Li, S.S. (2019) "Large eddy simulation of turbulent flow in ice-covered channels." CSME-CFDSC 2019 Congress, London, ON, Canada, 2–5 June 2019

7.3 Suggestions for future research

For future research, the following suggestions are purposed:

(1) Fit the hump in different types of expansions to gain a better understanding of their impact on flow characteristics and their effectiveness in reducing flow bistability; investigate the optimal dimensions, shapes and locations of the hump to enhance flow control and hydraulic efficiency in expanding flows.
(2) Study the evolution of turbulent bistable flow states, including the time required to reach equilibrium, to gain insights into their dynamics.
(3) Conduct extensive experiments and simulations on pipe transitions with varying slopes, discharges, and lengths, with a focus on water flow, to develop relationships for estimating aeration length, roller length and sequent depth of hydraulic jump in pipe transitions with changing slopes.
(4) Examine hydraulic jump in a pipe network to enhance practical engineering applications; investigate the impact of vertical curvature in pipe transitions on the location and mitigation of the hydraulic jump.
(5) Analyze boundary shear stress distributions in open-channel expansions and explore effective methods to reduce flow separation and minimize the risk of channel erosion.
(6) Investigate the influence of varying downstream channel length on LES results to further improve numerical predictions.
(7) Conduct experimental work to collect densely distributed data and analyze higher-order statistics of turbulence to develop more effective and efficient simulation techniques and strategies.
(8) Use more advanced synthetic methods for inlet turbulence fluctuations and Sustain turbulence in the approach channel.

Addressing these research areas can lead to advancements in understanding and controlling turbulent expanding flows in various hydraulic structures.

REFERRENCES

Abdelhady, M., & Wood, D. H. (2021). Studying the flow dynamics and heat transfer of stranded conductor cables using large eddy simulations. *Physics of Fluids*, *33*(1), 015120.

Ai, Z. T., & Mak, C. M. (2015). Large-eddy Simulation of flow and dispersion around an isolated building: Analysis of influencing factors. *Computers and Fluids*, *118*, 89–100.

Akan, A. O. (2006). Open Channel Hydraulics. In *Open Channel Hydraulics*.

Alauddin, M., & Basak, B. C. (2006). Development of an expansion transition in open channel sub critical flow. *Journal of Civil Engineering (IEB)*, *34*(2), 91–101.

Albayrak, I., & Lemmin, U. (2011). Secondary Currents and Corresponding Surface Velocity Patterns in a Turbulent Open-Channel Flow over a Rough Bed. *Journal of Hydraulic Engineering*, *137*(11), 1318–1334.

Antoniou, N., Montazeri, H., Wigo, H., Neophytou, M. K. A., Blocken, B., & Sandberg, M. (2017). CFD and wind-tunnel analysis of outdoor ventilation in a real compact heterogeneous urban area: Evaluation using "air delay." *Building and Environment*, *126*(June), 355–372.

Asnaashari, A., Akhtari, A. A., Dehghani, A. A., & Bonakdari, H. (2016). Experimental and numerical investigation of the flow field in the gradual transition of rectangular to trapezoidal open channels. *Engineering Applications of Computational Fluid Mechanics*, *10*(1), 272–282.

Austin, L., Skogerboe, G., & Chang, K. (1970). Subcritical Flow at Open Channel Structures Bridge Constructions. In *Reports*.

Baggett, J. S., Jimenez, J., & Kravchenko, A. G. (1997). Resolution requirements in large-eddy simulations of shear flows. *Annual Research Briefs*, 51–66.

Bailey, R. S. (2013). *Sewer Design Guide*. *858*, 248.

Bayon, A., Valero, D., García-Bartual, R., Vallés-Morán, F. J., & López-Jiménez, P. A. (2016). Performance assessment of OpenFOAM and FLOW-3D in the numerical modeling of a low Reynolds number hydraulic jump. *Environmental Modelling and Software*, *80*, 322–335.

Bervida, M., Patruno, L., Stanič, S., & de Miranda, S. (2020). Synthetic generation of the atmospheric boundary layer for wind loading assessment using spectral methods. *Journal of Wind Engineering and Industrial Aerodynamics*, *196*(December 2019).

Bhagat, R. K., Jha, N. K., Linden, P. F., & Wilson, D. I. (2018). On the origin of the circular hydraulic jump in a thin liquid film. *Journal of Fluid Mechanics*, *851*, R5.

Blanckaert, K., & Graf, W. H. (2004). Momentum Transport in Sharp Open-Channel Bends. *Journal of Hydraulic Engineering*, *130*(3), 186–198.

Box, G. E., Jenkins, G. M., Reinsel, G. C., & Ljung, G. . (2015). *Time series analysis: forecasting and control* (3rd ed.). John Wiley and Sons.

Brown, S. A., Schall, J. D., Morris, J. L., Doherty, C. L., Stein, S. M., & Warner, J. C. (2013). Urban Drainage Design Manual. Hydraulic Engineering Circular 22. *Hydraulic Engineering Circular No. 22*, *2009*(22), 478.

Burton, D., Wang, S., Tudball Smith, D., Scott, H. N., Crouch, T. N., & Thompson, M. C. (2021). The influence of background turbulence on Ahmed-body wake bistability. *Journal of Fluid Mechanics*, *926*, 1–15.

Camnasio, E., Erpicum, S., Orsi, E., Pirotton, M., Schleiss, A. J., & Dewals, B. (2013). Coupling between flow and sediment deposition in rectangular shallow reservoirs. *Journal of Hydraulic Research*, *51*(5), 535–547.

Carvalho, R. F., Lemos, C. M., & Ramos, C. M. (2008). Numerical computation of the flow in hydraulic jump stilling basins. *Journal of Hydraulic Research*, *46*(6), 739–752.

Cataño-Lopera, Y. A., Landy, B. J., & García, M. H. (2017). Unstable flow structure around partially buried objects on a simulated river bed. *Journal of Hydroinformatics*, *19*(1), 31–46.
Çengel, Y. A., & Cimbala, J. M. (2018). *Fluid Mechanics: Fundamentals and Applications* (Forth Edit).
Chapman, D. R. (1979). Computational aerodynamics development and outlook. *AIAA Journal*, *17*(12), 1293–1313.
Chen, L., Li, C., Wang, J., Hu, G., Zheng, Q., Zhou, Q., & Xiao, Y. (2022). Consistency improved random flow generation method for large eddy simulation of atmospheric boundary layer. *Journal of Wind Engineering and Industrial Aerodynamics*, *229*(September).
Cheng, H. Y., Bai, X. R., Long, X. P., Ji, B., Peng, X. X., & Farhat, M. (2020). Large eddy simulation of the tip-leakage cavitating flow with an insight on how cavitation influences vorticity and turbulence. *Applied Mathematical Modelling*, *77*, 788–809.
Cheng, Z., Hsu, T. J., & Chauchat, J. (2018). An Eulerian two-phase model for steady sheet flow using large-eddy simulation methodology. *Advances in Water Resources*, *111*(September 2017), 205–223.
Choi, B. H., Anand, N. K., Hassan, Y. A., & Sabharwall, P. (2022). Large eddy simulation of flow through an axisymmetric sudden expansion. *Physics of Fluids*, *34*(6).
Choi, H., & Moin, P. (2012). Grid-point requirements for large eddy simulation: Chapman's estimates revisited. *Physics of Fluids*, *24*(1), 011702.
Chow, V. T. (1959). *Open Channel Flow*. McGraw-Hill.
Chung, T. J. (2002). *Computational fluid dynamics*. Cambridge University Press.
Courant, R., Friedrichs, K., & Lewy, H. (1928). Über die partiellen Differenzengleichungen der mathematischen Physik. *Mathematische Annalen*, *100*(1), 32–74.
De Padova, D., & Mossa, M. (2021). Hydraulic jump: A brief history and research challenges. *Water (Switzerland)*, *13*(13).
De Padova, D., Mossa, M., Sibilla, S., & Torti, E. (2013). 3D SPH modelling of hydraulic jump in a very large channel. *Journal of Hydraulic Research*, *51*(2), 158–173.
Dewals, B., Erpicum, S., Archambeau, P., & Pirotton, M. (2012). Experimental study of velocity fields in rectangular shallow reservoirs. *Journal of Hydraulic Research*, *50*(4), 435–436.
Dhamankar, N. S., Blaisdell, G. A., & Lyrintzis, A. S. (2018). Overview of turbulent inflow boundary conditions for large-eddy simulations. *AIAA Journal*, *56*(4), 1317–1334.
Dimitriadis, P., Koutsoyiannis, D., Iliopoulou, T., & Papanicolaou, P. (2021). A global-scale investigation of stochastic similarities in marginal distribution and dependence structure of key hydrological-cycle processes. *Hydrology*, *8*(2).
Drazin, P. G., & Howard, L. N. (1966). Hydrodynamic Stability of Parallel Flow of Inviscid Fluid. *Advances in Applied Mechanics*, *9*(C), 1–89.
Durst, F. (2008). Fluid mechanics: An introduction to the theory of fluid flows. In *Fluid Mechanics: An Introduction to the Theory of Fluid Flows*. Springer.
Durst, F., Melling, A., & Whitelaw, J. H. (1973). Low Reynolds Number Flow Over a Plane Symmetrical Sudden Expansion. *Journal of Fluid Mechanics*, *64*(1), 111–128.
Ead, S. A., & Ghamry, H. K. (2002). Hydraulic jumps in circular conduits. *Proceedings, Annual Conference - Canadian Society for Civil Engineering*, *2002*(11), 789–798.
Edwards, K. B., & Edwards, D. J. M. S. A. (2018). Computation of hydraulic jump's sequent depth in sloped circular water pipe. *Advancing Hydraulic Engineering Through Innovation and Resilient Design*.
Felder, S., & Chanson, H. (2015). Phase-detection probe measurements in high-velocity free-

surface flows including a discussion of key sampling parameters. *Experimental Thermal and Fluid Science*, *61*, 66–78.
Ferrara, V., Erpicum, S., Archambeau, P., Pirotton, M., & Dewals, B. (2018). Flow field in shallow reservoir with varying inlet and outlet position. *Journal of Hydraulic Research*, *56*(5), 689–696.
Fluent, A. (2018). *ANSYS Fluent Theory Guide, release 19.2*. ANSYS, Inc.
Foti, D., Yang, X., Campagnolo, F., Maniaci, D., & Sotiropoulos, F. (2017). On the use of spires for generating inflow conditions with energetic coherent structures in large eddy simulation. *Journal of Turbulence*, *18*(7), 611–633.
García, J., Muñoz-Paniagua, J., Jiménez, A., Migoya, E., & Crespo, A. (2015). Numerical study of the influence of synthetic turbulent inflow conditions on the aerodynamics of a train. *Journal of Fluids and Structures*, *56*, 134–151.
Gargano, R., & Hager, W. H. (2002). Undular hydraulic jumps in circular conduits. *Journal of Hydraulic Engineering, ASCE*, *128*(11), 1008–1013.
Georgiou, M., & Papalexandris, M. V. (2017). Numerical study of turbulent flow in a rectangular T-junction. *Physics of Fluids*, *29*(6), 065106.
Germano, M., Piomelli, U., Moin, P., & Cabot, W. H. (1991). A dynamic subgrid-scale eddy viscosity model. *Physics of Fluids A*, *3*(7), 1760–1765.
Gousseau, P., Blocken, B., & Van Heijst, G. J. F. (2013). Quality assessment of Large-Eddy Simulation of wind flow around a high-rise building: Validation and solution verification. *Computers and Fluids*, *79*, 120–133.
Gualtieri, C., & Chanson, H. (2021). Physical and numerical modelling of air-water flows: An Introductory Overview. *Environmental Modelling and Software*, *143*(June), 105109.
Hager, W. H. (2013). *Energy dissipators and hydraulic jump* (1st ed.). Springer Dordrecht.
Han, L., Guo, C., Sun, E., & Tan, H. (2022). *Vortex dynamics downstream two-side lateral expansion in shallow open channel*. 0–20.
Haque, A. K. M. (2009). *Some characteristics of open channel transition flow*. Concordia University.
Hartley, G. E., Jain, J. P., & Bhattacharya, A. P. (1940). Report on the model experiments of fluming of bridges on Purwa branch. *Technical Memorandum*, *9*, 94–110.
He, K., Minelli, G., Su, X., Gao, G., & Krajnović, S. (2022). On state instability of the bi-stable flow past a notchback bluff body. *Journal of Fluid Mechanics*, *931*, 1–14.
He, X., Apte, S. V., Karra, S. K., & Doğan, Ö. N. (2021). An les study of secondary motion and wall shear stresses in a pipe bend. *Physics of Fluids*, *33*(11).
Henderson, F. M. (1966). *Open channel flow*. Macmillan.
Hinds, J. (1928). The Hydraulic Design of Flume and Siphon Transitions. *Transactions of the American Society of Civil Engineers*, *92*(1), 1423–1459.
Hinze, J. (1959). *Turbulence: An Introduction to Its Mechanism and Theory*. McGraw-Hill.
Holmes, P., Lumley, J. L. L., Berkooz, G., & Rowley, C. W. (2012). *Turbulence, coherent structures, dynamical systems and symmetry*. Cambridge university press.
Hotchkiss, R. H., Flanagan, P. J., & Donahoo, K. (2003). Hydraulic Jumps in Broken-Back Culverts. *Transportation Research Record*, *1985*(1851), 35–44.
Houichi, L., Dechemi, N., Heddam, S., & Achour, B. (2013). An evaluation of ANN methods for estimating the lengths of hydraulic jumps in U-shaped channel. *Journal of Hydroinformatics*, *15*(1), 147–154.
Huang, S. H., Li, Q. S., & Wu, J. R. (2010). A general inflow turbulence generator for large eddy

simulation. *Journal of Wind Engineering and Industrial Aerodynamics*, *98*(10–11), 600–617.
Hwang, N. H., Houghtalen, R. J., Akan, A. O., & Hwang, N. H. (1996). *Fundamentals of hydraulic engineering systems* (Issue Mi). Prentice Hall.
Hyatt, M. L. (1965). *Design, calibration, and evaluation of a trapezoidal measuring flume by model study*. Utah State University.
Ippen, A. T. (1949). Channel transitions and controls. *In Engineering Hydraulics: Proc.*, 496–588.
Isern-Fontanet, J., Font, J., García-Ladona, E., Emelianov, M., Millot, C., & Taupier-Letage, I. (2004). Spatial structure of anticyclonic eddies in the Algerian basin (Mediterranean Sea) analyzed using the Okubo-Weiss parameter. *Deep-Sea Research Part II: Topical Studies in Oceanography*, *51*(25-26 SPEC. ISS.), 3009–3028.
Islam, M. R., & Mohany, A. (n.d.). Vortex shedding characteristics in the wake of circular finned cylinders. *Physics of Fluids*, *32*(4), 045113.
Jesudhas, V., Balachandar, R., Roussinova, V., & Barron, R. (2018). Turbulence Characteristics of Classical Hydraulic Jump Using DES. *Journal of Hydraulic Engineering*, *144*(6), 1–15.
Jesudhas, V., Balachandar, R., Wang, H., & Murzyn, F. (2020). Modelling hydraulic jumps: IDDES versus experiments. *Environmental Fluid Mechanics*, *20*(2), 393–413.
Jirka, G. H. (2001). Large scale flow structures and mixing processes in shallow flows. *Journal of Hydraulic Research*, *39*(6), 567–573.
Kang, S., & Sotiropoulos, F. (2011). Flow phenomena and mechanisms in a field-scale experimental meandering channel with a pool-riffle sequence: Insights gained via numerical simulation. *Journal of Geophysical Research: Earth Surface*, *116*(3), 1–22.
Keating, A., Piomelli, U., Balaras, E., & Kaltenbach, H. J. (2004). A priori and a posteriori tests of inflow conditions for large-eddy simulation. *Physics of Fluids*, *16*(12), 4696–4712.
Kim, W. W., & Menon, S. (1997). Application of the localized dynamic subgrid-scale model to turbulent wall-bounded flows. *In Meeting Papers on Disc of the 35th Aerospace Sciences Meeting and Exhibit*, 97–0210.
Kline, S. J. (1969). Film Notes for Flow Visualization. In *National Comittee for for Fluid Mechanics Films*.
Kolmogorov, A. N. (1941). Dissipation of energy in the locally isotropic turbulence. *In Dokl. Akad. Nauk.*, *32*, 19–21.
Kraichnan, R. H. (1970). Diffusion by a random velocity field. *Physics of Fluids*, *13*(1), 22–31.
Li, L. X., Liao, H. S., Liu, D., & Jiang, S. Y. (2015). Experimental investigation of the optimization of stilling basin with shallow-water cushion used for low Froude number energy dissipation. *Journal of Hydrodynamics*, *27*(4), 522–529.
Li, P., Zhu, D. Z., Xu, T., & Zhang, J. (2022). Air Demand of a Hydraulic Jump in a Closed Conduit. *Journal of Hydraulic Engineering*, *148*(2), 1–12.
Li, S. S. (2022). Harmonic Function for 3D Warped Transition Geometry and Its Practical Use. *Journal of Irrigation and Drainage Engineering*, *148*(6), 1–6.
Li, S. S., Thapa, D. R., & Ramamurthy, A. S. (2019). Using Vanes to Reduce Flow Separation and Head Loss in Warped Transition. *Journal of Irrigation and Drainage Engineering*, *145*(2), 1–12.
Li, Z., Liu, C., Wan, D., & Hu, C. (2021). High-fidelity simulation of a hydraulic jump around a surface-piercing hydrofoil. *Physics of Fluids*, *33*(12).
Li, Z. W., Huai, W. X., & Han, J. (2011). Large Eddy Simulation of the interaction between wall jet and offset jet. *Journal of Hydrodynamics*, *23*(5), 544–553.
Lilly, D. K. (1966). On the application of the eddy viscosity concept in the inertial sub-range of

turbulence. In *NCAR Manuscripts*.
Lilly, D. K. (1992). A proposed modification of the German0 closure method h J axi. *Phys. Fluids*, *4*(3), 633–635.
Liu, J., Niu, J., Du, Y., Mak, C. M., & Zhang, Y. (2019). LES for pedestrian level wind around an idealized building array—Assessment of sensitivity to influencing parameters. *Sustainable Cities and Society*, *44*(October 2018), 406–415.
Liu, M., Rajaratnam, N., & Zhu, D. Z. (2004). Turbulence Structure of Hydraulic Jumps of Low Froude Numbers. *Journal of Hydraulic Engineering*, *130*(6), 511–520.
Liu, X. D., Liu, Z. Q., Tang, L. C., Han, Y., Chen, J., & Yang, S. Q. (2021). Analysis of vegetation resistance based on two typical distribution types in ecological channel. *Ecological Engineering*, *169*(June), 106325.
Liu, Z., Yu, Z., Chen, X., Cao, R., & Zhu, F. (2020). An investigation on external airflow around low-rise building with various roof types: PIV measurements and LES simulations. *Building and Environment*, *169*(December 2019), 106583.
Long, D., Steffler, P. M., & Rajaratnam, N. (1990). LDA study of flow structure in submerged hydraulic jump. *Journal of Hydraulic Research*, *28*(4), 437–460.
Long, Y., Long, X., Ji, B., & Xing, T. (2019). Verification and validation of Large Eddy Simulation of attached cavitating flow around a Clark-Y hydrofoil. *International Journal of Multiphase Flow*, *115*, 93–107.
Long, Y., Long, X. ping, Ji, B., Huai, W. xin, & Qian, Z. dong. (2017). Verification and validation of URANS simulations of the turbulent cavitating flow around the hydrofoil. *Journal of Hydrodynamics*, *29*(4), 610–620.
Lund, T. S., Wu, X., & Squires, K. D. (1998). On the Generation of Turbulent Inflow Conditions for Boundary Layer Simulations. *Journal of Computational Physics*, *140*, 233–258.
Maryami, E., Mohammadpour, R., Beirami, M. K., & Haghighi, A. T. (2021). Prediction of hydraulic jump characteristics in a closed conduit using numerical and analytical methods. *Flow Measurement and Instrumentation*, *82*(June).
Mathey, F., Cokljat, D., Bertoglio, J. P., & Sergent, E. (2006). Assessment of the vortex method for large eddy simulation inlet conditions. *Progress in Computational Fluid Dynamics*, *6*(1–3), 58–67.
MathWorks. (2022). *MATLAB version: 9.13.0 (R2022b)*. MathWorks Inc.
Mehta, P. R. (1979). Flow characteristics in two dimensional expansions. *Journal of Hydraulic Engineering*, *105*(5), 501–516.
Meile, W., Ladinek, T., Brenn, G., Reppenhagen, A., & Fuchs, A. (2016). Non-symmetric bi-stable flow around the Ahmed body. *International Journal of Heat and Fluid Flow*, *57*, 34–47.
Meneveau, C., & Sreenivasan, K. R. (1991). The multifractal nature of turbulent energy dissipation. *Journal of Fluid Mechanics*, *224*, 429–484.
Mignot, E., & Cienfuegos, R. (2010). Energy Dissipation and Turbulent Production in Weak Hydraulic Jumps. *Journal of Hydraulic Engineering*, *136*(2), 116–121.
Mignot, E., & Cienfuegos, R. (2011). Spatial evolution of turbulence characteristics in weak hydraulic jumps. *Journal of Hydraulic Research*, *49*(2), 222–230.
Minakov, A. V., Platonov, D. V., Litvinov, I. V., Shtork, S. I., & Hanjalić, K. (2017). Vortex ropes in draft tube of a laboratory Kaplan hydroturbine at low load: an experimental and LES scrutiny of RANS and DES computational models. *Journal of Hydraulic Research*, *55*(5), 668–685.
Mizushima, J., Adachi, T., & Yukinobu, S. (1999). Transitions and instabilities of flow in a

symmetric channel with a suddenly expanded and contracted part. *First Symposium on Turbulence and Shear Flow Phenomena.*, 977–982.
Mokhtarpoor, R., & Heinz, S. (2017). Dynamic large eddy simulation: Stability via realizability. *Physics of Fluids*, *29*(10), 1–22.
Montano, L., & Felder, S. (2020). LIDAR Observations of Free-Surface Time and Length Scales in Hydraulic Jumps. *Journal of Hydraulic Engineering*, *146*(4), 1–10.
Montes, S. (1998). *Hydraulics of open channel flow*. ASCE Press.
Monti, A., Omidyeganeh, M., & Pinelli, A. (2019). Large-eddy simulation of an open-channel flow bounded by a semi-dense rigid filamentous canopy: Scaling and flow structure. *Physics of Fluids*, *31*(6).
Moreno, C. J. G. (2011). Bistable flow spectral analysis. Repercussions on jet pumps. *Nuclear Engineering and Design*, *241*(7), 2437–2447.
Morris, H. M., & Wiggert, J. M. (1972). *Open Channel Hydraulics*.
Mortazavi, M., Le Chenadec, V., Moin, P., & Mani, A. (2016). Direct numerical simulation of a turbulent hydraulic jump: Turbulence statistics and air entrainment. *Journal of Fluid Mechanics*, *797*, 60–94.
Mullin, T., Shipton, S., & Tavener, S. J. (2003). Flow in a symmetric channel with an expanded section. *Artificial Intelligence in Medicine*, 1118.
Murty Bhallamudi, S., & Hanif Chaudhry, M. (1992). Computation of flows in open-channel transitions | Calcul des écoulements à surface libre avec des changements de geometrie. *Journal of Hydraulic Research*, *30*(1), 37–41.
Najafi-Nejad-Nasser, A., & Li, S. S. (2015). Reduction of flow separation and energy head losses in expansions using a hump. *Journal of Irrigation and Drainage Engineering*, *141*(3), 1–9.
Najafzadeh, M. (2019). Evaluation of conjugate depths of hydraulic jump in circular pipes using evolutionary computing. *Soft Computing*, *23*(24), 13375–13391.
Najmeddin, S., & Li, S. S. (2016). Numerical study of reducing the flow separation zone in short open-channel expansions by using a hump. *Journal of Irrigation and Drainage Engineering*, *142*(7), 1–5.
Nakagawa, H. (1993). *Turbulence in Open Channel Flows* (1st ed.). ImprintRoutledge.
Nashta, C. F., & Garde, R. J. (1988). Ecoulements fluviaux dans des élargissements brusques. *Journal of Hydraulic Research*, *26*(1), 49–65.
Nicoud, F., & Ducros, F. (1999). Subgrid-scale stress modelling based on the square of the velocity gradient tensor. *Flow, Turbulence and Combustion*, *62*(3), 183–200.
Nikoo, H. M., K., B., & Hao, H. (2018). Effectiveness of using pipe-in-pipe (PIP) concept to reduce vortex-induced vibrations (VIV): Three-dimensional two-way FSI analysis. *Ocean Engineering*, *148*, 263–276.
Nikora, V. I., Stoesser, T., Cameron, S. M., Stewart, M., Papadopoulos, K., Ouro, P., McSherry, R., Zampiron, A., Marusic, I., & Falconer, R. A. (2019). Friction factor decomposition for rough-wall flows: Theoretical background and application to open-channel flows. *Journal of Fluid Mechanics*, *872*, 626–664.
Nordin, C. F., McQuivey, R. S., & Mejia, J. M. (1972). Hurst phenomenon in turbulence. *Water Resources Research*, *8*(6), 1480–1486.
Ohtsu, B. I., & Yasuda, Y. (1991). Hydraulic jump in sloping channels. *Journal of Hydraulic Engineering, ASCE*, *117*(7), 905–921.
Okaze, T., Kikumoto, H., Ono, H., Imano, M., Ikegaya, N., Hasama, T., Nakao, K., Kishida, T., Tabata, Y., Nakajima, K., Yoshie, R., & Tominaga, Y. (2021). Large-eddy simulation of flow

around an isolated building: A step-by-step analysis of influencing factors on turbulent statistics. *Building and Environment*, *202*(October 2020), 108021.
Olinto, C. R., Indrusiak, M. L. S., & Möller, S. V. (2006). Experimental study of the bistable flow in tube arrays. *Journal of the Brazilian Society of Mechanical Sciences and Engineering*, *28*(2), 233–241.
Ottolenghi, L., Adduce, C., Roman, F., & La Forgia, G. (2020). Large eddy simulations of solitons colliding with intrusions. *Physics of Fluids*, *32*(9).
Pagliara, S., Lotti, I., & Palermo, M. (2008). Hydraulic jump on rough bed of stream rehabilitation structures. *Journal of Hydro-Environment Research*, *2*(1), 29–38.
Pagliara, S., & Palermo, M. (2015). Hydraulic jumps on rough and smooth beds: aggregate approach for horizontal and adverse-sloped beds. *Journal of Hydraulic Research*, *53*(2), 243–252.
Park, J. C., Kim, M. H., & Miyata, H. (1999). Fully non-linear free-surface simulations by a 3D viscous numerical wave tank. *International Journal for Numerical Methods in Fluids*, *29*(6), 685–703.
Patankar, S. (2018). *Numerical heat transfer and fluid flow*. Taylor & Francis.
Perić, R., & Abdel-Maksoud, M. (2016). Reliable damping of free-surface waves in numerical simulations. *Ship Technology Research*, *63*(1), 1–13.
Piomelli, U. (1993). High Reynolds number calculations using the dynamic subgrid-scale stress model. *Physics of Fluids A: Fluid Dynamics*, *5*(6), 1484–1490.
Pope, S. B. (2001). *Turbulent Flows*. Cambridge university press.
Qian, S. tuo, Zhang, Y., Xu, H., Wang, X. sheng, Feng, J. gang, & Li, Z. xiang. (2021). Effects of surface roughness on overflow discharge of embankment weirs. *Journal of Hydrodynamics*, *33*(4), 773–781.
Qian, Y., Zhu, D. Z., Zhang, W., Rajaratnam, N., Edwini-Bonsu, S., & Steffler, P. (2017). Air Movement Induced by Water Flow with a Hydraulic Jump in Changing Slope Pipes. *Journal of Hydraulic Engineering*, *143*(4), 1–11.
Rahman, M., & Chaudhry, M. H. (1997). Computation of flow in open-channel transitions. *Journal of Hydraulic Research*, *35*(2), 243–256.
Rajaratnam, N. (1967). Hydraulic Jumps. *Advances in Hydroscience*, *4*, 197–280.
Ramamurthy, A. S., Han, S. S., & Biron, P. M. (2013). Three-Dimensional Simulation Parameters for 90° Open Channel Bend Flows. *Journal of Computing in Civil Engineering*, *27*(3), 282–291.
Ramamurthy, A. S., Sanjay, B., & Rama, R. P. (1970). Open Channel Expansions Fitted with Local Hump. *Journal of the Hydraulics Division*, *96*(5), 1105–1113.
Ramamurthy, A. S., Thapa, D. R., & Li, S. S. (2017). Experimental study of flow past a warped transition. *Journal of Irrigation and Drainage Engineering*, *143*(8), 1–11.
Ramos, P. X., Schindfessel, L., Pêgo, J. P., & Mulder, T. De. (2019). Flat vs. Curved rigid-lid LES computations of an open-channel confluence. *Journal of Hydroinformatics*, *21*(2), 318–334.
Rodi, W., Constantinescu, G., & Stoesser, T. (2013). Large-eddy simulation in hydraulics. In *Journal of Hydraulic Research*. CRC Press,.
Roshko, A. (1953). On the drag and shedding frequency of two- dimensional bluff bodies. In *Technical Note 3169*.
Roy, D., Das, S., & Das, R. (2021). Characterisation of B type hydraulic jump by experimental simulation and numerical modeling using MacCormack technique. *Modeling Earth Systems and Environment*, *7*(4), 2753–2768.

Ruan, X., Zhang, X., Wang, P., Liu, W., Hu, L., & Xu, Z. (2020). Investigation on the boundary layer transition with the effects of periodic passing wakes. *Physics of Fluids*, *32*(12).
Sahu, M., Mahapatra, S. S., Biswal, K. C., & Khatua, K. K. (2014). Prediction of flow resistance in a compound open channel. *Journal of Hydroinformatics*, *16*(1), 19–32.
Salim, S., Pattiaratchi, C., Tinoco, R., Coco, G., Hetzel, Y., Wijeratne, S., & Jayaratne, R. (2017). The influence of turbulent bursting on sediment resuspension under unidirectional currents. *Earth Surface Dynamics*, *5*(3), 399–415.
Samadi, M., Sarkardeh, H., & Jabbari, E. (2020). Explicit data-driven models for prediction of pressure fluctuations occur during turbulent flows on sloping channels. *Stochastic Environmental Research and Risk Assessment*, *34*(5), 691–707.
Schatzmann, M., Olesen, H., & Franke, J. (2010). *COST 732 model evaluation case studies: approach and results.*
Scobey, F. C. (1933). The flow ofwaters in flumes. In *US Department of Agriculture Technical Bulletin 393*.
Sergent, E. (2002). *Vers une methodologie de couplage entre la Simulation des Grandes Echelles et les modeles statistiques*. Ecully, Ecole centrale de Lyon.
Sethian, J. A., & Osher, S. (1987). Fronts propagating with curvature-dependent speed: Algorithms based on Hamilton-Jacobi formulations. *Journal of Computational Physics*, *79*(87), 12–49. https://ntrs.nasa.gov/archive/nasa/casi.ntrs.nasa.gov/19880001113.pdf
Shang, J., Zhou, Q., Alam, M. M., Liao, H., & Cao, S. (2019). Numerical studies of the flow structure and aerodynamic forces on two tandem square cylinders with different chamfered-corner ratios. *Physics of Fluids*, *31*(7), 075102.
Shettar, A. S., & Murthy, K. K. (1996). A numerical study of division of flow in open channels. *Journal of Hydraulic Research*, *34*(5), 651–675.
Shin, B., & Kondo, M. (2019). Effect of gap ratio on the wake behind two side-by-side flat plates. *Journal of Applied Fluid Mechanics*, *12*(4), 1213–1222.
Singh, K. M., Sandham, N. D., & Williams, J. J. R. (2007). Numerical simulation of flow over a rough bed. *Journal of Hydraulic Engineering*, *133*(4), 343–462.
Smagorinsky, J. (1963). General Circulation Experiments With the Primitive Equations. *Monthly Weather Review*, *91*(3), 99–164.
Smirnov, A., Shi, S., & Celik, I. (2001). Random flow generation technique for large eddy simulations and particle-dynamics modeling. *Journal of Fluids Engineering, Transactions of the ASME*, *123*(2), 359–371.
Smith, C. D., & Chen, W. (1989). The hydraulic jump in a steeply sloping square conduit. *Journal of Hydraulic Research*, *27*(3), 385–399.
Smith, C. D., & Yu, J. N. G. (1966). Use of Bafflesin open channel expansions. *Journal of the Hydraulics Division*, *92*(2), 1–17.
Soulsby, R. L. (1980). Selecting record length and digitization rate for near-bed turbulence measurement. *Journal of Physical Oceanography*, *10*(2), 208–219.
Stahl, H., & Hager, W. H. (1999). Hydraulic jump in circular pipes. *Canadian Journal of Civil Engineering*, *26*(3), 368–373.
Stanković, B. D., Belošević, S. V., Crnomarković, N. D., Stojanović, A. D., Tomanović, I. D., & Milićević, A. R. (2017). Specific aspects of turbulent flow in rectangular ducts. *Thermal Science*, *21*, S663–S678.
Stojnic, I., Pfister, M., Matos, J., & Schleiss, A. J. (2021). Effect of 30-Degree Sloping Smooth and Stepped Chute Approach Flow on the Performance of a Classical Stilling Basin. *Journal*

of Hydraulic Engineering, *147*(2).
Sukhodolov, A. N., Schnauder, I., & Uijttewaal, W. S. J. (2010). Dynamics of shallow lateral shear layers: Experimental study in a river with a sandy bed. *Water Resources Research*, *46*(11), 1–18.
Sukhodolov, A. N., & Uijttewaal, W. S. J. (2010). Assessment of a River Reach for Environmental Fluid Dynamics Studies. *Journal of Hydraulic Engineering*, *136*(11), 880–888.
Swamee, P. K., & Basak, B. C. (1991). Design of rectangular open-channel expansion transitions. *Journal of Irrigation and Drainage Engineering*, *117*(6), 827–838.
Swamee, P. K., & Basak, B. C. (1993). Open-channel transition design expansion. *Irrigation and Drainage Engineering*, *119*(1), 1–17.
Tabor, G. R., & Baba-Ahmadi, M. H. (2010). Inlet conditions for large eddy simulation: A review. *Computers and Fluids*, *39*(4), 553–567.
Takahashi, M., & Ohtsu, I. (2017). Effects of inflows on air entrainment in hydraulic jumps below a gate. *Journal of Hydraulic Research*, *55*(2), 259–268.
Tennekes, H., & Lumley, J. L. (1972). *A First Course in Turbulence*. MIT press.
Thapa, D. R., Li, S. S., & Ramamurthy, A. S. (2018). Experimental study of flow characteristics in wedge and modified wedge transitions. *Journal of Hydraulic Engineering*, *144*(8), 1–12.
Thomas, T. G., & Williams, J. J. R. (1995). Large eddy simulation of turbulent flow in an asymmetric compound open channel. *Journal of Hydraulic Research*, *33*(1), 27–41.
Thordal, M. S., Bennetsen, J. C., & Koss, H. H. H. (2019). Review for practical application of CFD for the determination of wind load on high-rise buildings. *Journal of Wind Engineering and Industrial Aerodynamics*, *186*(October 2018), 155–168.
Thysen, J. H., van Hooff, T., Blocken, B., & van Heijst, G. J. F. (2021). CFD simulations of two opposing plane wall jets in a generic empty airplane cabin: Comparison of RANS and LES. *Building and Environment*, *205*(May), 108174.
Tokyay, T., & Sinha, S. (2020). Channel width, bedform length and turbulence: numerical investigation of flow dynamics over laboratory-scale pool–riffle sequences. *Environmental Fluid Mechanics*, *20*(4), 819–842.
Tominaga, A., Nezu, I., Ezaki, K., & Nakagawa, H. (1989). Structure turbulente à trois dimensions dans des écoulements à surface libre en canal rectiligne. *Journal of Hydraulic Research*, *27*(1), 149–173.
Tuna, M. C., Ozkan, F., & Baylar, A. (2014). Experimental investigations of aeration efficiency in high-head gated circular conduits. *Water Science and Technology*, *69*(6), 1275–1281.
Uijttewaal, W. (2014). Hydrodynamics of shallow flows: Application to rivers. In *Journal of Hydraulic Research* (Vol. 52, Issue 2).
USACE. (1991). Hydraulic Design of Flood Control Channels. In *Engineer Manual No. 1110-2-1601*. Department of the Army Corps of Engineers.
Valero, D., Bung, D. B., & Crookston, B. M. (2018). Energy Dissipation of a Type III Basin under Design and Adverse Conditions for Stepped and Smooth Spillways. *Journal of Hydraulic Engineering*, *144*(7).
Vasaturo, R., Kalkman, I., Blocken, B., & van Wesemael, P. J. V. (2018). Large eddy simulation of the neutral atmospheric boundary layer: performance evaluation of three inflow methods for terrains with different roughness. *Journal of Wind Engineering and Industrial Aerodynamics*, *173*(January 2017), 241–261.
Vatankhah, A. R. (2021). Conjugate depths in partially filled sewers and pipes. *Environmental Fluid Mechanics*, *21*(3), 605–617.

Vittal, N., & Chiranjeevi, V. V. (1983). Open channel transitions: Rational method of design. *Journal of Hydraulic Engineering*, *109*(1), 99–115.
Walter, R. K., Nidzieko, N. J., & Monismith, S. G. (2011). Similarity scaling of turbulence spectra and cospectra in a shallow tidal flow. *Journal of Geophysical Research: Oceans*, *116*(C10).
Wang, C., & Samuel Li, S. (2018). Hydraulic jump and resultant flow choking in a circular sewer pipe of steep slope. *Water (Switzerland)*, *10*(11), 1–18.
Wang, H., & Murzyn, F. (2017). Experimental assessment of characteristic turbulent scales in two-phase flow of hydraulic jump: from bottom to free surface. *Environmental Fluid Mechanics*, *17*(1), 7–25.
White, F. M. (2009). *Fluid mechanics.* McGraw-Hill.
Wilcox, D. C. (2006). *Turbulence Modeling for CFD* (Third Edit). Dcw Industries, Incorporated.
Witt, A., Gulliver, J. S., & Shen, L. (2018). Numerical investigation of vorticity and bubble clustering in an air entraining hydraulic jump. *Computers and Fluids*, *172*, 162–180.
Wu, J. hua, Zhou, Y., & Ma, F. (2018). Air entrainment of hydraulic jump aeration basin. *Journal of Hydrodynamics*, *30*(5), 962–965.
Wu, X. (2017). Inflow Turbulence Generation Methods. *Annual Review of Fluid Mechanics*, *49*(May 2016), 23–49.
Xiao, Y., Huai, W., Gao, M., Yang, Z., & Ji, B. (2019). Evaluating the hydrodynamics of a round jet in a vegetated crossflow through large eddy simulation. *Environmental Fluid Mechanics*, *19*(1), 181–201.
Xie, B., Gao, F., Boudet, J., Shao, L., & Lu, L. (2018). Improved vortex method for large-eddy simulation inflow generation. *Computers and Fluids*, *168*, 87–100.
Xie, Z., Lin, B., & Falconer, R. A. (2013). Large-eddy simulation of the turbulent structure in compound open-channel flows. *Advances in Water Resources*, *53*, 66–75.
Yan, C., Nepf, H. M., Huang, W. X., & Cui, G. X. (2017). Large eddy simulation of flow and scalar transport in a vegetated channel. *Environmental Fluid Mechanics*, *17*(3), 497–519.
Yang, X. I. A., & Griffin, K. P. (2021). Grid-point and time-step requirements for direct numerical simulation and large-eddy simulation. *Physics of Fluids*, *33*(1), 1–11.
Younus, M., & Hanif Chaudhry, M. (1994). A depth-averaged k-ε turbulence model for the computation of free-surface flow: Modèle de turbulence k-ε moyenne sur la verticale pour ie calcul des écoulements à surface libre. *Journal of Hydraulic Research*, *32*(3), 415–444.
Yu, Y., Yang, Y., & Xie, Z. (2018). A new inflow turbulence generator for large eddy simulation evaluation of wind effects on a standard high-rise building. *Building and Environment*, *138*(March), 300–313.
Yue, W., Lin, C. L., & Patel, V. C. (2005). Large eddy simulation of turbulent open-channel flow with free surface simulated by level set method. *Physics of Fluids*, *17*(2), 1–12.
Zang, T. A. (1991). Numerical simulation of the dynamics of turbulent boundary layers: perspectives of a transition simulator. *Philosophical Transactions of the Royal Society of London. Series A: Physical and Engineering Sciences*, *336*(1641), 95–102.
Zeng, R., & Li, S. S. (2022). Bistability of turbulent flow in open-channel expansion: Characterization and suppression. *Physics of Fluids*, *34*(6).
Zhan, J. M., Li, Y. T., Wai, W. H. O., & Hu, W. Q. (2019). Comparison between the Q criterion and Rortex in the application of an in-stream structure. *Physics of Fluids*, *31*(12).
Zhang, G., Wang, H., & Chanson, H. (2013). Turbulence and aeration in hydraulic jumps: Free-surface fluctuation and integral turbulent scale measurements. *Environmental Fluid Mechanics*, *13*(2), 189–204.

Zhang, J., Minelli, G., Rao, A., Basara, B., Bensow, R., & Krajnović, S. (2018). Comparison of PANS and LES of the flow past a generic ship. *Ocean Engineering*, *165*(July), 221–236.

Zhang, S., Kwok, K. C. S., Liu, H., Jiang, Y., Dong, K., & Wang, B. (2021). A CFD study of wind assessment in urban topology with complex wind flow. *Sustainable Cities and Society*, *71*(March 2020).

Zhang, Y., Cao, S., & Cao, J. (2022). An improved consistent inflow turbulence generator for LES evaluation of wind effects on buildings. *Building and Environment*, *223*(May), 109459.

Zhao, F., Wang, R., Zhu, H., Ping, H., Bao, Y., Zhou, D., Cao, Y., & Cui, H. (2021). Large-eddy simulations of flow past a circular cylinder near a free surface. *Physics of Fluids*, *33*(11).

Zheng, X., Montazeri, H., & Blocken, B. (2020). CFD simulations of wind flow and mean surface pressure for buildings with balconies: Comparison of RANS and LES. *Building and Environment*, *173*(February), 106747.

Zheng, X., Montazeri, H., & Blocken, B. (2021). CFD analysis of the impact of geometrical characteristics of building balconies on near-façade wind flow and surface pressure. *Building and Environment*, *200*(December 2020), 107904.

Zigunov, F., Sellappan, P., & Alvi, F. (2020). Reynolds number and slant angle effects on the flow over a slanted cylinder afterbody. *Journal of Fluid Mechanics*.